Oxidative dehydrogenation of ethane with carbon dioxide over iron-nickel nano-alloys supported on metal oxide overlayers

By

Shaine Raseale

MSc in Structural Chemistry and Spectroscopy, Universität Leipzig (Germany, 2017)

BSc (Hons) Chemistry, University of Limpopo (South Africa, 2013)

BSc Chemistry and Biochemistry, University of Limpopo (South Africa, 2012)

Thesis submitted to the University of Cape Town

in fulfilment of the requirements for the degree of

Doctor of Philosophy

DSI-NRF Centre of Excellence in Catalysis (c*change)

Catalysis Institute

Department of Chemical Engineering

University of Cape Town

South Africa

Jun 2022

CATCENTRE
Centre for Catalysis Research

cchange
DST-NRF Centre of Excellence in Catalysis

“Festina lente.”

-Augustus

Declaration

I, **Mr Shaine Raseale**, declare that the content of this unique thesis submission is my own unaided work, except for the information acquired from literature sources and my prescribed supervisors. All formal sources of information from literature have been adequately acknowledged and referenced in honour of the efforts of all the authors and their work. I have not received assistance from any other source in completing this work. This thesis has also not been, is not being and is not to be submitted for another degree at the University of Cape Town or any other university. I consent the University of Cape Town to reproduce either the whole or any part of the contents of this work in any manner whatsoever for the purpose of research.

Signature: Signed by candidate ..... Date: 13/06/2022 .....

Acknowledgements

Firstly, I am grateful to God for the grace and the emotional, mental and physical strength to endeavour, endure and navigate through the cul-de-sac and ordeal of this journey with tenacity and determination.

I also express my particular and heartfelt gratitude to my supervisors, A/Prof. Nico Fischer and Prof. Michael Claeys (UCT), for granting me a chance to join their research group, working under their insightful supervision. I am specifically indebted to A/Prof Nico Fischer for taking a challenge to train me despite my inexperience in catalysis, for his patience, trust and confidence in me, constant support, encouragement and selfless guidance, the will to share his knowledge and the time he has always availed and dedicated towards my PhD training and life at large.

I also convey special thanks to our collaboration partner, Dr Gonzalo Prieto for welcoming me in his lab at Max-Planck-Institut für Kohlenforschung (Germany), introducing me to his kind research group and playing a role as my supervisor away from home. Thanks to Sebastian Haben for introducing me to the synthesis of overlayers. Thanks to Kai Jeske, Dr. Bidyut Bikash Sarma, Dr. Jonglack Kim, Eva Andres and Marcos Garcia Farpón for their help in the lab. I further extend this gratitude also to Norbert Pfänder (Max-Planck-Institut für Chemische Energiekonversion) for his kind help with STEM analysis.

To Wijnand Marquart and Dr. Thulani Nyathi, I am wholeheartedly grateful for your help in the lab, reviewing my work and also your frequent availability to offer such invaluable inputs and advice during the discussions we always had. The success of most of this work depended on your inputs. I also extend this to Dr. Mohamed Fadlalla, Dominic De Oliveira, Dr. Sundaram Ganesh Babu and Dr. Moritz Wolf. The contributions by Bongani Mtetwa, Malcolm Mapeta, Christoper Mullins and Hélda Mandlate during their 4th year chemical engineering course as well Jara Landschoff during her 2nd year vac work cannot go unnoticed also.

To Motlokoa Khasu and other current and past members of our research group as well as Noluvuyo Ndila, Musa Dumisani Maluleke, Dr. Temitope Oladele and all the other friends I made in the Department of Chemical engineering, your help in the lab/friendship is greatly appreciated. I wish you well for the future.

I am also thankful to the Department of Chemical engineering Analytical Lab for help with ICP-OES and the access to H_2-TPR, N_2-Physisorption and NH_3-TPD analysis. To the Aaron Klug Centre for Imaging and Analysis (UCT), Mohamed Jaffer and Miranda Waldron, thank you for help with TEM and SEM/EDX analysis.

Thanks to the National Research Foundation (NRF) and the DSI-NRF Centre of Excellence in Catalysis (*c**change) as well as *Bundesministeriums für Bildung und Forschung* (BMBF, Germany) for funding throughout this journey. I also acknowledge the Catalysis Society of South Africa (CATSA) and the 17th International Congress on Catalysis (IACS) for the ICC 2020 Young Scientist Travel Support awards despite the cancellation of the conference which followed.

Finally, I express my deepest gratitude to my family for their lifelong and consistent love, sacrifices, support and encouragement. I also thank my loving partner Malebo Ella Moloko for her love, support, patience and understanding during my entire postgraduate journey. My friends Dr. Penny Mathumba, Wilson Mhlari and Thato Malatji, I thank you too for the support since we met.

This thesis is dedicated to my late father Herry Tloutswala Raseale and late sister Kgaugelo Raseale. Your lives remain a blessing and your memories a treasure. You are loved beyond words and missed beyond measure.

Synopsis

The CO_2-mediated oxidative dehydrogenation of ethane (CO_2-ODHE) is one of the promising alternative routes for simultaneous conversion of ethane and the greenhouse gas (GHG) CO_2 into high-demand monomers: ethylene and CO [1,2]. It has been extensively investigated on oxide catalysts with those based on Cr, V and Ga exhibiting high yields and selectivity for ethylene but those deactivate rapidly [3–12]. The reaction follows a Mars van Krevelen mechanism where the oxide is partially reduced upon ethane activation and subsequently re-oxidized upon CO_2-activation [13]. Thus, suitable redox properties as well as Lewis acidity of metal oxides are some essential properties governing catalytic performance [13–15]. The lower stability of these materials is linked to their failure to act as multifunctional catalysts that can prevent carbon build-up *via* the dissociation of CO_2 while co-activating ethane. Promoters such as Fe-based oxides have been studied to enhance the CO_2-activation functionality and stability of the oxides [5].

A Density Functional Theory (DFT) study suggested that bimetallic alloys can have superior activity for CO_2-activation compared to their monometallic counterparts [16]. Therefore, bimetallic alloys in conjunction with metal oxides may serve as stable bifunctional CO_2-ODHE catalysts with enhanced CO_2-activation ability. Improved CO_2-activation can boost the re-oxidation rate of the metal oxide *via* a spillover-type mechanism and aid in coke removal *via* the reverse Boudouard reaction [5,11]. Recent studies have already demonstrated this experimentally with a series of supported Fe_xNi_y catalysts prepared *via* impregnation which, depending on Fe : Ni ratio and support, can promote either the CO_2-ODHE or the competing ethane dry-reforming (DRE) reactions with enhanced CO_2-activation [17,18,18–20]. However, composition and crystallite size uniformity are difficult to attain *via* impregnation as Ni and Fe oxide phases present in parallel make it challenging to extract the influence of the Fe_xNi_y alloy metallic composition [21]. This work aims to synthesize catalytically active metal oxide overlayers of a comparable pore structure, anchor Fe_xNi_y nano-alloys of uniform composition with Fe and Ni in close proximity and investigate the combined effect of the overlayer support's acidity/reducibility and alloy composition on the catalytic performance under CO_2-ODHE conditions.

The close proximity of Fe and Ni in the alloy is introduced by the use of oxidic Ni-ferrite spinel structures as precursors of the alloy which is formed upon their reduction in H_2 atmosphere and was found to exist as a mixture of a bcc and an fcc phases depending on Fe : Ni ratio. A higher Fe content in the alloy increases the fraction of the bcc phase as confirmed *via* H_2-TPR studies

in *in situ* XRD. *In situ* XRD temperature-programmed CO_2-activation studies also revealed that CO_2 is only able to react with the bcc phase of the alloy which is re-oxidised into the oxidic Ni-ferrite spinel while the fcc phase is stable against re-oxidation.

While they deactivate rapidly due to a limited re-oxidation and coking caused by insufficient CO_2-activation, the bare metal oxide overlayers exhibit an initial activity that reduces with a decrease of the surface acid site strength until a minimum is reached and then slightly increases with increasing basicity under CO_2-ODHE conditions. Their catalytic stability increases with weakening of the acid site strength. Decreasing the overlayer acidity enhances the CO_2-ODHE/DD (DD : direct dehydrogenation) activity resulting in increased ethylene and decreased CO selectivity. Spent catalyst analysis revealed the formation of surface carbonaceous deposits suspected to cause catalyst deactivation. Increasing the concentration of CO_2 in the feed results in improved and sustained CO_2-activation which enhances the reverse Boudouard reaction and improves the catalyst stability by reducing carbon deposition while reducing ethylene and increasing CO selectivity.

Deposition of the Fe_xNi_y nano-alloys of Fe : Ni atomic ratios of 1, 3 and 5 on the reducible and acidic $CrO_x@Al_2O_3$ results in an alloy composition-dependent catalyst performance, while the alloys are essentially inactive over the less acidic and unreducible $ZrO_x@Al_2O_3$. This clearly confirms a bifunctional character of these materials and reveals that their catalytic performance depends on both the overlayer reducibility/acidity and the metallic composition of the alloy. Over $CrO_x@Al_2O_3$, the alloy enhances the CO_2-activation functionality with increasing Ni-content boosting the overall activity and stability of the catalyst. However, with increasing Ni-content, the CO selectivity increases while ethylene selectivity reduces due to the suppressed CO_2-ODHE/DD activity and promotion of the competing DRE reaction. The target CO_2-ODHE/DD reaction activity is maximal at an overall Fe : Ni atomic ratio of 5, about 10% at a ratio of 3 and completely suppressed at a ratio of 1. Spent catalyst analysis revealed formation of surface carbonaceous deposits and that the bcc phase of the alloy is re-oxidised into the Ni-ferrite oxidic spinel phase while the fcc phase of the alloy is stable against re-oxidation during the reaction. Increased CO_2 concentration in the feed has similar effects as described for the bare overlayers.

Deposition the Fe_3Ni_1 and Fe_5Ni_1 nano-alloys on $GaO_x@Al_2O_3$, $VO_x@Al_2O_3$, $SmO_x@Al_2O_3$ and $TiO_x@Al_2O_3$ revealed that despite the alloy composition, a predominant DRE activity is observed over the highly acidic and reducible $VO_x@Al_2O_3$. While $CrO_x@Al_2O_3$ and $GaO_x@Al_2O_3$ show a

similar performance when tested bare, the addition of the Fe_3Ni_1 and Fe_3Ni_1 alloys on the $GaO_x@Al_2O_3$ overlayer results in a high CO_2-ODHE/DD activity with stability decreasing with increasing Fe-content. Over $TiO_x@Al_2O_3$, the Fe_3Ni_1 nano-alloy exhibits a similar behaviour as over $GaO_x@Al_2O_3$ while higher iron contents resulted in an inactive catalyst. Over $SmO_x@Al_2O_3$ no alloy composition yields appreciable catalytic activity. The CO_2-ODHE/DD behaviour of $Fe_3Ni_1/GaO_x@Al_2O_3$ is in stark contrast to the high DRE activity over $Fe_3Ni_1/CrO_x@Al_2O_3$ emphasising that a specific alloy composition exists for each overlayer to yield a stable and dominating CO_2-ODHE/DD or DRE activity. For a high and stable CO_2-ODHE/DD activity, the optimum in atomic Fe : Ni ratio was found to be between the 3 and 5 at intermediate-intermittent overlayer acidity. In addition to improving stability, increased CO_2 concentration in the feed was found to significantly accelerate an observed active site re-construction during reaction which results in formation of more CO_2-ODHE/DD sites.

Contents

List of figures

List of tables

Nomenclature

Acronyms

2WV	Two-way valve
2WNV	Two-way needle valve
3WV	Three-way valve
ADF-STEM	Annular dark-field in the scanning transmission electron microscopy
AMCT	Adsorbate-to-metal charge transfer
bcc	body-centred cubic
BEP	Brønsted-Evans-Polanyi
BET	Brunauer-Emmett-Teller
CAPEX	Capital Expenditure
CCS	Carbon Capture and Sequestration
CCU	Carbon Capture and Utilization
CO_2-ODHE/P/B	Carbon Dioxide Mediated Oxidative Dehydrogenation of Ethane, propane or butane
CCR	continuous catalyst regeneration
DAC	Direct Air Capture
DCC	Deep Catalytic Cracking
DD	Direct Dehydrogenation
DFT	Density Functional Theory
DRM/E	Dry Reforming of Methane or Ethane
DR-UV/Vis	Diffuse Reflectance Ultra-violet/ Visible spectroscopy
DTA	Differential thermal analysis
EDX	Energy Dispersive X-ray analysis

EOR	Enhanced Oil Recovery
fcc	face-centred cubic
FIC	Flow indicator and control
FTIR	Fourier-transform infrared spectroscopy
FTS	Fischer-Tropsch Synthesis
FCC	Fluid Catalytic Cracking
GC	Gas chromatograph
GHGs	Greenhouse Gases
GTL	Gas to Liquid
ICP-OES	Inductively Coupled Plasma-Optical Emission Spectroscopy
IMCT	Intra-molecular charge transfer transition
IWI	Incipient Wetness Impregnation
KIT-6	Korea Advanced Institute of Science and Technology-6
MFC	Mass flow controller
MTO	Methanol-to-Olefins
MTBE	methyl tertiary butyl ether
MvK	Mars-van-Krevelen
OCM	Oxidative Coupling of Methane
PIC	Pressure indicator and control
PR	Pressure regulator
PTFE	Polytetrafluoroethylene
PTL	Power-to-Liquid
rpm	Revolutions per minute
RWGS	Reverse Water Gas Shift
SEM	Scanning Electron Microscopy

SC	Thermal Steam Cracking
SS	Stainless steel
STEM	Scanning Transmission Electron Microscopy
TEM	Transmission Electron Microscopy
TEOS	Tetraethoxysilane
TGA	Thermogravimetric analysis
TOS	Time on stream
TPD	Temperature-Programmed Desorption
TPR	Temperature-Programmed Reduction
UOP	Universal Oil Products
USD	United States Dollar
WGS	Water Gas Shift
XRD	X-ray Diffraction

1 Introduction

The development of reactions able to valorise alternative feedstocks, instead of the dwindling classic fossil resources, into high-demand chemicals is expected to play a key role in the transition towards a sustainable future. It is thus crucial that these reactions are economical and environmentally benign. Within this transition, catalysis research, which aims to innovatively develop stable catalysts that can effectively accelerate and steer reactions to desired products, plays a central role [22]. Unconventional light-alkane sources like shale, stranded and associated gas are deemed candidates to become the backbone of the future global chemical economy [23,24]. This is due to their estimated abundance, accessibility, and intrinsic lower carbon footprint than crude oil. Depending on the source, they may contain up to 15 vol.-% of a mixture of ethane (C_2H_6), propane (C_3H_8) and butane (C_4H_{10}) with C_2H_6 as the second most abundant compound succeeding methane [1]. Especially with the discovery of large global shale gas reserves, the C_2H_6 component is underutilized because it is available in surplus exceeding the demand, in spite of its affordability [25,26]. These light-alkanes contain C-C bonds that can be dehydrogenated to form value-added light olefins such as ethylene and propylene. Hence, their efficient conversion to such olefins would add value and potentially reduce flaring activities [24,27].

Ethylene and propylene are valuable building blocks among other light olefins with an annual market value beyond 250 billion USD [19,28]. This is due to their wide-range of applications in the manufacturing processes of chemical products such as plastics, synthetic lubricants, plasticizers, fibres, etc. Polyethylene makes up to 60% of the total use of the ethylene monomer. The world ethylene production capacity is expected to reach 290 Mt in 2030 with a growth rate of 4% pa [28–30]. Currently, routes such as thermal steam cracking (SC), catalytic direct dehydrogenation (DD), oil refinery upgrading, etc. are devoted to the industrial conversion of light-alkanes and crude oil derivatives to olefins [28,31,32]. SC of naphtha and C_2H_6 is the most dominant process, producing > 80% of the total global ethylene [28]. Unfortunately, these routes suffer from thermodynamic limitations of conversion and selectivity, high-energy demands, CO_2 and NO_x emissions, expensive noble metal usage, catalyst deactivation and heat transfer issues due to coking, over-oxidation and cracking [1,14,33]. Alternatively, light olefins can be produced from non-petroleum sources *via* the oxidative coupling of methane (OCM), methanol-to-olefins (MTO) and a modified Fischer-Tropsch synthesis (FTS) [34–37]. OCM and MTO are associated with high CO_2 emissions (6-10 CO_2 t/olefin t) whereas the modified FTS is not industrially employed and requires large CAPEX investments.

Another issue of tantamount importance, necessitating research to increase societal sustainability, is the development of efficient technologies for the mitigation of emissions of anthropogenic greenhouse gases (GHGs). Probably the most prominent of these gases is CO_2, showing a global climate change potential and ocean acidification effects [38–40]. CO_2 capturing and sequestration (CCS) from point sources (*i.e.* power plants, exhaust stack gas, etc.) has been the focus of intense research in the past with significant progress achieved as 40 Mt pa global capture capacity was reached in 2020 [41–45]. However, this is still not enough and comes with additional transportation and storage costs, despite efforts to increase the capacity to 5.64 Gt pa by 2050 [45]. Research efforts focusing on the development of technology for the direct capture of CO_2 from air to address decentralized emissions are also gaining momentum [46–49]. However, the strong reliance of this technology on the availability of excess, clean and cheap (renewable) energy makes its viability challenging. To date, interest has somewhat shifted to the development of CO_2 capture and utilization (CCU) technology to compensate the cost of capturing by forming value-added products instead of storage [47]. These processes encompass "recycling" CO_2 as a feedstock in novel or adapted processes (in)directly to value-added chemicals or fuels [41,50].

Currently, only six large-scale chemical processes utilizing CO_2 have found industrial application: (1) calcined soda production by the Solvay method, (2) production of urea (112 Mt CO_2 pa), (3) methanol synthesis (2 Mt CO_2 pa), (4) production of salicylic acid (30 kt CO_2 pa), (5) production of cyclic carbonates (40 kt CO_2 pa) and (6) CO_2-enhanced oil recovery (EOR, 70-80 Mt CO_2 pa) [51–53]. The latter is not a true utilization process but rather a CCS technique with added benefits. CO_2 is also used for cooling, fire suppression, metal fabrication and in the food and beverage industry. However, all these applications together with CCS are dwarfed by the global CO_2 emissions which were still increasing by 40 Gt/pa in 2020 [45,54]. Therefore, supplementary processes capable of converting large volumes of CO_2 to value-added commodity products are still sought. A wide-range of promising catalytic, electrochemical, biological, mineralization, photocatalytic and synthetic approaches have been proposed or are investigated [47,50,55–57]. Direct CO_2-hydrogenation to methanol, hydrocarbons or substitute natural gas, methane/ethane Dry Reforming (DRM/E) and ethane (light-alkane) CO_2-mediated Oxidative Dehydrogenation (CO_2-ODHE) represent some of the thermo-catalytic approaches [14,19,22,28,50,58,59].

CO_2-ODHE forms the core of the present work and it stands out due to its potential to co-activate C_2H_6 in tandem with CO_2 to the monomers, ethylene and CO, without the requirement of green hydrogen [14,27]. Thermodynamically, the reaction is feasible at temperatures greater than 550 °C, while still limited in conversion [60]. The major competing reactions are DRE and DD, with both also being thermodynamically feasible at these temperatures. Therefore, the promotion of CO_2-ODHE over competing reactions can only be achieved kinetically using catalysts designed to present the necessary active sites. Catalysts must be able to activate C_2H_6 by cleaving the C-H bond but preserving the C-C bond while dissociating/activating CO_2 to regenerate active surface/lattice oxygen (O*) species. Metal oxides with specific Lewis acid-base/redox properties are the most explored for this purpose [1,5,61]. The key challenges for catalyst systems in the CO_2-ODHE include:

1. The difficult activation/dissociation of the thermodynamically stable CO_2 molecule. This is important as it maintains the redox mechanism by replenishing the O* species which activate C_2H_6 and maintain catalyst stability by removing carbon deposits [14,19,28].
2. The requirement of a finely balanced oxidation activity by the catalyst, which should be enough to activate the C_2H_6 *via* H-abstraction (C-H bond cleavage) but not too strong to trigger DRE (C-C cleavage) and over-oxidation forming *syngas* and CO_x products respectively.
3. The reaction shares the temperature window of thermodynamic feasibility with DRE, DD, over-oxidation, etc. Therefore, the chosen catalyst must kinetically suppress the competing reactions to achieve high selectivity.

As a result, new systems such as the multifunctional bimetallic Fe_xNi_y nano-alloys and Mo_2C-based catalysts are starting to surface in the field [1,18,19,60,62–65]. Chen *et al*. [19] were the first to explore supported Fe_xNi_y nano-alloys and their work has shown that a Ni-rich composition (overall Fe : Ni atomic ratio of 0.33) of the nano-alloy favours DRE whereas the Fe-rich composition (overall Fe : Ni atomic ratio of 3), CO_2-ODHE. This suggests that by fine-tuning the Fe_xNi_y nano-alloy composition, the dominating pathway of the catalytic conversion of CO_2 and C_2H_6 can be manipulated. In the Fe_3Ni_1 sample, Fe was observed to partially segregate resulting in a Ni-rich alloy phase and a Ni-FeO_x interface. This interface is potentially responsible for the observed CO_2-ODHE activity [62]. A Density Functional Theory (DFT) study by Han *et al*. [16] suggests that the energy barrier for CO_2 dissociation in CO_2-involving reactions should be lower on certain bimetallic alloy surfaces compared to their monometallic counterparts. The role of the

alloy in the CO_2-ODHE is therefore to enhance CO_2-activation which is hard to achieve on metal oxides exclusively. When enhanced, CO_2 activation can help keep the oxidic phase stable and active by replenishing the O* species necessary for the continuous redox mechanism. In a more recent study, Chen *et al.* [18] also proposed that anchoring the Fe_3Ni_1 nano-alloy on a reducible metal oxide support further enhances the CO_2-ODHE activity. It is worth noting that the supported Fe_xNi_y nano-alloys used in the above-mentioned studies were deposited onto the supports *via* co-impregnation. Co-impregnation tends to yield catalysts with Ni and Fe oxide phases present in parallel with non-uniformity in crystallite sizes and composition in each crystallite [21].

In the present work, the effect of the physicochemical properties of both the supported Fe_xNi_y nano-alloys (metallic composition) and the metal oxide overlayer support (overall and Lewis surface acid site strength and reducibility) on the simultaneous catalytic conversion of CO_2 and C_2H_6 is presented. A novel approach was used to synthesize supports comprising of a highly dispersed overlayer of a metal oxide (CrO_x, GaO_x, SmO_x, TiO_x, VO_x and ZrO_x) coated onto a common γ-Al_2O_3 carrier. The obtained supports show different chemical properties (overall and Lewis surface acid site strength and reducibility) which are characteristic of the metal oxide overlayer while maintaining the physical properties (BET surface area, pore volume and diameter) of the γ-Al_2O_3 carrier. Although the surface dispersed overlayers offer these advantages, it is noteworthy that they will perform differently compared to their bulk counterparts due to the differences in certain chemical properties affecting active sites as reported in literature [66–70]. Furthermore, oxidic Fe_xNi_y nanoparticles were used as precursors of the supported nano-alloys and were prepared separately *via* a surfactant-free solvothermal route before immobilization onto the various metal oxide overlayer supports. This helped attain crystallites of uniform size (approx. 10 nm) and target composition enabling the formation of the corresponding Fe_xNi_y nano-alloys with close intimacy of metals compared to the common impregnation techniques. Additionally, this technique allowed a detailed *in situ* characterisation to capture the evolution of the supported oxidic Fe_xNi_y nanoparticles into the corresponding supported Fe_xNi_y nano-alloys during reduction unravelling the microstructural phases. This also allowed understanding of the behaviour of the materials in the presence of CO_2 without the co-reactant (C_2H_6) as well as the interaction of the supported nano-alloys with CO_2 and the effect of crystal space group on CO_2-activation ability.

2 Literature Overview

2.1 Ethylene and other light olefin formation processes

Ethylene is a widely used chemical monomer in the petrochemical industry which is converted into a broad spectrum of derivatives. These are ultimately converted into products such as plastics and synthetic fibres with high economic value. The plethora of ethylene products are ultimately utilized in the packaging, transportation and construction industries as well as many other consumer and industrial markets (see Figure 2.1).

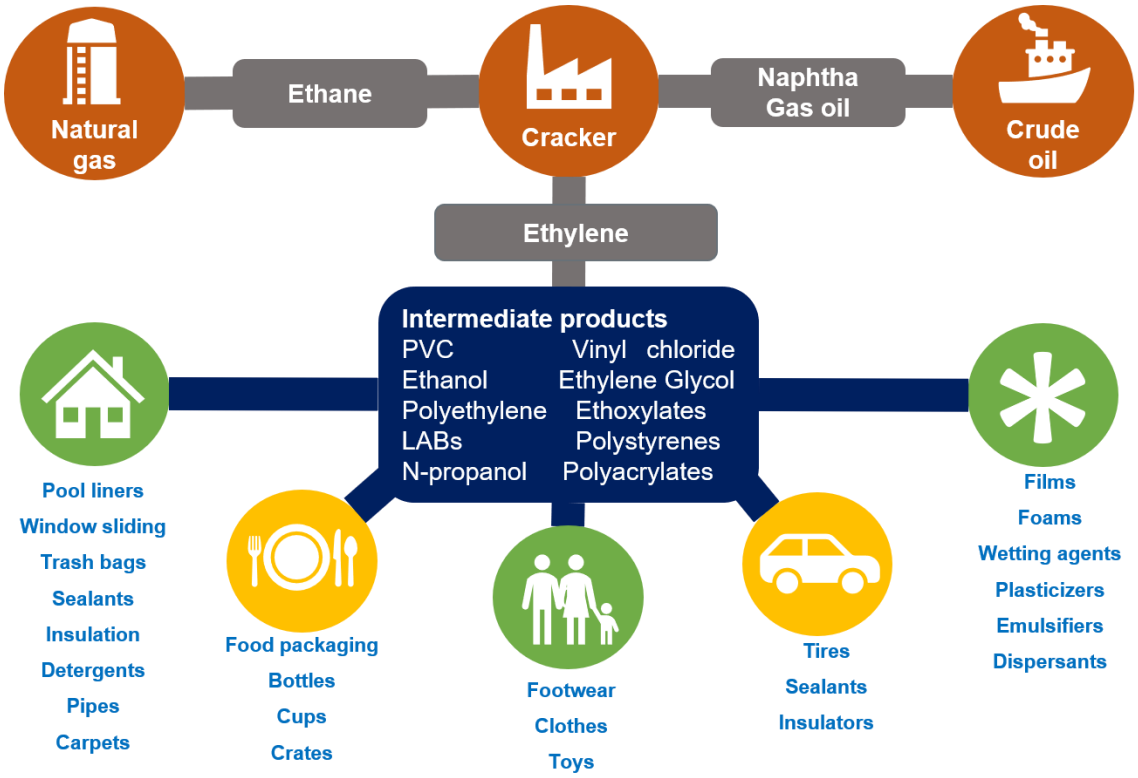

Figure 2.1:Some feedstocks mostly used in thermal cracking for ethylene production, ethylene derivatives and their major applications. Inspired by [71–73].

The packaging industry accounts for more than 50% of ethylene consumption globally [73]. Just like any olefin, this is mainly due to its high reactivity emanating from the carbon-carbon double bond compared to saturated hydrocarbons. Ethylene is converted to more chemical products than any other intermediate due to its properties, affordability and technical factors [71]. Ethylene conversion reactions yield fewer by-products than other olefins. Hence, its demand keeps

increasing steadily (4 - 5%) every year as a result of the increasing global population and the rise in living standards [72,74]. Its current commercial production processes are dominated by thermal steam cracking (SC) and fluid catalytic cracking (FCC) over H-ZSM-5 zeolite-containing catalysts [73]. Recently other promising alternative processes such as the modified Fischer Tropsch synthesis, methanol to olefins, oxidative coupling of methane, direct catalytic dehydrogenation, and oxidative dehydrogenation, have received increased attention in research.

2.1.1 Thermal stream cracking (SC)

Thermal steam cracking (SC) is currently the prevalent and most economically viable process for large-scale ethylene and propylene production. It is highly endothermic and consequently, operates at elevated temperatures in the range of 700 - 950 °C [75]. The operation temperature varies depending on the hydrocarbon feedstock. The process entails reacting diluted steam with pre-heated hydrocarbon feedstocks from fossil fuel derivatives (crude oil, naphtha, gasoil and condensates, natural gas, etc.) in a tubular reactor suspended in a gas-fired furnace [76,77].

Initiation:

$CH_3CH_3 \longrightarrow CH_3^{\cdot} + CH_3^{\cdot}$

Propagation:

$CH_3CH_3 + CH_3^{\cdot} \longrightarrow CH_4 + CH_3CH_2^{\cdot}$

$CH_3CH_2^{\cdot} \longrightarrow CH_2{=}CH_2 + H^{\cdot}$

$H^{\cdot} + CH_3CH_3 \longrightarrow H_2 + CH_3CH_2^{\cdot}$

Termination:

$2CH_3CH_2^{\cdot} \longrightarrow CH_3CH_2CH_2CH_3$

$CH_3CH_2^{\cdot} + H^{\cdot} \longrightarrow CH_3CH_3$

Disproportionation:

$CH_2{=}CH_2 + CH_3CH_2^{\cdot} \longrightarrow CH_3CH_2CH_2CH_2^{\cdot}$

$2CH_3CH_2CH_2CH_2^{\cdot} \longrightarrow CH_3CH_2CH_2{=}CH_2 + CH_3CH_2CH_2CH_3$

$CH_2{=}CH_2 + CH_3^{\cdot} \longrightarrow CH_3CH_2CH_2^{\cdot}$

$2CH_3CH_2CH_2^{\cdot} \longrightarrow CH_3CH_2{=}CH_2 + CH_3CH_2CH_3$

Figure 2.2: Thermal steam cracking radical-promoted reaction mechanism using C_2H_6 as the feedstock. Adopted from [78].

This thermochemical reaction occurs with short residence times through the uncatalyzed radical-promoted chain reaction mechanism involving initiation, propagation and termination steps as shown in Figure 2.2 describing the mechanism for a C_2H_6 feedstock. The initiation step involves the formation of free radicals *via* the homolysis of the C-C or C-H bonds. In the propagation step, the produced radicals abstract hydrogen atoms from the alkane molecules forming shorter alkanes and more alkyl radicals which then undergo β-cleavage to form the corresponding olefins, other non-radicals and shorter alkyl radicals. Thus, this process involves dehydrogenation and hydrogen transfer from hydrogen-rich hydrocarbons and cracking of hydrogen-deficient higher molecular hydrocarbons. Both these reactions account for the chain shortening, isomerization and cyclization reactions taking place in the system with other undesired secondary reactions resulting in a variety of products. Despite the secondary reactions, light olefins are the primary products of SC [7,8]. The formation of non-radical products results in the termination of the reaction since the products have no further reactivity with respect to chain initiation. Reaction conditions such as cracking temperature, residence time, hydrocarbon-to-steam ratio and pressure can be optimized to control ethylene selectivity depending on the hydrocarbon feedstock [34]. Traditionally, the residence time ranges from a fraction of a second to a few seconds [75]. The energy required during the reaction is generated by fuel combustion within the furnace. Crude oil derivatives are the major feedstocks for the process globally, but C_2H_6 extracted from shale gas is becoming a more attractive alternative feedstock due to affordability and abundance [76,79]. However, upgrading from liquid- to C_2H_6-based SC technology may present complications in the integrated downstream processing units since different reactor effluents will form [80]. This gaseous feedstock may also require a new separation technology which comes at a cost offsetting the affordability of C_2H_6. Direct SC, through which the cost can be reduced by up to 200 USD/t of ethylene by skipping the traditional refining step, is also gaining interest and becoming competitive. Exxon Mobil has already commissioned a world-scale SC facility in 2014 producing 1 Mt of ethylene per annum directly from crude oil. Sabic and Saudi Aramco also announced a joint venture to leverage on this cost-efficient crude-to-olefins route [81].

Due to the elevated operation temperatures and high endothermicity, SC is generally the most energy-intensive process in the petrochemical industry accounting for about 8% of the sector's energy demand. The energy cost is responsible for about 70% of the production cost. Consequently, the process accounts for a CO_2 global emission of more than 300 Mt pa and a significant amount of NO_x emissions [37,82]. Furthermore, a widely distributed spectrum of by-products such as CO, H_2, CH_4, C_2H_2, C_{3+}, etc. are formed during the process which makes

separation and purification difficult. The use of C_2H_6 as a feedstock results in less by-products formed. Intense coke formation on the inner surface of the reactor is also a great problem during SC since it influences the pressure drop, ethylene selectivity and heat transfer in the reactor. Thus, stopping the operation for decoking of the reactor is a common practice in SC plants and represents an additional topic for research and development of the technology [83]. These drawbacks fuel the search for sustainable alternative routes for commercial production of ethylene.

2.1.2 Catalytic cracking

Catalytic cracking is another route for the formation of light olefins. This process forms products similar to SC but proceeds at moderate temperatures (450 - 560 °C) in the presence of a heterogenous catalyst which helps to improve the process efficiency. Typical examples of catalytic cracking are fluid catalytic cracking (FCC), hydrocracking and deep catalytic cracking (DCC). FCC is primarily used for large-scale production of gasoline with high octane number over the zeolite Y in most oil refineries, with light olefins forming as secondary products from gasoline and distillate fuels in the fluidized bed reactor [34]. Thus, obtaining high light olefin selectivity is still a challenge in FCC. Although many other acidic solid catalysts have been tested, zeolites are the best performing materials for these cracking processes. Zeolite Y serves as the main component in several FCC process catalyst systems utilized industrially. These catalyst systems include the rare earth-exchanged HY (REHY), rare earth-exchanged Y (REY), H-form of ultra-stable Y (HUSY) and rare earth-exchanged H-form USY. Recently, the zeolite ZSM-5 is utilized as a co-component to maximize the selectivity towards light olefins while maintaining high gasoline yield during high severity FCC [84,85]. This high severity FCC process operates at temperatures above 550 °C at short contact times and high catalyst to oil ratios. During FCC, light olefins form through the β-cracking of long chain paraffins, olefin side chains of alkyl aromatics and naphthalenes. To increase the yield of light olefins, catalysts additives, such as dealuminated zeolites and ZSM-5, can help minimize the hydrogen transfer reaction to preserve olefins, maintain good throughput and gasoline quality [85]. Coking and formation of undesired products in low concentrations are typical during FCC and usually require sophisticated separations.

2.1.3 Modified Fischer-Tropsch synthesis (FTS)

The commercial CO hydrogenation (FTS) over transition metal catalysts such as Fe and Co for production of linear alkanes, terminal olefins and oxygenates has also been proposed to serve as an alternative for the production of light olefins. The product distribution depends strongly on reaction temperature. For instance, at low-temperature, high-molecular weight linear alkanes dominate whereas terminal olefins are dominant in the high-temperature mode. However, FTS plants are expensive to build mainly due to the air separation unit required for formation of the *syngas* (CO and H_2 mixture) feed *via* gasification of carbonaceous resources like coal, natural gas or biomass. For instance, the largest FTS- plant, Shell's PEARL GTL, producing 140 000 barrels of products per day and an additional 120 000 barrels of natural gas liquids and C_2H_6, required investments of about 18 - 19 billion USD. The air separation unit technology alone accounted for about 70% of the total cost of the plant [86]. Nonetheless, *syngas* production from methane is less expensive and associated with a higher carbon efficiency than from biomass and coal which is H_2-deficient and requires supplementation *via* the water gas shift (WGS) reaction. The WGS reaction has a negative impact on the overall carbon efficiency since it is associated with high carbon emissions [87]. Furthermore, the value and viability of the FTS process is heavily challenged and dictated by both crude oil and natural gas price fluctuations since it serves as an alternative for fuel production in regions without crude oil [80].

Research on this topic has been ongoing since the 1950s but the interest also fluctuates with the oil prices [88]. The research mostly focuses on the development of chemical promoters and supports for Fe-, Co-, Ni-, Mo- or Rh-based catalysts to enhance light olefin selectivity. Despite the number of publications, the process is still not commercialized due to high methane production with low light olefin selectivity and mechanical or chemical instability of the proposed catalysts. Fe-based catalysts are more attractive as they tend to lower methane production owing to the presence of active sites for C-C coupling and methane formation which are tuneable by modification with promoters, mixing with other oxides and use of different supports [88,89]. Fe-based catalysts also allow the direct conversion of a CO-rich *syngas* due to their higher water gas shift (WGS) activity. These materials can also withstand contaminants typically present in coal or biomass-based *syngas*. For instance, Torres Galvis *et al.* [89] observed a lower methane production with higher light olefin selectivity over Na/S-promoted Fe-based catalysts. This was attributed to a promoted termination *via* β-hydride abstraction and restricted termination of chain growth *via* hydrogenation caused by selective blockage of hydrogenation sites by sulphur. A

review by de Jong *et al.* [88] shows that Fe-based catalysts in bimetallic systems or mixed with oxides of Ti, V, Mo, W, Zn or Mn as well as with alkali metal promoters on supports like SiO_2, γ-Al_2O_3, TiO_2 and zeolites, are the most promising demonstrating high light olefin selectivity with lower methane yield. However, challenges such as extensive carbon deposition, catalyst reproducibility, complexity and stability still hinder commercialization.

2.1.4 Methanol-to-olefins (MTO)

A *syngas* mixture can alternatively be used to produce methanol, which can in turn be used to catalytically form a wide-range of commodity chemicals, including high-purity light olefins *via* the MTO process. This process, which leverages on active acid sites to convert methanol to hydrocarbons, was first introduced by ExxonMobil in the 1970s and later patented by both ExxonMobil and UOP/Hydro [80,90–92]. ExxonMobil uses the zeolite Socony Mobil-5 (ZSM-5) as the catalyst whereas silico-alumino phosphate-34 (SAPO-34) is used in the UOP/Hydro process. Research and development has resulted in an improved carbon selectivity (75-80%) towards ethylene and propylene on a shape selective SAPO-34 material at lower acidity. Furthermore, by tuning the process conditions, ethylene to propylene ratios in the range of 0.5 to 1.5 can be obtained and the light olefin yield can be increased by integration of the MTO and an olefin-cracking process [93]. China has already commissioned an MTO plant based on coal (coal-to-olefins; CTO) with a production capacity of 15.5 Mt pa However, the CO_2 emissions of CTO plants are estimated to be about 7 - 10 t/t of olefin which is significantly higher than the 1 t/t in SC. Another major drawback associated with the MTO process generally is the rapid catalyst deactivation as a result of coke deposition still being a major topic for research in the field [80].

2.1.5 Oxidative coupling of methane (OCM)

Instead of the indirect MTO and modified FTS pathways which rely on the formation of *syngas* to form light olefins, oxidative coupling of methane (OCM) can be used. OCM has the potential to directly activate methane (natural gas) to light olefins and valuable higher hydrocarbons avoiding the need to initially produce *syngas*. OCM stems from the pioneering work of Keller and Bhasin in 1982 and has resulted in substantial research activity since [36,80,94]. Despite having been the topic of interest for about 38 years with promising results, the process is still not commercialized due to the lack of an effective, stable and coke-resistant catalyst and remains a topic of research. In OCM, methane reacts with oxygen in the presence of a catalyst *via* intermediate C-C coupling steps to form C_2H_6 and H_2O. Subsequently, the formed C_2H_6 further reacts with the oxidant to form ethylene and H_2O. Some literature report the involvement of gaseous radicals where C_2H_6 or ethylene forms *via* C-C coupling of two $\cdot CH_3$ or $\cdot CH_2$ radicals respectively resulting from C-H bond cleavage by oxidized catalyst sites [80,95,96]. Undesired deep oxidation may also occur from unselective gas-phase radical reactions forming CO_x, especially in the presence of oxygen at high temperatures (600 - 900 °C). The major challenges of this reaction are the high exothermicity of reactions occurring, which may require novel reactor designs before commercialization, and the low ethylene yields [36,97]. To prevent the undesired deep oxidation, a softer oxidant such as CO_2, which does not promote intense unselective radical reactions, can be utilized [98]. This would make CO_2-mediated OCM (CO_2-OCM) a powerful multi-purpose process as it serves as a simultaneous CO_2 and CH_4 utilization route, co-activating them into high-demand intermediates such as ethylene. Mechanistically, CO_2-OCM would proceed in four steps, *viz* [36]:

a. Cleavage of the C-H bond of methane molecules on the solid surface
b. Dissociation of CO_2 into CO and O surface species which are ultimately incorporated into the lattice of the metal oxide (lattice oxygens)
c. Recombination of $\cdot CH_3$ or $\cdot CH_2$ radicals
d. Oxidative/radical dehydrogenation of the primary product C_2H_6 to ethylene

Although not commercialized, catalyst development for CO_2-OCM has been a subject of research for some time and several potential materials as well as properties playing key roles to influence catalytic performance have been identified. In general, strong basic metal oxides such as early lanthanides-based oxides, basic monophasic oxides loaded with group 1 or 2 elements (e.g.

Li/MgO, Ba/MgO, and Sr/La_2O_3) and transition metal oxides with group 1 cations ($Na_2WO_4/Mn/SiO_2$) and chloride promoters have been identified as potential catalysts for O_2/CO_2-OCM reactions [36,99–103]. The reaction has proven to depend strongly on physicochemical properties such as basicity, nature of promoter, surface area, reaction temperature, metallic compositions, etc.

2.1.6 Direct catalytic dehydrogenation

Another direct and commercial route for the production of light olefins, primarily propylene (ca. 14 Mt/year), is the catalytic dehydrogenation (DD) of saturated light alkane feedstocks [104]. DD has been industrially applied since the 1930s [105]. This process is an on-purpose route and therefore allows the formation of the target olefin product in very high selectivity, outperforming even the SC process. Tedious product separation is unnecessary. However, the formation of coke deposits which tend to deactivate the catalyst cannot be avoided in DD. Frequent catalyst regeneration, either cyclic or continuous, is necessary to maintain activity. These regeneration approaches have led to two major industrial processes currently operational at commercial scale. These are the Catofin (Lummus) and the Oleflex (UOP-Universal Oil Products) processes [77].

The Catofin process was pioneered by CBI Lummus and originates from the *Houdry* Catadiene process which was used exclusively in the dehydrogenation of isobutane to isobutene, a precursor for the methyl tertiary butyl ether (MTBE) production [106]. Due to environmental concerns, the use of MTBE as an octane enhancer was phased-out, resulting in the revamp of Catofin plants for the dehydrogenation of propane. The Catofin process is also used for the dehydrogenation of n-butane to butadiene and butylene. A total of 14 Catofin plants have been licensed for production of propylene and 15 for isobutylene. The process operates at 575 °C under a lower pressure between 0.2 - 1.0 bar in multiple (5 - 8) parallel adiabatic fixed-bed reactors which continuously alternate between the dehydrogenation, coked catalyst regeneration and purging process steps. CrO_x/Al_3O_3 with a Na or K promoter serves as the catalyst for this process and usually has a lifespan of about 2 - 3 years which is achieved by gradually increasing the temperature to counteract the progressive loss of activity over time. Catalyst deactivation due to coking and thermal sintering of the Al_2O_3 support, resulting in the loss of the surface area, are the major drawbacks associated with the Catofin process [77,107].

Comparatively, the Oleflex process by UOP (Honeywell) encompasses a fluidized bed reactor system (usually 3 or 4 adiabatic radial flow reactors) consisting of catalyst regeneration and product recovery units loaded with a Pt - Sn catalyst also supported on Al_2O_3 with a Na or K promoter. The catalyst flows through the system and is regenerated in the last reactor which is connected to the continuous catalyst regeneration (CCR) unit that burns off coke and re-disperses Pt on the support material. Regeneration of Pt before re-dispersion is achieved by treatment with a chlorine-air mixture. The regenerated catalyst is then cycled back into the first reactor with an entire cycle taking about 5 - 10 days to be completed. The Oleflex process operates at 525 - 705 °C and a pressure between 1 - 3 bar and is utilized for the dehydrogenation of propane and isobutane [108]. In addition to coking and thermal sintering of the Pt nanoparticles, catalyst attrition due to the fluidized bed is an issue leading to catalyst deactivation. The Oleflex catalyst has a lifetime of 1 - 3 years [104]. To reduce deactivation due to coking, techniques such as addition of hydrogen diluent have been developed. This increases the catalyst lifetime to a few days. However, it also causes a small decrease of the thermodynamic driving force [108]. Another major drawback associated with this process is the use of the noble metal Pt and the associated material costs.

Overall, DD processes suffer from two major drawbacks: (1) the endothermicity-induced thermodynamic limitation of the conversion of the alkane that necessitates high energy inputs and (2) the rapid catalyst deactivation which is mostly a result of coking. Thermodynamic limitations increase with decreasing carbon number of the saturated alkane. Thus, DD of C_2H_6 is more difficult than that of propane and higher hydrocarbons. Dehydrogenation of higher alkanes results in the formation of olefins with allylic hydrogens. H-abstraction from allylic positions has a greater susceptibility towards the formation of coke precursors due to its low bond dissociation energy relative to saturated substrates [36,109].

2.1.7 Oxidative dehydrogenation of light alkanes

Oxidative dehydrogenation (ODH) is generally described as a partial oxidation reaction in which H_2, that is otherwise evolved as the dehydrogenation product, is further oxidized to H_2O by atomic oxygen (O*) species [33]. Although not yet commercialized, this route garnered research interest in the last two decades as a potential alternative for on-purpose activation of light alkanes to olefins using O_2 as oxidant (*i.e.* O_2-ODH, see Equation 2.1 for O_2-ODHE). Due to the presence of

O_2, O_2-ODH is exothermic and therefore can be operated at a lower temperature range (300 - 600 °C) with lower thermodynamic restrictions than the on-purpose DD route [9,14,28].

$C_2H_6 + O_2 \leftrightarrow C_2H_4 + H_2O$ $\quad\quad \Delta H^{\circ}_{25\,^{\circ}C} = -149\ kJ/mol$ *Equation 2.1*

The presence of an oxidant also offers an increased equilibrium constant of the reaction by scavenging the dissociated hydrogen species. Thus, ethylene/olefin production is thermodynamically favoured due to the high enthalpy of formation of water which also removes the thermodynamic constraints typically associated with the DD. This offers advantages such as reduced external heat input which may result in less coke build-up and improved catalyst stability. O_2 is an inexpensive oxidant with low environmental impact. However, supressing the undesired over-oxidation of the saturated light alkanes forming CO_x (CO and CO_2 as well as H_2O) products under O_2-ODH conditions is a major challenge. Overoxidation occurs *via* the oxygen insertion in the C-H bond of the alkane reactant during the primary activation step or *via* oxygen addition to the alkene product. This reaction is highly likely due to the strong oxidation ability of O_2 and its suppression is still a topic of research with some considerable progress [9,110]. For instance, Lu *et al*. [111] and Hermans *et al*. [112] recently reported an SBA-15-supported boron oxide and a hexagonal boron nitride catalysts with 73.3% (14.8% propane conversion at 450 °C) and 79% (14% propane conversion at 490 °C) propylene selectivity, respectively. Even with this progress, there are still concerns about the need to remove excess heat of reaction and the flammability of the reaction atmosphere due to the presence of O_2 which may hinder practical implementation.

To counter the overoxidation challenge and increase olefin selectivity, the use of soft oxidants or H_2-acceptors such as CO_2, N_2O, S_2, SO_2, halogens/halides, etc. is considered an attractive alternative [113–118]. These soft oxidants are considered to have the potential to positively shift reaction equilibria, act as cocatalysts/promoters and possess competitive adsorption abilities. SO_2 can potentially form by-products such as COS and CS_2 which are toxic and corrosive [119]. Despite its thermodynamic feasibility, S_2 tends to compel operation of the process at higher temperatures (648 - 800 °C) to avoid formation of S-polymorphs, but thermal cracking cannot easily be avoided at such high temperatures [117].

Since the work of Krylov *et al.* [120], CO_2 is considered as prime candidate for a mild oxidant since it is less hazardous than N_2O and SO_2 and it has the highest heat capacity [5,121]. Despite

its endothermicity (see Equation 2.2 for CO_2-ODHE), which makes it less thermodynamically favourable relative to the exothermic O_2-ODH, CO_2-ODH is still more favourable than DD.

$$C_2H_6 + CO_2 \leftrightarrow C_2H_4 + CO + H_2O \qquad \Delta H^{\circ}_{25\,^{\circ}C} = 134\ kJ/mol \qquad \textit{Equation 2.2}$$

CO_2 can shift the reaction equilibrium towards olefin formation by acting as an acceptor for the H_2 product, consuming it *via* the reverse water gas shift reaction (RWGS) [5]. In fact, depending on the catalyst material, there are two proposed pathways through which CO_2-ODH can occur: (a) DD to form the olefin and H_2 followed by the RWGS reaction between the H_2-acceptor (CO_2) and H_2 (see Equation 2.3 and Equation 2.4) and; (b) selective ODH which forms the final products (especially H_2O) directly on the catalyst surface without the formation of H_2 (see Equation 2.2) [13]. In the former, CO_2 acts as the H_2-acceptor and consumes the H_2 product directly on the surface of a suitable catalyst whereas in the latter CO_2 provides the suitable catalyst with reactive oxygen species which in turn facilitate the dehydrogenation of the light alkane into the olefin and H_2O. Related mechanistic details will be discussed in section 2.3. These pathways may also occur concurrently [115].

$$C_2H_6 \leftrightarrow C_2H_4 + H_2 \qquad \Delta H^{\circ}_{25\,^{\circ}C} = 137\ kJ/mol \qquad \textit{Equation 2.3}$$

$$CO_2 + H_2 \leftrightarrow CO + H_2O \qquad \Delta H^{\circ}_{25\,^{\circ}C} = 41\ kJ/mol \qquad \textit{Equation 2.4}$$

CO_2 is also able to react with carbon deposits on a catalyst through the reverse Boudouard gasification reaction (see Equation 2.5). Thus, CO_2 may help reduce coke formation, which is believed to be prevalent and to play a key role in catalyst deactivation at high reaction temperatures, thereby removing the decoking step necessary for DD [8,122]. Suzuki *et al*. [9] showed that Ga_2O_3/TiO_2 catalysts tested for ODHE at 650 °C tend to form more and unreactive carbon deposits in the absence than in the presence of CO_2. Furthermore, addition of CO_2 proved to keep the catalyst active slightly longer though this effect was even enhanced upon addition of both CO_2 and steam. Using a pulsed reaction technique, CO_2 was also found to aid in the rapid desorption of the target ethylene product accounting for the typically observed increased selectivity [9,123]. CO_2 has also proven to exhibit some promoting effects during ODH. For instance, Wang *et al*. [124] has shown that CO_2 adsorbates that are either formed during or added to the reaction increased the selectivity towards ethylene from 75% to 83.8% on a Li^+/MgO catalyst at 650 °C. The enhanced selectivity was ascribed to CO_2's ability to poison active sites

on the catalyst surface that react with alkyl radicals in secondary reactions to form undesired products. Suzuki *et al*. [11] also observed an enhanced C_2H_6 conversion from 9.6% to 19.6% over Ga_2O_3 and 10.4% to 12.1% over Cr_2O_3 during ODHE in the presence of CO_2 compared to in its absence. The use of CO_2 as an oxidant in ODHE also makes it an eco-friendly process as it serves as an alternative vehicle for the large volume utilization of this greenhouse gas (GHG) thereby contributing to a future circular carbon economy [36].

$CO_2 + C \leftrightarrow 2CO \qquad \Delta H^{\circ}_{25\,^{\circ}C} = 172\ kJ/mol$ *Equation 2.5*

The main challenge in the presence of CO_2 is that, instead of the desired selective cleavage of the C-H bond *via* CO_2-ODH, both the C-H and C-C bonds can be cleaved *via* DR (see Equation 2.6 for DRE) which is thermodynamically feasible at the same temperature range [60]. This reaction is also a useful CO_2 utilization route which results in the formation of the slightly H_2-defficient value-added synthesis gas.

$C_2H_6 + 2CO_2 \leftrightarrow 3CO + 4H_2 \qquad \Delta H^{\circ}_{25\,^{\circ}C} = 429.7\ kJ/mol$ *Equation 2.6*

Extensive thermodynamic studies from our group and others show that more reactions are feasible at the same temperature range [1,13,20,60,65,117]. For instance, when C_2H_6 and CO_2 react together, the prospect of side reactions such as the non-selective oxidation of C_2H_6 (see Equation 2.7), C_2H_6 cracking (see Equation 2.8), disproportionation (see Equation 2.9) and coke formation (see Equation 2.10 and Equation 2.11), present even more drawbacks regarding olefin selectivity [13].

$C_2H_6 + 5CO_2 \leftrightarrow 7CO + 3H_2O \qquad \Delta H^{\circ}_{25\,^{\circ}C} = 421\ kJ/mol$ *Equation 2.7*

$C_2H_6 + H_2 \leftrightarrow 2CH_4 \qquad \Delta H^{\circ}_{25\,^{\circ}C} = -64.9\ kJ/mol$ *Equation 2.8*

$2C_2H_6 \leftrightarrow 2C_3H_8 + CH_4 \qquad \Delta H^{\circ}_{25\,^{\circ}C} = -113\ kJ/mol$ *Equation 2.9*

$C_2H_6 \leftrightarrow 2C + 3H_2 \qquad \Delta H^{\circ}_{25\,^{\circ}C} = 84.7\ kJ/mol$ *Equation 2.10*

$C_2H_4 \leftrightarrow 2C + 2H_2$ $\Delta H^{\circ}_{25\,^{\circ}C} = -52.3\ kJ/mol$ *Equation 2.11*

CO_2 is also chemically and thermodynamically stable and thus difficult to activate. On the other hand, light alkane activation is also a challenging task requiring high energy input due their low intrinsic reactivity [36,109]. The olefin products are intrinsically more reactive with enhanced directed bonding onto several catalytic surfaces compared to the feed materials, especially the alkanes, which interact mainly *via* dispersion forces [105]. These factors make the development of suitable catalysts for the process challenging. However, the key to simultaneous conversion of CO_2 and the alkane lies in the cleavage of the C=O bond in CO_2 along with the competitive cleavage of the C–H (CO_2-ODH) or both C-H and C–C (DR) bonds in the respective alkane [19,62,63,125].

2.2 Overview of CO_2 capture and utilization technologies

Fossil fuel reserves such as crude oil, coal and natural gas, exploited for energy generation and chemical production, have allowed a faster development of our society since the end of the 19th century [126]. There was a steep increase in the exploitation of these raw materials in the middle of the 20th century owing to the industrial revolution which resulted in advancement of technology and rapid population and global economic growth (see Figure 2.3).

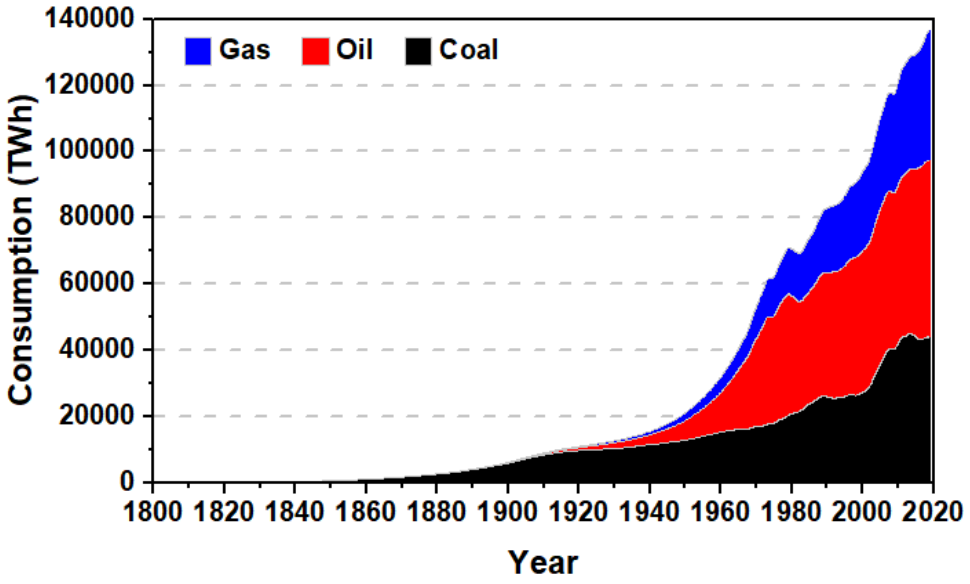

Figure 2.3: Global fossil fuel consumption since 1800 in terawatt-hour (TWh). Data sourced from [126].

However, fossil fuel reserves are diminishing and their utilization is directly linked to catastrophic climate change due to the emission of GHGs, largely CO_2 [127]. Based the stoichiometry of combustion, 1 t of fossil fuel yields 3.5 t of CO_2. Although 33% of the yearly emitted CO_2 (33.4 Gt in 2019) is fixated by plants *via* photosynthesis, 22% is absorbed by oceans causing palpable acidification and the remainder ultimately accumulates in the atmosphere [40,128]. The current atmospheric CO_2 level of 415 ppm has never been reached, at least in the past traceable 650 000 years and is largely a consequence of anthropogenic emissions [43]. High atmospheric CO_2 levels have increased the global surface temperature by 1.5 °C compared to before industrial revolution (see Figure 2.4) [129]. As long as emissions continue, unavoidable climate transitions will occur, and may proceed beyond a point of no return (above the “2 °C scenario”).

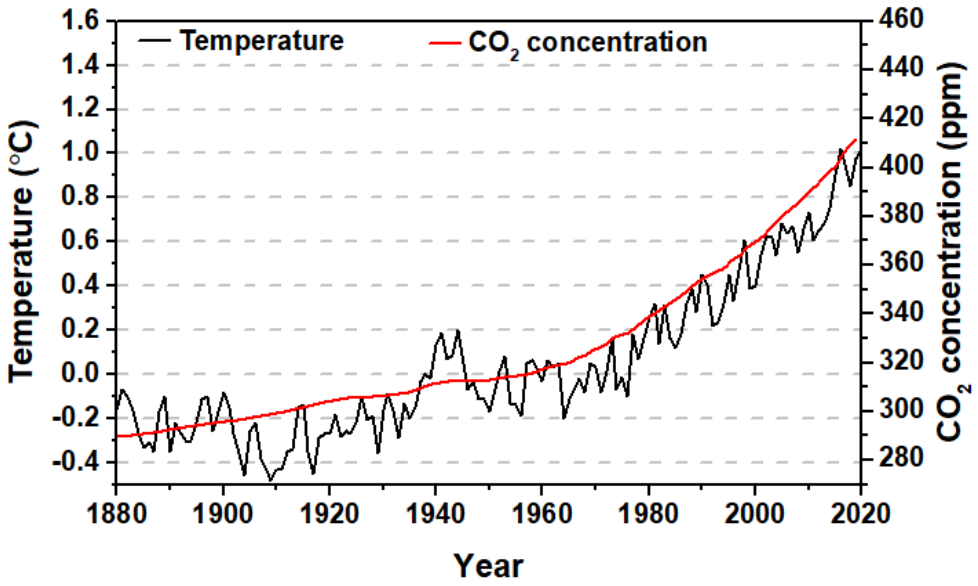

Figure 2.4: The global surface temperature increase and variation of CO_2 concentration in the atmosphere since 1880. CO_2 data sourced from [129] and temperature data from [127].

Since the Paris Agreement of 2015 almost all countries are committing to efforts to limit the global temperature increase to below 2 °C by mitigating the net CO_2 emissions and levels [130]. This will greatly reduce the associated effects and risks of climate change, especially if today's CO_2 emissions can be halved by 2030 [131]. Some of the ways to achieve this goal already implemented or proposed are CO_2 capture and storage (CCS), use of natural/shale gas over coal and replacement of some sources of emissions, especially in the energy sector, with renewable (e.g. wind, and solar) or nuclear energy sources [132]. According to IEA's 2020 global energy review, about 29% of the global electricity was already acquired from renewables, 10% from nuclear and 23% from natural gas in 2020, thus significantly reducing reliance on coal [128,133].

CCS entails capturing CO_2 directly from air or from localized point sources using pre-/post-combustion capture technologies with subsequent transportation and geological storage. Pre-/post-combustion capture from emission sources is currently more feasible because industrial and power plant flue gases typically consist of 3 - 35% CO_2 which allow efficient capture [134]. CO_2 point sources are localized industries emitting CO_2 as a by-product of fermentation, transportation, cement, steel, paper and chemical production plants, refineries, steam crackers and primarily (c.a. 33 - 40%) power plants [2].

The post-combustion capture approach, which entails capturing CO_2 from the source right before its discharge into the atmosphere, is more efficient as it can be easily blended into existing and new source infrastructure. The methods used for this are based on biological (photosynthesis, algae or bacteria), physical (physical adsorption, cryogenic condensation or membrane separation) and chemical (adsorption, absorption or chemical looping combustion) systems. Effective commercial methods rely on the use of amine solvents or cold methanol [135]. Typical examples of commercial post-combustion CCS facilities are the Anchant Energy and Lafarge Holcim CCS projects [45]. The pre-combustion capture approach involves separation of CO_2, which is formed as a co-product during processes such as natural gas reforming or gasification. During natural gas reforming for example, the CO_2 formed *via* the water-gas-shift reaction is separated directly during the process by means of membranes, adsorption, absorption or cryogenic processes. The choice of the separation method depends on conditions such as CO_2 partial pressure, process temperature and other by-products [43].

To achieve the goals set out in the Paris agreement, reduction of emissions alone will not suffice. There is a consensus that up to 30 Gt of negative emissions need to be achieved annually [46,130]. This can be achieved through the direct air capture (DAC) technology which captures CO_2 from air at an additional energy cost followed by storage, enabling the reduction of CO_2 from historic emissions. Unlike the technology localized at emission points, this approach offers the prospect of capturing CO_2 anywhere, also addressing emissions from mobile sources such as vehicles contributing about 16% of CO_2 emissions. The major drawbacks of this technology are its questionable energy efficiency and the low CO_2 atmospheric concentration (c.a. 415 ppm) which may thermodynamically impair the capture process especially at large scale. Nonetheless, several technology suppliers such as Climeworks, Global Thermostat and Carbon Engineering have developed first plants demonstrating economic viability [49,136,137]. The Carbon Engineering technology uses two connected chemical loops. CO_2 is captured in the first loop and then transferred to the second loop where it reacts with Ca^{2+} ions to form $CaCO_3$ [48]. Climeworks relies on a temperature-vacuum swing adsorption process [46].

Currently, there are 26 operating, 34 pilot and 3 under development commercial CCS facilities globally. The operational facilities are able to capture about 40 Mt of CO_2 annually from natural gas processing, refineries, chemical production, iron-and steel production and fertiliser industries. Since more facilities are currently under construction, the Global Institute of CCS projects a capacity increase to about 5.6 Gt in 2050 [45]. However, CO_2 capture technologies, especially

DAC, require additional energy and thus may lead to indirect emissions. Hence, this approach is only feasible if “free” excess energy from a renewable noncarbon-based energy source such as solar, wind or geothermal energy is utilized [136].For this reason, Climeworks recently partnered with Carbfix, a carbon storage company, and ON Power, the Icelandic geothermal energy provider, to build the new geothermal energy powered DAC plant (Orca) [138]. This plant which is currently under construction aims to scale-up the yearly carbon removal and storage in Iceland to 4 kt. In another joint venture with Norsk e-Fuel AS, Climeworks is building the first European plant for generation of renewable fuels from CO_2 and water *via* the power-to-liquid (PTL) technology using 100% renewable wind power [139]. The CCS technology efficiency also relies strongly on the availability of suitable and reachable geological formations for storage such as underground reservoirs which are limited and located far from capture points. This means a distributed network of CO_2 pipelines would need to be established for appropriate transportation of the captured CO_2 to this storage facilities [132].

While the technology for CCS is quite advanced in terms of cost and the energy penalty, to fully compensate for the associated transportation and storage costs, the captured CO_2 from CCS can be utilized as non-fossil carbon source (carbon capture and utilization, CCU) to produce value-added chemicals, fuels and materials [134]. Utilization of CO_2 can be both with and without conversion. Without conversion, it is for example used in EOR and EGR (enhanced gas recovery) where the gas is injected into an oil or gas reservoir in its supercritical form to enhance production [140,141]. EOR uses about 70 - 80 Mt of CO_2 annually. CO_2 is also used for fire extinguishing, foaming, beverage carbonation, food processing, welding, as dry ice, propellant, a solvent for decaffeination of coffee and drinking-water abstraction, a cleaning agent in textile and electronics industries and for stimulating plant growth in artificial greenhouses [47,141]. However, in most of these, the CO_2 is still ultimately released into the atmosphere.

CO_2 represents a thermodynamically stable form of carbon and this presents challenges in its utilization through conversion due to the need for a high-energy input to overcome the activation energy barrier. The use of highly reactive co-reactants (e.g. hydrogen, akenes, epoxides, ammonia, etc.) and catalysts are ways to provide an alternative pathway with a lower activation energy barrier resulting in CO_2 activation at temperatures as low as 190 °C (see Figure 2.5) [36,41,140]. To impose a reduction in the overall CO_2 emissions and minimize indirect emissions, the use of co-reactants such as H_2 in CCU processes should be avoided except if procured from cheap renewable sources [132].

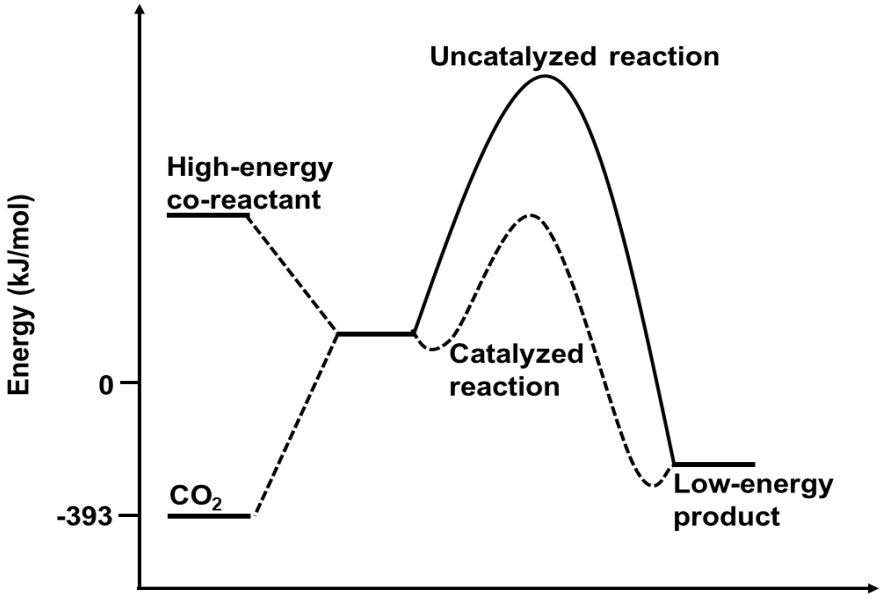

Figure 2.5: Energy level changes associated with CO_2 conversion reactions with high-energy co-reactants in the presence/absence of a catalyst. Adapted from [140].

Commercially operated processes such as the synthesis of urea, salicylic acid, methanol, formaldehyde, poly- and cyclic carbonates and fine chemicals represent examples of CO_2 utilization routes by conversion (see Figure 2.6) [40,41,140]. However, these only account for about 132 Mt of CO_2 annually. For emphasis, China's CO_2 emissions owing to only the coal, natural gas and oil combustion sectors was estimated at 9301 Mt in 2017 alone, about 71 times higher [128]. Urea synthesis is by far the largest consumer of CO_2 (112 Mt pa). To have a significant impact on the global CO_2 balance, any route for the utilization of CO_2 by conversion into value-added products must not only be net CO_2 negative but also operate at a global scale and form commodity products in large quantities.

Research is now focused on identifying and developing additional reaction pathways to utilize more CO_2. There are many potential CCU routes under development in catalysis, mineralization, biology, photocatalysis and photosynthetic processes [47]. In heterogeneous catalysis, the in-/direct CO_2 hydrogenation to fuels, such as the AIR TO FUELS system by Carbon Engineering in Canada and INERATEC in Germany, and DR of CO_2 with methane by BASF SE and Linde in Germany are already in advanced stages of development and close to commercialization [137,142]. Provided there is an environmentally benign source of hydrogen and cheap renewable energy, the RWGS reaction also represents one of the crucial reactions that can convert CO_2 into

CO, a component of *syngas* (CO + H_2), for further conversion into valuable chemicals and fuels. For this, several potentially effective catalysts have already been identified [143–145].

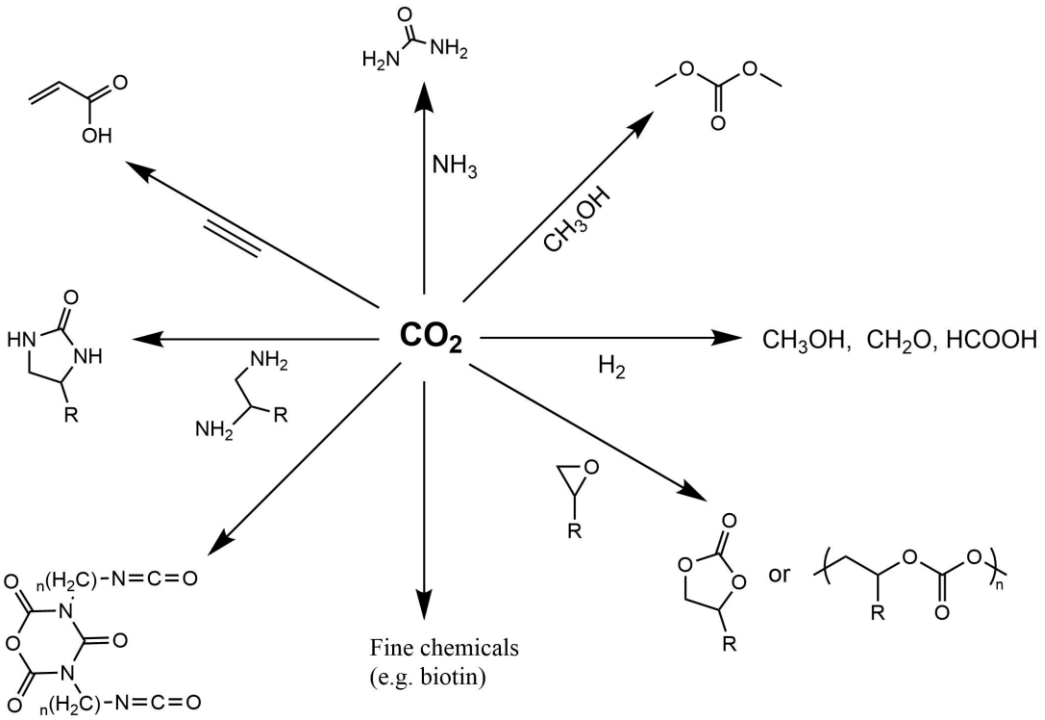

Figure 2.6: Commercially operational and possible CCU pathways and the corresponding products. Adapted from [140].

2.3 Common catalysts for CO_2-ODHE and their catalytic properties

Despite not being commercialized, a variety of catalysts with different physicochemical properties for the CO_2-ODHE have been studied and reported [10,19,28,63,120,121,123,124,146–148]. As a selective oxidation reaction, activation of the C_2H_6 or light alkane C-H bond is one of the main steps of the reaction and is considered to be rate determining [14,148]. In the presence of CO_2, its dissociation to avail the oxygen species required for the oxidation of the evolved H_2 is also crucial [5]. There is a consensus in literature, that this reaction requires a bifunctional catalyst system which can provide separate sites for dissociation CO_2 to CO and reactive oxygen species (O*) while co-activating the C_2H_6 to ethylene and H_2O [1,18,62,63,116,149].

Reducible transition and main group metal oxides represent some of the most suitable catalysts for CO_2-ODHE and have been extensively explored in literature [5,7,14,27,28,63]. This was demonstrated by the work of Suzuki *et al.* [11] in which different metal oxides presented promising

activity (up to 19.6% C_2H_6 conversion) in the order: Ga2O3 > Cr_2O_3 > V_2O_5 > TiO_2 > Mn_3O_4 > In_2O_3 > ZnO > La_2O_3 > (CeO_2, ZrO_2, Nb_2O_5, Fe_3O_4) (see Figure 2.7). The selectivity towards ethylene *via* dehydrogenation in the presence of CO_2 was also above 85% for most studied oxides. Oxides such as MgO, CaO, SiO_2, MoO_3, SnO_2, Al_2O_3, Ta_2O_5, Tl_2O_3 did not exhibit any activity. Transition metal oxides are generally employed due to their intrinsic ability to exist at different oxidation states. For example, the vanadium lattice cation can exist in the +3, +4 and +5 oxidation states allowing it to easily undergo redox cycles. This imposes different Lewis acid-base and electron transfer properties, making them potential catalysts for CO_2-ODHE and other heterogeneous partial oxidation reactions [14]. Oxides based on other transition metals like Ni and Co have also been reported [79,150].

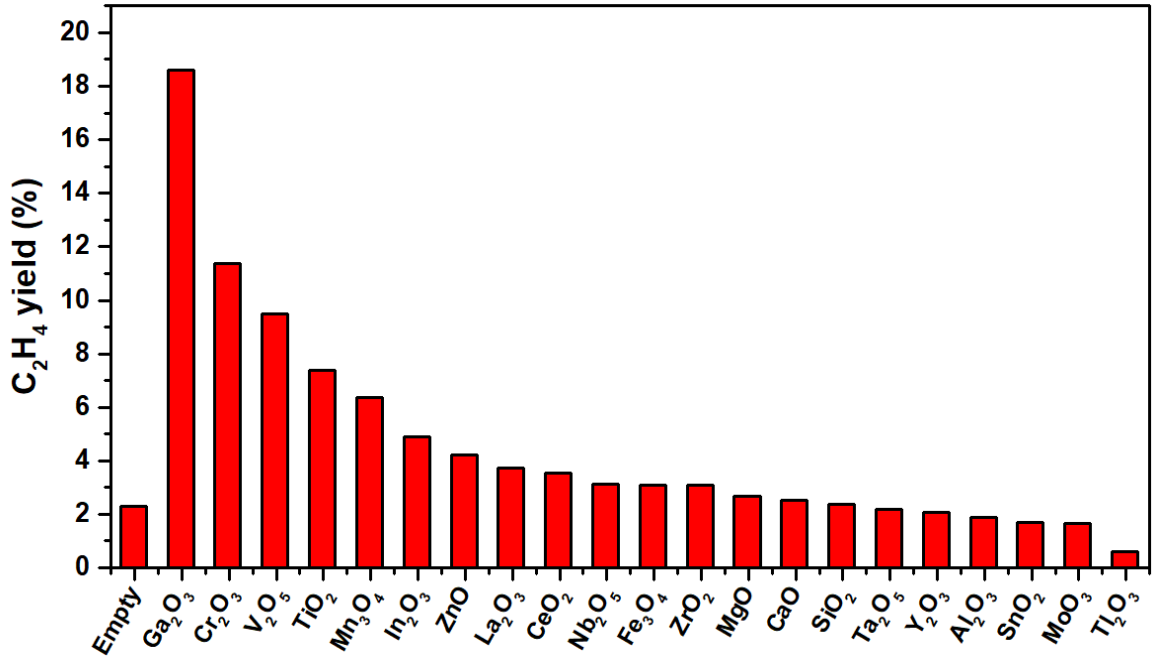

Figure 2.7: Ethylene yields of different metal oxides tested for 30 min TOS under CO_2-ODHE conditions (650 °C; C_2H_6 : CO_2 = 5 : 25 mL/min ; SV = 9000 mL·h^{-1}·g_{cat}^{-1}) as observed by [11].

Metal oxides contain lattice and surface reactive oxygen species (O*) which are responsible for the activation of the light alkane [14,148]. These oxygen species (O*) may be electrophilic (O_2^-, O_2^{2-}, O^-) or nucleophilic (O^{2-}). It is believed that nucleophilic O^{2-} are found within the lattice of metal oxides and are responsible for the C-H bond scission during ODH [148]. Electrophilic (O_2^-, O_2^{2-}, O^-) oxygen species are highly mobile and reactive surface species which result in both C-C and C-H bond scission associated with overoxidation or DRE. Since these latter oxygen species are involved in the side reactions, it is important to preclude the re-adsorption of the olefin onto the

catalyst surface. The nature (nucleophilicity or electrophilicity) and location (surface or lattice) of the oxygen species (O*) also vary with the oxidation state (electronegativity) of the lattice-metal cation [148].

CO_2-ODHE catalysed by metal oxides generally follows a Mars-van-Krevelen (MvK) mechanism (see Figure 2.8), similar to the mechanism reported for O_2-ODHE [14,151–153]. This involves activation of a surface adsorbed C_2H_6 by nucleophilic lattice oxygen species (O^{2-}) donated by the metal oxide to form ethylene and H_2O as a by-product. The metal oxide is left in a locally/partially reduced state with an oxygen vacancy. This vacancy is subsequently replenished by the surface-adsorbed CO_2 which dissociates into CO and oxygen species (O*) re-oxidizing the reduced metal oxide catalyst back to its original active state. While the MvK mechanism is preeminent on catalytically active reducible high valent metal oxides, there tends to be variations over different catalytic materials and some of which will be summarized in the catalyst-specific sections below.

The C_2H_6 C-H bond activation is effected by the nucleophilic lattice oxygen species (O^{2-}) *via* a dehydrogenation reaction which results in the corresponding ethylene and H_2O. This suggests that the rate of reaction depends on the concentration of oxygen sites in the catalyst. In turn, the concentration of oxygen sites is affected by the rate of re-oxidation of the oxide surface which relates to the ability of the surface to activate CO_2. Thus, variation of the nature of the metal oxide, namely acid-base and redox properties, is an efficient approach to control the re-oxidation rate and catalytic activity during CO_2-ODHE [13].

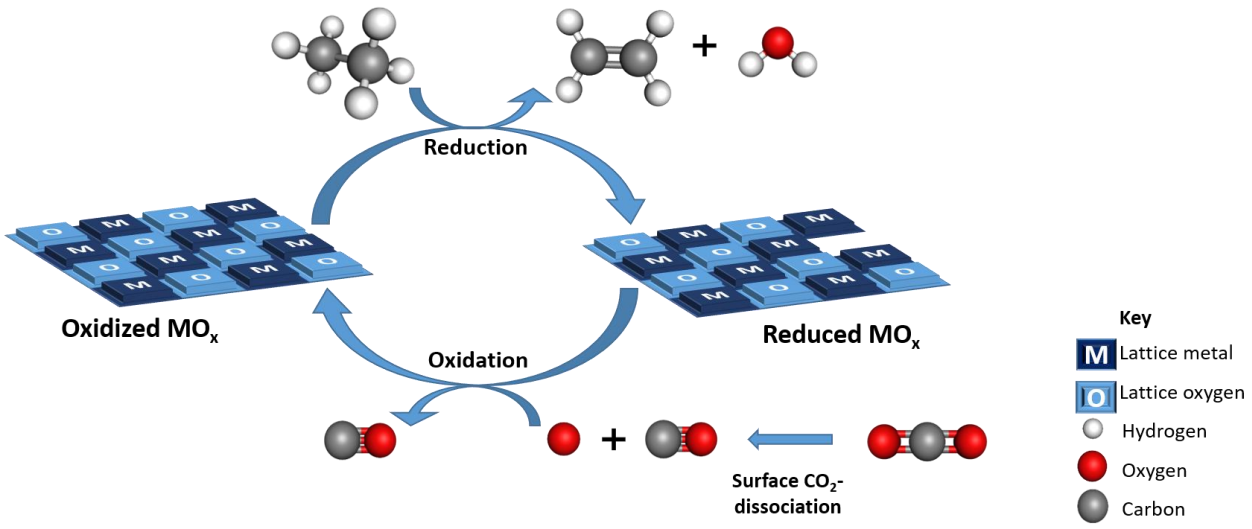

Figure 2.8: Simplified graphical illustration of the general MvK mechanism in place during CO_2-ODHE over metal oxide (MO_x) catalysts. Inspired by [153].

In the O_2-ODHE, the C-H bond activation may occur *via* either a homolytic or heterolytic bond cleavage route [105,154,155]. The homolytic cleavage route proceeds *via* the involvement of single unpaired electrons and higher energy barriers than when paired electrons are involved. This route is mostly triggered thermally *via* C-H bond polarization or by (alkyl) radicals formed on the active catalyst surface where they react or get desorbed into gas-phase to react. Free radicals react depending on their concentration and temperature. In gas-phase they recombine into undesired products. On the catalyst surface they are more likely to undergo β-hydride elimination to form the corresponding olefin product. Radicals may also react with the mobile electrophilic surface oxygen species forming non-selective oxidation products. While the understanding of the nature of the active sites responsible for it is limited, this radical C-H activation mechanism is typical on rare-earth and alkali metal oxides [154–156].

The heterolytic C-H cleavage mechanism proceeds *via* a simultaneous electron-pair transfer on redox metal oxides. Typically, this is achieved by a nucleophilic lattice oxygen at a basic site of the redox metal oxide catalyst, which abstracts a hydrogen atom from the alkane. It is still not clear whether electrophilic lattice metal cations are also capable of facilitating this cleavage. This mechanism is typical on oxides based on V and Mo [105,155].

2.3.1 Cr-based catalysts

Supported Cr-based oxide catalysts represent some of the predominantly explored and best performing materials for CO_2-ODH of light alkanes, perhaps due to their DD activity as demonstrated by the commercial Catofin and Catadien catalysts [31]. These materials often represent superior catalysts compared to V, Co, Fe, Ni and Mn based oxide catalysts, but their performance also depends strongly on other properties such as the support and promotion modifiers used [122]. Generally, supported Cr-based oxide catalysts exhibit high initial (short-term) activity as well as high selectivity to the olefin and CO [13,157].

Cr-based catalysts exist in the form of interconvertible Cr^{III} and Cr^{VI} redox centres taking part in CO_2-ODH and DD [7,158–161]. Cr^{VI} centres, which have a tetrahedral geometry and are coordinatively unsaturated, have been identified as active sites for activation of C_2H_6, reducing them in the process [122,162]. The bulky coordinatively saturated Cr^{III} centres with a stable octahedral geometry in Cr_2O_3 clusters are less active if not completely inactive [161]. During CO_2-ODH, the soft oxidant, CO_2, helps with the regeneration of the Cr^{VI} species, which facilitates the dehydrogenation of the alkane, by reacting with the inactive Cr^{III} species through a re-oxidation step. Thus, the mechanism on these catalysts involves the redox cycle between the Cr^{III} and Cr^{VI} centres in which the reduction step is faster than the re-oxidation (see Figure 2.9) as concluded by Mimura *et al.* [7,163].

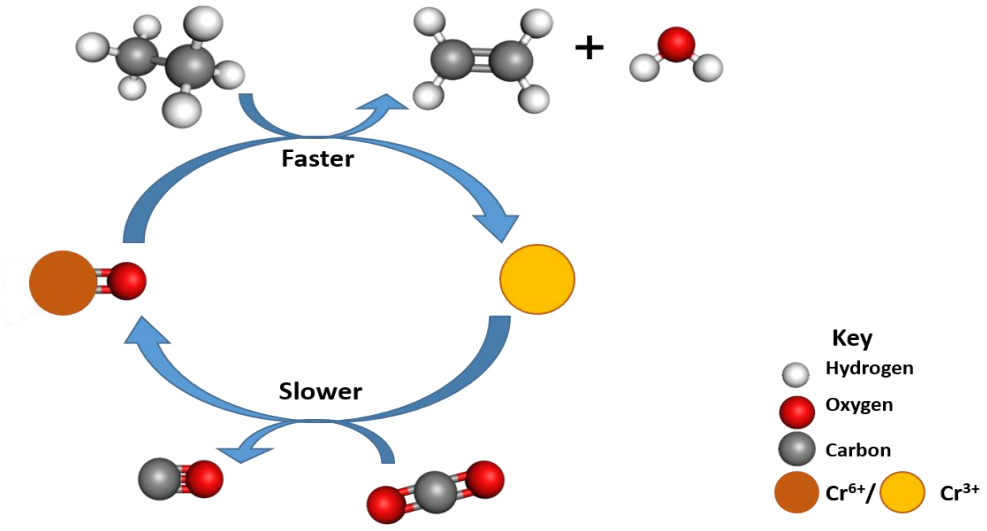

Figure 2.9: Simplified graphical illustration of the redox cycle based CO_2-ODHE mechanism over Cr based catalysts as suggested by Mimura et al. and Gomez et al. [1,7].

It cannot be said with absolute certainty that the identity of the high valent state Cr species is actually Cr^{VI} since it could possibly be Cr^{V} with a distorted tetrahedral/five-coordinate geometry or an octahedral symmetry with a tetragonal distortion, especially on zeolite materials [164–166]. Moreover, the topic of whether Cr^{III} or Cr^{VI} species are involved in C_2H_6 dehydrogenation during CO_2-ODH of light alkanes is still controversial. Some literature suggest that surface Cr^{III} species are the actual sites responsible for the dehydrogenation of the light alkane [5]. Other studies on CO_2-ODH of ethylbenzene claim that the redox cycle involves the participation of the Cr^{III}/Cr^{II} redox pair instead [167]. Whichever surface species represents the active site, a redox cycle plays a crucial role in the catalytic performance of the Cr-based catalysts. Based on this, it should be conceivable that the initial oxidation state of Cr plays a paramount role on the catalytic activity, stability and reaction pathway followed (DD accompanied by RWGS or direct CO_2-ODH).

Active research on Cr-based catalysts is focused on the understanding of material physicochemical properties such as the nature of support, oxide type (CrO_3, Cr_2O_3, CrO_x, etc.), Cr coverage and dispersion, and interaction with promoters which are added to influence the initial Cr oxidation state. For instance, on ZrO_2 and Al_2O_3, amorphous CrO_x comprising 65% and 35% poly-/mono-nuclear Cr^{VI} species, respectively, with the balance being Cr^{III} were formed as reported by Mamontov *et al.* [13]. Inactive and crystalline α-Cr_2O_3 phase as well as lower concentrations of Cr^{VI} formed on CeO_2. As a result, an increase in activity with Cr^{VI} content in the order; CrO_x/ZrO_2 > CrO_x/Al_2O_3 > CrO_x/CeO_2 was concluded. Besides the fraction of Cr species, the performance also proved to depend on the support properties (Lewis acidity and oxygen mobility) that enable overall bifunctionality and help co-activate CO_2. When the support is acidic and unable to activate CO_2 (CrO_x/Al_2O_3), the DD and subsequent RWGS pathway was observed. However, direct CO_2-ODH with less CO-forming routes was observed on the Lewis basic CrO_x/ZrO_2 while increased parallel CO-forming routes were observed on CrO_x/CeO_2. This bifunctional character also influences the catalyst stability since enhanced CO_2 activation can also induce the reverse Boudouard reaction for coke mitigation. ZrO_2 demonstrated superior performance as a support for Cr-based catalysts during CO_2-ODHE compared to Al_2O_3 and MgO in a study by Deng *et.al.* [6], probably due to its high relative basicity.

Mimura *et al*. [8] also showed that, depending on the SiO_2/Al_2O_3 ratio in H-ZSM-5, different Cr species can be formed which influence CO_2-ODHE differently. Si-rich H-ZSM-5 with Si/Al of 1900 forms reducible and active $Cr^{V/VI}$ responsible for the high catalytic activity towards CO_2-ODHE with C_2H_6 conversion of 68.2% whereas Al-rich H-ZSM-5 with Si/Al below 90 result in a low activity

(C_2H_6 conversion < 18.5%) [7,8]. A study by Wang *et al.* [168], which revealed the following order of activity $Cr_2O_3/SiO_2 > Cr_2O_3/ZrO_2 > Cr_2O_3/Al_2O_3 > Cr_2O_3/TiO_2$, also corroborates that the nature of support can influence the distribution, structure and fraction of active surface Cr-oxide species formed, which in turn influence the overall catalytic performance during CO_2-ODHE. Their results also suggest that on a Si-rich carrier, a larger fraction of highly active Cr species is formed.

Cr content on the support can also influence the catalytic performance. Shen *et al.* [164] prepared supported Cr-oxides of varying Cr content (1 - 20 wt.-%) on SiO_2. The activity increased with Cr loading until a maximum C_2H_6 conversion of 31% was reached at a 5 wt.-% Cr and then decreased with a further increase of Cr concentration. This was ascribed to the dispersion, which increased until 5 wt.-% Cr followed by crystallization of the Cr-oxide species to α-Cr_2O_3 at higher loadings. CO_2 conversion remained lower (2.7% at 5 wt.-% Cr loading) than C_2H_6 conversion, suggesting a DD pathway, possibly due to a lack of Lewis basicity. Ji *et al.* [161] also reported an increase of activity with Cr loading until an optimum of 5 wt.-% (C_2H_6 /CO_2 conversion of 67%/17.3% after 30 min on stream) on a highly stable Cr/SBA-15/Al_2O_3/FeCrAl monolithic catalyst. Due to the properties of the monolithic porous mixed-oxide support, the material exhibited enhanced CO_2 conversion which helped keep the catalyst active even after 1130 h time on stream (TOS) by preventing coking. Wang *et al.* [10] also report similar observations except their optimum Cr loading was 8 wt.-%.

The problem with most Cr-based catalysts is that they tend to have a short lifetime, especially when they exhibit high initial activity and ethylene formation rates [169]. This is due to the high temperature (550 - 750 °C) at which the reaction takes place, leading to deactivation through coking [1,169,170]. Coke formation *via* decomposition of ethylene, which is very reactive and polymerizes easily, is thermodynamically more favourable than *via* C_2H_6 decomposition [13]. Under such circumstances, only bifunctional catalysts with the ability to activate both C_2H_6 and CO_2 may promote the reverse Boudouard reaction supressing deactivation through coke formation. Most Cr-oxide catalysts, especially in the absence of enhancement promoters or supports with a high density of basic sites, can dehydrogenate C_2H_6 efficiently but not activate CO_2. As elaborated above and demonstrated for CrO_x/ZrO_2 and monolithic Cr/SBA-15/Al_2O_3/FeCrAl, bifunctional catalysts with higher Lewis-base site density supports or other catalytic/support properties that enhance CO_2 activation tend to be more stable than those with inactive or acidic supports like Al_2O_3 [13,161]. Modification of Cr-based catalysts with promoters such as Ni, Fe, Co, Mn and sulphates forming oxide composites also proved to enhance CO_2

activation and perhaps reduce coking as well as increase activity and selectivity towards ethylene [5,159,171]. Deng *et al.* prepared Cr_2O_3/ZrO_2 nano-composites modified with either Ni, Fe, Mn or Co oxide and investigated the effect of the modifiers on catalytic activity and ethylene selectivity in the CO_2-ODHE [171]. Based on their observations, modification by Fe, Co or Mn oxide introduces varying degrees of weak acidity, formation of additional surface oxygen species and increases the Cr^{VI}/Cr^{III} ratio which in turn decreases the activity slightly but increases ethylene selectivity significantly (Fe > Co > Mn). It was concluded that the Ni oxide modifier markedly improved conversion, but mainly promoted the dry reforming and cracking side reactions forming CO and CH_4 respectively. In addition to increasing the Cr^{VI}/Cr^{III} ratio, incorporation of the Ni oxide modifier induced partial phase transformation of a part of the tetragonal ZrO_2 within the nano-composite into the monoclinic phase. The monoclinic phase is believed to provide stronger sites for CO_2 adsorption. CO_2- and NH_3-TPD proved the existence of more and stronger sites for CO_2 activation and acid-base pairs in the nano-composite when the Ni oxide modifier was added which in turn resulted in a high CO_2 conversion and enhanced CO and CH_4 forming routes. A follow-up study by the same group [5] on Fe-Cr/ZrO_2 prepared *via* different routes (co-precipitation and co-precipitation/impregnation) demonstrated that the catalytic performance, can also be influenced by the catalyst synthesis method. When prepared by co-precipitation, the catalyst is prone to deactivation *via* coke deposition caused by the relatively low CO_2 conversion despite the high initial C_2H_6 conversion and ethylene selectivity. When synthesized *via* co-precipitation/impregnation, the catalyst exhibits a high stability against coke deposition and remains active through the entire experiment. As previously mentioned, the mechanism of this reaction varies over different materials. On Fe-Cr/ZrO_2, the suggested mechanism (see Figure 2.10) involves activation of C_2H_6 over Cr^{III} species forming ethylene and H atoms which either recombine to form H_2 or react with lattice O species from the iron oxide to form H_2O, reducing Fe^{III} to Fe^{II} and an oxygen vacancy (□). CO_2 dissociation occurs at the active site denoted [ ] forming CO and active O* species which subsequently replenish the oxygen vacancy (lattice oxygen) and regenerate the iron oxide phase. The Fe component is mainly responsible for promotion of the catalyst by enhancing CO_2 activation through the RWGS reaction while the Cr component activates C_2H_6 *via* DD.

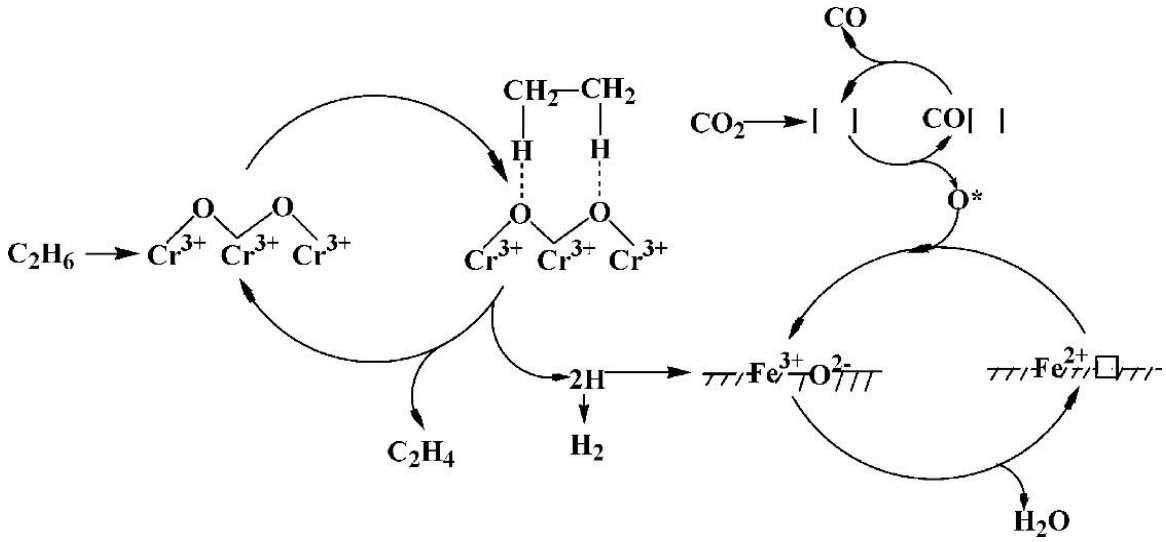

Figure 2.10: Mechanism of CO_2-ODHE over Fe-Cr/ZrO_2 [5].

Most Cr catalysts deactivate *via* coking. The higher the density of basic sites on the catalyst surface, the higher the stability of the catalysts in the presence of CO_2 due to enhanced CO_2 activation [22]. In addition, deactivation *via* sintering of Cr species to crystalline α-Cr_2O_3 is a challenge [170]. Another challenge associated with Cr-based catalysts is the toxicity associated with Cr which requires vigilance during catalyst preparation, use and disposal causing reluctance in commercial implementation despite the progress in research.

2.3.2 Ga-based catalysts

Ga-based oxides, which are environmentally benign compared to Cr-based materials, also exhibit catalytic activity for this reaction. In the study by Suzuki *et al.* [172], Ga_2O_3 was the most effective catalyst for CO_2-ODHE when compared to other oxides, yielding 19% ethylene with a selectivity of 94.5% at 650 °C (see Figure 2.7). Ethylene yield was found to halve in the absence of CO_2 demonstrating the importance of the oxidant in enhancing the performance of ODH catalysts. Unlike transition metal oxide-based catalysts, Ga which is a main group metal usually exist in the 3+ oxidation state and is nonreducible, especially in the Ga_2O_3 form which is amphoteric [1,173]. When anchored on supports like TiO_2, ZrO_2, Al_2O_3, SiO_2 and MgO, Ga-based catalysts are proposed to operate in a two-step CO_2-ODHE reaction pathway [1,174]. This involves the DD of the light alkane to corresponding olefin and H_2 on acid sites followed by the RWGS reaction in which H_2 reacts with CO_2.

Similar to the Cr-based catalysts, Ga loading, nature of support and overall catalyst acidity due to the amphoteric nature of Ga-oxide, and promotion additives influence the catalytic performance of reported catalysts. For instance, due to the difference in the nature of supports (acid-base properties) and surface area, Ga_2O_3 on TiO_2 proved to exhibit a superior catalytic performance (C_2H_6 conversion = 29%, ethylene selectivity = 71% and 20% yield) than on ZrO_2, ZnO, Al_2O_3, SiO_2, La_2O_3 and MgO in CO_2-ODHE at 650 °C [174]. TiO_2, ZrO_2 and ZnO were considered amphoteric resulting in a higher concentration of weak acid sites on Ga-oxide. Differences in the catalytic performance amongst them were associated with the difference in surface area. However, the difference in performance of Ga-oxide on TiO_2 with weak acidic sites, Al_2O_3 with strong acid sites and La_2O_3 with basic sites was ascribed to the nature of support (acid-base properties). The selectivity towards methane on TiO_2 was 28% suggesting a considerable cracking activity. Furthermore, a significant reduction in ethylene yield down to 2% was observed within 3 h TOS due to coking. The same study also showed that increasing the surface area of an unsupported Ga_2O_3 consisting predominantly of weak acid sites from 1 m^2/g to 50 m^2/g improved the ethylene yield from 3% to 25%. Similar observations were also reported by Yue *et al*. [175] when Ga_2O_3 was anchored on various supports and tested for CO_2-ODH of propane (CO_2-ODHP) at 600 °C. On ZrO_2, Al_2O_3 and TiO_2, Ga_2O_3 showed a higher propane conversion of 39%, 33% and 23%, respectively, compared to SiO_2 and MgO due to the presence of medium to strong surface acid sites in the former. CO_2 was found to enhance the activity of Ga_2O_3 on TiO_2 achieving a propane conversion of 32% while on Al_2O_3 and ZrO_2, the activity was suppressed resulting in propane conversions of 26% and 30%. The overall difference in behaviour of Ga_2O_3 on the various supports was ascribed to its varying interaction with these support materials. Lastly, CO_2 was found to easily remove the adsorbed H_2 formed from the RWGS reaction but to fail to replace propane adsorbed on basic sites.

Baiker *et al.* [176] observed an increase of the catalytic performance of GaO_x on TiO_2 with increasing Ga loading up to 10 wt.-% (ethylene selectivity of 38% at a C_2H_6 conversion of 57%; temperature of 700 °C). The TiO_2 support alone showed no activity. The catalysts with a Ga loading beyond 8 wt.-% tended to exhibit pronounced cracking and more coking also ascribed to a decreased overall acid site population coupled with the presence of more strong acid sites. Thus, Ga-based catalysts are effective for CO_2 activation, but since they are amphoteric, they may bind the alkane strongly in the presence of strong acid sites inducing the hydrogenolytic C–C cleavage (cracking) which ultimately leads to methane and coke formation. Tuning the acid-base sites of these materials is crucial for the modulation of their catalytic performance, especially

stability, in CO_2-ODHE [176,177]. It is important to note that CO_2 is also acidic and may modify the acid-base properties of catalyst materials upon surface adsorption. Modification of the acid-base properties of Ga-oxide by the addition of the basic promoter potassium was reported by Michorczyk *et al*. [177]. A decrease in propane conversion from 33% to 19% during CO_2-ODHP due to a reduction of the surface area after modification was observed. Interestingly, a significant decrease in propane conversion (from 19% to 1.3%) and propylene selectivity (from 92% to 67%), with increasing K/Ga ratio from 0.03 to 0.1 was observed. This implies that acid sites in Ga_2O_3 are active sites for propane activation and potassium, as a basic promoter, especially when provided in excess, blocks these acid sites thereby reducing activity. Shen *et al*. [178] also reported that when anchored on a HZSM-5 with a high Si/Al ratio of 97, Ga_2O_3 showed an initial C_2H_6 conversion of 24% which levelled to 15% at 94% ethylene selectivity after 10 h TOS and remained active resisting further deactivation for 70 h TOS. This behaviour was attributed to reduced catalyst acidity at Si/Al ratios above 90 which suppressed undesired side reactions and enhanced stability compared to a bulk β-Ga_2O_3 catalyst. Similar conclusions were drawn when Ga-oxide on HZSM-5 with different Si/Al ratios were tested for DD of propane [179]. Ga_2O_3 immobilized on a mesoporous (M)-HZSM-5 with Si/Al ratio of 240 also proved to withstand 30 h TOS without significant deactivation during CO_2-ODHP showing the best propylene yield of 22%, compared to zeolites with lower Si/Al ratios [180]. Despite this progress, deactivation of Ga-based catalysts due to coke formation is a major challenge still hindering their large-scale use for CO_2-ODH.

Based on density functional theory studies by Vlachos *et al*. [181] on Ga-modified γ-Al_2O_3 (110) surfaces, dehydrogenation of C_2H_6 on Ga-based catalysts occurs *via* a heterolytic C–H bond dissociation which is facilitated by the lattice oxygen species. This forms a surface proton and a metal-carbanion intermediate which further undergoes β-hydride elimination into the respective olefin. However, unlike in the redox mechanism, the lattice oxygen species is not lost to form oxygen an vacancy and the metal oxide is not partially reduced. Thus, it is conceivable that in the presence of CO_2, Ga-based materials are known to undergo ODH *via* the alkane heterolytic dissociation and CO_2 activation *via* the reverse water gas shift (RWGS) reaction facilitated by hydrogen especially because these materials are redox inactive [175,182,183].

2.3.3 V-based metal oxide catalysts

Just as the Cr-based catalysts, V-based catalysts also represent a class of catalysts that have been extensively studied for ODH of most of the light alkanes with both O_2 and CO_2 as oxidants due to their reducibility, high valence state of the metal and tuneable acid-base/redox properties [184]. These catalysts typically exhibit very high activity for ODHE [67,185,186]. The catalytic performance depends strongly on the structure of the VO_x species exposed on the surface of the catalyst. The most important structures of the VO_x species are monomeric VO_4 species, dimeric or oligomeric chain- or sheet-like vanadate structures, poly-vanadates and 3D V_2O_5 species of nano- or micro-structural range which form at higher V-loadings. Previous research has shown that the support, promoter, amount of the VO_x precursor loaded as well as the synthesis method employed can significantly influence and determine the ultimate type and nature of the surface VO_x species formed and thus the catalytic performance [66–70]. For instance, $VOPO_4$ supported on TiO_2 exhibits a higher selectivity towards the target ethylene product than the bulk VO_x and $(VO)_2P_2O_7$ under O_2-ODHE conditions [66]. The use of a Nb promoter in VO_x -Nb/La-γAl_2O_3 has also proven to be crucial for the improvement of ethylene selectivity by enhancing surface VO_x species isolation, thereby minimising the formation of V_2O_5 crystallites which are undesirable for the ODHE activity [67].

Just as the Cr-based catalysts, the redox properties due to the V^{IV} and V^{V} couple drive the ODH activity of V-based catalysts which proceeds *via* the MvK mechanism [66]. The acidity of the materials also plays a significant role. Both these properties vary in the different possible surface VO_x species which are influenced by the support, promoter additives, synthesis method and V-loading [66–70]. Generally, high ethylene selectivity is typically achieved at low alkane conversion, thus alkene productivity is usually far from that required for industrial application.

2.3.4 Other common catalysts

Other materials explored in literature for the CO_2-ODH of light alkanes include oxides based on In, Co, mixed metals and alkali and alkaline earth metals. In-based catalysts garnered considerable research interest, especially for CO_2-ODHP, mainly due to the presumed similarity in chemistry and catalytic performance of In_2O_3 and Ga_2O_3 [182]. Perhaps due to this similarity, CO_2-ODH tends to also proceed in a two-step pathway on In-based catalysts, *via* the DD followed by the RWGS. For instance, Zhuang *et al*. [187] tested the potential of In_2O_3-MO_x (M = Al, Zn, Zr,

Ti, Fe, Mg, Si and Ce) binary oxide systems as CO_2-ODHP catalysts at 600 °C. In_2O_3-Al_2O_3 with 20 mol.-% In loading was found to be most effective exhibiting 77% propylene selectivity at 29% propane conversion with no major deactivation over the tested 20 h period. In_2O_3-CeO_2 was the most inactive despite its reported excellent performance in the RWGS reaction [144]. The performance of In_2O_3-Al_2O_3 was attributed to its ability to easily form highly dispersed nanoparticles with surface stabilized metallic In^0 species upon *in situ* reduction. Based on TPR analysis, it was suggested that the redox mechanism is probably not applicable during CO_2-ODHP over these materials. Further studies by the same group revealed that the creation of highly dispersed metallic surface In^0 species is important for the DD activity of In_2O_3-Al_2O_3 [188]. Temperature-programmed reaction of CO_2 and H_2 showed that the metal centres In^0 and In^{3+} in the catalyst cannot be easily re-oxidized by CO_2. It was suggested that the reaction proceeds *via* the DD coupled with the RWGS. In_2O_3 immobilized on Al_2O_3 still proved more effective for CO_2-ODHP with a balanced CO_2 and propane conversion and high propylene selectivity than on ZrO_2 and SiO_2 in a study by Chen *et al*. [189]. This was also attributed to high dispersion of In_2O_3 on Al_2O_3 allowing the formation of stable surface In^0 and the balanced acid-base properties of this support. In contrast, on ZrO_2, the high density of basic sites compared to the acid sites overly enhanced CO_2 over propane conversion which resulted in a reduced propylene selectivity despite the high dispersion of In_2O_3. Thus, just as the Ga-based catalysts, the acid-base properties of the overall catalyst influenced by the support, dispersion and modifiers play a crucial role in modulation of CO_2-ODH performance of In-based catalysts.

Mixed oxides, in which each influence the physicochemical properties and thus the performance of the overall catalyst under CO_2-ODHE, have also been extensively explored. For instance, mixed oxides based on Ni-Nb-O in which the Nb cations fill cationic vacancies and/or partially substitute Ni atoms and form a Nb-rich amorphous phase in the parent NiO are also known for their high activity and ethylene selectivity, especially during O_2-ODHE at low temperatures [28,190–194]. The high ethylene selectivity is attributed to reduced electrophilic oxygen species resulting from Nb addition, but this also reduces the activity. In 2016, Martin *et al*. [28] showed that despite the parent Ni-Nb-O displaying better performance, promotion by Cr resulted in higher activity than Mo and W promoters during O_2-ODHE due to a high surface Nb content. Ethylene selectivity over all catalysts increased upon addition of CO_2 during the reaction while activity dropped. Among the modified catalysts, Ni-Nb-Cr-O still proved more active with a slight drop of C_2H_6 conversion from 25% to 21% and a significant increase in ethylene selectivity from 63% to 84% upon addition of CO_2. This is ascribed to the ability of CO_2 to limit oxygen diffusion over the

catalyst bed and thus reduce overoxidation, while poisoning some C_2H_6-activation sites. Another example of mixed oxide catalysts is the Cr_2O_3 anchored on mixed TiO_2-ZrO_2 supports in varying ratios (see Figure 2.11) reported by Haghighi *et al*. [195]. When tested under CO_2-ODHE conditions the catalyst with the support containing 75 wt.-% TiO_2 (25 wt.-% ZrO_2) exhibited the best C_2H_6 conversion of 48% and ethylene yield of 46% at 700 °C. The different performances of the materials were ascribed to differences in textural and crystal structures for the various TiO_2 : ZrO_2 ratios. The catalyst with the support containing 75 wt.-% TiO_2 (25 wt.-% ZrO_2) displayed small particles of uniform morphology and a high surface area allowing a high dispersion of the active phase and thus enhanced catalytic performance.

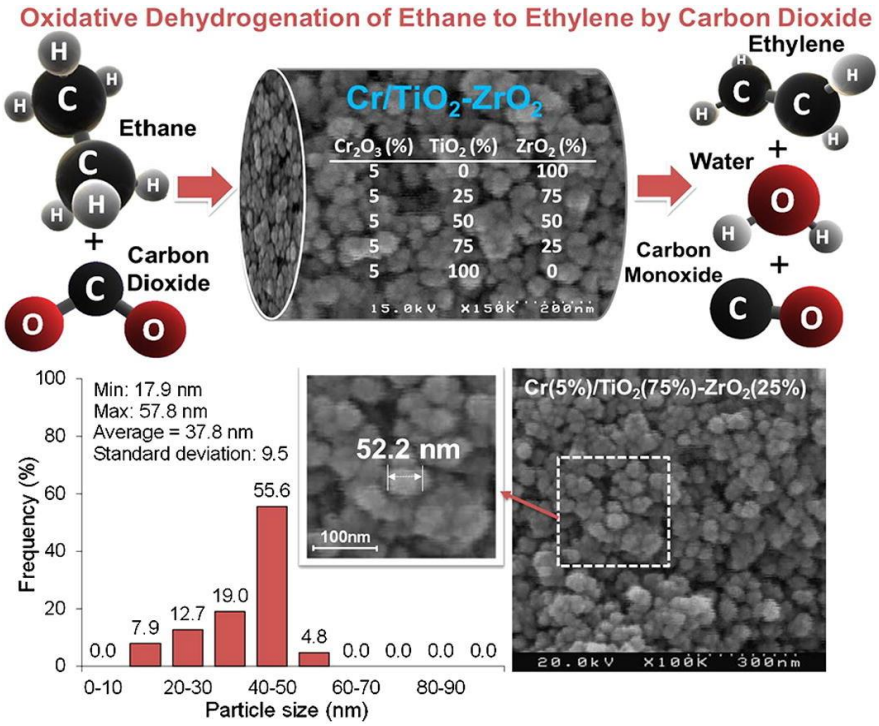

Figure 2.11: Summary of the different Cr/TiO_2-ZrO_2 catalyst compositions and morphology and particle size distribution of the catalyst with 75 wt.-% TiO_2 (25 wt.-% ZrO_2) [195].

Na_2WO_4/Mn/SiO_2, which is also effective for OCM, was decorated with different loadings of Co and studied for CO_2-ODHE at a temperature of 750 °C [196–199]. Upon increasing the loading of Co by steps of 2 wt.-% from 2 to 12 wt.-%, C_2H_6 conversion decreased while CO_2 conversions increased with stabilization reached from 4 wt.-% Co loading. At the Co loadings of 4-12 wt.-%, approximately 93% ethylene selectivity, 56% C_2H_6 and 15% CO_2 conversions were obtained with an C_2H_4 : CO : H_2 product ratio of 1 : 1 : 1 which is balanced and suitable for potential use in hydroformylation to propanal. This ratio was with a lower CO fraction for Co loadings below 2

wt.-%. The effect of Co was attributed to its ability to inhibit aggregation of Na and W at the catalyst surface. Furthermore, it was concluded that during the reaction, Co oxides in the catalysts reduce to metallic Co which are considered active sites for CO and H_2 formation *via* the competing reforming of C_2H_6 with CO_2.

Other mixed metal oxide catalysts reported for CO_2-ODHE include the coke-resistant Fe on MgO-ZrO_2 which doubled in activity at 70% ethylene selectivity upon modification of the support with NiO [153]. The enhanced performance of the Fe/NiO-MgO-ZrO_2 was ascribed the formation of an Fe-oxide-Ni interface which facilitates C_2H_6-activation. The spent catalyst also consisted of more surface Fe^{2+} species than "as-prepared" suggesting that a redox cycle involving Fe occurs during the reaction (see Figure 2.12), just as suggested for the Fe-Cr/ZrO_2 highlighted in section 2.3.1 above. Fe-based catalysts or addition of Fe to underperforming catalysts can support the redox properties necessary to better activate both the CO_2 and C_2H_6 and facilitate the MvK mechanism keeping the catalyst stable during CO_2-ODHE. However, it seems these redox properties depend on the interaction of Fe with the support or promoting metal such as Ni or Cr.

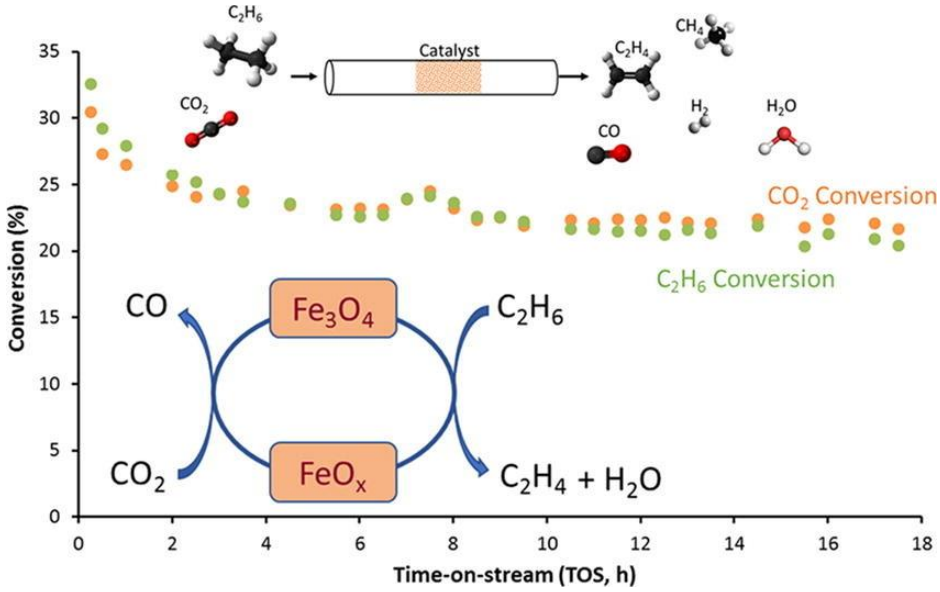

Figure 2.12: Redox mechanism for the activation of CO_2 and C_2H_6 during CO_2-ODHE at 600 °C on carbon resistant Fe/NiO-MgO-ZrO_2 catalyst [153].

2.3.5 Catalysts based on Mo-carbides

Instead of oxidising the active metals, the electronic, redox and catalytic properties can be influenced by alloying with carbon (carburization) forming metal carbides [1]. Recently, a novel class of carbides based on Mo are starting to garner interest for CO_2 activation reactions and

specifically CO_2-ODHE, pioneered in the work of Solymosi and Nemeth [147]. An unsupported and SiO_2-supported Mo_2C (Mo_2C/SiO_2) catalyst was studied in the CO_2-ODHE at 600 °C. The Mo_2C/SiO_2 achieved up to 87% ethylene selectivity at an C_2H_6 conversion of 15 - 16% within the tested 4 h TOS, outperforming the less active and selective Mo_2C. The C_2H_6 conversion increased (6 - 60%) with temperature (527 - 690 °C) enhancing the DRE resulting in a reduced ethylene selectivity. This shows Mo_2C-based system's ability to either cleave both the C-C and C-H (DR) or only the C-H (ODH) bonds depending on the reaction conditions. FTIR results obtained upon adsorption of C_2H_6 and CO_2 separately on this material revealed the formation of a surface-adsorbed ethylidyne and a partially oxidised Mo_2C surface (Mo-oxycarbide MoO_xC_y). This MoO_xC_y surface was suggested as the active/intermediate phase for the selective CO_2-ODHE. Thus, mechanistically, Mo_2C first activates CO_2 to form CO while it is partially oxidised into a transient surface MoO_xC_y phase which reverts to Mo_2C by reacting with C_2H_6 to form ethylene and H_2O. However, the formation of the adsorbed ethylidyne, a likely transition state for ethylene formation, also suggests that DD on the Mo_2C surface cannot be ruled out. This implies the prospect of a DD followed by RWGS reaction mechanistic pathway, which is typical on non-redox catalysts as explained in sections above, cannot be ignored. Similarly, in a study focusing on CO_2-ODHP, XPS and mass spectrometric analysis further corroborated the partial oxidation of Mo_2C into MoO_xC_y and formation of CO, respectively [64]. The notion that no catalyst oxidation was observed in the presence of both CO_2 and propane verified that the surface MoO_xC_y phase formed upon CO_2 activation is transient and quickly re-carburizes to Mo_2C upon propane activation during CO_2-ODHP.

Despite most studies focusing on the bulk form, Mo-carbide-based catalysts are effective for CO_2 activation or C=O scission even in the presence of H_2, a stronger reducing agent than light alkanes. This is due to their fast oxygen mobility. Thus, they also exhibit promising activity (close to thermodynamic equilibrium), stability and high CO selectivity during RWGS reaction, outperforming noble metal- (Pt and Pd) based catalysts at 300 - 600 °C [143,145,200,201]. Mo_2C also show activity for DRM or DRE [141,202]. These systems have a dual functionality for C=O bond scission (CO_2 activation) and H_2 dissociation or light alkane C-H/C-C bond cleavage.

In addition to reaction temperature as observed in the abovementioned studies, the type of support, gas admixtures and ad-metals can influence the catalytic performance of Mo-carbides. Chen *et al.* [63] reported a Mo_2C catalyst which improved in CO_2-ODHE activity when supported on the typically Lewis acidic γ-Al_2O_3 with the activity diminishing on a CeO_2 support, known for its

good redox properties. The unsupported bulk Mo_2C exhibited C_2H_6 (CO_2) conversion of 2% (1%), while supported on γ-Al_2O_3 a CO_2 conversion to 1.8% was reported, with a decrease in CO selectivity (from 47% to 36%) whereas on CeO_2 conversions diminished. The materials were tested at 600 °C in an equimolar CO_2 : C_2H_6 feed ratio. These observations clearly demonstrate the significant influence the support has on the performance of these catalysts. However, for all catalysts, the activity declined significantly within 150 mins TOS, potentially due to Mo_2C oxidation (especially on CeO_2 with enhanced C=O bond scission ability) or due to the high ethylene binding energy of Mo_2C leading to its decomposition to coke. 5 vol.-% H_2 admixture in the feed helped stabilize the catalyst (500 h TOS) with only slight deactivation. This was related to hydrogen's ability, as a stronger reducing agent, to remove the inactive oxide species and restore the active carbidic phase completing the catalytic cycle as previously observed in the RWGS reaction [143,202]. The addition of H_2 to the feed also greatly improved CO_2 conversion/activation (from 1.8% to 8.8%) as well as CO selectivity to 73.4% ascribed to the promotion of the RWGS reaction in addition to CO_2-ODHE.

Clearly, Mo-carbide can efficiently activate CO_2 which may result in its excessive oxidation and subsequent catalyst deactivation depending on the reducing power of the co-reactant (H_2 vs light alkane). Thus, a way to improve its performance in the CO_2-ODHE may be to add another active component such as a metal oxide with good redox properties in tandem to enhance C_2H_6 activation. A recent study from our research group explored the feasibility of several supports as tandem partners for Mo-carbide nanoparticles and the effect of catalyst preparation method as well as H_2 admixture on the catalytic performance in CO_2-ODHE at 600 °C [65].

The need for the formation of the active transient MoO_xC_y phase and subsequent oxygen removal suggests that the oxygen binding energy (OBE) of transition metal carbides also plays a role in their ability to activate CO_2. Mo-carbides are considered candidates for CO_2 activation because they have a stronger affinity for oxygen (and carbon) which enables them to spontaneously cleave the C-O bond [63,203]. However, relative to other transition metal carbides such as TiC, Mo-carbides have a lower OBE [141]. This means, Mo-carbides can easily form the MoO_xC_y *via* oxidation and revert to a MoC_y phase *via* reduction. Additionally, the transition metal to carbon ratio (M : C) is another general descriptor for the performance of transition metal carbides and gives an indication of their surface reactivity [204,205]. Besides the metcar systems such as Mo_8C_{12}, transition metal carbides with an M : C greater than 1 (Mo_2C and Fe_3C) are considered more reactive. However, this descriptor is quite impractical for Mo-carbide systems as there exist

different stable compositions: Mo_2C, MoC and the metcar (Mo_8C_{12}). Theoretical studies on orthorhombic β-Mo_2C (001) and cubic δ-MoC (001) surfaces attest that the crystal structure and Mo : C ratio serve as descriptors of the chemical activity of Mo-carbide systems [203,206]. The reactivity of the surface increases with Mo : C (from δ-MoC (001) to β-Mo_2C (001)), due to a decrease in the positive charge on Mo centres and structural changes that maximize the number of exposed Mo atoms.

2.3.6 Bimetallic alloy catalysts based on Fe_xNi_y

The catalytic performance, electronic and structural properties of transition metal-based catalyst systems can be improved, modified or supressed by alloying with other metals into multimetallic systems [1]. Often, the resulting alloys are distinct from their individual parent monometallic counterparts offering opportunities to tailor-make supported novel catalysts with enhanced activity, selectivity and stability [207,208]. Theoretical studies by Han *et al*. [16] predict the prospect of bimetallic alloys as superior catalysts for CO_2 dissociation compared to their monometallic counterparts. Based on their DFT calculations, bimetallic alloy surfaces have a lower activation energy for CO_2 activation than the monometallics. It was found that the degree of CO_2 activation varies over the different types of surfaces. Reaction energies showed a linear Brønsted-Evans-Polanyi (BEP) relation with the activation energy of CO_2 dissociation, while the sum of adsorption energies of CO and O showed a linear scaling relationship with the adsorption energy of the $CO_2^{\delta-}$ chemisorbed transition state as well as the reaction energy of CO_2 dissociation. By using these relations, a map of the variation of CO_2 dissociation activation energy over various bimetallic alloy surfaces was developed (see Figure 2.13). It is clear from their results that bimetallic alloy combinations of abundantly available non-noble metals with a lower predicted activation energy barrier for CO_2 dissociation consist of Fe, Ni and Co. Several studies have since then emerged demonstrating experimental verifications of these predictions in various CO_2-involving reactions.

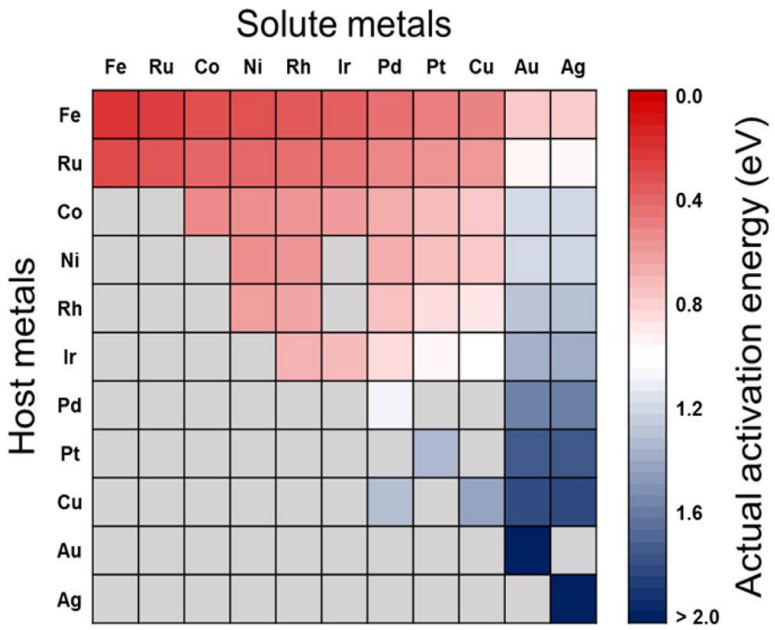

Figure 2.13: DFT estimated variation of activation energy for CO_2 dissociation over different pure metals and bimetallic alloy combinations [16]. The grey squares represent unpreferred bimetallic alloys due to surface segregation of solute atoms.

The group of Chen [19] tested CeO_2-supported Co_3Pt, Co_3Mo, Ni_3Mo and Fe_3Ni alloys and their monometallic counterparts for the conversion of CO_2 with C_2H_6 at 600 °C, a temperature at which CO_2-ODHE and DRE compete. Flow reactor studies show enhanced stability for alloys compared to their corresponding monometallic counterparts. Furthermore, Fe_3Ni/CeO_2 proved to promote C-H bond cleavage with 31% ethylene selectivity at 9.1% C_2H_6 and 10.8% CO_2 conversions whereas other alloys promoted cleavage of both C-H and C-C bonds with greater than 98% CO selectivity. This renders Fe_3Ni/CeO_2 a promising CO_2-ODHE catalyst. The observations were supported by DFT calculations which showed different reaction pathways on mixed Fe_xNi_y (111) and Pt-terminated CoPt (111) surfaces. The catalytic effect of metallic composition over the Fe_xNi_x/CeO_2 catalysts was further investigated in a follow up study by the same group [1,62]. The Fe-poor Fe_1Ni_3/CeO_2 and Fe_1Ni_1/CeO_2 as well as monometallic Ni/CeO_2 exhibited high (> 98%) CO selectivity supporting DRE. This is not surprising as Ni-based systems are widely known for their DR activity with rapid deactivation due to severe coking and sintering [209]. Conversely, the Fe-rich systems exhibited a high (> 66%) ethylene selectivity formed *via* CO_2-ODHE with Fe_3Ni_1/CeO_2 considered as the optimal content reaching up to 78% ethylene selectivity, calculated as the yield of ethylene over C_2H_6 conversion [1,62]. During the reaction, part of the Fe phase in the Fe-rich Fe_3Ni_1/CeO_2 is reported to partially segregate from the alloy leaving it Ni-rich with an fcc structure and an oxidised highly dispersed amorphous FeO_x overlayer at the perimeter of the

alloy forming an Ni-FeO_x interface was suggested. ADF-STEM imaging show that this FeO_x overlayer also extends to the surface of the CeO_2 support particles. The interface is identified as a potential active site for the selective cleavage of the C_2H_6 C-H bond *via* CO_2-ODHE. Under the same conditions, the Fe-poor fcc-alloy in Fe_1Ni_3/CeO_2 did not show significant segregation suggesting that Ni-CeO_x interfacial sites are the potential active sites for DR in Ni-based catalysts on reducible supports [210]. Overall, the metallic composition strongly influences ethylene and CO selectivity and this implies that by changing the Fe : Ni ratio in the alloy, we can control which of the parallel DRE and CO_2-ODHE reactions is promoted (See Figure 2.14).

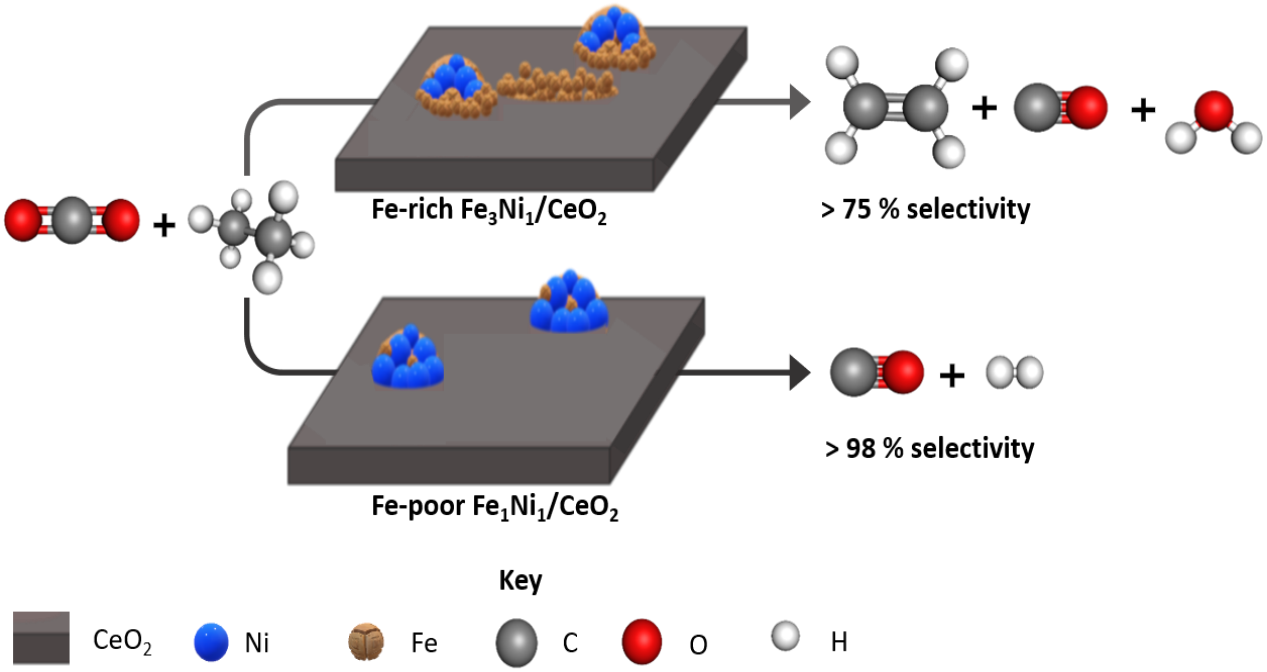

Figure 2.14: Dependence of ethylene and CO selectivity as reaction pathway followed over Fe_xNi_y/CeO_2 catalysts reported by Chen et al. [62]. Reaction scheme inspired by [1].

Similar studies were performed under the same reaction conditions for the conversion of CO_2 with propane and n-butane instead of C_2H_6 to evaluate the performance of Fe_3Ni_1/CeO_2 compared to other bimetallic systems [1,17,20,211]. For the conversion of CO_2 with propane, Ni_3Pt_1/CeO_2 was identified as the most active and stable DR catalyst with up to 96% CO selectivity at 12% and 39% propane and CO_2 conversion respectively [1,17]. In the presence of n-butane (1 : 2 : 17 n-butane : CO_2 : Ar ratio), the Fe_1Ni_3/CeO_2 was found to promote the DR pathway, just as previously reported for C_2H_6, with up to 91% CO selectivity at 59% and 31% CO_2 and n-butane conversions respectively [211]. The previously reported Fe_3Ni_1/CeO_2 proved promising for CO_2-ODHP as well exhibiting up to 58% propylene selectivity with great stability at 3% and 4% propane and CO_2

conversions. Similarly, this catalyst also showed some appreciable activity for CO_2-ODH of butane (CO_2-ODHB) achieving up to 21% of 1,3-butadiene selectivity at 19% and 12% CO_2 and n-butane conversions, respectively [211]. Similar conclusions as drawn for CO_2-ODHE in terms of the active sites facilitating the catalytic performance were also drawn for conversion of CO_2 with propane or butane over Fe_3Ni_1/CeO_2 [1,17,20,211]. The olefin selectivity over this material seems to decrease with increasing paraffin chain number.

Different supports can also influence the performance of these bimetallic Fe_xNi_y-based catalysts during conversion of CO_2 with light alkanes [18,211]. For C_2H_6, Fe_3Ni_1 was supported on reducible (CeO_2) and non-reducible (SiO_2 and ZrO_2) supports at different loadings [18]. Fe_3Ni_1/CeO_2 outperformed all other compositions exhibiting high stability with up to 80% ethylene selectivity at 4% (7%) C_2H_6 (CO_2) conversion with Fe_3Ni_1/SiO_2 barely active for either DRE or CO_2-ODHE and Fe_3Ni_1/ZrO_2 promoting DRE as well as displaying severe deactivation within 13 h TOS. The performance of Fe_3Ni_1/CeO_2 was again linked to the formation of the Ni-FeO_x/CeO_x interfacial sites which is potentially only possible on a reducible support while the performance of Fe_3Ni_1/ZrO_2 is ascribed to the formation of Ni-ZrO_2 interfacial sites on the non-reducible support. The CeO_2 is also beneficial as due to its reducibility and oxygen mobility, it can release reactive surface/lattice oxygen species and subsequently 'recover' them by inducing direct C=O scission. Interestingly, a 4-fold increase of the Fe_3Ni_1 loading on to the CeO_2 support results in the formation of Fe_xNi_y-CeO_x sites which selectively promote DRE. All lower loadings result in sparsely and evenly dispersed nanoparticles which selectively promoted CO_2-ODHE. The authors conclude that the high loading sample forms larger nanoparticles which do not form sufficient FeO_x at the perimeter of the Ni-rich alloy. For n-butane, similar conclusions were drawn with the supports, CeO_2 and CeO_2-ZrO_2, demonstrating CO_2-ODHB promotion owing to their good reducibility and oxygen mobility necessary for efficient CO_2 activation during the reaction [211]. It is proposed that the role of the support is to assist in the formation of the active interfacial sites and to mediate the activation of the CO_2 during the reaction.

The segregation behaviour of Fe from Fe_xNi_y alloy *via* oxidation by CO_2 has previously been proposed during DRM over highly active and stable Fe_1Ni_4 nanoparticles supported on a $Mg_xAl_yO_z$ matrix [212]. In this regard, Fe in the $Fe_1Ni_4/Mg_xAl_yO_z$ is partially oxidized to FeO segregates from the fcc alloy leaving it Ni-richer and migrates to the surface/perimeter where it settles in the form of small domains with a thickness of a few layers (overlayer islands). At the surface, FeO switches in the redox cycle $Fe^{2+}O/Fe^0$ when it reacts with carbon deposits preventing the typical

deactivation *via* coking and gets reduced back into metallic Fe. The metallic form re-alloys or gets re-incorporated into the Ni-rich fcc alloy phase (see Figure 2.15). This supports the DRE behaviour observed in the study by Chen *et al*. [19] presented above over Ni-rich Fe_xNi_y alloys and experimentally corroborates the suitability of the Fe_xNi_y bimetallic alloys for the activation of CO_2 as theoretically predicted by Han *et al*. [16].

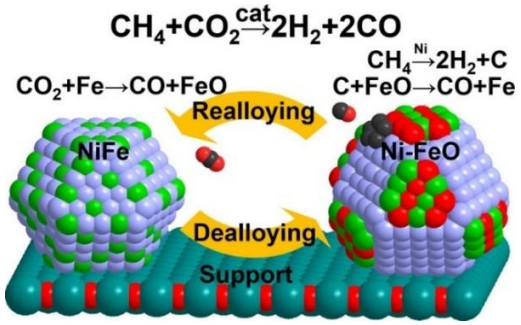

Figure 2.15: Graphical representation of the highly active and stable Ni-rich $Fe_1Ni_4/Mg_xAl_yO_z$ re-alloying and dealloying mechanism for cooperative methane-activation and coke removal via CO_2-activation during DRM. Figure taken from [212].

In the presence of the H_2 reducing agent instead of C_2H_6, this Ni-FeO_x interface, formed *via* the same segregation behaviour and accurately captured using ADF-STEM imaging with elemental mapping of the spent catalyst (see Figure 2.16), was also reported to be potentially responsible for the high RWGS activity and stability of the Fe-rich Fe_xNi_y alloy in the Fe_9Ni_3/ZrO_2 catalyst [125]. In this instance, the Ni-FeO_x interface possesses a weak interaction with the surface adsorbed CO product and this allows for its fast desorption from the surface before it can be further hydrogenated to CH_4 *via* the competing undesired methanation reaction.

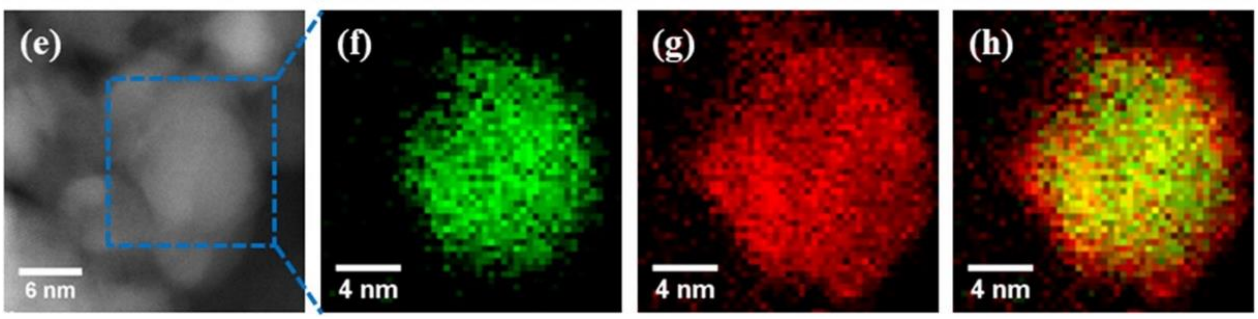

Figure 2.16: ADF-STEM image (e) and the corresponding individual (f) and (g) and combined (h) elemental maps of Ni (green) and Fe (red) for the RWGS spent Fe_9Ni_3/ZrO_2 catalyst reported by [125].

These studies clearly demonstrate the catalyst design opportunity of two transition metals in intimate contact within bimetallic systems. The type of active sites formed depend on the types of metals combined to form the alloy, the metallic composition of the alloy, the type or nature of the

support to which the alloy is anchored and the dispersion/particle size (influenced by loading). The resulting different active sites lead to significant differences in the mechanism or pathway through which the reactions proceed and thus to variations in product selectivity. Even with the progress achieved thus far, numerous degrees of freedom remain unstudied, potentially holding the key to improve the performance of these materials. In the Fe_xNi_y-based alloy catalysts specifically, Fe is more easily oxidized by CO_2 (into amorphous FeO_x, Fe_2O_3, Fe_3O_4 or a mixture of all) than Ni [21,125]. The degree of oxidation, types of oxides formed and coverage of oxide species increases with the Fe content in the alloy [21]. This determines the types of the active sites formed in the catalyst which influence its behaviour during the reaction. Since this strongly emphasizes the importance of the composition, it also signifies that the uniformity of the composition in the alloy nanoparticles plays a very crucial role. To understand the optimal composition necessary, it is important to synthesize these materials with controlled and uniform composition [21]. This is a difficult task with the conventionally used (co-)impregnation synthesis methods.

2.4 The Fe_xNi_y alloy system - structure and properties

Substitutional bimetallic Fe_xNi_y alloys exhibit several interesting (magnetic and catalytic) properties which makes them desirable for application in different fields [213]. As detailed for the catalytic properties in section 2.3.6, the characteristics of these noble-metal-free alloy materials are highly dependent on the metallic composition or atomic ratio and distribution (composition uniformity) of the Fe and Ni elements. Thus, these materials are also categorized or classified according to their compositions. Fe_xNi_y alloys with 50 - 80 at.-% of Ni are termed *permalloys* and are known for their high magnetic permeability, low coercivity and energy loss as well as high magnetic saturation and Curie temperature [214–217]. They are mostly utilized in magnetic resonance imaging (MRI), electromagnetic microwave absorption and shielding, magnetic refrigeration systems, sensors and recording devices [213,218–221]. The other class is known as Invar alloys which comprise of 30 - 40 at.-% of Ni and exhibit a thermal expansion coefficient of almost zero, unusual magnetic and thermoelastic properties and are also widely used [217,222,223]. Under a suitable atmosphere, these materials can adopt different phase configurations or crystal structures and magnetic properties depending strongly on the metallic composition and temperature (see Figure 2.17) [215,217,218,223]. Depending on these factors, the materials can exist as the γ austenitic solid solution with a face-centred cubic structure or the α or δ solid solutions both with a body-centred cubic (bcc) crystal structure. Co-existence of the

solid solutions with the bcc and fcc phases is also possible especially below 70 at.-% of Ni. However, the variation of phase compositions with temperature and Fe : Ni atomic ratio is still not fully understood [223,224]. The α phase is formed by destabilization of the γ phase *via* the formation of the so called “γ-loop”. The γ phase is stabilized by thermal excitations of the high-spin state instigated by the moment-volume instabilities. The excitation energies associated with the moment volume instabilities and the occupation of the electronic bands are influenced by alloying, so that the γ-region closes or opens depending on the valence electron number [225].

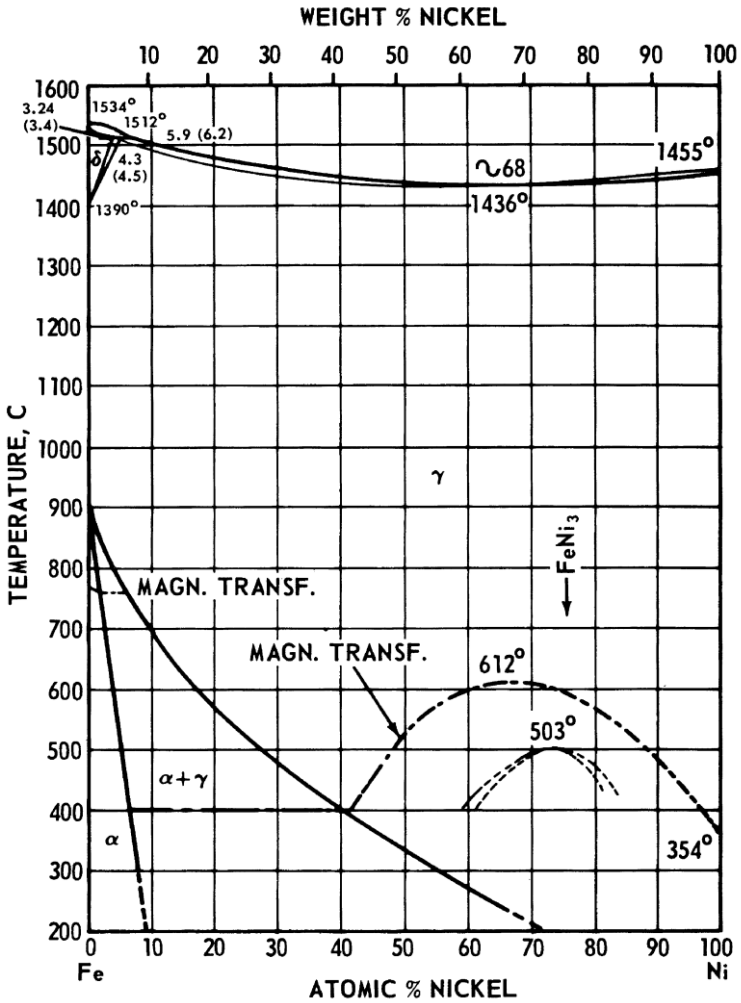

Figure 2.17: Fe_xNi_y equilibrium phase diagram showing possible temperature-dependent phase and magnetic transitions [223].

For Fe_xNi_y alloys with Ni contents greater than 30 at.-%, the austenitic solid solutions (usually fcc phase) stable at elevated temperatures are also stable at room temperature under any condition of cooling. This is due to the efficacy of Ni in depressing the γ to α phase transformation. Despite

the stability of phases at lower temperatures (below 300 °C) with varying atomic compositions, the phase transition boundaries have only been estimated *via* theoretical means and extrapolation. This is mainly due to the slow atomic diffusion kinetics at lower temperatures posing experimental difficulty. Fe, usually the host, adopts these different phases upon alloying with other metals (Ni in this regard) whose atomic sizes do not exceed ± 15% of the atomic size of Fe [225]. This is mainly because the solubility of alloying is limited by the elastic deformation energy which varies with the atomic size.

Since the properties of these materials depend on composition and uniformity of composition which in turn affect the crystal structure, it is expected that the different possible phases also influence some of their properties. This has been demonstrated already for maximum magnetization and coercivity of $Fe_{63}Ni_{37}$ samples of different shapes and phase (fcc and bcc) configurations [224]. It is also likely that the different phase configurations influence the catalytic performances beyond the reported effect of atomic composition.

2.5 Bimetallic-derived heterogeneous catalyst preparation methods

2.5.1 Conventional synthesis methods

Typically, immobilization of highly dispersed catalytically active bimetallic particles or their precursors onto support materials is achieved by using the wet or incipient wetness co-impregnation and sequential-impregnation techniques [17,18,21,209,226,227]. Wet co-impregnation entails suspension of the support in an excess volume of a diluted aqueous or organic solution containing two target metal precursors. The precursor solution is typically formed by dissolving metal precursor salts in the form of nitrates, chlorides, alkoxides, acetates, sulphates, etc., in solvents such as water, methanol, ethanol, etc. An excess volume of the solution relative to the pore volume of the support is used and this helps to attain a high dispersion of the precursor both in and outside the pores of the support. This method mainly relies on the diffusion of the bimetallic precursor and its adsorption on the support which may be improved/influenced by using different solvents or tuning the pH of the solution. Wet impregnation is most suitable for precursors with facile precursor-support interaction. However, nanoparticles with a relatively wide size distribution are typically obtained [227,228].

Incipient wetness co-impregnation leverages on capillary forces to draw the precursor solution into the pores of the support until its pore volume is filled, the state of incipient wetness (see Figure 4.1.) The volume of the precursor supplied is equal or below the pore volume of the support. Thus, this method is suitable for precursors with low affinity for adsorption on the chosen support since the metallic precursor species are forced into the pores. Typically, resulting active site clusters formed *via* this technique are highly distributed within the pores of the support and have sizes smaller than the pore diameter [227]. The main disadvantage of this technique is that the dispersion of larger concentrations of the precursor are challenging to attain in a single step and often multiple impregnation steps are required for this purpose. This is mainly because the maximum volume of the precursor to be impregnated is dictated by the pore volume which is often small and restricts the formation of higher precursor concentrations due to solubility limitations.

Instead of co-impregnation, sequential impregnation involves successive addition of the second metal precursor to a support already containing the first precursor. This can be done using either the wet or incipient wetness impregnation approaches. A combination can also be used. The main disadvantage of this route is the prospect of forming nanoparticles with non-uniform composition which is often necessary for attaining synergy in bimetallic systems [21]. Unlike incipient wetness impregnation (IWI), another advantage of wet impregnation is that since a larger volume of the solution is used independent of the pore-volume of the support, larger concentrations of the precursor can be easily dispersed onto the support in a single step.

For all these approaches, some post-treatment steps are necessary for the removal of the solvents. Typically, this is achieved by evaporation, filtration or drying. During drying, redistribution of the metal precursor is achieved depending on its interaction with the support. The heating rate and the drying temperature can influence the redistribution of the precursor and ultimately the size of the clusters formed. A high temperature calcination in air/inert gases sometimes followed by a reduction step is applied for the decomposition of the salts into immobilized nanoparticles of the target active phase. All these methods can be controlled, depending on the support-type, precursor salts, solvents as well as pre- or post-treatments like drying and calcination conditions, to form metallic clusters/nanoparticles with varying dispersion and synergy influencing the catalytic activity [229].

Another common method is precipitation. An insoluble solid is formed from a metal precursor solution when a precipitating agent (precipitant) is added. Supersaturation occurs when the

concentration of the precursor exceeds its solubility and this can be induced by temperature or pH changes, solvent mixing or evaporation [229,230]. The chemical nature of the solvent and precipitant determines the reaction through which the precipitate is formed and its chemical nature. Hydroxides or carbonates as precipitants tend to undergo ion exchange reactions with the precursor to yield precipitates that are hydroxides or carbonates in nature. During the process, the principles of nucleation and growth determine the size and dispersion of the resulting particles in the precipitate. For instance, an initial rapid nucleation of crystallites followed by growth without the formation of new nuclei can yield small monodisperse nanoparticles [229]. Depending on their size and attraction forces, which determine particle aggregation, the particles formed may remain dispersed in the suspension or settle down. The particles formed *via* this approach are separated from the solution by centrifugation or filtration and drying, often followed by calcination and reduction. This method can also be carried out in the presence of a support to which the particles formed adhere to immediately (precipitation-deposition) [231]. For bimetallic systems (oxides or alloys), co-precipitation which involves the simultaneous use of two different metal precursors to form the precipitate is a commonly described synthesis approach [232,233].

Despite their economic viability, these methods often yield particles with compositional heterogeneity which may impair efficient catalytic performance and make structure performance studies challenging [209]. Other methods such as the colloidal based reverse micro-emulsion and sol-gel synthesis can also be used to enhance size and composition homogeneity. However, they often require the use of structure directing agents/surfactants which cap particle surfaces and are difficult to completely remove, potentially affecting the catalytic performance of the synthesized material [209,234].

2.5.2 Surfactant-free solvothermal synthesis

The solvothermal synthesis method broadly involves the use of a solvent under moderate to high pressures and temperatures for the decomposition of precursors such as metal acetates and alkoxides to form nanoparticles, ceramics or polymers directly from the solution in a closed system. The operation temperatures can range from 100 °C to 1000 °C while the pressure ranges from 1 to 10 000 bar [235]. There are several ways in which the solvothermal synthesis can be performed. The most typical is when water is used as the solvent which is known as hydrothermal synthesis [235,236]. Most hydrothermal syntheses are used in combination with co-precipitation in one-pot approaches where a precipitant is used in addition to the solvent to further enhance

the kinetics [237]. Microwave introduction can also be used to enhance the kinetics for nanoparticle formation with the pH playing a key role during the synthesis [238].

Other solvothermal routes involve the use of substances such as ethylene glycol which serve as both a reducing agent and solvent in the presence of surfactants to prevent particle agglomeration [3,4]. Since stabilization agents are difficult to remove, recently the use of solvents such as benzyl alcohol, hexanol or benzylamine alone or with additional solvents such as ammonia has been studied [236,239,240]. This route is typically chosen because it is non-aqueous, surfactant-free, economical and simple for a scale-up and controlled synthesis of monodisperse nanoparticles of tuneable size and shape, in comparison to the typical impregnation, precipitation and reverse micelle routes. The use of alcohols as solvents allows operation at relatively low temperatures (<250 °C). Benzyl alcohol and hexanol have proven to act as both the solvents and ligands during the synthesis preventing agglomeration while affording monodisperse nanoparticles. This synthesis can also be used for the preparation of nanoparticles of bimetallic oxides such as ferrites, which can further serve as alloy precursors, using alcohol soluble metal precursors such as metal acetylacetonates or acetates [60,236]. Unlike impregnation which typically results in non-uniformity in composition per individual particle due to formation of separate mixed oxide crystallites as well as non-uniform particle sizes, this route is suitable for producing nanoalloys of uniform composition [21].

Parameters such as synthesis temperature and pressure, reaction time, solvent used (benzyl alcohol or hexanol), amount of ammonia added, precursor and reaction volume have proven to influence the crystallinity and crystal structure of the formed crystallites, particle size distribution, shape and bimetallic composition [4,236,239,241]. For instance, the use of hexanol as a solvent prevents reduction of Ni^{2+} to Ni^{0} resulting in facile formation of $NiFe_2O_4$ with accurate target composition [236]. The precursor solubility is another parameter that determines the success of this synthesis [235]. This method offers the possibility to control the crystal growth and the option to easily form large quantities (for laboratory synthesis approaches) of well-defined nanoparticles in a relatively short time.

2.6 Catalyst deactivation

One of the main challenges associated with the use of heterogeneous catalysts is that they are prone to undergoing some physical or chemical changes which may cause loss of activity with

time on stream. Often, the loss of catalytic activity also influences the products selectivity. This necessitates measures for catalyst replacements or regeneration from time to time. Some materials such as the Fe-based catalysts used for ammonia synthesis and Ni-based catalysts for methanation can remain active for periods as long as 5 to 10 years while others (e.g. Zeolites in fluid catalytic cracking) can only operate for seconds [242–246]. Catalysts operational for short periods are maintained by frequent re-activation or replacement. This mainly depends on the nature of the catalyst material and the reaction. The loss of activity proceeds *via* several mechanisms which are either due to the catalyst's normal working conditions (inherent) or exposure to impure feed/harsh conditions (operational) typical in industry [247]. Understanding of deactivation mechanisms plays a central role at the heart of catalyst development as it helps in the design of materials able to withstand deactivation. The most typical of these mechanisms encompass poisoning, fouling, attrition, thermal degradation, vapour formation, vapour-solid and soli-solid reactions (see Table 2.1) [244].

Table 2.1: Summary of catalyst deactivation mechanisms. Adapted from [244].

Mechanism	Type	Description
Poisoning	Chemical	Blockage of catalytic active sites due to strong chemisorption of species on the catalyst surface
Fouling	Mechanical	Physical deposition of species from fluid phase onto the available catalyst surface
Vapour-solid and solid-solid reactions	Chemical	Reaction of fluid, support, or promoter with catalyst to produce an inactive phase
Vapour formation	Chemical	Reaction of gas with catalyst to produce volatile compounds
Attrition/crushing	Mechanical	Loss of catalytic material due to abrasion Loss of internal surface area due to mechanical-induced crushing of the catalyst particle
Thermal degradation/sintering	Thermal	Thermally induced loss of catalytic surface area, support area, and active phase-support reactions

Some of these processes have also been reported to be potentially responsible for deactivation catalysts during the CO_2-ODHE process. For instance, Cr-based catalysts under CO_2-ODHE tend to deactivate by forming α-Cr_2O_3 crystallites and loss of surface area through sintering. Fouling of active sites by coke deposits is also typical on Cr-, Ga-, and V-based catalysts [9,11,13,248–250]. Mo-carbides tend to deactivate through excessive oxidation of the active molybdenum

oxycarbide (MoO_xC_y) or carbide phase [65,251]. Ga-based materials as well as metal oxides with strong Lewis acid sites tend to exhibit pronounced cracking and coking which result in their deactivation during CO_2-ODH [176,249,250].

2.6.1 Thermal degradation

Thermal degradation causes a decrease of surface area and the number of available catalytically active sites. Since it is thermally induced, it can occur at any stage of the catalyst's life from preparation (*i.e.* calcination and activation) to during the CO_2-ODHE reaction or during catalyst regeneration [252].

Sintering, which entails loss of surface area of the catalytically active phase *via* growth of nanoparticles/crystallites, is the most typical. This process is often driven by the effects of surface diffusion (surface energy) which in turn depend on the nature and pore structural properties of the support material (surface area, porosity and surface texture), crystallite size and temperature. Very small nanoparticles have high surface energies and it is the need to minimise this surface energy that drives sintering [244,245,253]. Sintering can occur when atoms (Ostwald ripening) or whole crystallites (coalescence) highly dispersed on a support migrate, collide and grow together into larger entities (See Figure 2.18).

The specific temperature at which sintering can occur is related to the melting point ($T_{melting}$) of the solid material. Atomic migration usually occurs at temperatures lower than particle migration. Approximations for the atomic (Hüttig) and particle (Tamman) migration temperatures can be calculated using Equation 2.12 and Equation 2.13 , respectively.

$$T_{\text{Hüttig}} = 0.3 \cdot T_{melting} \qquad \textit{Equation 2.12}$$

$$T_{\text{Tamman}} = 0.5 \cdot T_{melting} \qquad \textit{Equation 2.13}$$

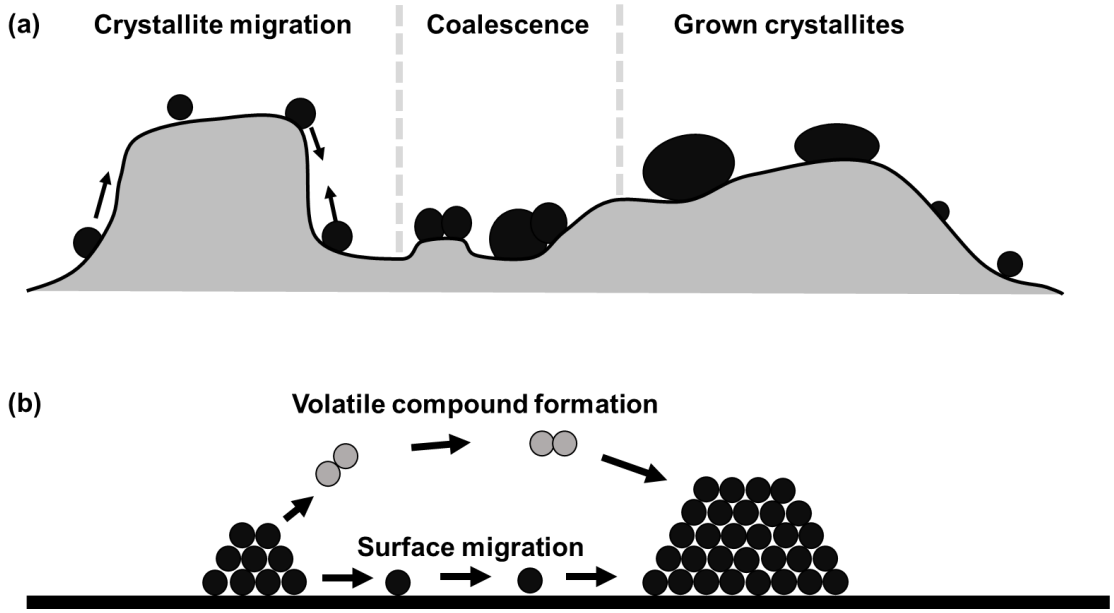

Figure 2.18: Graphical illustration of particle growth through sintering: (a) particle coalescence and (b) Ostwald ripening. Adapted from [244,245,252,254].

2.6.2 Fouling

Fouling occurs when the catalytically active phase surface is covered by deposits. The deposits may be originating from the catalytic reaction or originate from foreign species, even dust. The loss of catalytic activity originates from the physical blockage of active sites [252].

Carbon deposition or coking is a form of deactivation by fouling that is often reported for CO_2-ODHE catalysts, especially on catalyst materials with stronger Lewis acid sites such as metal oxides based on Ga and In as well as those supported on Al_2O_3. The type of carbon deposited on these catalysts can be graphitic or amorphous mainly depending on the degree of deposition and reaction temperature [5,9,11,174,187,255]. However, at optimal CO_2 activation, this carbon depositions can be supressed *via* the reverse Boudouard reaction.

2.6.3 Poisoning

Poisoning occurs when impurities, which are not directly involved in the reaction of interest, reactants or products chemisorb onto the catalyst surface resulting in blockage of available active sites. This limits accessibility to these sites for reactants and intermediates and may also have spatial and electronic influence on the adsorption efficacy of available neighbouring sites. The

poison may be selective or non-selective towards the active sites to which it binds. Selective poisons have an exclusive affinity for the catalytically active sites on the surface of the catalyst. However, non-selective poisons tend to adsorb on the whole catalyst surface blocking even sites that may not be necessarily relevant for the reaction of interest. Feed components and desired products can also bind to and limit site accessibility for other feed reactants/products *via* competitive adsorption. Some poisons bind to sites temporarily while others may bind permanently, thereby inducing irreversible modification of the catalytically active phase. [244–246,252]

3 Scope of the thesis

As previously discussed, the primary drawback associated with the promising metal oxide catalysts is their rapid loss of the CO_2-ODHE activity. A higher stability can be achieved at improved CO_2 conversions. This require that a catalyst is bifunctional availing sites for conversion/dissociation of the thermodynamically stable CO_2 in addition to the C-H bond cleavage effected by metal oxides. When its conversion is enhanced, CO_2 can aid in reducing or mitigating carbon deposition which causes catalyst deactivation. These are attested by literature demonstrating that, due to its high CO_2 conversion *via* the RWGS pathway, an Fe-Cr/ZrO_2 catalyst prepared by coprecipitation of Cr and Zr precursors and subsequent impregnation of the Fe precursor exhibited better stability than when the Cr, Fe and Zr precursors were coprecipitated altogether [3,5]. The high CO_2 conversion was speculated to aid in decoking the catalyst *via* the reverse Boudouard reaction resulting in improved catalyst stability. The CO_2-activation *via* RWGS was identified to occur over the iron oxide component in a redox mechanism while, in tandem, the Cr-oxide component activated C_2H_6 *via* the DD reaction. This demonstrates the need for bifunctional character of CO_2-ODHE catalysts.

Additionally, given that the CO_2-ODHE reaction can proceed through the redox (MvK) mechanism, it is conceivable that the rapid loss of activity may also be due to an insufficient replenishment of oxygen vacancies generated upon C-H bond cleavage. This is also possible at a lower CO_2-activation functionality impairing re-oxidation. The redox character of the metal oxide is also essential as upon C-H bond cleavage by the nucleophilic lattice oxygen, the oxygen vacancy generated can be replenished at ease. This is if the catalyst allows facile re-oxidation by the oxygen species from CO_2 dissociation. In principle, the nature of the lattice oxygen species and thus the redox character is also interconnected with the acid-base properties as both these properties influence the metal-oxygen bond strength and vary in different metal oxides [15]. Several studies have highlighted that on reducible metal oxide catalysts, C-H bond activation proceeds *via* direct ODHE (MvK) and on unreducible oxides *via* heterolytic dissociative adsorption for alkane activation followed by RWGS [14,15,250]. In both cases, strong acidity induces cracking which may cause coke formation. However, surface acid sites are deemed essential for the ethane activation ability of metal oxides [1,13,175,177,249]. On the other hand, surface basicity of metal oxides is suggested to play a role in the activation of both C_2H_6 and CO_2 [249].

Several studies have also explored addition of promoters for bifunctionality with impregnated Fe_xNi_y alloys amongst those promising (depending on composition and support) potentially because they are among alloys theoretically predicted to harbour good CO_2-activation ability [1,2,5,16–20,62,209,211,226]. However, composition and crystallite size uniformity are difficult to attain *via* impregnation as Ni and Fe oxide phases present in parallel make it challenging to understand influence of the Fe_xNi_y alloy composition. To the best of our knowledge no study has focused on the influence of the composition of Fe_xNi_y alloys with uniform composition and particle size supported on metal oxides in the form of overlayers with different reducibility and acidity but a constant pore structure during CO_2-ODHE.

This work aims to investigate the combined effects of both the supported Fe_xNi_y nano-alloy metallic composition as well as the catalytically active metal oxide overlayer support's overall and Lewis acid site strength and reducibility on the catalytic performance (*i.e.* activity, stability and selectivity towards CO_2-ODHE or any competing pathway products) during the simultaneous catalytic conversion of C_2H_6 and CO_2.

Novel approaches were undertaken to synthesize the two catalyst components and to combine them into the overall catalyst to overcome foreseeable challenges likely. Oxides of Cr, Ga, Sm, Ti, V and Zr, selected based on their reported wide range of characteristic acidity, were synthesized in the form of amorphous overlayers highly dispersed on a common γ-Al_2O_3 carrier [256–258]. This approach forms supports with chemical properties guided by the metal oxide while maintaining the structural properties (BET surface area, pore volume, etc.) of the γ-Al_2O_3 carrier, allowing the decoupling of the catalytic influence of the physical structure. Incipient wetness impregnation (IWI) of the oxide precursors to a thermally pre-treated γ-Al_2O_3 carrier was employed to synthesize these overlayer supports [257,259]. The metal loading, crystal structure, structural properties, nature of the chemical species, reducibility, strength of the Lewis acid sites and the overall acid site strength of these metal oxide overlayers were probed using SEM-EDX, offline XRD, N_2-physisorption, Raman spectroscopy, conventional H_2-TPR, DR-UV/Vis of adsorbed alizarin and TPD of adsorbed NH_3, respectively.

Secondly, oxidic Fe_xNi_y nanoparticles in the form of $(Ni_xFe_{1-x})Fe_2O_4$ or a mixture of $Ni(OH)_2$ and $(Ni_xFe_{1-x})Fe_2O_4$ were used as precursors of the target Fe_xNi_y nano-alloys and were prepared separately *via* a surfactant free solvothermal decomposition route adopted from Wolf *et al.* [239,241] before supporting to the metal oxide overlayers. Synthesizing them separately helped

attain crystallites of uniform sizes and composition enabling the formation of the corresponding Fe_xNi_y alloys with close intimacy of metals, compared to the common impregnation techniques. Since this synthesis was adopted from literature where it was used for formation of mostly Co-based systems, an investigation of the conditions necessary to obtain nanoparticles of 10 nm and a fixed composition was conducted. Afterwards, these conditions were adopted to synthesize the target nanoparticles with target overall Fe : Ni atomic ratios of 1, 3 and 5 which were supported on the overlayers *via* ultrasonication. STEM, TEM, offline XRD and ICP-OES were employed for characterization of these samples as synthesized. Additionally, *in situ* XRD analysis was also employed to prove the reducibility of the synthesized supported oxidic precursor nanoparticles and to capture, for the first time, the composition-dependent evolution of the alloy microstructure under temperature-programmed reduction conditions. The ability of the supported alloy microstructures to activate CO_2 and their evolution during CO_2-activation was also studied in an *in situ* XRD temperature-programmed CO_2-activation experiment.

Finally, the synthesized model bifunctional catalysts as well as the bare overlayers were evaluated for catalytic performance in a fixed-bed reactor for 24 h under an equimolar feed of CO_2 and C_2H_6 as well as a feed with an over-stoichiometric amount of CO_2 with a CO_2 : C_2H_6 ratio of 5. Under both streams, the influence of the bare overlayer acidity on activity, stability and selectivity towards likely products was studied. For the bifunctional catalysts with the alloy added to enhance CO_2-activation, the catalytic performance studies were divided into two as two batches of the oxidic Fe_xNi_y precursors obtained from separate autoclaves resulting in minor differences in metallic composition of the alloy were employed to support on the various overlayers. The first batch was only supported on the strongly acidic and reducible Cr-based and the weakly acidic Zr-based overlayer supports to study the influence of alloy composition on catalytic performance on these very different supports under the two feed streams. This also shed some light on the influence of the overlayer differences on the catalytic performances. Based on the conclusions drawn in this study, two out of the three metallic compositions of the alloy were selected and supported on the remainder of the supports to study the influence of the support per composition on the catalytic performance in detail. For this purpose, the second batch of oxidic Fe_xNi_y precursors with a slightly different metallic composition was employed. After exposure to catalytic testing conditions, all the spent catalysts were passivated and characterized using offline XRD and, for some Raman spectroscopy and TGA analysis to understand the changes that took place on the material as a result of exposure to reaction conditions.

4 Experimental

Table 4.1 provides a list and the details (suppliers and purity) of the chemicals used for the preparation of all the catalyst materials used in this study. All chemicals were used as received.

Table 4.1: Summary of all chemicals used for the preparation of catalysts as well as their purity and suppliers.

Chemical name	Formula	Supplier	Purity
Acetone	$(CH_3)_2CO$	Kimix	≥ 99.30%
Alizarin (1,2-Dihydroxy-9,10-anthraquinone)	$C_{14}H_8O_4$	Sigma-Aldrich	≥ 97.00%
Ammonium hydroxide	NH_4OH	Kimix	25.00 wt.-%
Benzyl alcohol	$C_6H_5CH_2OH$	Sigma-Aldrich	≥ 99.90%
n-Butanol	$CH_3CH_2CH_2CH_2OH$	Sigma-Aldrich	99.80%
Chromium(III) nitrate nonahydrate	$Cr(NO_3)_3{\cdot}9H_2O$	Sigma-Aldrich	≥ 99.90%
Ethanol	CH_3CH_3	Kimix	≥ 99.90%
Gallium(III) nitrate hydrate	$Ga(NO_3)_3{\cdot}xH_2O$	Sigma-Aldrich	99.90%
Hydrochloric acid	HCl	Kimix	25.00 wt.-%
Iron(II) acetate	$Fe(O_2CCH_3)_2$	Sigma-Aldrich	≥ 95.00%
Nickel(II) acetate tetrahydrate	$Ni(O_2CCH_3)_2{\cdot}4H_2O$	Sigma-Aldrich	≥ 98.00%
Titanium(IV) oxide (85 : 15 anatase : rutile) or P25	TiO_2	Sigma-Aldrich	-
Pluronic P123	$HO(CH_2CH_2O)_{20}(CH_2CH_2(CH_3)O)_{70}(CH_2CH_2O)_{20}H$	Sigma-Aldrich	-
n-Propanol	$CH_3CH_2CH_2OH$	Kimix	-
i-Propanol	$(CH_3)_2CHOH$	Kimix	≥ 99.98%
Puralox SCCa 5-150	γ-Al_2O_3	SASOL	98.00%
Samarium(III) nitrate hexahydrate	$Sm(NO_3)_3{\cdot}6H_2O$	Sigma-Aldrich	99.90%
Samarium(III) oxide	Sm_2O_3	Sigma-Aldrich	99.90%
Tetraethoxysilane (TEOS)	$Si(OCH_2CH_3)_4$	Sigma-Aldrich	98.00%
Titanium(IV) tetrabutoxide	$Ti(OCH_2CH_2CH_2CH_3)_4$	Sigma-Aldrich	97.00%
Vanadium(V) oxytriisopropoxide	$OV(OCH(CH_3)_2)_3$	Sigma-Aldrich	-
Vanadium(V) oxide	V_2O_5	Sigma-Aldrich	99.95%
Water	H_2O		Deionized

Zirconium(IV) oxide	ZrO_2	Sigma-Aldrich	99.00%
Zirconium(IV) tetrapropoxide	$Zr(OCH_2CH_2CH_3)_4$	Sigma-Aldrich	70 wt.-%

4.1 Synthesis of supports

4.1.1 Synthesis of metal oxide overlayers

The Lewis basicity and nucleophilicity of the metal oxide lattice/surface oxygen are expected to be kinetically relevant physicochemical parameters of the catalysts since they control the activation of C_2H_6 *via* H-abstraction during CO_2-ODHE. For control over this parameter and decoupling them from influences of textural properties (surface area, pore volume and diameter), model oxide overlayers (MO_x) were prepared instead of using bulk metal oxides. An incipient wetness impregnation (IWI) method (see Figure 4.1) reported by Wachs's group [68], and recently adopted by Prieto *et al.* [58,258,259], was employed for the synthesis of these overlayers with similar textural properties. The method entails coating a common porous carrier with oxides of transition, common and lanthanide metals (M = Ga, Cr, Sm, Ti, V, and Zr) in amounts equating to a theoretical two-dimensional overlayer. Oxides from the selected metals have a wide range of intrinsically varying Lewis acid site strength which imposes varying basicity/nucleophility of the lattice oxygen as well as redox properties [148,258,259]. High-surface area (151 m^2/g) mesoporous γ-Al_2O_3 (Puralox SCCa 5-150, SASOL) was used as the common carrier for the overlayers providing its textural properties and mechanical strength to the resulting MO_x@ γ-Al_2O_3 overlayers.

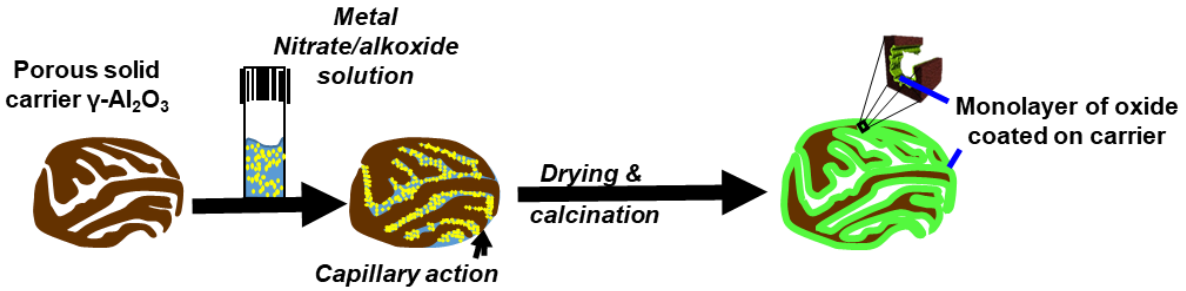

Figure 4.1: Schematic representation of the steps during the IWI technique used for the synthesis of metal oxide overlayers coated on the γ-Al_2O_3 common carrier.

The metal oxide overlayers were dispersed onto the surface of the γ-Al_2O_3 carrier *via* IWI targeting surface-specific metallic (M) coverages/loadings between 5 and 6.5 metal-atoms(M)/nm^2. These

coverages are sufficient to achieve a nominal monolayer saturation of MO_x on the surface of the carrier and were adopted from previous studies [68,257–259]. The γ-Al_2O_3 carrier was sieved to obtain 5 g of a 100 - 150 µm particle size fraction which was calcined in a muffle furnace (LT5/12 Nabertherm GmbH, Germany) under static air at 450 °C for 18 h and then immediately transferred into a 250 mL pear-shaped Schlenk flask that allowed storage under vacuum. The γ-Al_2O_3 was further subjected to thermal treatment at 280 °C using a heating mantle and a Schelenk setup in the pear-shaped Schlenk flask for 3 h for the removal of surface-adsorbed water. During the heating to and at the target temperature of 280 °C, a vacuum suction was applied. After cooling to 25 °C, Ar gas was flowed slowly to keep the sample in an inert and dry environment. 2.3 mL of a 2.73 M metal concentration (3.54 M for vanadium) precursor stock solution was added to the γ-Al_2O_3 under Ar flow. The resulting impregnated solid was dried at 70 °C for 12 h in a Memmert oven under static air and ultimately calcined at 600 °C (heating rate: 2 °C/min) for 4 h under air flow (flow rate: 50 mL/min). For the zirconium-based overlayer, the precursor stock solution used for the impregnation had a lower metal concentration than required (2.23 M). In this case, the entire impregnation procedure, including drying and calcination, was first performed using the 2.23 M stock solution and then repeated using a 0.50 M stock solution to achieve the target nominal surface coverage. The MO_x precursors used, solvents for preparation of corresponding precursor solutions, corresponding target coverage, resulting model oxide overlayer supports (denoted $MO_x@Al_2O_3$), and further synthesis information are summarized in Table 4.2 below.

Table 4.2: Target nominal overlayer coverage, precursors and solvents used for the synthesis of $MO_x@Al_2O_3$ supports.

$MO_x@Al_2O_3$	IWI steps	δ (M at/nm^2) [a]	δ (M wt.-%) [b]	Precursor	Solvent
$CrO_x@Al_2O_3$	1	5.0	6.1	$Cr(NO_3)_3{\cdot}9H_2O$	H_2O
$GaO_x@Al_2O_3$	1	5.0	8.0	$Ga(NO_3)_3{\cdot}xH_2O$	H_2O
$SmO_x@Al_2O_3$	1	5.0	15.9	$Sm(NO_3)_3{\cdot}6H_2O$	H_2O
$TiO_x@Al_2O_3$	1	5.0	6.0	$Ti(OCH_2CH_2CH_2CH_3)_4$	n-Butanol
$VO_x@Al_2O_3$	1	6.5	7.7	$OV(OCH(CH_3)_2)_3$	i-Propanol
$ZrO_x@Al_2O_3$	2	5.0	10.3	$Zr(OCH_2CH_2CH_3)_4$	n-Propanol

[a] Nominal overlayer surface coverage in number of metal atoms/nm^2. [b] Nominal overlayer surface coverage in weight percentage of metal loaded.

4.1.2 Synthesis of high-surface area mesoporous silica (KIT-6)

The molar composition of the gel used for the synthesis of the Korea Advanced Institute of Science and Technology-6 (KIT-6) mesoporous silica material, with a cubic Ia3d symmetry, was: 1 TEOS/1.9 HCl/0.017 P123/195 H_2O/1.31 n-butanol, as adopted from the study by Kleitz *et. al.* [260]. For the synthesis, 6 g of Pluronic P123 was dissolved in a mixture of 217 g deionized water and 11.8 g of 25 wt.-% aqueous HCl by stirring. After complete dissolution, 6 g of n-butanol was poured into the solution while stirring at 35 °C and the mixture was allowed to react for 1 h under stirring after which, 12.9 g of TEOS was added. The resulting mixture was further stirred at 35 °C for 24 h and subsequently subjected to a hydrothermal treatment at 100 °C for another 24 h in a 300 mL in-house PTFE-lined stainless-steel autoclave. The solid product obtained was collected by filtration, washed twice with 200 mL of deionized water, and then dried at 80 °C for 24 h in a Memmert oven under static air. Ultimately, the dry sample was calcined at 550 °C for 3 h in a muffle furnace (LT5/12 Nabertherm GmbH, Germany) using a temperature ramp rate of 20 °C/min under static air to remove the residual templating surfactant.

4.2 Synthesis of oxidic Fe_xNi_y nanoparticles *via* a solvothermal nonaqueous surfactant-free method

Oxidic Fe_xNi_y nanoparticles were synthesized through a modified nonaqueous surfactant-free solvothermal method (see Figure 4.2) [239,261].This entails a solvothermal treatment of a mixture of Fe and Ni acetate solutions in benzyl alcohol in the presence ammonium hydroxide.

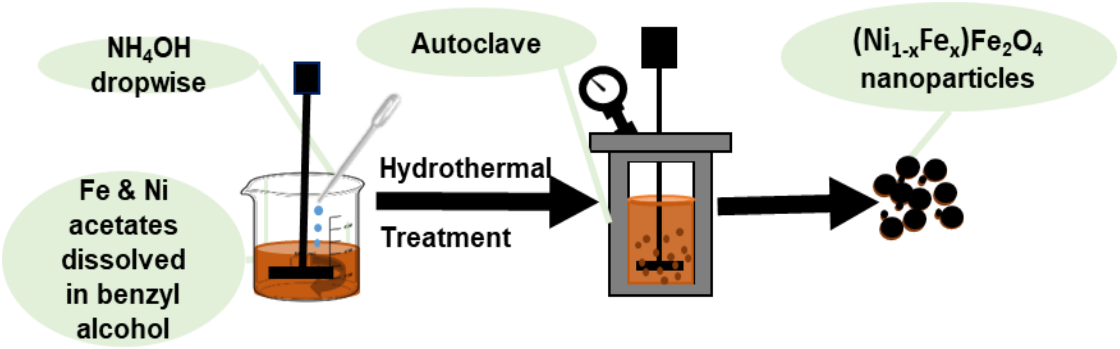

Figure 4.2: Schematic representation of the surfactant-free hydrothermal treatment method used for the synthesis of the oxidic $(Ni_{1-x}Fe_x)Fe_2O_4$ nanoparticles.

The synthesis conditions suitable for the formation of oxidic Fe_xNi_y nanoparticles were investigated as well as their effect on particle size. At a target fixed Fe : Ni atomic ratio of 3, the total mass of the acetate precursors, volume of ammonium hydroxide and synthesis temperature, were varied (samples T1.3 - 9.3 in Table 4.3).

A solid mixture of iron(II) acetate and nickel(II) acetate tetrahydrate at a fixed Fe : Ni atomic ratio of 3 was dissolved in 140 mL benzyl alcohol. The solution was stirred at 500 rpm for 2 h using a magnetic stirrer to ensure complete dissolution. Subsequently, ammonium hydroxide solution was added dropwise to the solution, resulting in a colour change from brown to black. This solution was transferred into an autoclave (BR-1500, Berghof, Germany) with PTFE lining and subjected to a hydrothermal treatment under stirring (500 rpm) with rapid heating to the target reaction temperature (see Table 4.3). The mixture was allowed to react for 5 h under stirring and at a vapour pressure below 25 bar, regulated by a pressure relief valve. After cooling the mixture to room temperature, its volume was tripled with iso-propanol and subjected to centrifugation in an Avanti J.E centrifuge (Beckman coulter, USA) at 25 °C and 10 000 rpm for 15 min to yield a deep dark-brown solid. The solid was re-dispersed in 400 mL of ethanol, re-centrifuged and then washed several times with 400 mL volumes of acetone and using centrifugation to separate the product from the solvent. The washing step was repeated until the supernatant was transparent, typically after 4 or 5 cycles.

Based on the synthesis conditions employed for sample T1.3 (see Table 4.3), nanoparticles of the same particle size but varying composition (Fe : Ni atomic ratio of 1, 3 and 5) were synthesized and described as TT1.1, TT1.3 and TT1.5. Due to instrument availability and material requirements in the present study, the synthesis was repeated in a second in house designed autoclave reactor using the same conditions as TT1.3 and TT1.5 but adjusting for the smaller total volume and without pressure release due to the high-pressure rating of the reaction vessel. The corresponding samples obtained using these conditions are labelled TT1-2.3 and TT1-2.5 (see Table 4.3). Lastly, to account for the higher water concentration in the reaction due to the higher reaction pressure and guided by previous studies in our laboratories identifying the water quantity as crucial parameter, the ammonium hydroxide concentration was reduced by a third yielding TT1-3.3 and TT1-3.5 [239].

Table 4.3: Summary of all the samples and parameters/conditions applied during the surfactant-free synthesis route of oxidic Fe_xNi_y nanoparticles.

Sample	Temperature (°C)	Acetates total mass (g)	Target Fe : Ni atomic ratio	Benzyl alcohol (mL)	NH_4OH (mL)	Synthesis autoclave
T1.3	200	1.93	3	140	85	Berghoff
T2.3	200	0.77	3	140	34	Berghoff
T3.3	200	0.31	3	140	13	Berghoff
T4.3	170	1.93	3	140	85	Berghoff
T5.3	170	0.77	3	140	34	Berghoff
T6.3	170	0.31	3	140	13	Berghoff
T7.3	150	1.93	3	140	85	Berghoff
T8.3	150	0.77	3	140	34	Berghoff
T9.3	150	0.31	3	140	13	Berghoff
TT1.1	210	1.93	1	140	85	Berghoff
TT1.3	210	1.93	3	140	85	Berghoff
TT1.5	210	1.93	5	140	85	Berghoff
TT1-2.3	210	1.45	3	105	64	Small
TT1-2.5	210	1.45	5	105	64	Small
TT1-3.3	210	1.45	3	105	21	Small
TT1-3.5	210	1.45	5	105	21	Small

4.3 Dispersion of oxidic Fe_xNi_y nanoparticles onto supports

The oxidic nanoparticles were anchored onto the various metal oxide overlayer supports and the mesoporous silica (KIT-6) using an ultrasonication technique previously demonstrated in our laboratories [239,262]. 0.21 g of the solid, corresponding to a target loading of 10 wt.-% metallic Fe_xNi_y, was added to 500 mL of ethanol and subjected to ultra-sonication at 100% power setting in a UBM22 ultrasonic bath (Labcon, USA) for 4 h to achieve re-dispersion of the nanoparticles in the solvent. Subsequently, a total of 1.5 g of the support was also subjected to ultrasonication for 4 h in 300 mL ethanol during which the nanoparticle dispersion was added dropwise. The mixture

was allowed to further sonicate for 4 h before it was transferred to a rotary evaporator in a 1000 mL Büchi round-bottom flask, which was stirred for 1 h at 240 rpm and 60 °C, before the ethanol was evaporated from the suspension at 460 mbar.

4.4 Material characterization

4.4.1 Diffuse reflectance ultra-violet /visible (DR-UV/Vis) spectroscopy

Diffuse reflectance ultra-violet/visible (DR-UV/Vis) spectroscopy analysis of the various metal oxide overlayer supports, with and without the adsorbed alizarin probe molecule, was performed at the Max-Planck-Institut für Kohlenforschung (Mülheim an der Ruhr, Germany). The spectra were recorded at room temperature using a double-beam UV/VIS Lambda 365 spectrophotometer (Perkin Elmer, USA) with a tungsten-halogen and deuterium interface. The instrument is equipped with an integrating sphere, and barium sulfate was used as a reflectance standard. Spectra were collected at a wavelength range of 200 - 800 nm (6.20 - 1.55 eV), taking 1 nm steps and the diffuse reflectance obtained was converted into the proportional absorption coefficients *via* the Kubelka-Munk (K-M) formalism using Equation 4.1 [256,263,264].

$$F(R_\infty) = \frac{k}{s} = \frac{(1 - R_\infty)^2}{2R_\infty} \qquad \textit{Equation 4.1}$$

Where $F(R_\infty)$ is the function of reflectance proportional to the absorption coefficients, k is the absorption coefficient, s is the scattering coefficient accounting for the internal scattering processes in the sample and R_∞ is the measured diffuse reflectance of the sample across the range of the acquisition wavelength. For the analysis without the alizarin adsorbate, the samples were analysed as prepared.

For the samples with adsorbed alizarin, the adsorbate was first deposited onto the various $MO_x@Al_2O_3$ overlayer supports following a method reported by Jeong *et al*. [256]. 200 mg of the $MO_x@Al_2O_3$ powdered sample was first subjected to a thermal pre-treatment for decarbonation and removal of any unwanted surface adsorbates. The sample was heated (4 °C /min) to 600 °C under a constant air flow (flow rate: 50 mL/min) and held at the target

temperature for 2 h. Subsequently, the sample was dehydrated at 200 °C in a 100 ml tubular Schlenk flask under vacuum (3 mbar) for 8 h and then stored inside a glovebox with <0.1 ppm O_2 and <0.1 ppm H_2O. In the glovebox, 150 mg of the sample was added to 20 mL anhydrous ethanol, forming a suspension. 20 mL of a 0.125 mM stock solution of alizarine in anhydrous ethanol was added. The resulting suspension was subjected to vigorous stirring for 10 min and the solid was filtered off and further washed several times with dry ethanol to remove the excess (unbound) alizarin until the filtrate was colourless. The solid was collected and dried under vacuum (3 mbar) at room temperature for 12 h.

The surface-adsorbed alizarin molecules serve as a probe for the relative strength of the Lewis acidity of the exposed MO_x species on the overlayer supports. As depicted in Figure 4.3, the alizarin molecules interact with the exposed lattice metal cations of the metal oxide ($MO_x@Al_2O_3$, depicted as M_xO_y) *via* the adsorbate-to-metal charge transfer (AMCT). As a result, the intra-molecular charge transfer (IMCT) transition energy (E_{IMCT}) is affected. E_{IMCT} is the energy required to transfer electrons from the catechol moiety to the ring system of the adsorbed alizarin molecule and is usually the lowest energy transition. E_{IMCT} can be measured using DR-UV/Vis spectroscopy and is directly proportional to the relative Lewis acid strength of the metal oxide onto which the alizarin molecule is adsorbed. That is, a high E_{IMCT} indicates the presence of strong Lewis acid sites.

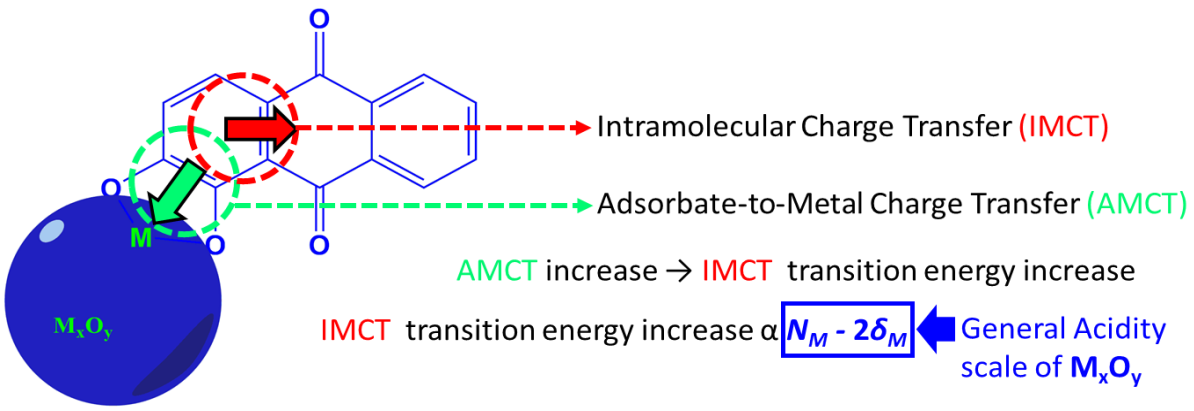

Figure 4.3: Scheme illustrating interactions between an adsorbed alizarin molecule and a metal oxide (M_xO_y) surface. Adapted from Jeong et al [256].

4.4.2 Raman spectroscopy

Raman spectra were recorded under ambient conditions using a commercial WITec Confocal Raman Microscope (WITec alpha300, Ulm, Germany) consisting of a CCD detector and confocal microscope combined with a Raman (UHTS 300) spectrometer which covers the Vis-NIR range. Depending on the samples, the spectra were either collected in the range of 100 - 1100 cm^{-1} for $MO_x@Al_2O_3$ samples or 85 - 1600 cm^{-1} for the oxidic spinel nanoparticles. The sample excitations were induced using a green Ar ion laser with λ = 532 nm and the laser power output was kept constant at 10 mW. The sample exposure time was 60 s. The software used for the data analysis is WITec Suite 5. A small sample of the powdered materials was deposited on a glass slide. Sample scanning in this instrument is achieved by using a fitted piezoelectric scan stage. Furthermore, the reflected laser and Rayleigh-scattered radiation during the acquisition are filtered by an edge filter. The Raman scattering from the sample is focused into a multi-mode optical fibre. This fibre serves as a pinhole for confocality as well as entrance slit to the UHTS 300 spectrometer.

Alternatively, an inVia Raman microscope (Renishaw, UK) with a 532 nm wavelength laser was used. Spectra were acquired at a laser power of 20 mW and an exposure time of 60 s in the same ranges as described above. The software used for the data analysis was WiRE 3.4 HF5925 build 2377.

4.4.3 Nitrogen physisorption analysis

Nitrogen adsorption/desorption isotherms were recorded using a Micromeritics TriStar II 3020 instrument after degassing a sample of approximately 500 mg at 120 °C overnight using a heating rate of 5 °C/min. The specific-surface areas were determined using the Brunauer-Emmett-Teller (BET) method which is based on physical adsorption and was applied in the relative pressure (P/P_0) range of 0.05 - 0.30 [265]. Where necessary, the total pore volumes reported were extrapolated to the volume of nitrogen uptake at a relative pressure (P/P_0) of 0.95. The pore size distributions and average pore diameters were derived using the Barrett-Joyner-Halenda (BJH) model applied on the desorption branch of the isotherms [266].

4.4.4 *Ex situ* X-ray diffraction (XRD)

X-ray diffraction (XRD) patterns of powdered samples were acquired in a D8 Advance laboratory X-ray diffractometer (Bruker, Germany) equipped with a Co radiation source ($\lambda_{K\alpha1}$ = 1.788973 Å) and a position-sensitive detector (LYNXEYE XE, Bruker AXS) in a Bragg-Brentano geometry. The instrument was operated with the power setting of 35 kV and 40 mA. The 2θ range of 20 - 120 °, corresponding to a 1/d range of 0.19 - 0.97 $Å^{-1}$, using a step size of 0.043 ° (4.2 x 10^{-4} $Å^{-1}$) and a time per step of 0.75 s, resulting in a total scan time of 29 min and 50 s were chosen for the XRD measurements.

Phase identification was achieved by comparison of the acquired diffraction patterns with reference patterns provided in the Powder Diffraction Files, PDF-2 (released in 2008) and PDF-4+ (released in 2019), published by the International Centre for Diffraction Data (ICDD) [267,268]. Quantitative analysis of identified phases was achieved *via* Rietveld refinement methods implemented in the software package TOPAS 5 (Bruker AXS) [269].

4.4.5 Electron microscopy

4.4.5.1 Transmission electron microscopy (TEM)

Transmission electron microscopy (TEM) was performed with a FEI Tecnai 20 instrument equipped with a lanthanum hexaboride field emission gun operated at 200 kV. The microscope is also fitted with a Tridiem 863 UHS Gatan image filter system and a 2k x 2k CCD Gatan camera. Prior to the TEM imaging, samples were prepared by re-dispersing a small amount of the powder in ethanol to form a suspension, followed by ultrasonication for 30 min for unsupported nanoparticles and for 1 min for all other samples. A droplet of the top suspension was deposited onto a holey film carbon-coated copper grid and dried in air for 1 h.

Both the number- ($\bar{d}_n$) and volume- ($\bar{d}_v$) based average particle sizes, as well as their corresponding standard deviations (sd_n and sd_v) were calculated (see Equation 4.2 - Equation 4.5). A minimum of 150 particles were measured per sample using the open-source software package ImageJ [270].

$$number-based\ average\ (\bar{d}_n) = \frac{\sum_{i=1}^{N} n_i d_i}{N} \quad \text{Equation 4.2}$$

$$volume-based\ average\ (\bar{d}_v) = \frac{\sum_{i=1}^{N} n_i d_i^4}{\sum_{i=1}^{N} n_i d_i^3} \quad \text{Equation 4.3}$$

$$number-based\ standard\ deviation\ (sd_n) = \sqrt{\frac{\sum_{i=1}^{N} n_i (d_i - \bar{d}_n)^2}{N-1}} \quad \text{Equation 4.4}$$

$$volume-based\ standard\ deviation\ (sd_v) = \sqrt{\frac{\sum_{i=1}^{N} n_i d_i^3 (d_i - \bar{d}_v)^2}{\frac{N-1}{N}\sum_{i=1}^{N} n_i d_i^3}} \quad \text{Equation 4.5}$$

Where d_i is the measured diameter of the nanoparticle i, n_i is the number of nanoparticles with the measured size d_i and N represents the total number of nanoparticles measured.

4.4.5.2 Scanning transmission electron microscopy (STEM)

High-angle annular dark-field scanning transmission electron microscopy (HAADF-STEM) micrographs and the energy dispersive X-ray (EDX) elemental maps of selected samples were acquired using a C_s-corrected probe in a Hitachi HD-2700 scanning transmission electron microscope operated at 200 kV at the at Max-Planck-Institut für Chemische Energiekonversion (Mülheim an der Ruhr, Germany). The instrument is equipped with a cold-field emission gun and two EDAX Octane T Ultra W EDX detectors. Powder samples were dry-casted onto holey carbon film coated Cu grids before being introduced into the measurement chamber. For reduced samples, reductions were performed at 500 °C for 3 h using a heating rate of 1 °C/min under a gas mixture of 10% H_2 in N_2 (flow rate: 50 mL/min) prior to the analysis. The reduced samples were then transferred into a glovebox where they were embedded into low-viscosity Spurr resins and then casted on TEM grids for analysis.

4.4.5.3 Scanning electron microscopy (SEM)

Scanning electron micrographs as well as energy dispersive X-ray (SEM-EDX) elemental maps were recorded on a high-resolution field emission Nova NanoSEM 230 (FEI) equipped with high resolution in-lens secondary, low voltage backscatter, STEM, as well as Oxford X-Max silicon drift EDX detectors. Prior to the analysis, the dry powder samples were sprinkled on a carbon tape that was attached to an aluminium stub. The powder that did not attach to the tape was removed with a burst of compressed air. The same instrument was also used for low EDX elemental mapping of selected samples. For this purpose, samples were deposited onto a holey film carbon-coated copper grid as previously described for TEM analysis.

4.4.6 Inductively coupled plasma optical emission spectroscopy (ICP-OES)

Elemental analysis of the various materials was carried out *via* inductively coupled plasma optical emission spectroscopy (ICP-OES) using a Varian ICP-OES 730 Series (Agilent) spectrometer. The instrument is equipped with a radial torch configuration and uses scandium as an internal standard. Prior to the analysis, the samples were acid digested using aqua-regia (3 : 1 mixture of HCl:HNO_3 molar ratio) for 24 h followed by heating to a temperature of 180 °C for 40 min at a rate of 6.4 °C/min in a Mars 6 Microwave digester (1600 W). Where the digestion method proved challenging, HF was added to aqua regia in a 1 : 4 molar ratio and during all the acid digestion steps, H_3BO_3 was used for neutralization.

4.4.7 Temperature-programmed reduction (TPR)

Temperature-programmed reduction studies were performed in either an AutoChem II 2920 or an AutoChem 2950 Micrometrics instrument. A 150 mg of sample was loaded into a U-shaped quartz reactor tube. The samples were heated to a temperature of 120 °C and held for 1 h using a heating rate of 10 °C/min for dehydration and removal of unwanted surface adsorbed species under 50 mL/min He flow. Thereafter, the sample was cooled to 50 °C before heating to 950 °C, with a heating rate of 5 °C/min under a constant flow of 50 mL/min 5 vol.-% H_2 in Ar. The H_2 consumption was measured using a thermal conductivity detector (TCD).

4.4.8 *In situ* X-ray diffraction (XRD)

In situ XRD was used to monitor the phase transitions of the catalyst materials under reduction and CO_2 activation conditions. A commercial Anton Paar XRK-900 sample analysis reaction chamber was used in a D8 advance (Bruker, Germany) laboratory X-ray diffractometer. The diffractometer is equipped with a molybdenum X-ray source ($\lambda_{k\alpha 1}$: 0.70932 Å) and a position-sensitive detector (Vantec, Bruker AXS). The optics and detector were set to a parallel beam geometry to minimize peak shifts due to sample displacement. The instrument was operated at 42 - 50 kV and 35 mA.

About 200 mg of the sample was loaded onto a cylindrical plate-like ceramic holder with a geometry allowing a maximum sample diameter of 14 mm and gas flow through the sample. For the reduction studies, the samples were exposed to a stream of 5 vol.-% H_2 in N_2 (flow rate: 50 mL/min/g of sample) at atmospheric pressure and heated at 1 °C/min from 50 to 700 °C. Diffraction patterns were collected throughout the heating period, every 5 minutes, scanning from a 2θ of 15 to 29.5 ° (a 1/d from 0.37 to 0.72 $Å^{-1}$) using a step size of 0.02 ° and a time per step of 0.2 s, amounting to a total scan time of about 4.07 min. To study the CO_2-activation ability of the catalysts, the samples were reduced at 500 °C for 3 h with a heating rate of 1 °C/min. The chamber was subsequently cooled to 50 °C under N_2 before introducing 1 vol.-% CO_2 in N_2 (flow rate: 100 mL/min) and heating to 750 °C at 1 °C/min.

4.4.9 Thermogravimetric analysis (TGA)

Thermogravimetric and differential thermal analyses (TGA/DTA) were performed in a Discovery SDT 650 (TA instruments, USA) instrument. For the decomposition surface carbon deposits from the spent catalysts, a 30 - 50 mg of a powdered sample was loaded into a 50 µL alumina crucible and exposed to air flow (flow rate: 100 mL/min) while heating from a temperature of 50 to 1200 °C at a rate of 5 °C/min. For the temperature-programmed reduction and subsequent the temperature-programmed CO_2 activation reaction experiments, the samples were exposed to stream of 5 vol.-% H_2 in inert (flow rate: 100 mL/min) while heating from 50 to 500 °C at a rate of 1 °C/min, cooled to 300 °C under inert and exposed to a stream of 1 vol.-% CO_2 in inert (flow rate: 100 mL/min) for 3 h before heating to 1000 °C at a rate of 4 °C/min.

4.5 Reactor-based catalytic testing of materials

The test unit employed in the present study (see Figure 4.4) has three feed lines which allow for simultaneous feeding of up to three different gases sourced from a central gas reticulation system (Ar, N_2 and H_2) and stand-alone gas cylinders (gas mixes, C_2H_6 and CO_2). Two feed gas mixes consisting of 25% C_2H_6, 25% CO_2, 45% Ar and 5% He (AFROX) and 8.3% C_2H_6, 41.7% CO_2, 45% Ar and 5% He (AFROX) were used for catalytic testing under CO_2-ODHE conditions with CO_2 : C_2H_6 feed gas ratios of 1 : 1 and 5 : 1, respectively. The former feed gas ratio is above while the latter is within the explosive range of ethane (3 – 12.4 vol-%) and was handled meticulously for safe experimentation. The same feed gas compositions could be generated by directly combining the individual gases whereby only Ar gas was used for dilution. The flow rates were controlled by three Delta Smart II mass flow controllers (Brooks Instruments); MFC-1, MFC-2, and MFC-3. The feed gas mixture is simultaneously fed into the two testing reactors, after spitting *via* two fused silica columns of equal length. The reactor outlet lines were heated to 80 °C up to the catch pots (which were kept at room temperature) to prevent any premature water condensation. The total feed gas flow can also be set to bypass the reactors. In this case, three needle valves were employed to realize the same pressure drop as observed across the fused silica capillaries. The reactors themselves were made of quartz glass tubing with a length of 150 mm and an outer (inner) diameter of 6.35 (4.00) mm. These reactors are placed horizontally sandwiched by two stainless steel heating blocks each with two heating elements to achieve the desired temperature measured by a thermocouple also sandwiched by the blocks. A maximum temperature of 750 °C can be attained *via* this reactor set-up.

Reactor outlet gas or bypassed feed gas compositions were analysed using an Agilent Technologies 490 Micro-GC equipped with three individual channels and dedicated TCDs (more details on gas analysis provided later in this section). Two molecular sieve 5 Å PLOT columns of 10 and 20 m lengths and a 10 m PoraPlot Q column were used to separate the products and unreacted gas components. The 20 m molecular sieve column is operated with H_2 as the carrier gas for the separation of Ar, N_2, CH_4 and CO. The 10 m molecular sieve column uses Ar as the carrier gas to separate He and H_2. Lastly, the 10 m PoraPLOT Q column also uses H_2 as the carrier gas to separate CO_2, C_2H_4 and C_2H_6. Gaseous H_2O is qualitatively separated in the 10 m PoraPLOT Q column as well. To select between the two reactor outlet streams for the GC-TCD analysis, two three-way solenoid valves are installed which can be programmed *via* an in-house

developed Arduino-based control unit. While the reactor outlet stream of one reactor is guided towards the Micro-GC the outlet stream of the other is vented *via* the extraction system.

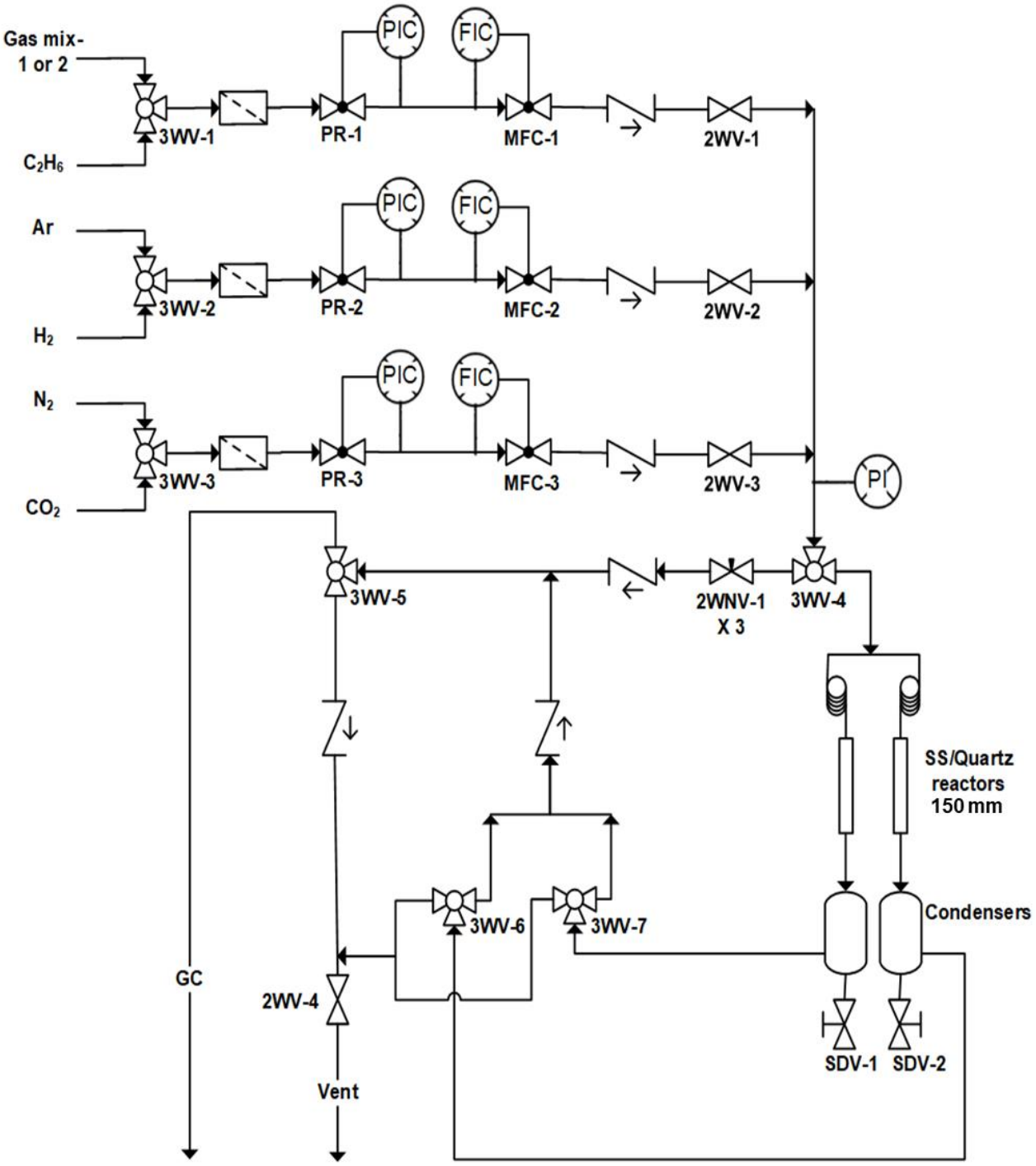

Figure 4.4: Piping and instrumentation diagram of the two-reactor test unit set-up used to test the activity and selectivity of the synthesized catalyst materials.

The reactor effluents were sampled every 5 minutes during all experiments. The software program Varian Galaxie Chromatography Data System 1.9.3.2 was used to perform the gas chromatographic analysis and to integrate peak areas of each gas component. The full details of the conditions and parameters used to achieve separation of gaseous components are summarized in Table 4.4.

Table 4.4: Summary of the different column properties and the conditions used to achieve gas separation in each column of the micro-GC.

Analysis channel	**1**	**2**	**3**
Column stationary phase	Molecular sieve 5 Å PLOT	Molecular sieve 5 Å PLOT	PoraPLOT Q
Column length (m)	10	20	10
Detector	TCD	TCD	TCD
Carrier gas	Ar	H_2	H_2
Injection time (ms)	60	60	70
Injector temperature (°C)	80	80	80
Column temperature (°C)	80	70	60
Column pressure (kPa)	150	120	80
Duration (s)	270	270	270
Gasses separated in order of retention time	He and H_2	Ar, N_2, CH_4 and CO	CO_2, C_2H_4, C_2H_6 and H_2O

The micro-GC was calibrated using two different certified calibration gas mixtures (20% C_2H_6, 9.7% C_2H_4, 20% CO_2, 45.5% Ar, 4.8% He; and 10.1% CO_2, 15.9% CH_4, 18.5% CO, 39.8% H_2, 9.9% Ar,5.8% N_2 both from AFROX). Response factors for each gas (except for N_2) were calculated using Ar as the internal standard (see Equation 4.6).

$$f_x = \frac{A_x \cdot \upsilon_{Ar,in}}{A_{Ar} \cdot \upsilon_{x,in}} \qquad \textit{Equation 4.6}$$

Where f_x, A_x and $\upsilon_{x,in}$ are the response factor, peak area measured in the chromatogram and molar gas flow rate (mol/min) of gas component x. A_{Ar} and $\upsilon_{Ar,in}$ are the peak area measured from chromatogram and the molar gas flowrate (mol/min) of Ar. To calculate the molar flow rate

$\upsilon_{x,out}$ (mol/min) of each gas component x exiting the reactor system during the CO_2-ODHE and CO_2-activation experiments, Equation 4.7 employing the identified calibration parameters was used.

$$\upsilon_{x,out} = \frac{A_x \cdot \upsilon_{Ar,in}}{A_{Ar} \cdot f_x} \qquad \text{Equation 4.7}$$

The catalytic performance of the materials during CO_2-ODHE was evaluated by calculating conversions of C_2H_6 and CO_2. The conversions were expressed as the amount of the reacting component (C_2H_6 or CO_2) converted relative the amount of the reactant (C_2H_6 or CO_2) fed into the reactor (see Equation 4.8).

$$X_y(\%) = \frac{\upsilon_{y,in} - \upsilon_{y,out}}{\upsilon_{y,in}} \cdot 100 \qquad \text{Equation 4.8}$$

Where $X_y(\%)$ is the conversion expressed in %, $\upsilon_{y,in}$ is the reactor inlet molar flow rate of (mol/min) and $\upsilon_{y,out}$ is the reactor effluent molar flow rate (mol/min) of compound y (C_2H_6 or CO_2).

The carbon-based selectivity towards ethylene, CO or methane was calculated as shown in Equation 4.9.

$$S_z(C-\%) = \frac{n_z \cdot \upsilon_{z,out}}{\sum_n (n \cdot \upsilon_{out})} \cdot 100 \qquad \text{Equation 4.9}$$

Where $S_z(C-\%)$ is the selectivity expressed in C-%, n_z is the number of carbon atoms and $\upsilon_{z,out}$ is the reactor effluent molar flow rate (mol/min) of the carbon-containing compound z (ethylene, methane or CO). The term in the denominator represents the sum of the molar flow rates (mol/min) υ_{out} of all the possible carbon containing product compounds, each multiplied by the corresponding number of carbon atoms n. Since the selectivity is carbon-based, 67 C-% selectivity towards ethylene and 33 C-% towards CO products would represent a CO_2-ODHE pathway in the absence of any side reactions. A lower selectivity towards ethylene would indicate that methanation or CO-forming reactions such as C_2H_6 dry-reforming or over-oxidation are taking place, whereas a significantly higher ethylene selectivity would suggest that the direct dehydrogenation (DD) pathway is proceeding in parallel. Due to unfeasible analysis at lower

concentrations, H_2 was not analysed although it was often observed especially when DRE was promoted.

The yield of ethylene was calculated as the ratio of the molar flow rate of ethylene formed to the molar flow rate of C_2H_6 fed into the reactor (see Equation 4.10 below).

$$Y_{C2H4}(C-\%) = \frac{\upsilon_{C2H4,out}}{\upsilon_{C2H6,in}} \cdot 100 \qquad \textit{Equation 4.10}$$

Where $Y_{C2H4}(C-\%)$ is the yield of ethylene expressed in C-% whereas $\upsilon_{C2H4,out}$ and $\upsilon_{C2H4,out}$ are molar flow rates (mol/min) of ethylene and the C_2H_6 in the feed gas, respectively.

Each reactor tube was loaded with 100 mg of the catalyst forming a packed bed held in place by plugs of glass wool. Beyond the glass wool plugs, packings of SiC provided a preheating zone of the feed gas as well as secured the catalyst bed in the isothermal zone of the reactor. The catalysts were first reduced in 25 mL/min/reactor of H_2 at 500 °C for 3 h using a heating rate of 1 °C/min. After reduction, the temperature was increased to 600 °C using a heating rate of 5 °C/min under inert N_2 flow of 50 mL/min/reactor. The activity and selectivity of the active materials for the CO_2-ODHE were investigated at two different CO_2 : C_2H_6 ratios, *i.e.*, 1 and 5. For both ratios, 25 mL/min/reactor of the feed gas mixture was set varying in composition: 25% C_2H_6, 25% CO_2, 45% Ar and 5% He (6.25 mL/min C_2H_6, 6.25 mL/min CO_2, 12.5 mL/min He and/or Ar) for attaining the CO_2 : C_2H_6 target feed ratio of 1; and 8.3% C_2H_6, 41.7% CO_2, 45% Ar and 5% He (2.2 mL/min C_2H_6, 10.3 mL/min CO_2, 12.5 mL/min He and/or Ar) for attaining the CO_2 : C_2H_6 target feed ratio of 5. Blank experiments, in the absence of active material but with a packed bed of SiC were performed at 600 - 700 °C in a quartz reactor tube which only exhibited negligible conversion. For CO_2 activation experiments performed on Fe_xNi_y nano-alloys supported on KIT-6, the temperature after reduction was decreased to 50 °C at a cooling rate of 10 °C/min. At 50 °C, 100 mL/min/reactor of 1 vol.-% CO_2 in Ar was fed to the reactor and the temperature was increased to 700 °C at a heating rate of 1 °C /min.

5 Physicochemical characterization of metal oxide overlayers

Some results reported in this chapter are part of the publication: S. Raseale, W. Marquart, K. Jeske, G. Prieto, M. Claeys, N. Fischer, Supported Fe_xNi_y catalysts for the co-activation of CO_2 and small alkanes, Faraday Discuss. 229 (2020) 208-231. https://doi.org/10.1039/C9FD00130A.

One of the core objectives of this work was to synthesize model metal oxide overlayer support materials ($MO_x@Al_2O_3$) which exhibit comparable physical properties such as surface area, pore volume and average pore diameter and mechanical properties imposed by a common carrier. However, these overlayers should also exhibit different chemical properties such as relative total and Lewis surface acid site strength as well as reducibility which are related to the corresponding bulk metal oxides. To achieve this, overlayers of different target metal oxides were coated on the surface of a γ-Al_2O_3 carrier *via* the incipient wetness impregnation (IWI) preparation technique. The physicochemical properties of the synthesized metal oxide overlayers were characterized in terms of the metal content (M), overlayer coverage (δ), physical/textural properties and the relative surface Lewis acid site strength described by the intra-molecular charge transfer energy (E_{IMCT}) of surface-adsorbed alizarin (see Table 5.1).

Table 5.1: Physicochemical properties (chemical composition, relative surface Lewis acid site strength and pore structural properties) of γ-Al_2O_3 and the different $MO_x@Al_2O_3$ supports.

Sample	Chemical composition		Textural properties				E_{IMCT} (eV)
	M (wt.-%)[a]	δ (M/nm²)	$S_{B.E.T.}$ (m²/g)[b]	V_p (cm³/g)[c]	D_p (nm)[d]	V_p (cm³/g Al_2O_3)[e]	
γ-Al_2O_3	-	-	151	0.50	9	0.50	2.51
$CrO_x@Al_2O_3$	7.5	6.2	128	0.44	11	0.49	2.27 (2.54)[f]
$SmO_x@Al_2O_3$	18.9	6.2	123	0.33	9	0.42	2.38
$TiO_x@Al_2O_3$	7.9	7.1	141	0.44	9	0.50	2.46
$GaO_x@Al_2O_3$	8.3	5.2	133	0.44	9	0.50	2.48
$ZrO_x@Al_2O_3$	11.5	5.7	144	0.43	9	0.50	2.49
$VO_x@Al_2O_3$	9.9	8.6	111	0.40	8	0.49	2.60[f]

[a] Based on SEM-EDX analysis; [b] BET mass-specific surface area; [c] Total mass-specific pore volume and [d] average pore diameter acquired via the BJH formalism of the desorption branch of the corresponding N_2-physisorption isotherm; [e] Total pore volume normalised by the mass of γ-Al_2O_3 assuming the bulk oxide stoichiometry for estimation of the MO_x mass. [f] Obtained from the alizarin adsorbed on a $MOx@Al_2O_3$ support thermally pre-treated in air.

Based on the pore-structural properties obtained from the low-temperature N_2 physisorption studies of the bare γ-Al_2O_3 carrier and the MO_x@Al_2O_3 overlayer materials, incorporation/dispersion of the MO_x overlayers on the surface of the carrier γ-Al_2O_3 results in a reduction, by a factor below one-third, of the mass-specific surface area (S_{BET}) and pore volume (V_p). The reduction of surface area was by up to 26% (*i.e.* 151 m^2/g to 111 m^2/g) recorded for VO_x@Al_2O_3, while the pore volume (V_p) decreased by up to 34% (*i.e.* 0.50 cm^3/g to 0.33 cm^3/g) recorded for SmO_x@Al_2O_3. This reduction is attributed to the increased density of the obtained materials in comparison to γ-Al_2O_3 and pore-filling of smaller as well as pore-narrowing of larger mesopores caused by coating the carrier with the MO_x overlayers. The average pore diameter for most of the MO_x@Al_2O_3 samples remained comparable to γ-Al_2O_3 (≈ 9 nm), while that of CrO_x@Al_2O_3 increased slightly to 11 nm. This is an indication of pore-plugging of the smallest mesopores of the γ-Al_2O_3 carrier by CrO_x, which decreases the smaller mesopore volume (below 5nm) in the pore size distribution (see Figure 5.1(b)).

Despite the comparable average pore diameter of the MO_x@Al_2O_3 overlayer materials with M = Sm, Ti and Ga, the MO_x overlayer causes a reduction of both the larger and smaller mesopore volume as well as the total mesopore volume resulting in a slightly narrower pore size distribution compared to the bare γ-Al_2O_3. This effect is more apparent for the SmO_x@Al_2O_3 overlayer material with a significantly narrowed pore size distribution compared to bare γ-Al_2O_3. For ZrO_x@Al_2O_3, a higher degree of pore-narrowing with preservation of smaller mesopores is observed. For the VO_x@Al_2O_3 overlayer material, pore-plugging results in a significant reduction of the mesopores below 7 nm in diameter and the emergence of larger ones above 20 nm attributed to surface roughness and increased particle density. When normalized by the mass of γ-Al_2O_3, the pore volumes of the MO_x@Al_2O_3 samples are comparable to that of the bare γ-Al_2O_3 with a decrease of less than 16% for SmO_x@Al_2O_3 accounting for the volume occupied by the dense overlayer. This also rules out any extensive mesopore-plugging by the loaded MO_x overlayers.

For all the samples, a type IV N_2-physisorption isotherm with a marked H1 hysteresis loop, typical for materials with well-defined cylindrical-like mesopore channels or agglomerates of almost uniform spheres according to IUPAC classification, was observed (see Figure 5.1(a)) [271]. This corroborates the sole presence of mesopores in γ-Al_2O_3 and their preservation after coating with the various MO_x overlayers as also suggested by the pore size distributions (see Figure 5.1(b)). This means that coating with the various overlayers does not significantly affect the type of pores

in the final $MO_x@Al_2O_3$ overlayer materials. Besides the $SmO_x@Al_2O_3$ overlayer material with 200 cm^3/g due to the significantly reduced total pore volume (0.33 cm^3/g), the total volume of N_2 adsorbed was comparable (between 250 and 265 cm^3/g) for all the $MO_x@Al_2O_3$ materials. These are all slightly reduced from 295 cm^3/g observed for the bare γ-Al_2O_3 which is appreciable. This also correlates with the trend of the total pore volume observed for these materials (see Table 5.1) which are also comparable and lying between 0.40 and 0.44 cm^3/g, reduced from 0.50 cm^3/g for γ-Al_2O_3.

Overall, these results suggest that the deposition of the various MO_x overlayers on the surface of the γ-Al_2O_3 carrier is a successful strategy to maintain comparable textural properties of the γ-Al_2O_3 carrier for the various targeted $MO_x@Al_2O_3$ overlayer materials. The theoretical coverage corresponding to the formation of a MO_x monolayer coating on γ-Al_2O_3 is about 6.5 metal atoms (M)/nm^2 for VO_x and 5 M/nm^2 for MO_x with M = Cr, Sm, Ti and Zr [13,257,258,272,273]. Since 5 M/nm^2 is the typical theoretical monolayer coverage for most MO_x in this study, this value was also adopted for the formation of the $GaO_x@Al_2O_3$ overlayer material. Based on the experimentally obtained metallic wt.-% loadings, the coverages (δ) obtained for the various $MO_x@Al_2O_3$ overlayer materials are above the target nominal monolayer coverages (see Table 4.2) with a deviation of ≤ 42% (see Table 5.1). This suggests the existence of the various MO_x in the form of a nanoscale-thin overlayer (rather than monolayer) coating highly dispersed on the surface of the γ-Al_2O_3 carrier as targeted.

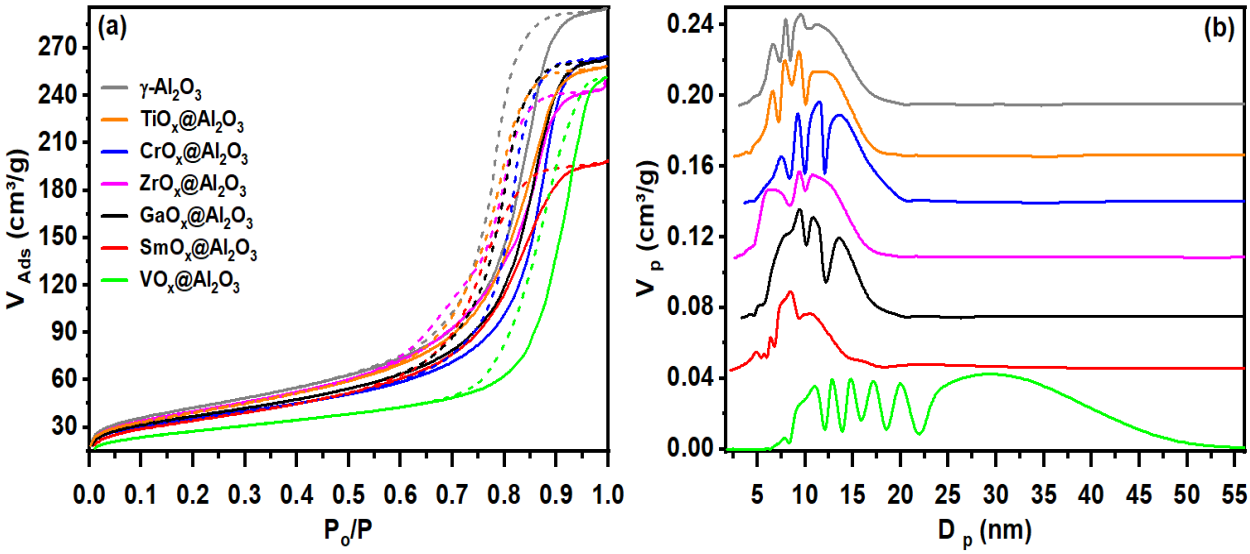

Figure 5.1: N_2-physisorption isotherms (a) and pore size distributions (b) of γ-Al_2O_3 and the various $MO_x@Al_2O_3$ supports (M = Cr, Ga, Sm, Ti, V and Zr). The legend applies to both (a) and (b). In (a) the dashed lines represent the desorption branch of the isotherm and the solid lines the adsorption.

As in several previous literature reports [257,259,274], the presence of the MO_x in the form of a thin overlayer in all of the $MO_x@Al_2O_3$ overlayer materials was further corroborated by the absence of additional X-ray diffraction reflexes, in addition to those corresponding to the bulk γ-Al_2O_3 (see Figure 5.2). For the $SmO_x@Al_2O_3$ overlayer material, which required a higher metal loading to form the overlayer, a decrease in the intensity of the γ-Al_2O_3 X-ray diffraction reflexes is observed likely due to the masking effect of the dense amorphous SmO_x overlayer [259]. Furthermore, all the MO_x overlayers only contribute a broad scattering reflection overlapping with the γ-Al_2O_3 reflexes in the range of 0.30 - 0.47 $Å^{-1}$, which is more apparent for the $ZrO_x@Al_2O_3$ overlayer material at 0.35 $Å^{-1}$. For the $ZrO_x@Al_2O_3$ overlayer material, this specific feature in the XRD pattern has also been reported in literature and was described as characteristic for amorphous zirconia synthesized at low temperatures [275,276]. This implies that all the synthesized MO_x overlayers are either highly dispersed and amorphous in character or exist in the form of very small crystallites (< 3 nm) that have no long-range ordering as expected for thin surface 2D overlayers [186].

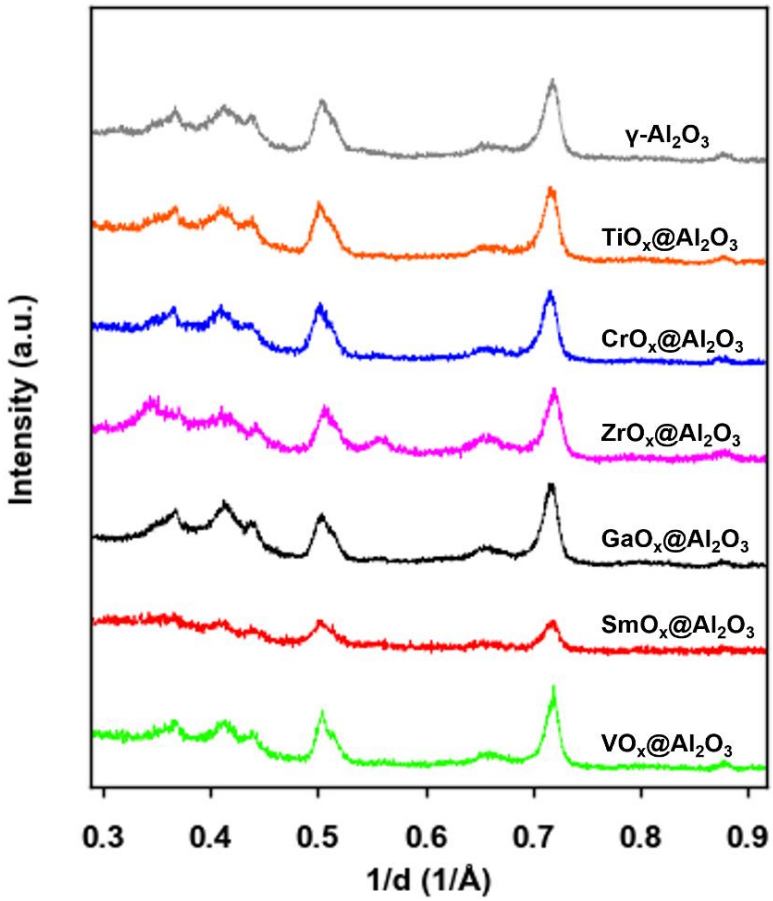

Figure 5.2: XRD patterns of γ-Al_2O_3 and the varios $MO_x@Al_2O_3$ supports (M = Ti, Cr, Zr, Ga, Sm and V).

As part of studying their chemical properties, the near-surface sensitivity of Raman spectroscopy was also leveraged to further investigate the structural features of the XRD-silent amorphous $MO_x@Al_2O_3$ overlayer materials. A comparison of the Raman spectra of the various overlayer materials and their bulk metal oxide counterparts is used to gain clarity on the chemical species present (see Figure 5.3). The γ-Al_2O_3 shows no Raman scattering features in this range of 110 - 1110 cm^{-1} due to the ionic character of the Al-O bond [277]. Therefore, all the bands observed on the Raman spectra of the $MO_x@Al_2O_3$ overlayer supports are solely associated with the vibrations of the surface MO_x overlayer's chemical species (see Figure 5.3(a)). Overall, it is evident that all the bulk metal oxide reference samples are strong Raman scatterers with material-specific fingerprint spectra (see Figure 5.3(b)). This is shown by the presence of bands below 770 cm^{-1} for oxides of V, Sm, Cr, Ti and Ga which are characteristic of the bulk crystalline metal oxide chemical species vibrational modes and are absent in the Raman spectra of the $MO_x@Al_2O_3$ overlayer materials. This suggests that the bulk oxides consist of certain highly polymerized chemical species which are representative for subsurface/bulk/crystalline phase of the materials which are not present in the $MO_x@Al_2O_3$ overlayer. For ZrO_2, the bulk oxide-specific bands appear across the entire scan range.

Contrary to the bulk crystalline ZrO_2, consisting of the monoclinic crystal structure, the Raman spectrum of the $ZrO_x@Al_2O_3$ overlayer shows no distinctive bands and this is a typical fingerprint for the amorphous phase as envisaged and corroborated by the XRD pattern (see Figure 5.2) [276,278]. The spectra of the other $MO_x@Al_2O_3$ overlayer materials show weak scattering bands with shoulders in the range of 700 - 1110 cm^{-1} (M = Cr, V and Sm) or 110 - 880 cm^{-1} (M = Ti and Ga) originating from the Raman vibrational modes of the poly- (M-O-M and O-M-O linkages) and mono- (M=O) nuclear species. For $CrO_x@Al_2O_3$, these bands at 265 (usually weakest), 781 (shoulder), 861, 928 (shoulder) and 1006 cm^{-1} are assigned to the bending and stretching modes υ_s (Cr-O-Cr), υ_{as} (Cr-O-Cr), υ_s (O-Cr-O), υ_s of the CrO_2 surface-terminating polymeric units and υ_s (Cr=O), attributed to poly- and mononuclear Cr^{VI} in surface oxide species [13]. The complete absence of other Raman bands present as fingerprint markers of crystalline Cr_2O_3 (535 cm^{-1}) and CrO_3 (304 and 339 cm^{-1}) in the spectrum of the bulk Cr_2O_3 supports that CrO_x indeed exists as a 2D overlayer [68]. $VO_x@Al_2O_3$ exhibits a single band, at 1030 cm^{-1}, which is typical for a VO_x overlayer and is ascribed to the vibrational modes caused by the bonds of the vanadyl (V=O) species of the surface vanadium oxide species [277,279–281].

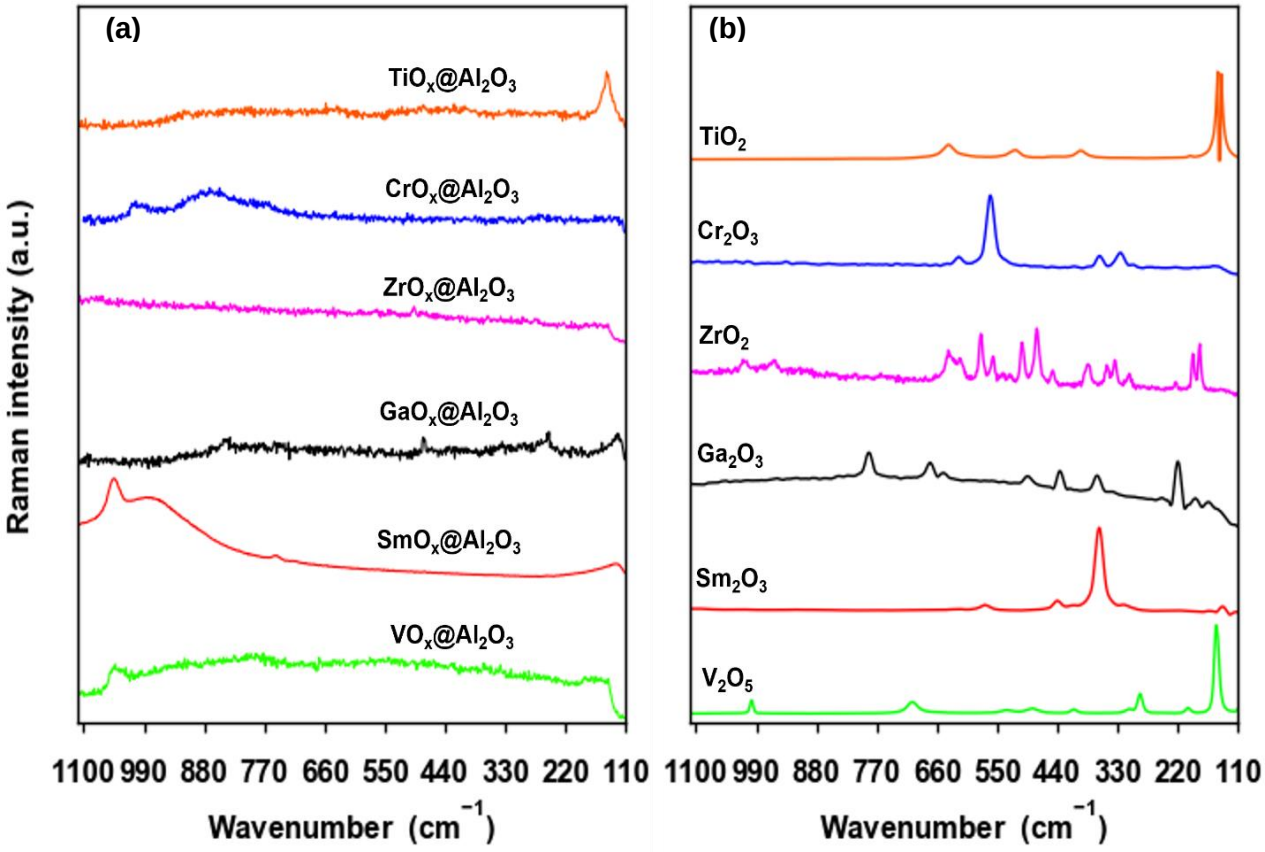

Figure 5.3: Visible excitation (532 nm) Raman spectra of (a) the various $MO_x@Al_2O_3$ overlayer supports (M = Ti, Cr, Zr, Ga, Sm and V) supports and (b) the corresponding bulk metal oxide reference samples. The spectra were acquired under ambient conditions (hydrated surface samples).

In the bulk V_2O_5 spectrum, this band appears at a lower wavenumber (998 cm^{-1}) due to unperturbed isolated vanadyl bonds (V=O) and occurs with other bands typical for crystalline V_2O_5 which are not observed for the overlayer sample [277]. For $GaO_x@Al_2O_3$, several weak and broad bands attributed to the bending and stretching vibrational modes of the Ga-O bonds associated with amorphous γ-Ga_2O_3 were observed, consistent with the XRD results [282]. The $TiO_x@Al_2O_3$ sample only exhibit a band at 166 cm^{-1} with very weak and broad features across the range of 220 - 1000 cm^{-1} as observed for the monolayer system in literature [68]. The band at 166 cm^{-1} is also often associated with the E_g mode in Ti-oxide thin films in literature (although at 143 cm^{-1}) and this further corroborates the presence of a thin oxide overlayer in the $TiO_x@Al_2O_3$ sample [283,284]. This band also occurs at 143 cm^{-1} in the Raman spectrum of the bulk TiO_2 reference suggesting that the interaction of the TiO_x overlayer with the γ-Al_2O_3 carrier causes the shift. For $SmO_x@Al_2O_3$, the bands observed are also different from the bulk oxide reference suggesting the presence of different chemical species on the surface of the carrier. Furthermore, the broadening

and shifting behaviour of the band at 127 cm^{-1}, which is associated with the A_g mode is typical for thin layers of Sm-oxides as also observed on Sm-oxide spin-coated films where it was recorded at 152 cm^{-1} [285]. Thus, all the overlayer materials synthesized show surface chemical features that can be related to or are also found on the surface of their corresponding bulk metals oxides as desired for the purpose of this study. Detailed assignments of the Raman bands of the bulk metal oxides confirming that most highly intense bands absent in the overlayers are due to layered structure lattice vibrations and chains of chemical species can be found in Table 10.1 of the Appendix section.

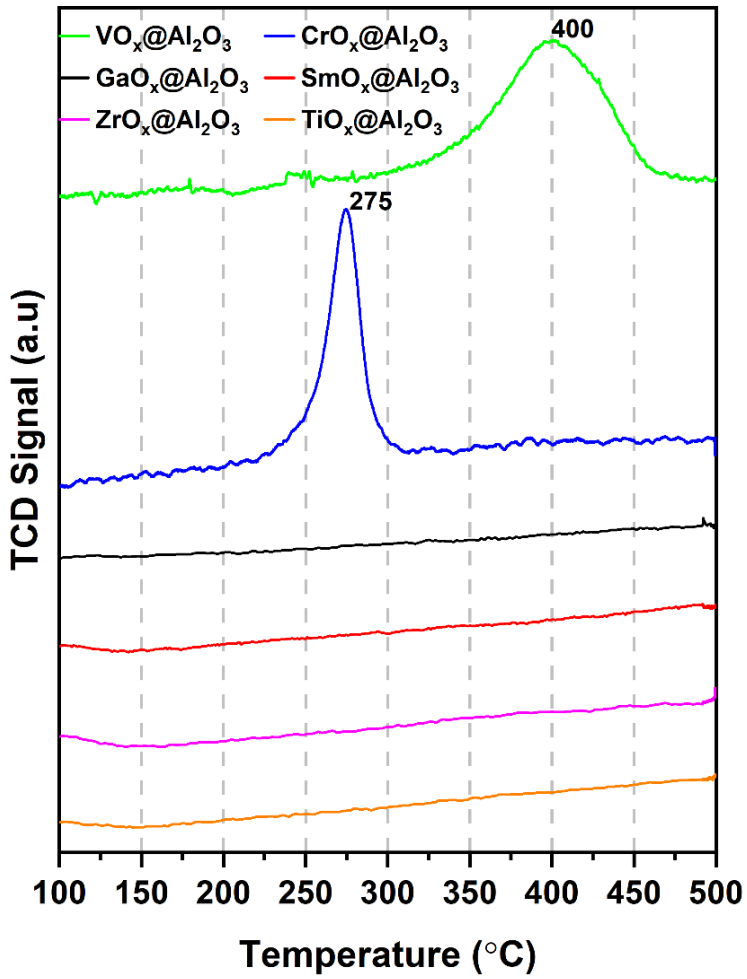

Figure 5.4: H_2-TPR profiles of the various $MO_x@Al_2O_3$ supports.

In addition to the preservation of the surface chemical species related to the surface of the corresponding bulk oxides and maintaining comparable textural properties in the various $MO_x@Al_2O_3$ supports, the overlayer formation route also yields supports with varying chemical properties (overall and relative Lewis surface acid site strength and reducibility). To understand

the differences in the chemical reducibility of the various $MO_x@Al_2O_3$ supports, H_2 temperature-programmed reduction (H_2-TPR) studies were conducted (see Figure 5.4). For $GaO_x@Al_2O_3$, $SmO_x@Al_2O_3$, $TiO_x@Al_2O_3$ and $ZrO_x@Al_2O_3$, no discernible reducibility features in the temperature range of 100 - 500 °C, are observed, suggesting a predominant retention of the oxidation state (stability). This is a typical behaviour for the latter three overlayers as reported by Prieto *et al*. [259] and their bulk counterparts as suggested by literature in this temperature range [286–288]. While Ga-oxides supported on Al_2O_3 are known to be reducible under H_2 in this temperature range, some studies also report very low degrees of reduction (partial reduction) when highly dispersed and in small crystallites [250,289]. On the other hand, $CrO_x@Al_2O_3$ and $VO_x@Al_2O_3$ display recognisable reduction signals with $CrO_x@Al_2O_3$ being the most easily reducible at 275 °C followed by $VO_x@Al_2O_3$ with a maximum H_2 consumption at 400 °C ascribed to reduction of monomeric or polymeric CrO_x and VO_x surface species, respectively [13,259]. Previous studies revealed that bulk Cr_2O_3 exhibits two reduction peaks at 244 and 518 °C while V_2O_5 show reduction features above 500 °C [290,291]. The observed shifts in reduction peaks of the overlayers compared to the bulk metal oxides are also common in literature [13,259,290,292].

To further understand their chemical properties, the relative Lewis surface acid site strength of the coordinatively unsaturated M^{x+} sites on the $MO_x@Al_2O_3$ overlayer materials was probed by employing DR-UV/Vis of surface-adsorbed alizarin (1,2-dihydroxyanthraquinone) as reported by Jeong *et al.* [256] and Prieto *et al*. [258,259,272,274] (see Figure 5.5). This surface-sensitive method entails the extrapolation of the photon energy (E_{IMCT}) required to trigger the intramolecular charge transfer transition of electrons from the catechol moiety to the aromatic ring system in the surface-adsorbed alizarin molecules. The photon energy (E_{IMCT}) is typically the lowest energy transition in the DR-UV/Vis spectra of metal oxides and its band in the spectra is easy to interpret as it does not usually overlap with the bands resulting from the possible d-d transitions in metal oxides. Thus, E_{IMCT} an excellent descriptor of the relative electron-withdrawing/donating strength of the coordinatively unsaturated M^{x+} sites to which alizarin is bound on the surface of the $MO_x@Al_2O_3$ overlayer materials.

The DR-UV/Vis spectra of the alizarine surface-saturated uncalcined $CrO_x@Al_2O_3$ and calcined $MO_x@Al_2O_3$ (M = Ga, Sm, Ti and Zr) clearly show that these materials exhibit the characteristic band corresponding to alizarine E_{IMCT} peaking at different values (see Figure 5.5 (a)). Difference spectra were derived to expose the alizarine E_{IMCT} band for the calcined $VO_x@Al_2O_3$ and $CrO_x@Al_2O_3$ since it overlaps/interferes with d-d transition bands of the MO_x (see Figure 5.5 (b)

and (c)). All these spectra show a shift of the alizarine E_{IMCT} band because of its interaction with the different MO_x overlayers.

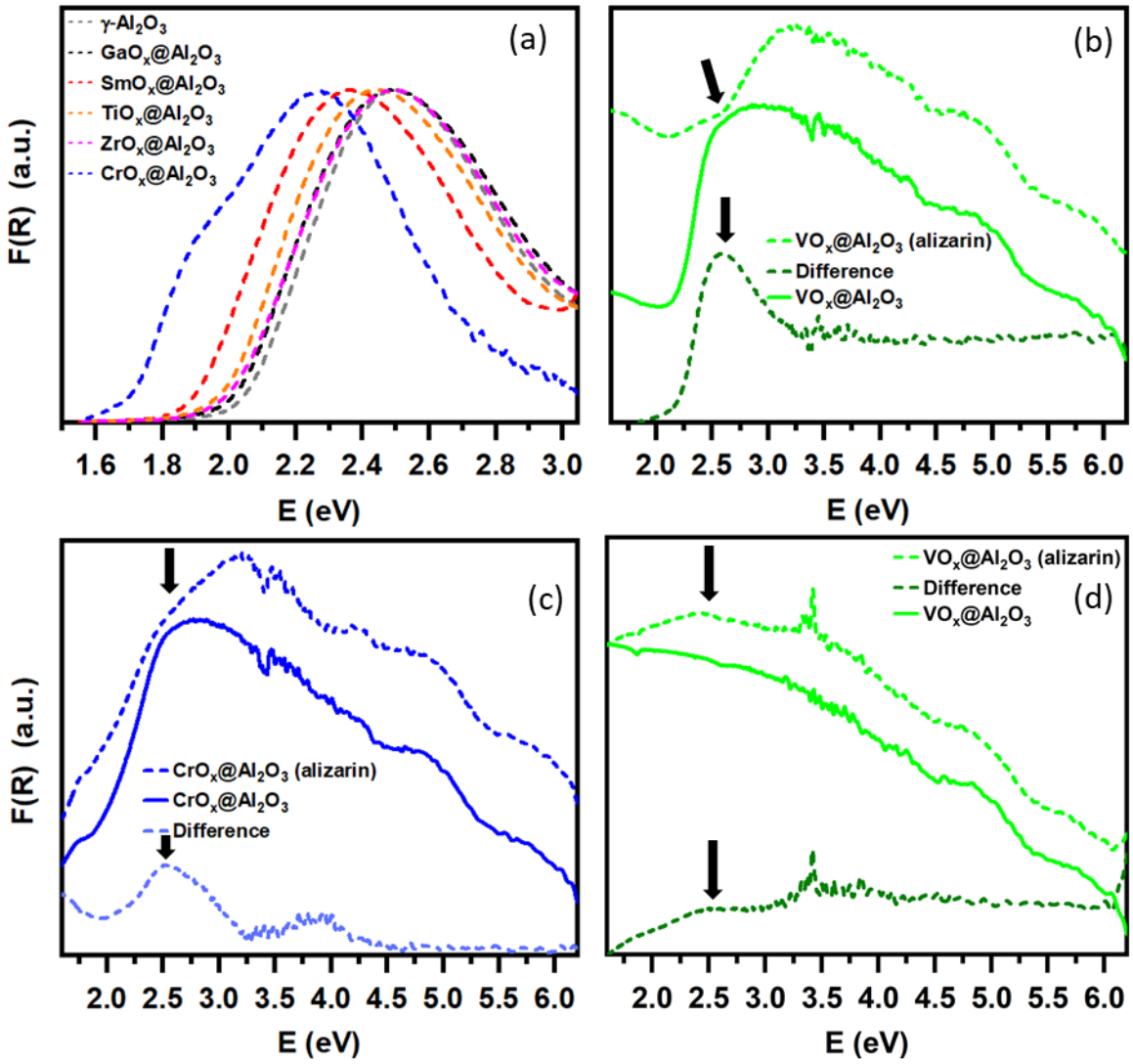

Figure 5.5: (a) DR-UV/Vis spectra of uncalcined $CrO_x@Al_2O_3$ and calcined $MO_x@Al_2O_3$ (M = Ga, Sm, Ti and Zr) supports after saturation adsorption of alizarine. Only the energy range with apparent alizarine IMCT bands is displayed. (b) and (c) DR-UV/Vis spectra before and after saturation adsorption of alizarine as well as the difference spectra showing the alizarine IMCT band for the calcined $VO_x@Al_2O_3$ and $CrO_x@Al_2O_3$, respectively. (d) DR-UV/Vis spectra before and after saturation adsorption of alizarine as well as the difference spectra showing the alizarine IMCT band for the reduced $VO_x@Al_2O_3$. The black arrow markers point to the band characteristic to surface-adsorbed alizarin probe molecules.

A lower surface alizarine energy (E_{IMCT}) band implies that the oxide possesses relatively weak Lewis acid sites. Overall, alizarine E_{IMCT} band values derived from the spectra span from 2.27 and 2.38 eV, for the weakly acidic uncalcined $CrO_x@Al_2O_3$ and calcined $SmO_x@Al_2O_3$, to 2.6 eV for the strongly acidic calcined $VO_x@Al_2O_3$ (See Table 5.1). Thus, the Lewis acid sites on the

surfaces of the uncalcined $CrO_x@Al_2O_3$ and calcined $SmO_x@Al_2O_3$ are weakly electron withdrawing and bind the lattice oxygen weakly compared to $VO_x@Al_2O_3$ which should bind it more strongly. For $ZrO_x@Al_2O_3$ and $CrO_x@Al_2O_3$, alizarin analysis was first made without calcination, due to the unavailability of a glovebox and the calcination rig, and later with calcination under a stream of synthetic air for decarbonation. Decarbonation is only necessary for certain materials depending on their surface sensitivity as they tend to adsorb organics when exposed to ambient conditions [259]. The results before and after calcination were the same for $ZrO_x@Al_2O_3$ but differed for $CrO_x@Al_2O_3$ confirming the need for calcination for this material. Note that both values were adopted for clarity (see Table 5.1). Subsequently, this analysis was performed on calcined materials for all the remaining samples.

Relying on the data for the calcined samples, the following order of relative surface Lewis acid strength was obtained: $VO_x@Al_2O_3$ > $CrO_x@Al_2O_3$ > γ-Al_2O_3 > $ZrO_x@Al_2O_3$ > $GaO_x@Al_2O_3$ > $TiO_x@Al_2O_3$ > $SmO_x@Al_2O_3$. The relative Lewis surface acid site strength on the bare γ-Al_2O_3 is also different to all the $MO_x@Al_2O_3$ overlayer materials. Since the $VO_x@Al_2O_3$ and $CrO_x@Al_2O_3$ overlayers exhibit some reducibility in the temperature range of 100 - 500 °C (see Figure 5.4), an attempt to measure the relative surface Lewis acidity of the $VO_x@Al_2O_3$ sample in its reduced state was also made (see Figure 5.5. (d)). The alizarin band was not well-resolved in the difference spectrum obtained suggesting that a very small amount of the alizarin molecules could be adsorbed on the surface of the sample in its reduced state. Although it is difficult to conclude with absolute certainty, it seems there is no change in the value of E_{IMCT} observed for this small band compared to the unreduced sample. Reduction does not seem to influence the overall surface Lewis acidity of the sample but only reduced the population of the Lewis acid sites.

Since the DR-UV/Vis of surface-adsorbed alizarin only offers information about the average surface Lewis acid site strength, NH_3-TPD analysis was also employed to further uncover the overall surface acidity (*i.e.* the surface acidity as a result of both the Brønsted and Lewis acid sites and their distinction in terms of relative strength) (see Figure 5.6). Overall, the NH_3-TPD profiles of all the samples are characterised by three well-resolved peaks as well as an additional overlapping shoulder-like peak observed in the temperature range of 180 - 300 °C, for $VO_x@Al_2O_3$, $CrO_x@Al_2O_3$ and $GaO_x@Al_2O_3$, and 170 - 2 40 °C for $SmO_x@Al_2O_3$, $TiO_x@Al_2O_3$ and $ZrO_x@Al_2O_3$. These indicate the presence of three types of adsorption sites for NH_3 on all the

overlayer support materials associated with three types of surface acid site populations which differ in strength (*i.e.* weak, intermediate and strong acid sites).

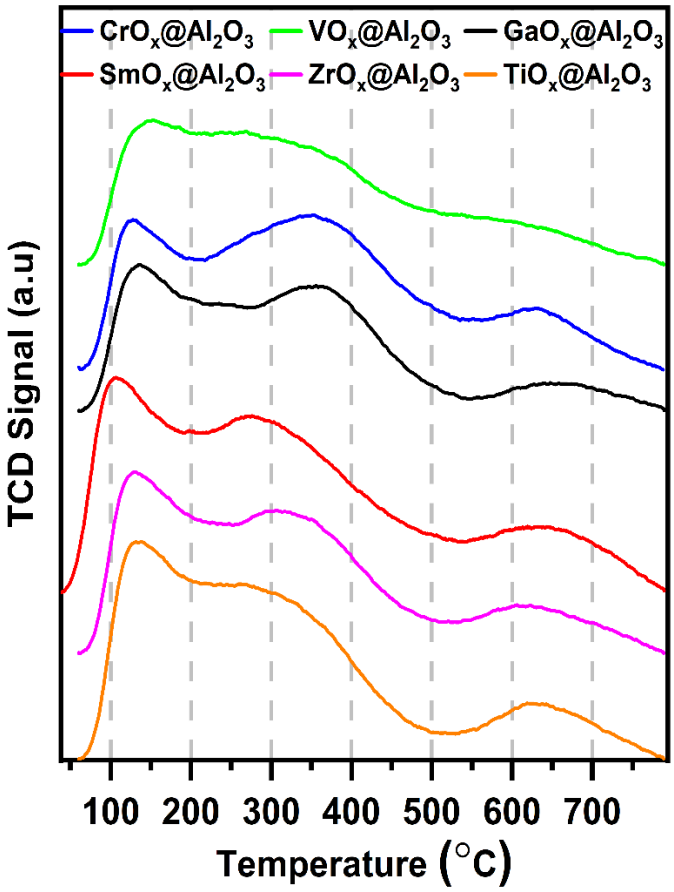

Figure 5.6: NH_3-TPD profiles of the various $MO_x@Al_2O_3$ supports.

Overall, the three main desorption peaks are observed at the lowest temperature for $SmO_x@Al_2O_3$ suggesting that this material exhibits the weakest overall surface acid site strength, correlating well with the DR-UV/Vis of surface-adsorbed alizarin results. For $GaO_x@Al_2O_3$, $TiO_x@Al_2O_3$ and $ZrO_x@Al_2O_3$, the desorption peak at the lowest temperature corresponding to weak acid sites is recorded at a comparable temperature value, suggesting a similarity while this peak appears at a lower temperature for $CrO_x@Al_2O_3$ and a higher temperature for $VO_x@Al_2O_3$. However, the middle and high temperature desorption peaks corresponding to the intermediate and strong acid sites, respectively, occur at different temperatures for all the overlayer materials, suggesting that all the overlayer materials exhibit differences in their overall surface acid site strength. Despite these differences, a close inspection of the data suggests a stronger acidity for $CrO_x@Al_2O_3$, $VO_x@Al_2O_3$ and $GaO_x@Al_2O_3$, especially with regards to the intermediate and strong acid sites,

which show desorption at higher temperatures than $SmO_x@Al_2O_3$, $TiO_x@Al_2O_3$ and $ZrO_x@Al_2O_3$. Thus, the acid site populations in $SmO_x@Al_2O_3$, $TiO_x@Al_2O_3$ and $ZrO_x@Al_2O_3$ are weaker compared to $CrO_x@Al_2O_3$, $VO_x@Al_2O_3$ and $GaO_x@Al_2O_3$. The order of acid strength based on the intermediate acid sites is proposed as follows: $VO_x@Al_2O_3$ > $CrO_x@Al_2O_3$ > $GaO_x@Al_2O_3$ > $ZrO_x@Al_2O_3$ > $TiO_x@Al_2O_3$ > $SmO_x@Al_2O_3$, again correlating well with the results obtained *via* DR-UV/Vis except for the order of $GaO_x@Al_2O_3$ and $ZrO_x@Al_2O_3$. However, this trend might be affected by the potential of the redox materials, $VO_x@Al_2O_3$ and $CrO_x@Al_2O_3$, to decompose NH_3. DR-UV/Vis studies by Prieto *et al*. [259,274] suggests the following ranking based on E_{IMCT}: $VO_x@Al_2O_3$ > $TiO_x@Al_2O_3$ > $ZrO_x@Al_2O_3$ > $SmO_x@Al_2O_3$, which also correlates well with our proposed trend. Based on the study of Jeong *et al*. [256], the corresponding bulk oxides exhibit the following ranking of relative theoretical Lewis acid site strength: V_2O_5 > TiO_2 > ZrO_2 > Ga_2O_3 > Cr_2O_3 > Sm_2O_3, which is different despite the correlation of the V-containing samples. These differences are attributed to differences in the chemical species present on the $MO_x@Al_2O_3$ overlayer materials compared to the bulk oxides as also demonstrated by the Raman spectra (see Figure 8.3 (a)) and also probable when oxides are pre-treated in heat [256,293]. Nonetheless, since the NH_3-TPD results were obtained on samples that were pre-treated under reduction conditions, it is deemed that the order obtained *via* NH_3-TPD is more representative of the chemical state of the overlayer materials under reaction conditions. Based on the cumulative peak areas obtained from fitting the NH_3-TPD results (see Figure 10.1 in the Appendix section), the following rank is obtained in terms of the relative amount of NH_3 desorbed from the materials: $SmO_x@Al_2O_3$ > $CrO_x@Al_2O_3$ > $TiO_x@Al_2O_3$ > $ZrO_x@Al_2O_3$ > $VO_x@Al_2O_3$ > $GaO_x@Al_2O_3$.

6 Synthesis and characterization of unsupported oxide precursor nanoparticles

Some results reported in this section are part of the publication: S. Raseale, W. Marquart, K. Jeske, G. Prieto, M. Claeys, N. Fischer, Supported Fe_xNi_y catalysts for the co-activation of CO_2 and small alkanes, Faraday Discuss. 229 (2020) 208-231. https://doi.org/10.1039/C9FD00130A.

The solvothermal synthesis employed in this work, has been demonstrated in literature as a facile way to produce crystalline and monodisperse monometallic (Co and Fe) and bimetallic (ferrites, $(M_xFe_{1-x})Fe_2O_4$, with M = Ni, Mn or Co) oxide nanoparticles of a defined shape and size in the absence of long-chain surfactant or precursor anion contaminants [236,240]. Typically, the synthesis involves the decomposition of a metal acetylacetonate or acetate precursor dissolved in benzyl alcohol or benzylamine *via* heat treatment in an open or closed system at temperatures in the range of 100 - 200 °C. These solvents have a low reducing power, and thus, only metal oxides form *via* this synthesis route. The main drawback of this route is that nanoparticles are often synthesized at small-scale (using up to 1 g of the precursor) and require long reaction times of up to 48 h due to the use of small autoclaves [240,261]. Studies from our lab have demonstrated that this synthesis route can be scaled-up, using up to 3.2 g of the precursor, when a metal acetate precursor is used and the decomposition is carried out in benzyl alcohol in the presence of ammonium hydroxide at shorter reaction times for the formation of Co_3O_4 nanoparticles [239,241]. This has not been demonstrated yet for the formation of bimetallic nanoparticles of $(M_xFe_{1-x})Fe_2O_4$. Since literature-reported synthesis conditions vary considerably between bimetallic and monometallic systems, the Co_3O_4 nanoparticles conditions cannot be assumed to be applicable for bimetallic systems without experimental confirmation. Especially because in addition to particle size and shape, controlling the metallic composition becomes necessary for bimetallic systems.

A similar study to that reported by Wolf *et al.* [239] was undertaken to investigate the efficacy of the benzyl alcohol solvothermal route in yielding monodisperse inverse spinel structured Ni-ferrite ($(Ni_xFe_{1-x})Fe_2O_4$) nanoparticles with control over the metallic composition (*i.e.* the overall Fe : Ni atomic ratio). For this, nine experiments were conducted through which the synthesis parameters - synthesis temperature, total precursor mass and the volume of the precipitating agent - were varied to understand their role in yielding monodisperse $(Ni_xFe_{1-x})Fe_2O_4$ nanoparticles with a target overall Fe : Ni atomic ratio of 3 (*i.e.* $(Ni_{0.75}Fe_{0.25})Fe_2O_4$). Since most literature report the

synthesis of Fe-containing oxide nanoparticles to be performed in an autoclave under pressure, this was also adopted in this work, which is a deviation from the procedure reported by Wolf *et al.* [236,240]. These syntheses were performed in a Berghoff autoclave with a 1.5 L volume equipped with a pressure relief valve which was set to a 25 bar gauge pressure.

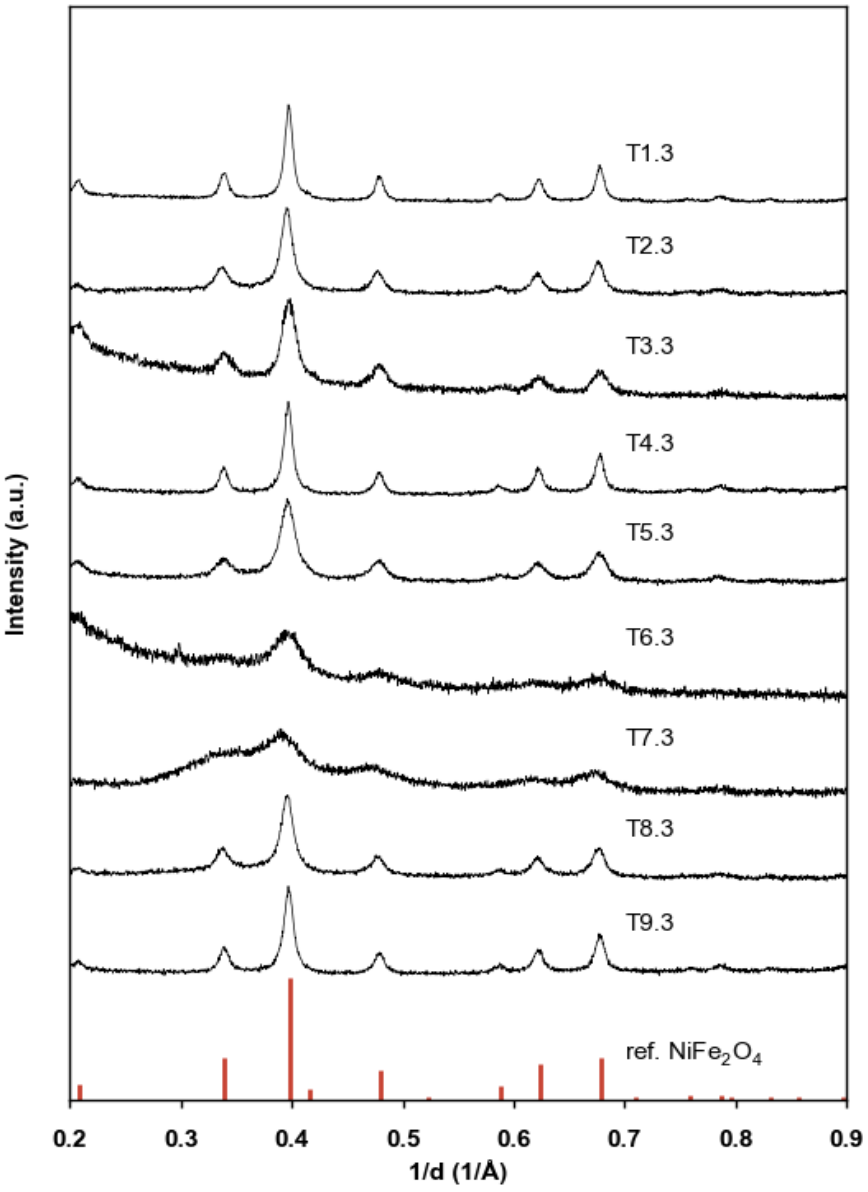

Figure 6.1: XRD patterns of the obtained $(Ni_{0.75}Fe_{0.25})Fe_2O_4$ nanoparticles synthesized via the benzyl alcohol solvothermal thermal route at various synthesis temperatures, total precursor masses and ammonium hydroxide precipitating agent volumes added to a 1.5 L Berghoff autoclave. Exact synthesis conditions are provided in Table 6.1. The reference pattern included is for the $NiFe_2O_4$ inverse spinel phase ($NiFe_2O_4$: PDF-4 04-018-7641) [267,268].

The crystal structures of the obtained nanoparticles were studied by means of X-ray diffraction (see Figure 6.1). As expected, in all the synthesized materials, a single crystalline phase material, unambiguously indexed as a cubic structure closest to the standard Ni-ferrite ($NiFe_2O_4$) inverse spinel, was identified. The observed clear diffractions ($1/d = 0.2 - 0.7$ $Å^{-1}$) correspond to the (111), (220), (311), (400), (422), (511) and (440) planes. The fact that no additional phases were observed demonstrates the efficacy of the solvothermal synthesis method in yielding the Ni-ferrite ($(Ni_xFe_{1-x})Fe_2O_4$) inverse spinel even when the ferrous precursor (iron(II) acetate) is used instead of the typical ferric precursor (iron(III) acetylacetonate) as the source of Fe. Typically, the ferric precursor is used, which gets partially reduced by benzyl alcohol during the synthesis to avail the Fe^{II} species required to form the $(M_xFe_{1-x})Fe_2O_4$ inverse spinel [236,240,294]. This observation implies that just as it is possible to reduce Fe^{III} to Fe^{II} during this kind of synthesis, it is equally possible to partially oxidise Fe^{II} to Fe^{III} when necessary for the formation a stable ($(Ni_xFe_{1-x})Fe_2O_4$) inverse spinel phase under these modified solvothermal synthesis conditions. Oxidation in the monometallic cobalt system has been previously associated with both the metal precursor and the water present in the aqueous ammonium hydroxide solution as well as the efficiency of mixing [239]. However, the degree of crystallinity of the ($(Ni_xFe_{1-x})Fe_2O_4$) inverse spinel phases obtained varies with the different synthesis conditions applied, suggesting differences in long-range ordering within the different samples, probably linked to differences in crystallite size.

Rietveld refinement of all the patterns reveals varying mean crystallite sizes with changing synthesis parameters (see Table 6.1). The mean crystallite sizes obtained suggest that at the same synthesis temperature, a high volume of ammonium hydroxide and total acetate precursor mass yields larger crystallites. However, this is only valid at 170 °C to 200 °C. At the lowest temperature of 150 °C, the crystallite size decreases with an increase in the volume of ammonium hydroxide and total acetate precursor mass added. This behaviour is attributed to the improved mixing kinetics of the emulsion at high temperature, which allow for particle formation even when the acetate precursor mass is larger. This observation is also supported by the analysis of the TEM-derived particle size distributions and the average number- and volume-based particle sizes (see Figure 6.2 and Table 6.1, respectively). The sample T7.3 formed at 150 °C (lowest temperature) was found to exhibit a bimodal behaviour predominantly consisting of large structures of a thin-layered material, with a layer thickness of about 3 nm, which is mixed with spherical nanoparticles of about 8 nm average particle size (see Figure 6.2. T7.3). Since these large thin-layered structures dominated the sample, it is conceivable that they account for the observed crystallite size of 3.3 nm from the Rietveld refinement, which stems from the layer

thickness. The formation of these large structures at this lowest temperature is attributed to slow crystallisation kinetics.

Table 6.1: Conditions applied in the solvothermal synthesis of the different $(Ni_xFe_{1-x})Fe_2O_4$ nanoparticles targeting overall Fe : Ni atomic ratio of 3 as well as the ICP-OES-derived compositions, Rietveld refinement lattice parameters and crystallite sizes, and TEM-derived particle sizes.

Sample	Temp (°C)	Total mass of acetates (g)	25 wt. -% NH_4OH volume (mL)	ICP-OES Fe : Ni atomic ratio	Lattice parameter (Å)	Crystallite size and $[\bar{d}_n/\bar{d}_v \pm sd_n/sd_v]$ (nm)
T1.3	200	1.93	85	3.8	8.353	11.9 [9.8/11.3 ± 2.0/2.8]
T2.3	200	0.77	34	4.7	8.355	8.5 [7.5/9.3 ± 2.1/3.4]
T3.3	200	0.31	13	3.5	8.351	7.1 [6.0/6.7 ± 1.2/1.2]
T4.3	170	1.93	85	6.7	8.360	11.7 [8.3/11.4 ± 2.6/2.8]
T5.3	170	0.77	34	3.4	8.350	6.0 [8.8/12.7 ± 3.4/3.7]
T6.3	170	0.31	13	3.5	8.323	2.9 [3.5/4.1 ± 0.8/0.9]
T7.3	150	1.93	85	2.8	8.336	3.3 [6.2/9.3 ± 3.4/2.1]
T8.3	150	0.77	34	6.4	8.379	7.5 [5.3/8.0 ± 2.2/2.3]
T9.3	150	0.31	13	10.9	8.355	10.2 [10.4/16.1± 4.8/4.0]

In square baskets are the average number- ($\bar{d}_n$) and volume- ($\bar{d}_v$) based particle sizes obtained via TEM analysis and their respective standard deviations (sd_n and sd_v).

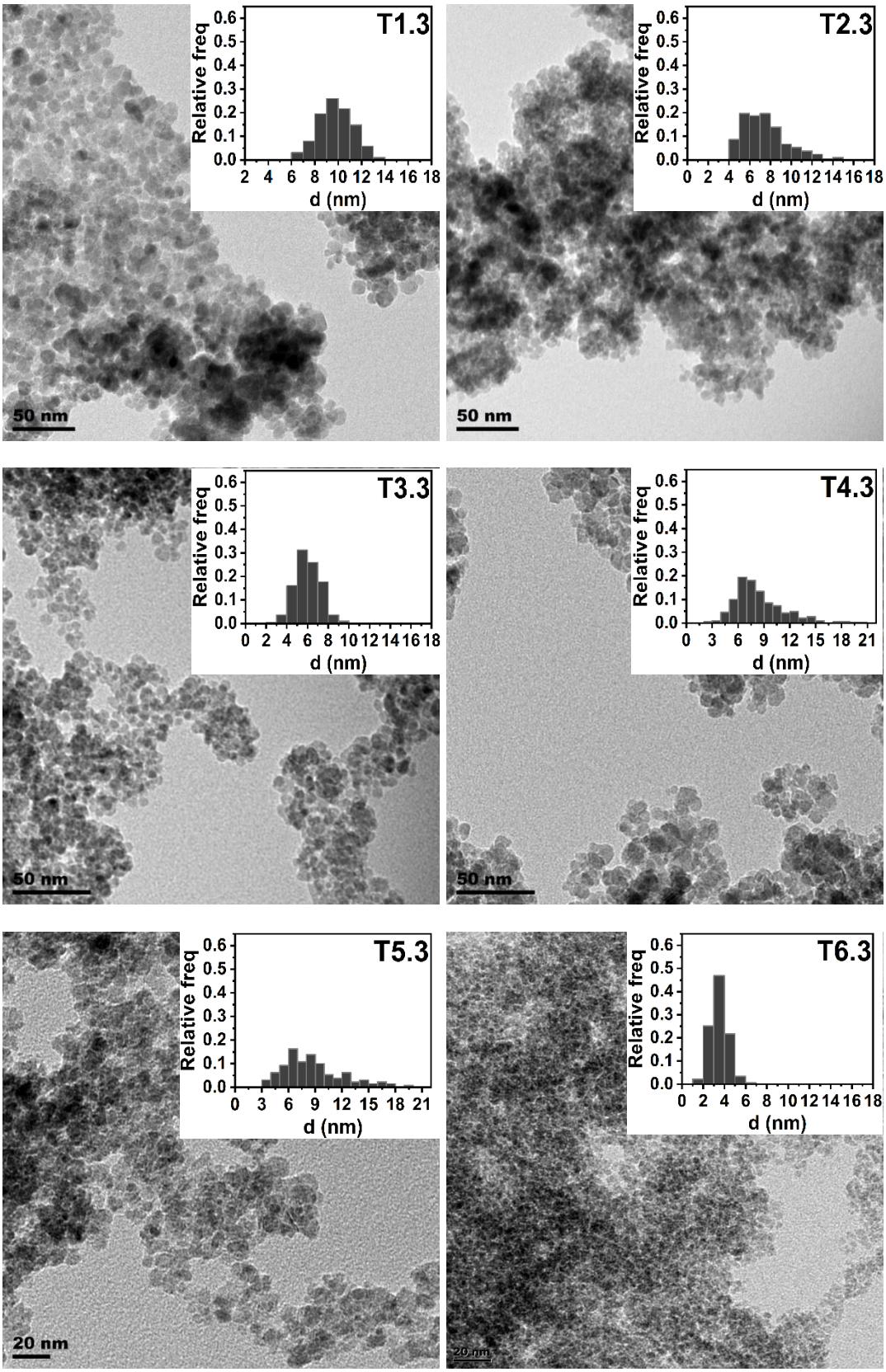
T1.3
Relative freq
d (nm)
50 nm
T2.3
Relative freq
d (nm)
50 nm
T3.3
Relative freq
d (nm)
50 nm
T4.3
Relative freq
d (nm)
50 nm
T5.3
Relative freq
d (nm)
20 nm
T6.3
Relative freq
d (nm)
20 nm

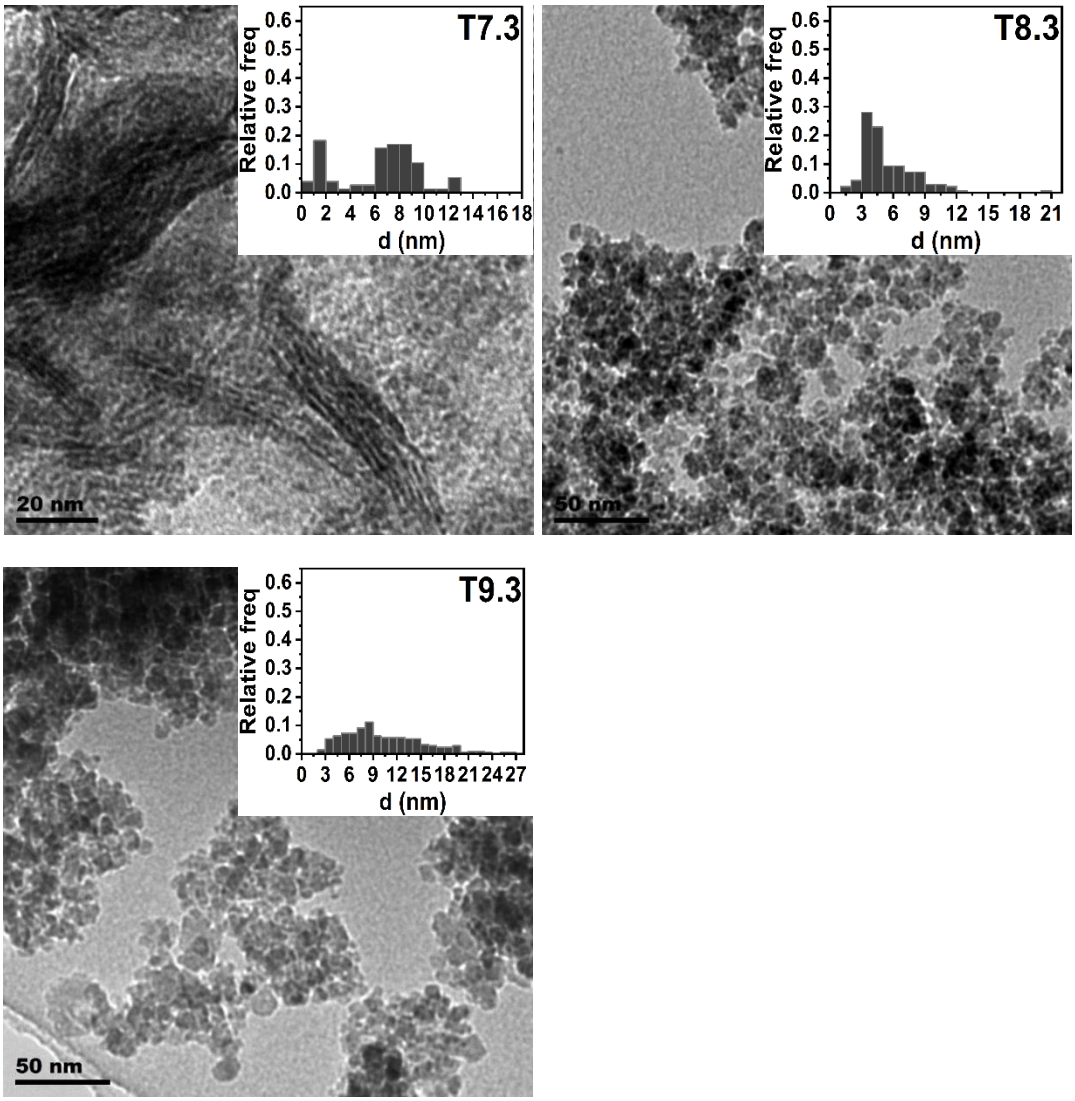

Figure 6.2:TEM images and number-based size distributions of the oxidic (Ni_xFe_{1-x})Fe_2O_4 nanoparticles obtained via the solvothermal treatment of respective acetates in the presence of benzyl alcohol and ammonium hydroxide at different synthesis conditions targeting an overall Fe : Ni atomic ratio of 3.

To a lesser extent, smaller fragments of this layered material were also found to be present in the form of flat platelet-like structures within the other low-temperature samples (see T8.3 and T9.3 in Figure 6.2). This accounts for the observed wide particle size distributions for these samples. However, no signs of the presence of any organic material (such as derivatives of benzyl alcohol or acetates) were observed in the TEM images, implying that the washing procedure was effective.

These observations clearly show that the synthesis temperature, metal precursor mass and volume of ammonium hydroxide (and water) in the system play a crucial role on the particle size,

monodispersity and morphology of the nanoparticles obtained. The combination of a high volume of ammonium hydroxide and metal precursor mass results in larger nanoparticles/crystallites at a given temperature ≥ 170 °C. Additionally, the particle size distribution becomes narrower suggesting that monodisperse nanoparticles of a defined shape (*i.e.* spherical) are predominantly formed at these high temperatures (see Table 6.1and Figure 6.2). The particle size distribution peak and average number- ($\overline{d}_n$) and volume- ($\overline{d}_v$) based particle sizes also shift towards a larger magnitude. The average particle sizes obtained from TEM also correlate well with the mean crystallite sizes calculated using Rietveld refinement, except where the layered material dominates or a wider particle size distribution is obtained. The narrowing of the particle size distribution with increasing temperature is attributed to differences in growth rates. At higher temperatures, smaller nanoparticles are presumed to grow and/or aggregate faster than larger ones. This implies that high temperatures are necessary for the synthesis of monodisperse nanoparticles.

The overall Fe : Ni atomic ratio (chemical composition) also varies significantly with varying synthesis parameters and is mostly above the target of 3 suggesting a loss of Ni during the synthesis (see Table 6.1). The samples T1.3, T3.3, T5.3, T6.3 and T7.3 lie very close to the target ratio. Although there is no observable trend in relation to the synthesis parameters, this loss of Ni was more pronounced at low synthesis temperatures. This is possibly due to the slow mixing kinetics of the synthesis emulsion at low temperatures and the complexation of the divalent Ni ions with excess ammonia, forming stable hexamine complexes (indicated by a blueish supernatant) during the synthesis which hindered its inclusion into the ($(Ni_xFe_{1-x})Fe_2O_4$) inverse spinel [295]. Additionally, at 150 °C and 170 °C, where the overall Fe : Ni atomic ratio varied significantly, the lattice parameter obtained from XRD does not correlate with the ratio acquired through ICP-OES analysis, especially for samples T6.3, T8.3 and T9.3 which deviated too far from the expected trend of increasing lattice parameter with the ratio (see Figure 6.3, left). Although slight deviations are possible, more Fe content incorporated into the ($(Ni_xFe_{1-x})Fe_2O_4$) inverse spinel structure by replacing Ni sites should increase the lattice parameter as demonstrated by the data of the refence patterns obtained from the ICDD database (see Figure 6.3, right). This is because Fe^{II} has a slightly larger radius (77 pm) than Ni^{II} (70 pm) [296]. For samples T6.3 and T9.3, the lattice parameter obtained is small for the amount of Fe detected to be present *via* the ICP-OES analysis (see Figure 6.3, left), potentially suggesting that part of the Fe in these samples may not have been incorporated into the inverse spinel structure and exists in the form of an XRD silent amorphous phase. Conversely, for sample T8.3, the lattice parameter

is much bigger suggesting that some Ni is not incorporated into the inverse spinel structure. However, for all the other samples, the estimated lattice parameter values are acceptable as they lie closer to the expected linear increase and vary in the following order: T8.3 > T2.3 > T1.3 > T3.3 > T5.3 > T7.3, consistent with the ICP-OES results and suggesting that most of the Fe and Ni in the samples are within the $((Ni_xFe_{1-x})Fe_2O_4)$ inverse spinel structure. Thus, all the samples synthesized at a high temperature of 200 °C are consistent with the formation of the $((Ni_xFe_{1-x})Fe_2O_4)$ inverse spinel with most Fe and Ni incorporated in the crystal structure.

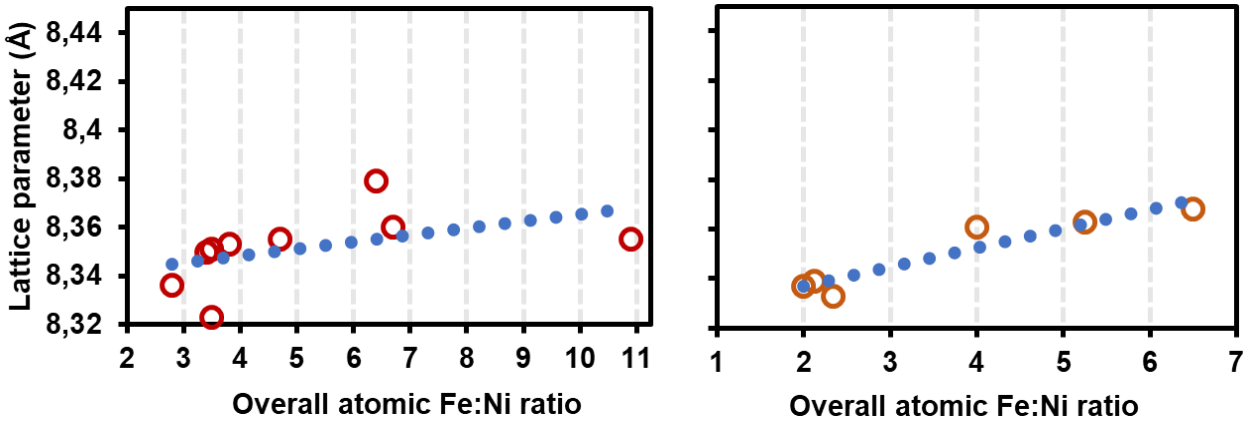

Figure 6.3: XRD Rietveld refinement-derived lattice parameter as a function of the ICP-OES-derived overall Fe : Ni atomic ratios for the $((Ni_xFe_{1-x})Fe_2O_4)$ inverse spinel materials synthesized under different conditions targeting overall Fe : Ni atomic ratio of 3 in a 1.5 L Berghoff autoclave (Left) as well as the theoretical relationship (Right) obtained by using XRD reference patterns of samples with different overall Fe : Ni atomic ratios from the ICDD database. The closed circles represent the linear fit (trendline) to the data while open circles represent real data. The XRD reference patterns used are for $NiFe_2O_4$ (PDF-00-054-0964), $(Ni_{0.96}Fe_{0.04})Fe_2O_4$ (PDF-01-076-6119), $(Ni_{0.9}Fe_{0.1})Fe_2O_4$ (PDF-01-076-6118), $Ni_{0.6}Fe_{2.4}O_4$ (PDF-01-087-2338), $Fe_{2.52}Ni_{0.48}O_4$ (PDF- 04-021-1089) and $Ni_{0.4}Fe_{2.6}O_4$ (PDF-01-087-2335) [267,268].

Based on these observations and the further need to synthesize crystalline and monodisperse nanoparticles of a defined spherical shape and about 10 nm diameter while attaining the targeted overall Fe : Ni atomic ratio, the synthesis conditions used for T1.3 were adopted for synthesizing $((Ni_xFe_{1-x})Fe_2O_4)$ inverse spinel catalyst precursors with varying overall Fe : Ni atomic ratios (*i.e.* 5, 3 and 1). Since a high synthesis temperature proved important in attaining the targeted overall Fe : Ni atomic ratio of the $((Ni_xFe_{1-x})Fe_2O_4)$ inverse spinel material, it was slightly increased to 210 °C.

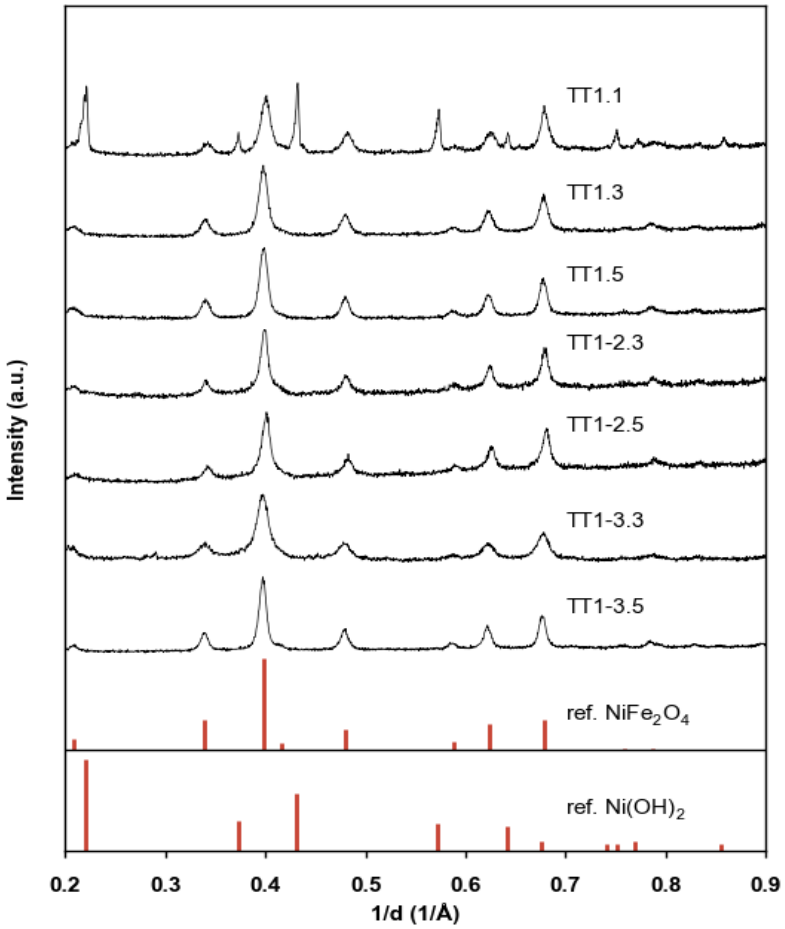

Figure 6.4: XRD patterns of the $(Ni_xFe_{1-x})Fe_2O_4$ nanoparticles synthesized via the benzyl alcohol solvothermal route using the modified T1.3 conditions at 210 °C inside the Berghoff or small in-house autoclave. The reference patterns included are for the $NiFe_2O_4$ inverse spinel phase ($NiFe_2O_4$: PDF-4 04-018-7641) and the $Ni(OH)_2$ phase ($Ni(OH)_2$: PDF-4 00-059-0463) [267,268].

X-ray diffraction analysis still confirm the presence of an inverse spinel phase in all the samples with varying overall Fe : Ni atomic ratios (see Figure 6.4). For the sample TT1.1 with the highest Ni content (*i.e.* overall atomic Fe : Ni of 1), additional diffractions which could be indexed to a nickel hydroxide ($Ni(OH)_2$) phase are observed. The formation of an additional hydroxide phase from the excess Ni amount is expected as Ni^{II} occupies octahedral sites in the inverse spinel structure within which stoichiometry limits the maximum attainable overall Fe : Ni atomic ratio to 2. However, the lattice parameter obtained *via* Rietveld refinement for sample TT1.1 (see Table 6.2) suggests that the inverse spinel phase in this sample contains more Fe than expected as it is even higher than that of sample TT1.3, which contains more Fe (overall atomic Fe : Ni of 3). Based on the phase composition obtained *via* Rietveld refinement, Ni seems to be equally distributed between both phases as almost half is found in $Ni(OH)_2$ and the remainder in the

inverse spinel phase to attain a maximum overall Fe : Ni atomic ratio of 2, corresponding to the standard inverse spinel stoichiometry ($NiFe_2O_4$). This suggests that the lattice parameter change when there is more than the stoichiometric Ni content is not reliable also probably because part of the Ni exists in the form of an XRD silent amorphous phase.

Overall, the Fe : Ni atomic ratios obtained *via* ICP-OES for the samples TT1.1, TT1.3 and TT1.5 synthesized under the same conditions and autoclave are close to the targeted overall Fe : Ni atomic ratios (*i.e.*1, 3 and 5, respectively). For the samples TT1.3 and TT1.5, the lattice parameter of the inverse spinel phase increases with an increase of the Fe content in the material as expected due to a slight unit cell volume expansion by the larger Fe^{II}.

Table 6.2: ICP-OES-derived compositions, Rietveld refinement phase compositions, lattice parameter and crystallite sizes, and TEM-derived particle sizes of the $(Ni_xFe_{1-x})Fe_2O_4$ nanoparticles synthesized via the benzyl alcohol solvothermal route using the modified T1.3 conditions at 210 °C inside the Berghoff or small in-house autoclaves.

Sample	Temp (°C)	Synthesis autoclave	Phase composition (wt.- %)	ICP-OES Fe : Ni atomic ratio	Lattice parameter (Å)	Crystallite size $[\bar{d}_n/\bar{d}_v \pm sd_n/sd_v]$ (nm)
TT1.1	210	Berghoff	$Ni(OH)_2$ = 45 $NiFe_2O_4$ = 55	1.2	8.364	9.4 [10.3/12.3 ± 2.6/3.6]
TT1.3	210	Berghoff	$NiFe_2O_4$	2.5	8.347	10.6 [9.7/11.9 ± 2.6/4.0]
TT1.5	210	Berghoff	$NiFe_2O_4$	4.4	8.373	12.1 [11.2/13.8 ± 3.1/4.2]
TT1-2.3	210	Small	$NiFe_2O_4$	2.9	8.352	10.6 [-]
TT1-2.5	210	Small	$NiFe_2O_4$	3.0	8.357	11.0 [-]
TT1-3.3	210	Small	$NiFe_2O_4$	2.9	8.358	8.0 [9.4/11.4 ± 2.4/3.4]
TT1-3.5	210	Small	$NiFe_2O_4$	4.8	8.378	13.4 [11.1/12.8 ± 2.5/3.2]

In square brackets are the average number- ($\bar{d}_n$) and volume- ($\bar{d}_v$) based particle sizes obtained via TEM analysis and their respective standard deviations (sd_n and sd_v).

TEM analysis of the samples TT1.1, TT1.3 and TT1.5 also show that spherical nanoparticles of 10.3 ± 2.6 nm, 9.7 ± 2.6 nm and 11.2 ± 3.0 nm average particle size, respectively, were formed (see Figure 6.5). The observed slight increase in TEM-derived average particle size with the decrease in the Ni content also correlate well with the XRD-derived average crystallite sizes (see Table 6.2). Thus, this approach is very effective and proves that $(Ni_xFe_{1-x})Fe_2O_4$ inverse spinel nanoparticles can be synthesized with varying overall Fe : Ni atomic ratio as desired for use as catalyst precursors in this study. Therefore, the samples TT1.1, TT1.3 and TT1.5 were used as catalyst precursors in this work. However, since these materials had to be used for both characterization and immobilization on the six different overlayers (discussed in Chapter 5) to form the overall targeted multicomponent catalysts, a single synthesis batch did not suffice. Thus, more samples (especially TT1.3 and TT1.5) had to be synthesized by reproducing the synthesis. Unfortunately, the Berghoff autoclave could not be used for the repeat/further syntheses due to technical problems experienced, but an in-house small autoclave of a 300 mL inner volume was used to reproduce these samples in a second batch, instead (*i.e.* samples TT1-2.3 and TT1-2.5).

The ICP-OES results of the sample TT1-2.5 (see Table 6.2) synthesized under the same conditions as in the Berghoff autoclave in an attempt to reproduce TT1.5, suggest a loss of Fe during the synthesis as an overall Fe : Ni atomic ratio of 3.0 is attained when using the small autoclave. The main difference between these autoclaves is the inner volume and the attainable vapour pressure limit. The Berghoff autoclave limits the vapour pressure at 25 bar during the synthesis by use of a pressure-relief valve, while the small autoclave does not vent as it can withstand higher vapour pressures of up to 150 bar. Yet, no significant loss of Fe occurred in the Berghoff autoclave. This may suggest that the venting and pressure limits play a role to some extent. When the synthesis was attempted in the small in-house autoclave using a third of the volume of ammonium hydroxide, neither Fe nor Ni was significantly lost as attested by the ICP-OES results of the samples TT1-3.3 and TT1-3.5 (see Table 6.2). Furthermore, the XRD patterns of these samples (see Figure 6.4) and the lattice parameters (see Table 6.2) are comparable with those of samples TT1.3 and TT1.5 as desired. Thus, for reproduction at a high synthesis pressure, a smaller volume of the ammonium hydroxide solution is necessary to attain overall Fe : Ni atomic ratios similar to those samples synthesized in the Berghoff autoclave. It is still not clear how the loss of Fe occurred during the synthesis at high pressure and how reducing the volume of ammonium hydroxide circumvented it.

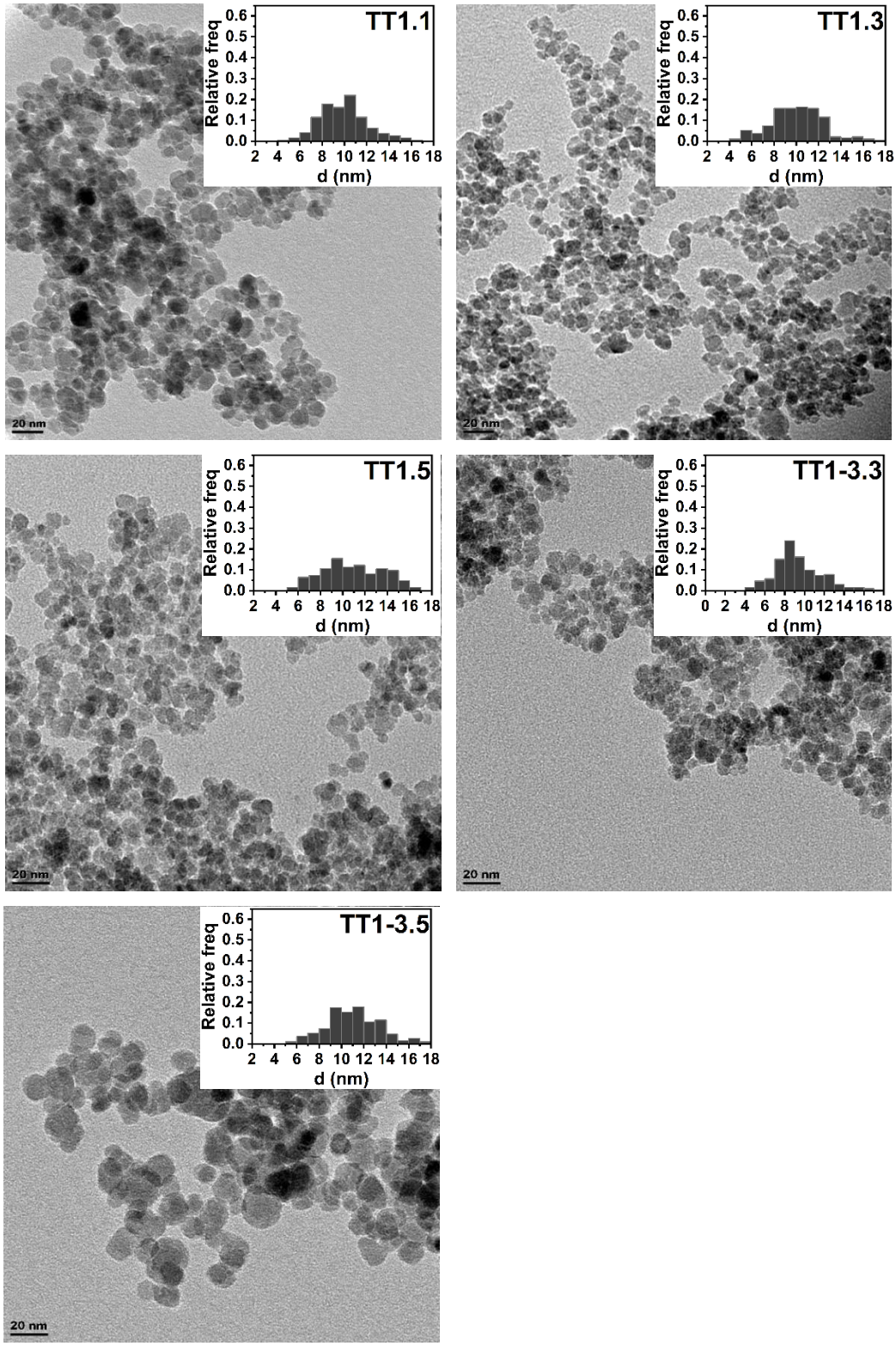

Figure 6.5: TEM images of $(Ni_xFe_{1-x})Fe_2O_4$ nanoparticles of varying overall Fe : Ni atomic ratios to be used as catalysts. TT1.1, TT1.3 and TT1.5 were synthesized in the Berghoff while TT1-3.3 and TT1-3.5 were synthesized in the in-house autoclave.

TEM analysis of both the TT1-3.3 and TT1-3.5 samples also reveal that mostly spherical nanoparticles comparable to those obtained in the Berghoff autoclave with 9.4 ± 2.4 nm and 11.1 ± 2.5 nm average particle size, respectively, were formed (see Figure 6.5). The particle size still increased with the decrease in Ni content. The TEM images of the samples TT1-2.3 and TT1-2.5 are shown in the Appendix section (see Figure 10.2) and also confirm formation of small spherical nanoparticles with XRD-derived crystallite sizes of 10.4 and 11.0 nm, respectively. Overall, the presented characterization results demonstrate that it is possible to synthesize nanoparticles of $(Ni_xFe_{1-x})Fe_2O_4$ inverse spinel phases with varying overall Fe : Ni atomic ratio *via* the solvothermal route and that obtaining the accurate target overall Fe : Ni atomic ratio depends on the temperature, pressure limits of the synthesis chamber and the volume of the ammonium hydroxide solution. The stoichiometry of the standard inverse spinel phase, limits incorporation of Ni up to an overall Fe : Ni atomic ratio of 2 and if more Ni precursor is added as in the case of sample TT1.1, then the excess forms an additional phase identified as $Ni(OH)_2$.

To gain more insight about the properties of these samples, further characterizations were conducted. However, since the above characterizations already revealed similarities between the two batches of samples obtained from synthesis in different autoclaves, only the samples obtained in the Berghoff autoclave (*i.e.* TT1.1, TT1.3 and TT1.5) were used for these further characterizations. STEM-EDX mapping (see Figure 6.6) supports the presence of a majorly $(Ni_xFe_{1-x})Fe_2O_4$ inverse spinel phase in which both the Fe and Ni are closely associated/intimate and homogeneously distributed in the samples TT1.3 and TT1.5 with overall Fe : Ni atomic ratio s of 3 and 5, respectively. Neither Ni nor Fe localization/clustering is observed. For the sample TT1.1, with the highest Ni concentration (*i.e.* overall Fe : Ni atomic ratio of 1), additional needle like structures which could be identified as a Ni-rich localizations and most likely represent the $Ni(OH)_2$ phase detected using the XRD, are observed.

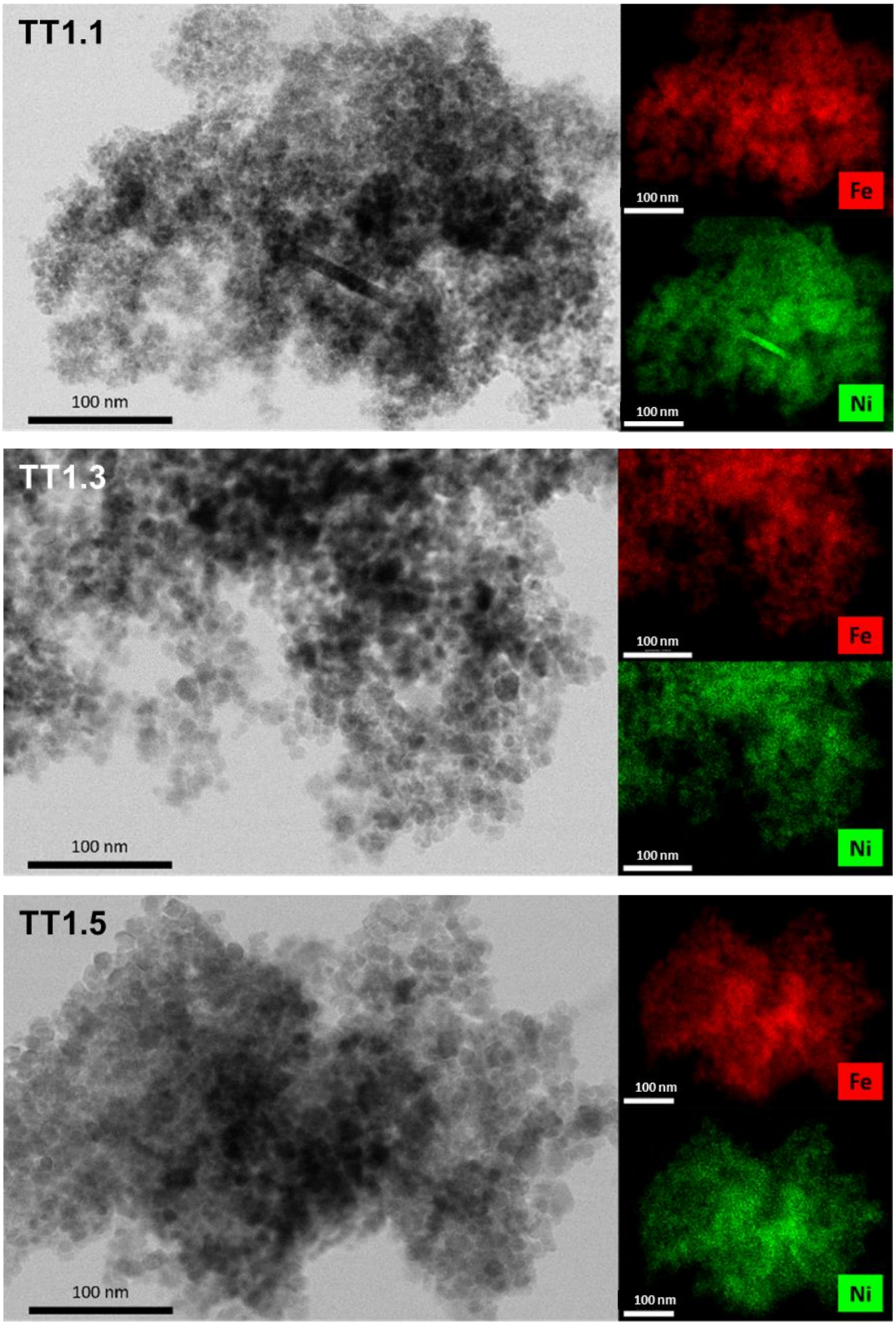

Figure 6.6: STEM images (left) and STEM-EDX elemental maps (right) of the TT1.1, TT1.3 and TT1.5 $(Ni_xFe_{1-x})Fe_2O_4$ inverse spinel nanoparticles of target overall Fe : Ni atomic ratio of 1, 3 and 5, respectively.

7 Reducibility of supported oxide precursor nanoparticles, microstructure, composition dependence and stability of resulting nano-alloy phase configurations captured *in situ*

Some results reported in this section are part of the publication: S. Raseale, W. Marquart, K. Jeske, G. Prieto, M. Claeys, N. Fischer, Supported Fe_xNi_y catalysts for the co-activation of CO_2 and small alkanes, Faraday Discuss. 229 (2020) 208-231. https://doi.org/10.1039/C9FD00130A.

The prepared $(Ni_xFe_{1-x})Fe_2O_4$ nanoparticles of samples TT1.1, TT1.3 and TT1.5 were immobilized *via* ultrasonication onto the porous metal oxide overlayers ($MO_x@Al_2O_3$). To investigate their reducibility into the respective metallic alloy phases, temperature-programmed reduction (TPR)-type experiments were conducted in a stream of diluted H_2 with the temperature increased up to 700 °C and an *in situ* XRD set-up (Anton Paar XRK-900 cell) being used to monitor the resulting phase changes (see Figure 7.1 for the samples anchored on $CrO_x@Al_2O_3$). It should be noted that the refinement of the obtained XRD patterns for site occupancy and changes in lattice parameter could not be achieved. This is due to the overlapping diffractions of supported crystallites with those of the MO_x overlayer carrier (γ-Al_2O_3), the short scan times employed for optimal temporal resolution, as well as temperature and sample related shifts in the diffraction positions. It is also worth mentioning that due to the same reasons, the phase compositions presented in this section may not be completely accurate but are reported as trends instead. For both the $(Ni_xFe_{1-x})Fe_2O_4$ precursor with an inverse spinel structure and the emanating metallic Fe_xNi_y alloy phases, the overall Fe:Ni atomic ratios previously identified were assumed in the refinement (see Table 6.2 above).

The intensity of the reflex at a 1/d of about 0.49 $Å^{-1}$ (marked ♦ in Figure 7.1) in sample TT1.1 (with an overall Fe:Ni atomic ratio of 1) corresponds to metallic Ni and begins to appear at a temperature of 185 °C due to the reduction of $Ni(OH)_2$. With increasing temperature, both the intensities of the reflexes associated with the metallic Ni and the $(Ni_xFe_{1-x})Fe_2O_4$ inverse spinel (marked ●) decrease concurrently and are completely absent at about 324 °C.

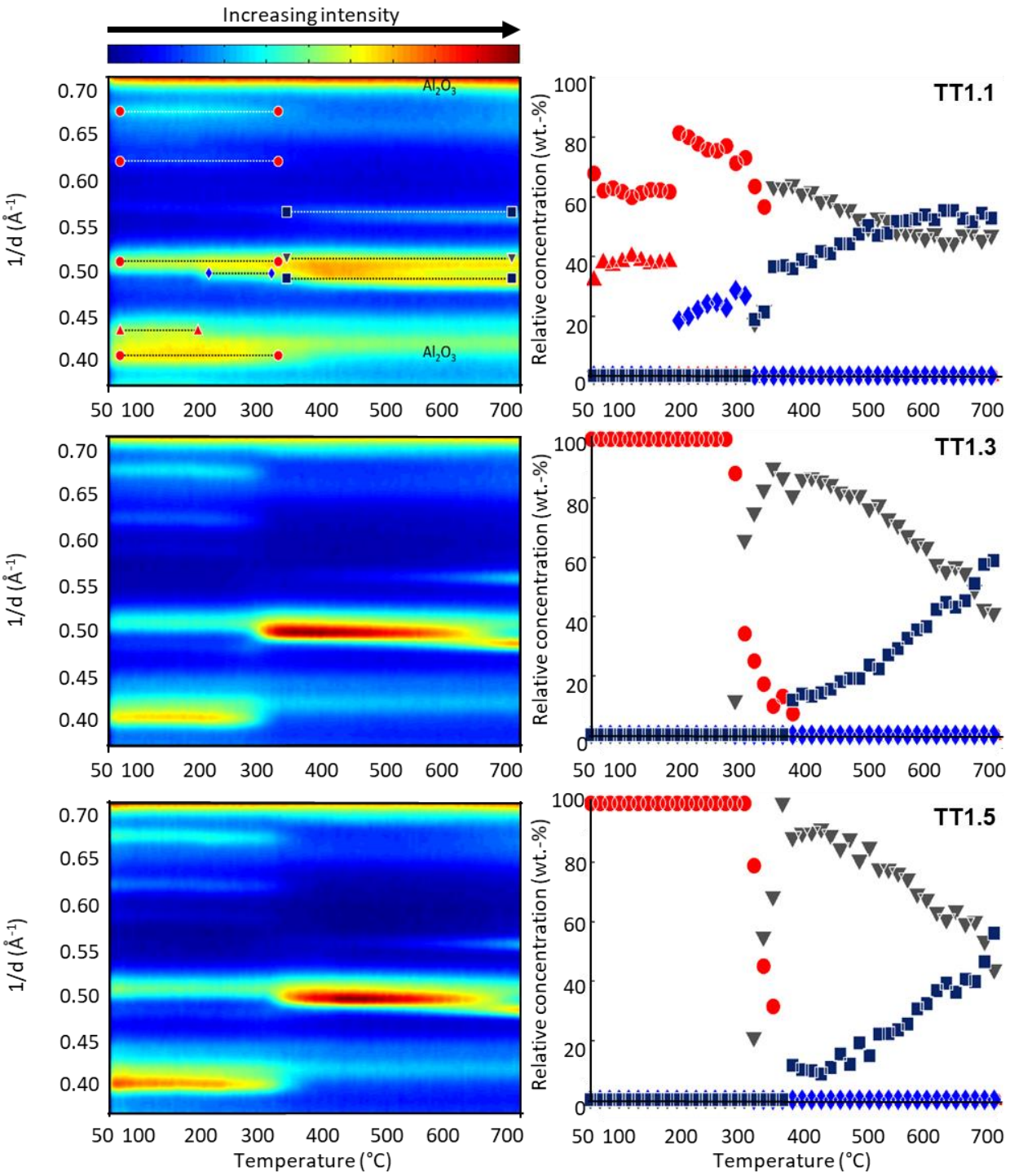

Figure 7.1: Top view of in situ XRD patterns (left) and evolution of Fe and Ni phases (right) of the samples TT1.1, TT1.3 and TT1.5 with the overall Fe:Ni atomic ratio of 1, 3 and 5, respectively, anchored on CrO_x@Al_2O_3 as a function of temperature recorded during reduction in a 5 vol.-% H_2 in N_2 gas stream. $(Ni_xFe_{1-x})Fe_2O_4$ = ●; $Ni(OH)_2$ = ▲; fcc Ni^0 = ♦; bcc Fe_xNi_y = ▼; fcc Fe_xNi_y = ■. The positions of the reflexes of the respective phases are indicated in the in situ XRD pattern of sample TT1.1. For clarity reasons, only the Rietveld refinement results of every third diffraction pattern are displayed in the phase composition figures (right).

Parallel to this, reflexes indexed to a mixture of the fcc (marked ■) and bcc (marked ▼) phases of the Fe_xNi_y alloy emerge at approximately 293 °C. This mixture initially consists, predominantly, of the bcc phase of the Fe_xNi_y alloy. With increasing temperature, its concentration decreases in favour of the fcc phase. For emphasis, in the complete absence of an oxidic phase (from 325 °C upwards), a bcc-to-fcc ratio of 60:40 is calculated, while a steady ratio of 44:56 is attained from 550 °C onwards.

In comparison, the Fe-rich samples, TT1.3 and TT1.5, initially transform only into a bcc phase at 275 °C and 300 °C, respectively, as a result of the reduction of the $(Ni_xFe_{1-x})Fe_2O_4$ inverse spinel phase, which is completely absent in the diffraction pattern recorded at 380 °C for TT1.3 and 360 °C for TT1.5. Unlike TT1.1, this bcc phase remains as the only stable Fe_xNi_y alloy phase until full reduction of the $(Ni_xFe_{1-x})Fe_2O_4$ inverse spinel phase. Upon full reduction, the fcc alloy phase starts to emerge in concentrations of 10 - 12 wt.-% and both the bcc and fcc alloy phases co-exist. The fcc fraction increases gradually with temperature, slightly faster in the case of the sample TT1.3 and reaches approximately 58 wt.-% at 700 °C. For the sample TT1.5, the bcc-to-fcc alloy phase transformation is slower and slightly more of the bcc phase is retained at 700 °C. This behaviour, *i.e.* the initial sole presence and increased stability of the bcc alloy phase with increasing overall Fe:Ni atomic ratio correlates well with the unsupported Fe-Ni alloy binary phase diagram reported in literature (see Figure 2.17 in section 2.4) [223,297], which also supports the presence of an alloy phase instead of segregated Fe and Ni.

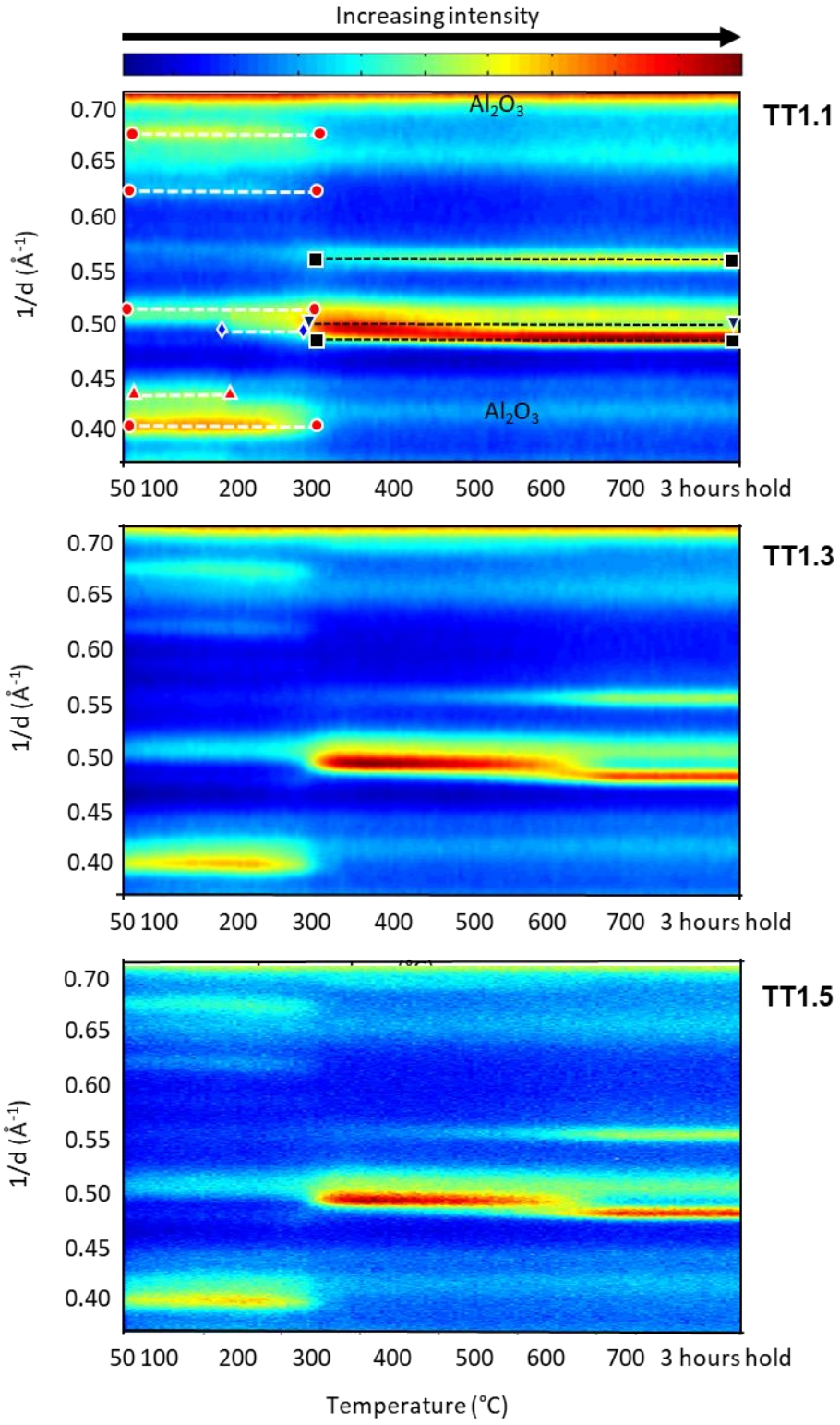

Figure 7.2:Top view of the in situ XRD patterns of the samples TT1.1, TT1.3 and TT1.5 with overall Fe:Ni atomic ratio of 1, 3 and 5, respectively, anchored on $ZrOx@Al_2O_3$ as function of temperature recorded during reduction in a 5 vol.-% H_2 in N_2 gas stream. The positions of the reflexes of the respective phases are only indicated in the in situ XRD pattern of sample TT1.1. ($Ni_xFe_{1-x})Fe_2O_4$ = ●; $Ni(OH)_2$ = ▲; fcc Ni^0 = ♦; bcc Fe_xNi_y = ▼; fcc Fe_xNi_y = ■.

It is worth noting that the onset temperatures of these observed phase transformations do not exactly correlate with those in the reported Fe_xNi_y alloy phase diagram. For instance, for the sample TT1.1 with an overall Fe:Ni atomic ratio of 1 (*i.e.* 50 at.-% Ni), the mixture consisting of both the α/bcc and γ/fcc- Fe_xNi_y alloy phases remains stable even at 700 °C, where only the single γ/fcc phase should be stable according to the Fe-Ni phase diagram. These discrepancies are attributed to the differences in the particle/crystallize size, nature of the precursors used as well as the chosen decomposition/reduction gas environments. The phase transformations of Fe_xNi_y alloys into the bcc and fcc phase configurations as a result of the reduction of oxidic $(Ni_xFe_{1-x})Fe_2O_4$ nanoribbons in H_2 have also been observed in a study by Jing *et al.* [218]. Their phase transformation onset temperatures, especially the emergence of the bcc and fcc mixture, are close to the temperature in the present study although a full phase transformation of the mixture into a single fcc phase at a temperature of 500 °C is reported. Lastly, in our case, no significant sintering of the formed Fe_xNi_y nano-alloys is observed throughout the reductive treatment since the crystallite sizes, at 700 °C, ranged from 10.3 to 12.9 nm for the fcc phase and slightly lower from 4.8 to 5.5 nm for the bcc phase, independent of the Fe:Ni atomic ratio. Although, the conventional H_2-TPR results of the bare $CrO_x@Al_2O_3$ overlayer suggests some reduction of the periphery CrO_x at about 275 °C (see Figure 5.4), no additional diffractions were observed in the *in situ* XRD patterns corroborating its continuous presence as an XRD-silent amorphous phase.

The reduction behaviour of the obtained oxidic Fe_xNi_y nanoparticles in these samples (TT1.1, TT1.3 and TT1.5) into the alloy also appears to be support independent as comparable results, especially in terms of the onset temperatures, were obtained when supported on the $ZrO_x@Al_2O_3$ overlayer (see Figure 7.2). STEM imaging and EDX mapping for the selected sample TT1.3 supported on $ZrO_x@Al_2O_3$ after reduction and passivation confirm good dispersion of the alloy nanoparticles on the support and intimate interaction of Fe and Ni in separate nanoparticles as desired (see Figure 7.3). Based on these results, a reduction temperature of 500 °C providing a full reduction of the oxidic precursors into the respective Fe_xNi_y alloys and yielding different ratios of fcc:bcc alloy phases was chosen for all further studies.

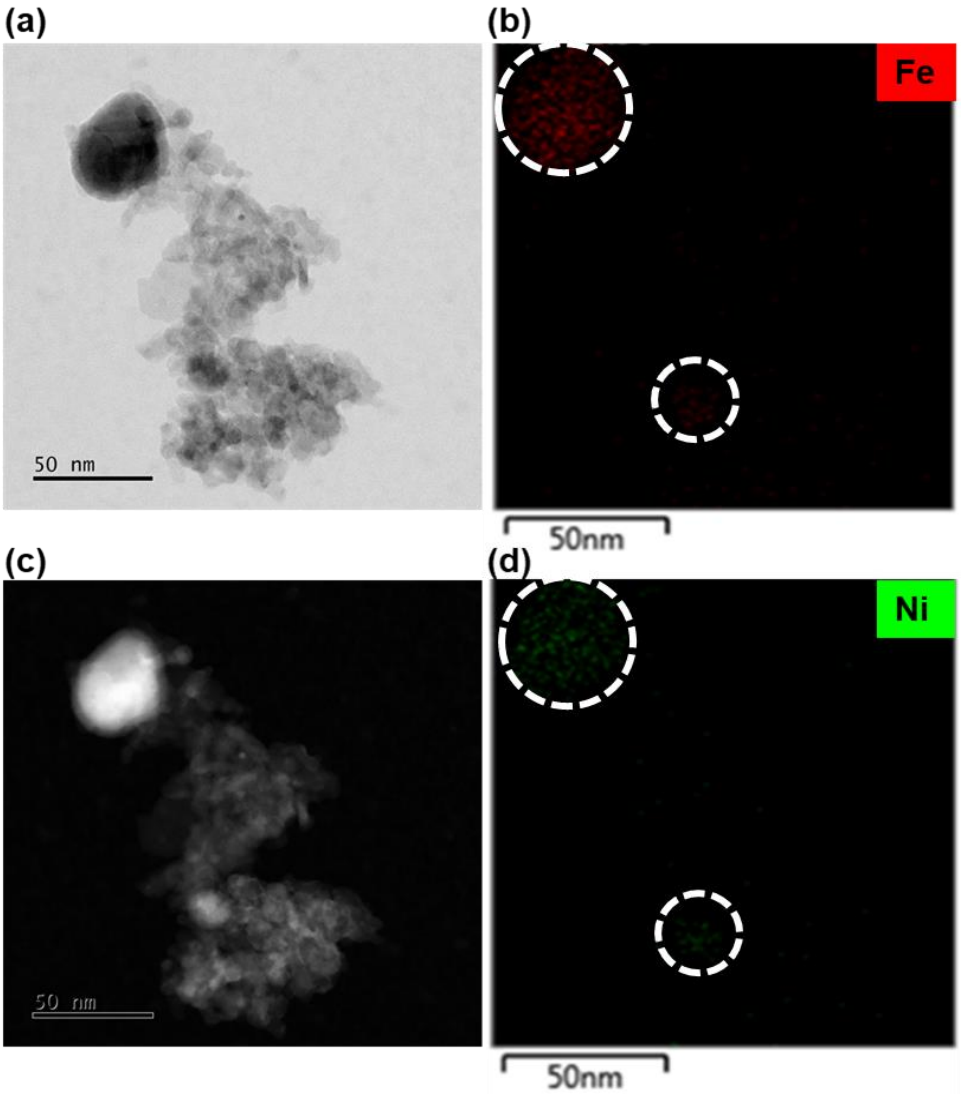

Figure 7.3: (a) Bright- and (c) dark-field STEM images as well as STEM-EDX maps of (b) Fe and (d) Ni for the sample TT1-3 with an overall Fe:Ni atomic ratio of 3 anchored on ZrO_x@Al_2O_3 overlayer after reduction in a 5 vol.-% H_2 in N_2 gas stream and then passivation in a 1 vol.-% O_2 in N_2 gas stream.

It is proposed that the Fe_xNi_y nano-alloys in the prepared model catalysts will provide catalytic activity for the CO_2-ODHE through the enhancement of the CO_2-activation step. When enhanced, CO_2-activation will avail reactive oxygen species which, depending on their nature, play a role in both the removal of H_2 as water and in the re-oxidation of the metal oxide overlayer reduced during C_2H_6-activation *via* the MvK mechanism. Direct temperature-programmed CO_2-activation experiments were performed with the Fe_xNi_y alloys by reducing the TT1.5 and TT1.1 oxidic precursors to understand their capacity to interact and activate CO_2. To eliminate the effect of the metal oxide overlayer, the TT1.5 and TT1.1 oxidic precursors, with overall Fe:Ni atomic ratios of 5 and 1 respectively, were dispersed onto a large surface area mesoporous silica (KIT-6) support.

The resulting materials were reduced into the respective Fe_xNi_y nano-alloys under a flow of 5 vol.-% H_2 in N_2 at 500 °C for 3 h using a 1 °C/min heating rate. Subsequently, the samples were cooled to 50 °C under N_2 and then exposed to a stream of 1 vol.-% CO_2 in N_2 at increasing temperatures up to 700 °C. *In situ* XRD was used to monitor the phase changes of the material as a result of both the reduction and the exposure to CO_2 (see Figure 7.4 (a) and Figure 7.5 (a) for TT1.1 and TT1.5 respectively).

After pre-treatment in 5 vol.-% H_2 in N_2 at 500 °C for 3 h (reduction), neither the residual crystalline $(Ni_xFe_{1-x})Fe_2O_4$ inverse spinel nor the hydroxide, $Ni(OH)_2$, were detected in both samples. The resulting bimetallic microstructure for both samples still consists of a mixture of both the fcc and bcc Fe_xNi_y alloy phases and cannot be described as pure monometallic phases following the same trend predicted by the Fe-Ni phase diagram (see Figure 2.17 in section 2.4) and the previously discussed *in situ* XRD-TPR results (see Figure 7.1 and Figure 7.2). However, the Ni-rich TT1.1 sample (see Figure 7.4 (a) and (b)) reduces into a bimetallic microstructure with crystallites predominantly in an fcc structure (83 wt.-%,) while the Fe-rich TT1.5 sample predominantly (see Figure 7.5 (a) and (b)) forms a bcc phase (80 wt.-%). No significant differences were observed in the reduction behaviour of these oxidic precursor materials, especially regarding to the onset temperature at which the phase transformation from the oxidic phase to the bimetallic phase occurs. This corroborates the claim that the reduction of these materials occurs differently only when the overall Fe:Ni atomic ratio varies but proceeds independent of the support material onto which they are anchored for a given overall Fe:Ni atomic ratio.

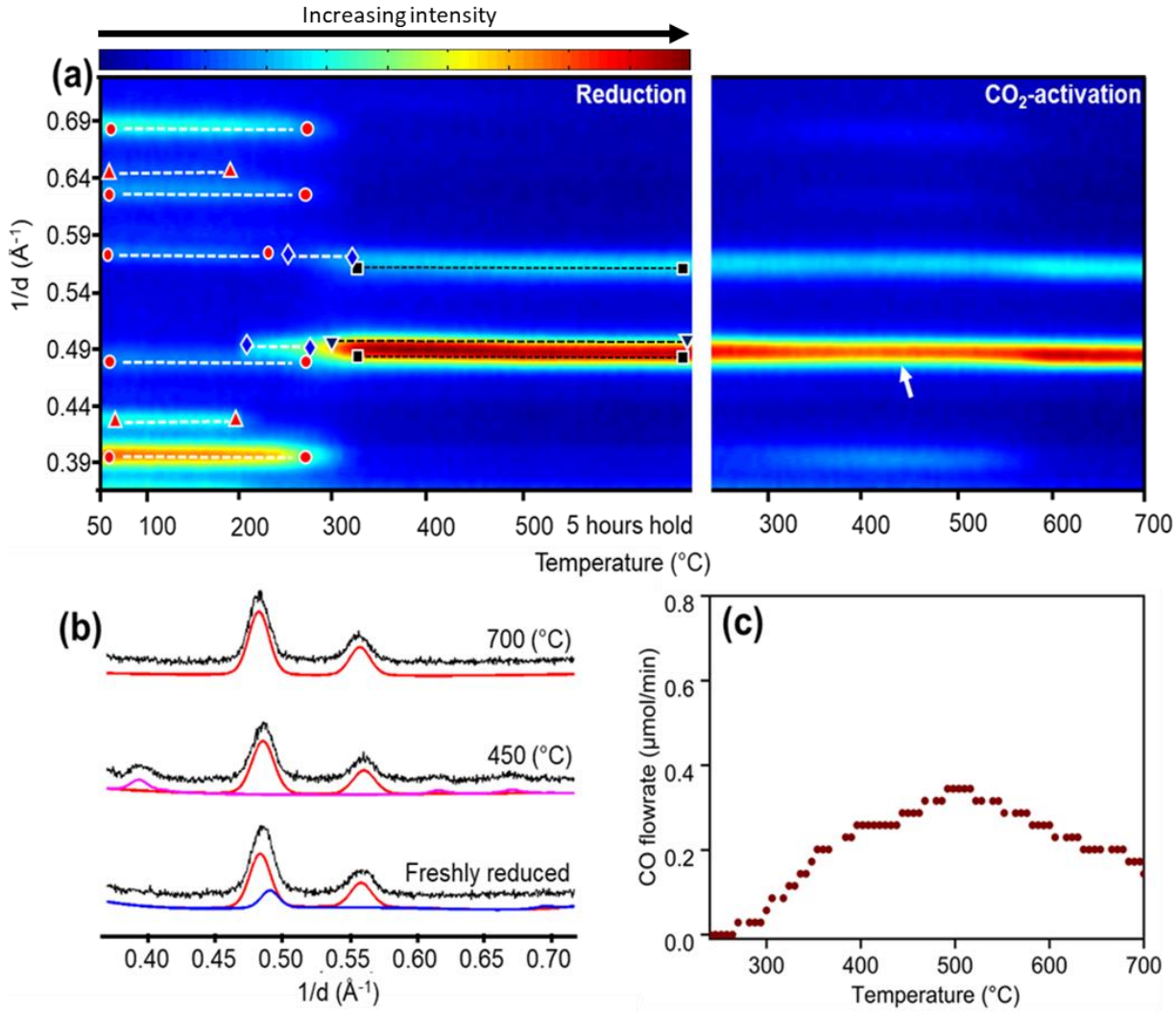

Figure 7.4: (a): Top view of in situ XRD patterns recorded during the reduction and the subsequent temperature-programmed CO_2-activation of TT1.1 supported on KIT-6. The reduction was performed at 500 °C for 3 h in 5 vol.-% H_2 in N_2 (left of the white vertical dividing line). The positions of the reflexes of the respective phases are indicated as: $(Ni_xFe_{1-x})Fe_2O_4$ = ●; $Ni(OH)_2$ = ▲; fcc Ni^0 = ♦; bcc Fe_xNi_y = ▼; fcc Fe_xNi_y = ■. The sample was subsequently cooled to 50 °C in N_2 and heated at 1 °C /min in 1 vol.-% CO_2/N_2 to 700 °C. For clarity, only the data above 225 °C during the temperature-programmed CO_2-activation experiment is shown (right of the white dividing line). The white arrow shows the narrowing of the diffraction at a 1/d of 0.49 $Å^{-1}$ due to CO_2-activation. (b): Corresponding selected diffraction patterns (bottom: freshly reduced at 500 °C; top: under exposure to 1 vol.-% CO_2/N_2 at different temperatures) and calculated diffraction patterns for bcc NiFe (blue), fcc NiFe (red) and $NiFe_2O_4$ (magenta). Experimental (black) and calculated patterns are stacked together per reaction stage for clarity. (c): The associated CO evolution as a function of temperature during the temperature-programmed CO_2-activation step measured in a parallel experiment in the fixed-bed reactor.

Above approximately 225 °C under a stream of 1 vol.-% CO_2 in N_2, both catalysts show a partial re-oxidation to the $(Ni_xFe_{1-x})Fe_2O_4$ inverse spinel structure. Parallel to this, the disappearance of the bcc phase is observed. This is clearly noticeable from the narrowing of the reflex at a 1/d of about 0.49 $Å^{-1}$, which is more pronounced for the sample TT1.5 (see CO_2-activation section in

Figure 7.4 ((a), Right) and Figure 7.5 ((a), Right)). Rietveld refinement reveals that only the bcc phase disappears upon re-oxidation during the temperature-programmed CO_2-activation (see Figure 7.4 (b): 450 °C and Figure 7.5 (b): 500 °C and 600 °C). Thus, independent of the Fe:Ni atomic ratio, only the bcc phase of the bimetallic Fe_xNi_y alloy is re-oxidized while the fcc fraction in this microstructural mixture remains unaffected. Concurrent to the increasing degree of bcc phase re-oxidation with temperature, CO is detected as the sole product in the reactor outlet (see Figure 7.4 (c) and Figure 7.5 (c)). This detected CO reaches higher formation rates for the sample TT1.5 in line with the larger fraction of the bcc phase compared to TT1.1. CO_2 is activated on the surface of the bcc phase of the Fe_xNi_y alloy, resulting in the desorption of gaseous CO and the incorporation of O* forming a bulk inverse spinel oxide structure (note that the CO formation rate was measured in a separate experiment using a fixed bed reactor set-up and not in the *in situ* XRD, Anton Paar XRK-900 cell, due to the unfavourable hydrodynamics in the cell resulting in back mixing and dead volumes). Upon full depletion of the bcc allotrope, the CO formation rate drops, even at increasing temperatures, while the fcc allotrope remains in the metallic state. This suggests that the fcc allotrope of the Fe_xNi_y alloy is essentially inert in the temperature-programmed CO_2-activation experiment. This supports the initial hypothesis of the present study proposing that Fe-rich Fe_xNi_y alloy systems should be better suited in reaction systems involving CO_2-activation, such as CO_2-ODHE. The CO formation rate also decreases slower at higher temperatures for the Ni-rich sample compared to the Fe-rich one suggesting that the presence of more fcc phase in the alloy stabilizes or slows the re-oxidation of the bcc phase.

A previous report has studied the CO_2 activation energy over bcc Fe and fcc Ni sites and has shown that the bcc Fe sites have a significantly higher propensity for CO_2-activation [298]. As previously discussed in section 2.3.6, a theoretical study by Han *et al*. [16] also predicted that several bimetallic alloy combinations are likely to represent good CO_2-activation capabilities. In their study, Fe_xNi_y alloys with Fe as the host are mapped among those alloy combinations predicted to exhibit the lowest activation energy for CO_2-activation/dissociation. The group of Chen *et al.* [1,17–19,209,211,226] presented scientific evidence that Fe_xNi_y alloys exhibit enhanced catalytic performance in the CO_2-ODH of ethane, propane or butane (CO_2-ODHE/P/B) depending on the support and the Fe:Ni atomic ratio. Although this was not discussed, it is conceivable based on the results presented in this study, that the enhanced catalytic performance and stability observed is a result of the CO_2-activation ability of the Fe_xNi_y alloy in their catalysts. However, no study has presented the microstructure and phase dependence of CO_2-activation

over Fe_xNi_y alloys or identified the potential Fe_xNi_y alloy allotrope responsible for the CO_2-activation.

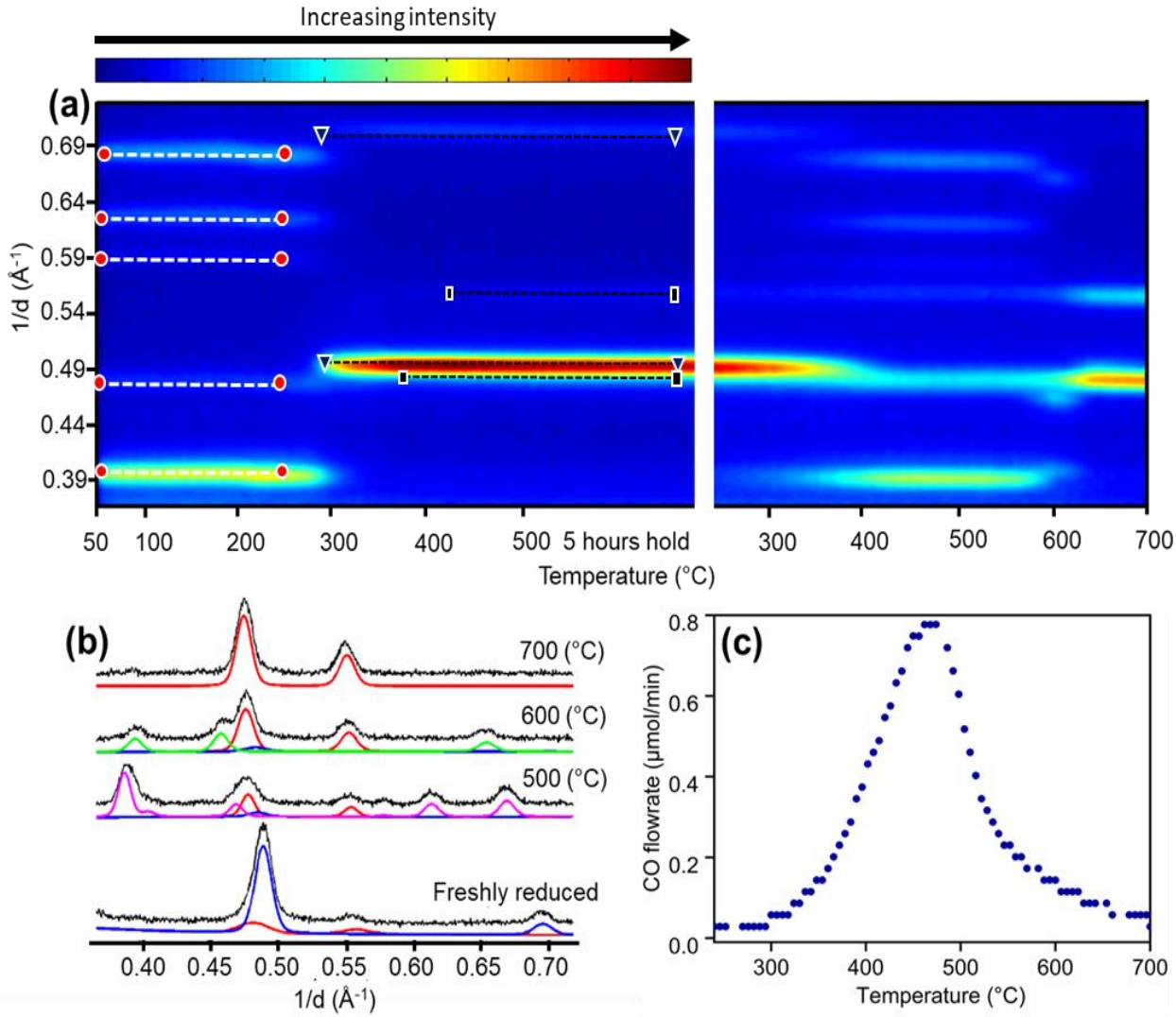

Figure 7.5: (a): Top view of situ XRD patterns recorded during the reduction and the temperature-programmed CO_2-activation of TT1.5 supported on KIT-6. The reduction was performed at 500 °C for 3 h in 5 vol.-% H_2 in N_2 (left of the white vertical dividing line). The positions of the reflexes of the respective phases are indicated as: $(Ni_xFe_{1-x})Fe_2O_4$ = ●; fcc Ni^0 = ♦; bcc Fe_xNi_y = ▼; fcc Fe_xNi_y = ■. The sample was subsequently cooled to 50 °C in N_2 and heated at 1 °C/min in 1 vol.-% CO_2/N_2 to 700 °C. For clarity, only the data above 225 °C during the temperature-programmed CO_2-activation is shown (right of the white vertical dividing line). (b): The corresponding selected diffraction patterns (bottom: freshly reduced at 500 °C; top: under exposure to 1 vol.-% CO_2/N_2 at different temperatures) and calculated diffraction patterns for bcc NiFe (blue), fcc NiFe (red) and $NiFe_2O_4$ (magenta). The experimental (black) and calculated patterns are stacked per reaction stage for clarity. (c): The associated CO evolution as function of temperature during the temperature-programmed CO_2-activation step measured in a parallel experiment in the fixed bed reactor.

Interestingly, upon further increase of temperature above 525 °C and 475 °C for sample TT1.1 and TT1.5, respectively, in parallel to the drop of the CO formation rate, the re-formed $(Ni_xFe_{1-x})Fe_2O_4$ fraction starts to diminish and is completely absent above 600 °C in both samples. In sample TT1.1, the oxidic phase is completely reduced into the fcc alloy at high temperatures. In TT1.5, the reduction proceeds *via* the formation of a Wüstite (FeO)-type structure before yielding the fcc alloy phase at the high temperatures. While a thermal decomposition of some spinel structures, such as Co_3O_4 to CoO between 900 and 1000 °C, is well described in literature, no such behaviour was reported for these iron- and nickel-involving spinel materials, especially in an oxidizing atmosphere [299]. It is proposed that carbon species deposited on the surface during CO_2-activation act as reducing agent at the higher temperatures. However, this does not rule out the possibility of secondary reduction by the left-over CO product due to the design of the Anton Paar XRK reaction chamber used which has a large dead volume. This is especially supported by the notion that this reduction behaviour was not observed when similar reactions were performed in the fixed-bed reactor as suggested by the offline XRD results of the spent catalysts (see Figure 7.6).

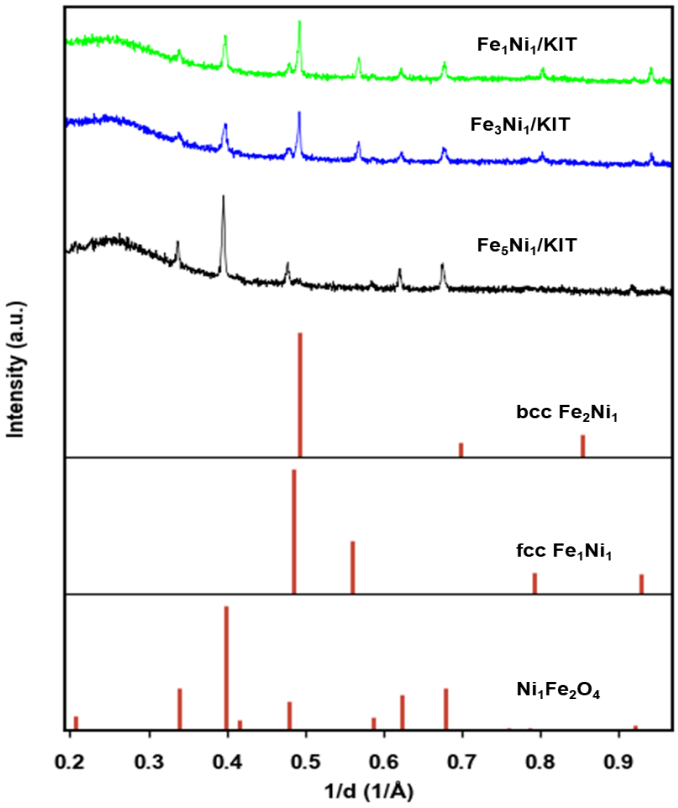

Figure 7.6: Offline XRD patterns of spent samples of T1.1, T1.3 and T1.5 supported on KIT after a temperature-programmed CO_2-activation experiments in the fixed-bed reactor.

Similar experiments were also performed using TGA analysis to further understand the weight changes associated with the oxidic precursors of TT1.5 and TT1.1 supported on the large surface area mesoporous silica (KIT-6), as a result of the treatment under reduction and the subsequent temperature-programmed CO_2-activation conditions (see Figure 7.7). For reduction into the respective Fe_xNi_y alloys, the samples were pre-treated in a 5 vol.-% H_2 in N_2 at 500 °C for 3 h using a 1 °C/min heating rate. Subsequently, the samples were cooled to 300 °C while under N_2 and then exposed to a stream of 1 vol.-% CO_2 in N_2 for 3 h at 300 °C. Afterwards, the temperature was increased to 1000 °C using a 10 °C/min heating rate while under a stream of 1 vol.-% CO_2 in N_2.

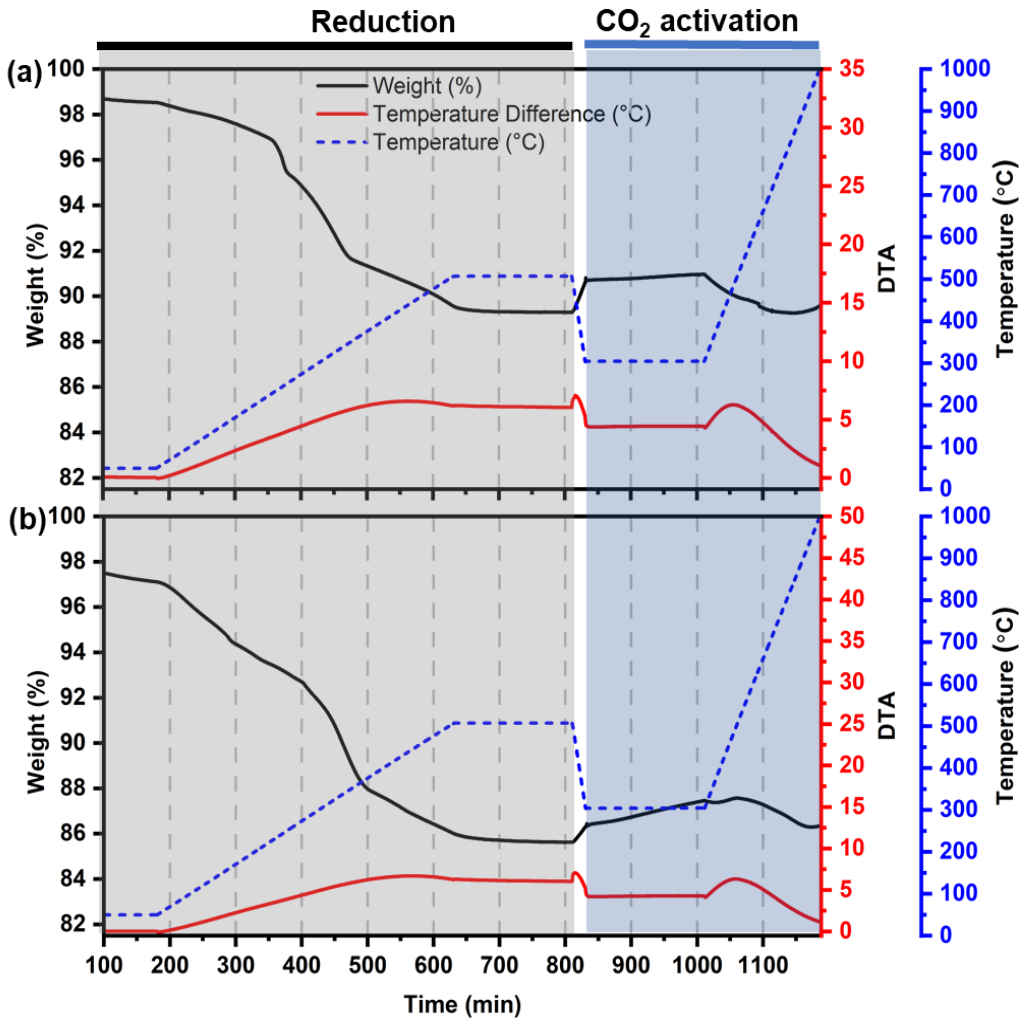

Figure 7.7: TGA/DTA analysis of the samples; (a) TT1.1 and (b) TT1.5 under reduction and the subsequent temperature-programmed CO_2-activation conditions.

Under reduction conditions, it is clear that the TT1.1 sample exhibits four stages of weight loss whereas the TT1.5 exhibits three stages. For TT1.1, the first weight loss takes place within 378 mins at a temperature of 248 °C associated with both the dehydration of the sample and the reduction of the $Ni(OH)_2$ phase while a single weight loss associated with dehydration of the sample occurs within 400 mins at 274 °C for TT1.5. This first weight loss is about 3.1 wt.-% for TT1.1 and 4.4 wt.-% for TT1.5 suggesting differences in the amount of adsorbed water due to the difference of the oxidic precursors. Subsequently, a two-stage overlapping weight loss resulting in further losses of 3.7 wt.-% after 474 mins (350 °C) and 2.4 wt.-% after 700 mins (500 °C) for TT1.1 as well as 4.7 wt.-% after 498 mins (370 °C) and 2.4 wt.-% after 794 mins (500 °C) for TT1.5 are observed. The onset of these two-stage weight losses is attributed to the reduction of the oxidic spinel phase into the corresponding alloy phases. The onset temperature of this spinel reduction correlates well with a previous report by Han *et al.* [300]. This transition from the oxidic phase to the alloy results in a larger weight loss and is slightly delayed for sample TT1.5 compared with sample TT1.1 correlating well with the observations made with *in situ* XRD experiments. The overlapping second part is potentially due to the reductive decomposition of the persistent residual surfactants in the pores of the porous KIT-6 carrier especially given that it is comparable and occurs at almost the same temperature for all samples (also see Figure 10.3 in appendix section for sample TT1.3).

After reduction, the temperature was decreased to 300 °C under N_2 followed by a change in the gas atmosphere to 1 vol.-% CO_2 in N_2. A considerable sample weight gain and an exothermic peak are observed caused by this change in conditions. While holding at 300 °C, a very slight weight gain (more apparent for sample TT1.5) is observed, which is attributed to re-oxidation in both samples. Although not so apparent due to weight uncertainties/losses caused by the change in temperature when the ramp was applied, this slight weight gain continues even when the temperature is increased above 300 °C for sample TT1.5 and is also associated with an exothermic peak at approximately 500 °C, attributed to re-oxidation as also witnessed in *in situ* XRD studies. With a further increase of temperature above 650 °C, a weight loss associated with the decomposition of the formed oxide is observed, consistent with the observations made during the *in situ* XRD experiments, for sample TT1.5. For sample TT1.1, the continuation of this weight-gain as well as the subsequent decomposition with increasing temperature (small hump just before 1100 mins) is surpassed by the weight loss caused by temperature change and is not clear to see. Similar observations to sample TT1.5 were made with the sample TT1.3, for which the re-oxidation and subsequent decomposition hump is more intense (see Figure 10.3 in appendix

section). The decomposition of the oxide after re-oxidation at higher temperatures is still attributed to secondary reduction by carbon or CO due to dead volume in the TGA reaction chamber as this was not observed in the fixed-bed reactor.

These observations clearly show that the chosen different oxidic precursors can be reduced into the corresponding target alloys consisting of the bcc and fcc phases. Interestingly, the alloy could be formed even from a mixed phase precursor consisting of $Ni(OH)_2$ and $(Ni_xFe_{1-x})Fe_2O_4$ through a transition from metallic Ni and the oxidic inverse spinel. Depending on the overall Fe:Ni atomic ratio, the fraction of these phases vary at a given temperature. Ni-rich alloys predominantly consist of the fcc phase, which reduces with increasing Fe content in the alloy while the bcc phase increases. The fcc phase is also stabilized by temperature, *i.e.* it increases with increasing temperature. The reduction behaviour is independent of the support material as it is similar for a given composition over the $ZrO_x@Al_2O_3$ and $CrO_x@Al_2O_3$ overlayers as well as over KIT-6. When exposed to a stream of CO_2, it was revealed that only the bcc phase of the alloy is able to activate CO_2 to form CO through which it is re-oxidised into the inverse spinel phase while the fcc phase remains stable. This CO_2-activation was found to be composition-dependent as it is significant over the Fe-rich alloy systems since they contain a larger faction of the bcc phase. When the bcc phase is fully consumed, the CO_2-activation functionality ceases despite the increase in temperature as proved by XRD analyses of the spent catalysts retrieved from the fixed-bed reactor. This suggests the further high-temperature decomposition of the oxidic inverse spinel phase into the fcc phase of the alloy after re-oxidation observed in *in situ* XRD and TGA experiments is due to back mixing and dead volume. The CO_2-activation happens at relatively low temperatures below 300 °C and these results serve as experimental evidence that bimetallic systems, especially Fe_xNi_y alloys, are future candidates of catalysts for CO_2-activation. While there are studies that made this claim, the composition-dependence of this CO_2-activation as well as the identification of the alloy microstructure responsible have not been reported before.

8 Oxidative dehydrogenation of ethane with carbon dioxide over various model catalysts

Some results reported in this chapter are part of the publication cited as: S. Raseale, W. Marquart, K. Jeske, G. Prieto, M. Claeys, N. Fischer, Supported Fe_xNi_y catalysts for the co-activation of CO_2 and small alkanes, Faraday Discuss. 229 (2020) 208-231. https://doi.org/10.1039/C9FD00130A.

The ultimate goal of this study is to investigate the physicochemical properties that play a role during CO_2-ODHE over the synthesized multifunctional multicomponent (combination of metal oxide overlayer and Fe_xNi_y nano-alloy) catalysts. Specific focus is directed to the joint catalytic influence of the metal oxide overlayer's surface acidity and reducibility as well as the anchored Fe_xNi_y nano-alloy composition. Since the target metal oxide overlayers are used in this study as reservoirs of lattice oxygen species that support catalytic activity, which is to be improved by the additional Fe_xNi_y nano-alloy, it is of great importance that these materials are first tested bare to understand their catalytic role and performance. This will enable the evaluation of how the Fe_xNi_y nano-alloys, which show good CO_2-activation abilities (see Chapter 7), further influence the catalytic performance of the metal oxide overlayers. For simplicity and coherence, the overlayer-supported Berghoff autoclave-synthesized TT1.1, TT1.3 and TT1.5 samples will be referred to as $Fe_1Ni_1/MO_x@Al_2O_3$, $Fe_3Ni_1/MO_x@Al_2O_3$ and $Fe_5Ni_1/MO_x@Al_2O_3$, respectively.

Since similar compositions of Fe_xNi_y nano-alloy precursors were synthesized in two separate batches obtained in different autoclaves to achieve the quantity necessary for deposition on the overlayers, the catalytic testing campaign was divided into two. This was done to counter the composition reproducibility challenge encountered during separate syntheses. The first batch of Fe_xNi_y oxidic precursors, which encompass the Berghoff autoclave-synthesized TT1.1, TT1.3 and TT1.5 samples with ICP-based Fe : Ni atomic ratios of 1.2, 2.5 and 4.4 (see Table 6.2 in Chapter 6) were anchored on $CrO_x@Al_2O_3$ and $ZrO_x@Al_2O_3$. The supported samples were then employed to study the effect of metallic composition of the alloy on the CO_2-ODHE reaction. The second batch of Fe_xNi_y oxidic precursors, which comprise of the small autoclave-synthesized TT1-3.3 and TT1-3.5 samples with ICP-based Fe : Ni atomic ratios of 2.9 and 4.8 (see Table 6.2 in Chapter 6) were anchored on the remainder of overlayers (*i.e.* $GaO_x@Al_2O_3$, $SmO_x@Al_2O_3$, $TiO_x@Al_2O_3$ and $VO_x@Al_2O_3$).

8.1 Catalytic performance of bare metal oxide overlayers

The synthesized bare metal oxide overlayers were tested for CO_2-ODHE activity in an equimolar feed of CO_2 (6.25 mL/min) and C_2H_6 (6.25 mL/min) with an inert dilution of 50 vol.-% (12.5 mL/min) at atmospheric pressure and 600 °C for 24 h, after reduction in H_2 for 3 h at 500 °C (see Figure 8.1). The pre-treatment conditions are suitable for the reduction of the oxidic precursors to the Fe_xNi_y nano-alloy as demonstrated by the reduction studies presented in Chapter 7. Under these catalytic testing conditions, thermodynamic calculations reported by our research group identified a thermodynamic equilibrium limit for the conversion of C_2H_6 of 24.4% *via* CO_2-ODHE and 91.6% *via* DRE [60,65].

The unreducible $SmO_x@Al_2O_3$, $TiO_x@Al_2O_3$ and $ZrO_x@Al_2O_3$ with the weaker total and Lewis acid sites, amongst the studied samples, record the lowest CO_2 and C_2H_6 conversions (below 2% and 1%, respectively) suggesting minimal activity for both the CO_2-ODHE and DRE reactions (see Figure 8.1, top). Amongst them, $SmO_x@Al_2O_3$ exhibits a 1.8% initial CO_2 conversion, the highest in this group of samples, possibly due to its basic nature as this material displays the weakest surface acid sites. $TiO_x@Al_2O_3$ only shows minor C_2H_6-activation (0.6% C_2H_6 conversion) while $ZrO_x@Al_2O_3$ displays no activity.

In contrast, the overlayers with intermediate-to-strong total and Lewis acid sites, *i.e.* the unreducible $GaO_x@Al_2O_3$ as well as the reducible $CrO_x@Al_2O_3$ and $VO_x@Al_2O_3$, display considerable initial C_2H_6 conversions of 4.2, 6.3 and 5.1%, respectively. Note that the initial C_2H_6 conversion of $VO_x@Al_2O_3$ is taken at 1 h TOS when the first data point was collected and is presumably higher before, considering the observed fast deactivation. The corresponding CO_2 conversions are 1.8, 3.6 and 5.2%. It is apparent that the activity of these materials varies with surface acid site strength as expected, making these materials good candidates for the purpose of this study. The initial activity decreases with the acid site strength, *i.e.* $VO_x@Al_2O_3$ > $CrO_x@Al_2O_3$ > $GaO_x@Al_2O_3$.

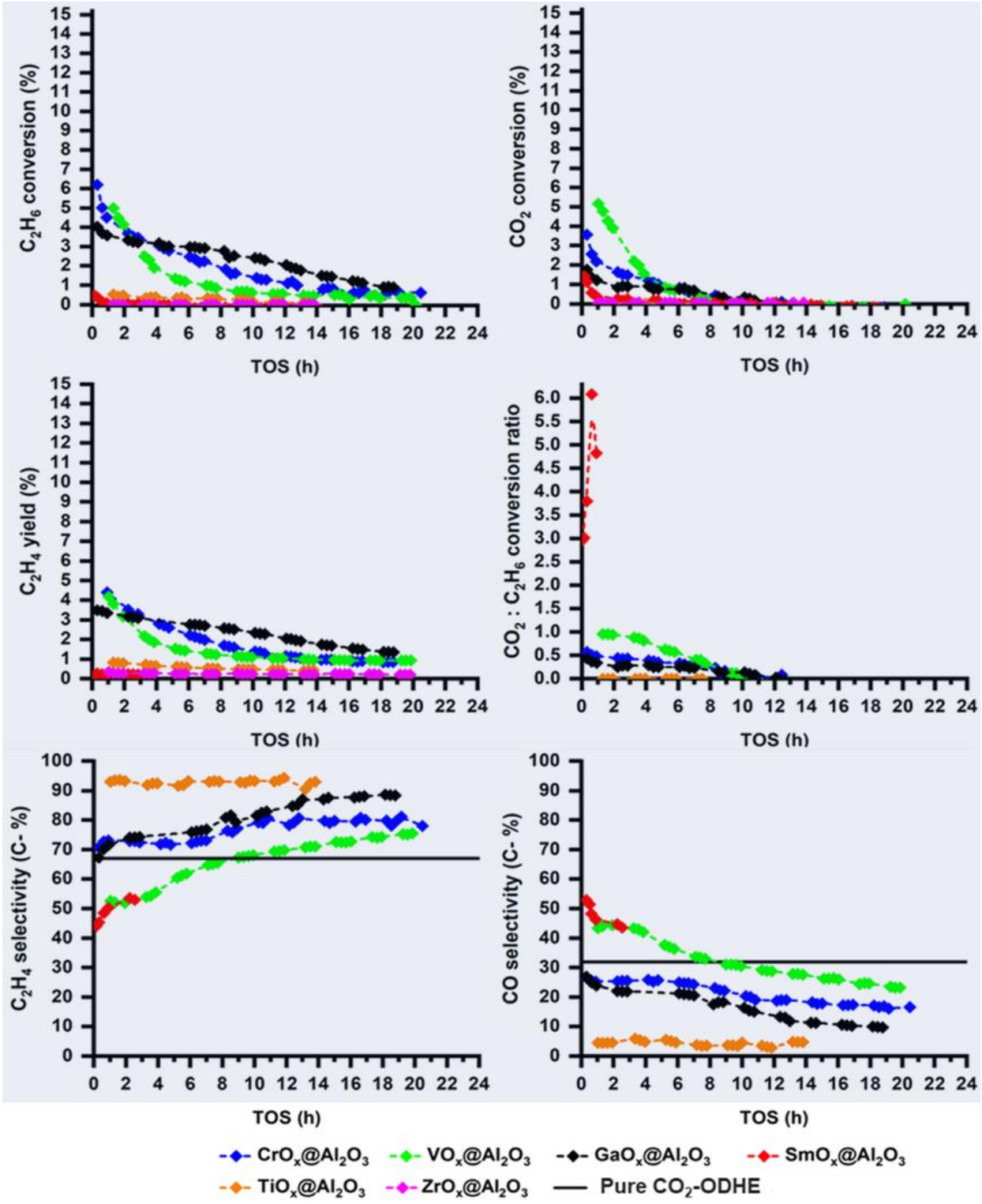

Figure 8.1: C_2H_6 and CO_2 conversions (top), C_2H_4 yield and CO_2 : C_2H_6 conversion ratio (middle) as well as C_2H_4 and CO selectivity (bottom) obtained during the reaction of C_2H_6 and CO_2 (6.25 mL/min each) diluted with 12.5 mL/min inert over the various $MO_x@Al_2O_3$ overlayers. Conditions: temperature = 600 °C, pressure = 1 atm, space velocity = 15 $L \cdot h^{-1} \cdot g_{cat}^{-1}$, CO_2 : C_2H_6 ratio = 1. Maximum possible carbon based C_2H_4 and CO selectivity for a perfect CO_2-ODHE system are indicated by the black solid line.

Conversely, in the set of overlayers with weaker total and Lewis acid sites (*i.e.* $SmO_x@Al_2O_3$, $TiO_x@Al_2O_3$ and $ZrO_x@Al_2O_3$), $SmO_x@Al_2O_3$, with the weakest acid sites, has the highest initial activity, but predominantly towards CO_2-activation. Overall, initial activity decreases with the overlayer acid site strength until a minimum is reached at $ZrO_x@Al_2O_3$ and then slightly increases with further weakening of acidity presumably due to increasing basicity enhancing CO_2-activation (see Figure 8.2, top).

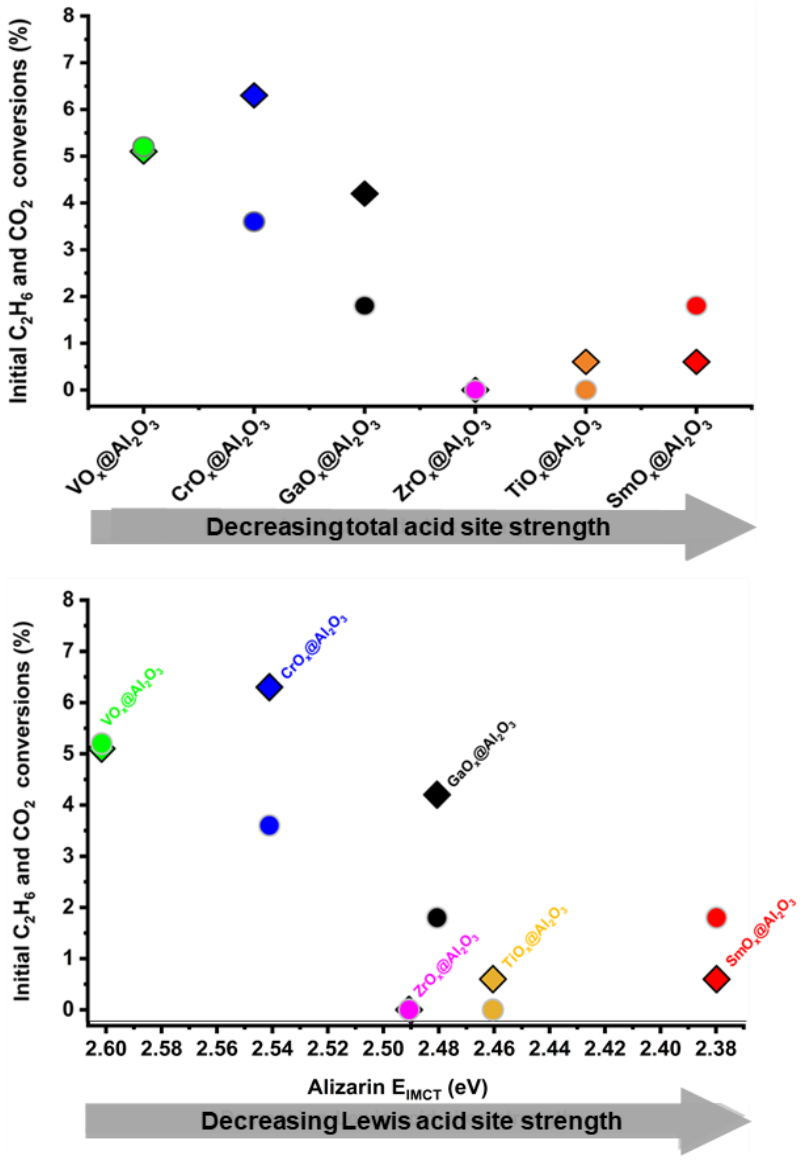

Figure 8.2: Extrapolated initial C_2H_6 (diamonds) and CO_2 (circles) conversions as a function of decreasing relative total (top) and Lewis (bottom) acid site strength of the various $MO_x@Al_2O_3$ overlayers during the reaction of C_2H_6 and CO_2 (6.25 mL/min each) diluted with 12.5 mL/min inert. The relative total acid strength used is based on the trend obtained via NH_3-TPD analysis while the Lewis acidity trend was obtained via DR-UV/Vis. Test conditions: temperature = 600 °C, pressure = 1 atm, space velocity = 15 $L \cdot h^{-1} \cdot g_{cat}^{-1}$, CO_2 : C_2H_6 ratio = 1.

Except for $ZrO_x@Al_2O_3$, this relationship is the same when the relative Lewis acid site strength, obtained *via* DR-UV/Vis of surface-adsorbed alizarin, is considered (see Figure 8.2, bottom).

The observed trend can be explained by the proposal by Ge *et al*. [249] suggesting that the surface basicity of a metal oxide (CeO_2/γ-Al_2O_3 in their case) plays a role in the activation of both C_2H_6 and CO_2. C_2H_6 is activated *via* H-abstraction which generates hydrogen atoms that further react with CO_2 *via* hydrogenation. This explains the initial activity of $TiO_x@Al_2O_3$ and $SmO_x@Al_2O_3$ which exhibit the weakest surface acidity. On the other hand, the decrease of the initial activity with the total and Lewis acid site strength in the order: $VO_x@Al_2O_3$ > $CrO_x@Al_2O_3$ > $GaO_x@Al_2O_3$ > $ZrO_x@Al_2O_3$ can be attributed to acid sites, deemed essential for the activation of light alkanes but, when too strong, induce cracking and coke formation [1,13,175,177,249].

In addition, the activity of these materials seemingly depends on their reducibility. While the H_2-TPR results (see Figure 5.4) imply that $GaO_x@Al_2O_3$ is unreducible, there might be some reduced $Ga^{+\delta}$ during dehydrogenation as suggested in a previous report for propane dehydrogenation over Ga-oxide supported on SiO_2 [301]. Considering this possibility, it is therefore understandable that only $VO_x@Al_2O_3$, $CrO_x@Al_2O_3$ and $GaO_x@Al_2O_3$ would be active while the unreducible $SmO_x@Al_2O_3$, $TiO_x@Al_2O_3$ and $ZrO_x@Al_2O_3$ are not. The general requirement of a redox property for materials to be active in the ODH reaction also supports this proposal. Alternatively, a previous study proposes that Ga-based systems are a special case undergoing CO_2-ODH *via* heterolytic dissociative adsorption for alkane activation followed by RWGS instead of the redox mechanism [250]. This mechanism is not reliant on material reducibility as the lattice oxygen species involved in alkane activation are not lost.

Except for $VO_x@Al_2O_3$, with CO_2 and C_2H_6 conversions balanced, CO_2 conversions for all overlayers are lower than C_2H_6 conversions demonstrating that these overlayers struggle with the activation of the oxygen source. This supports the initial proposal that this step is causing the low stability of oxide-based catalysts in the CO_2-ODH. The challenge of CO_2-activation can be overcome by adding another catalyst functionality to avail more sites for CO_2-activation as demonstrated by the addition of an Fe promoter which induced a RWGS functionality to a Cr-based DD catalyst [5]. Studies have also suggested that over certain metal oxides, CO_2-activation occurs on the same sites as C_2H_6-activation and has therefore a poisoning effect [124].

With increasing TOS, a progressive deactivation is observed as both the C_2H_6 and CO_2 conversions decrease rapidly (see Figure 8.1, top). Amongst the most active materials, a major loss of activity is measured for $VO_x@Al_2O_3$ which after the first 4 h TOS reaches C_2H_6 and CO_2 conversions of 1.8% and 1.3%, respectively, a more than 60% reduction compared to the initial conversions. At 4 h TOS, $CrO_x@Al_2O_3$ reaches C_2H_6 and CO_2 conversions of 3.1% and 1.3% (51% and 64% reduction), respectively, while $GaO_x@Al_2O_3$ reaches 3.2% and 1.0% (24% and 44% reduction), respectively, suggesting a better stability of $GaO_x@Al_2O_3$. The stability appears to correlate with the acid site strength of the metal oxides for these three samples. This could be rationalized with a reduced coke formation as a result of less cracking over strong acid sites. After 12 h TOS, no CO_2 conversion is recorded anymore, while some C_2H_6 activation functionality remains. This behaviour supports that indeed an MvK type mechanism is at play over these materials where the lack of efficient CO_2-activation functionality results in a gradual deactivation as the surface lattice oxygen species are depleted. The C_2H_6-activation functionality is also subsequently suppressed as the catalyst is reduced. The effect is also reflected in the CO_2 : C_2H_6 conversion ratio (see Figure 8.1, middle), which is below 1 (the stoichiometric ratio expected for a pure CO_2-ODHE) and progressively decreases with TOS suggesting insufficient or lost CO_2 activation ability.

A CO_2 : C_2H_6 conversion ratio greater than 1 would suggest an increased DRE activity and/or promotion of other CO-forming routes such as the reverse Boudouard and/or overoxidation reactions. Although the DRE reaction forms H_2 in addition to CO, the H_2 product was not considered for the interpretation of the data as it was Values below 1 could stem from an increased direct dehydrogenation (DD) activity and/or overoxidation reactions. For the acidic overlayers, a progressive decrease of the CO_2 : C_2H_6 conversion ratio with TOS is observed suggesting a shift towards DD and/or overoxidation. The observed apparent correlation between surface acidity and activity demonstrates that the surface acidity can be used to tune activity and stability and suggests that metal oxide catalysts should possess intermediate-to-strong total and Lewis acid sites in order to exhibit activity in the simultaneous conversion of CO_2 and C_2H_6. This is in line with literature reports describing oxide catalysts based on Cr, V and Ga as promising for CO_2-ODHE, with a Cr-based system also used industrially for the dehydrogenation of paraffins [9,11,174].

The selectivity of C_2H_4 and CO was calculated based on the total carbonaceous products (C_2H_4, CH_4 and CO) as detailed in section 4.4.9. Based on this, a completely CO_2-ODHE selective

catalyst can reach a maximum C_2H_4 selectivity of 67 C-% with a CO selectivity of 33 C-% (see Figure 8.1, bottom). A C_2H_4 selectivity above this value with a lower CO selectivity implies promotion of an additional C_2H_4-forming route (DD). C_2H_4 selectivity below this value with a higher CO selectivity can be explained through the presence of CO-forming routes such as DRE, overoxidation and/or the reverse Boudouard reaction. Since CO_2 is a soft oxidant, CO-formation *via* overoxidation is less likely.

C_2H_4 selectivity for the weakly acidic $TiO_x@Al_2O_3$ is constant with TOS at more than 90 C-%, at very low conversion levels, suggesting a DD mechanism. For $SmO_x@Al_2O_3$ the ethylene selectivity is below 67 C-% paralleled by an elevated CO formation at conversion ratios of CO_2 : C_2H_6 of 3 to 6 in the initial hour TOS. Note that for this material, only the data before 4 h TOS, where conversions are above zero, is considered. The selectivity for $ZrO_x@Al_2O_3$ could not be computed due to the low conversion levels attained resulting in very small amounts of products making their analysis unfeasible. The three acidic overlayers with considerable activity (*i.e.* $GaO_x@Al_2O_3$, $CrO_x@Al_2O_3$ and $VO_x@Al_2O_3$) show an increase of C_2H_4 selectivity with TOS and decreasing C_2H_6 and CO_2 conversions, associated to the progressive loss of CO_2-activation functionality. The C_2H_4 selectivity for $CrO_x@Al_2O_3$ and $GaO_x@Al_2O_3$ is initially close to 67 C-% (70 C-% and 66 C-%, respectively) while CO selectivity is close to 33 C-% (both at 27 C-%), suggesting an CO_2-ODHE dominant pathway. However, C_2H_4 selectivity increases significantly after 7 h TOS suggesting a shift towards the DD. In contrast, for $VO_x@Al_2O_3$, the initial C_2H_4 selectivity is about 53 C-% with 43 C-% CO selectivity. This suggests a promotion of additional CO-forming routes, most likely DRE and the reverse Boudouard reaction as coking is expected to be significant on strongly acidic oxides. For these three samples, the C_2H_4 and CO selectivity is accompanied by some CH_4 formation, attributed to a parallel cracking mechanism, which is initially below 6 C-% and decreases with TOS, further supporting the likelihood of coking (see Figure 10.4 in the Appendix). Interestingly, this cracking activity is more pronounced over the stable $GaO_x@Al_2O_3$ with least acidity compared to other strongly acidic overlayers. This can be explained by the fact that $GaO_x@Al_2O_3$ exhibits the strongest acid sites amongst all overlayer materials, albeit at low concentrations which are seemingly responsible for the cracking reaction (see NH_3-TPD in Figure 5.6). Note that the acidity ranking established was only based on the intermediate acid site strength without considering the strong acid sites due to their low concentration which would cause them to contribute less to the average acidity as observed *via* DR-UV/Vis studies. The deactivation of these sites is seemingly faster, probably due to coking which has a less significant poisoning effect on the sites responsible for C_2H_4-forming routes.

Alternatively, the CH_4 formation might be due to methanation of CO_x which is also feasible under these conditions especially because some H_2 was formed. Overall, the C_2H_4 selectivity increases with reducing acidity until a maximum is reached for $TiO_x@Al_2O_3$, at very low conversion levels, and then decreases for the basic $SmO_x@Al_2O_3$. The proposed CO-forming routes become more likely with increasing acidity. It is worth noting that the CO_2-activation functionality is not completely lost for most of these materials but rather decreases significantly and reaches levels that are difficult to quantify due to the unfeasible analysis of the very small change of CO_2 concentration during the reaction. This is supported by a measurable CO selectivity, which can only form *via* CO_2-entailing reactions.

After 24 h TOS, the materials were exposed to a flow of N_2 at 50 mL/min, cooled to 50 °C and then passivated by exposure to a stream of 1 vol.-% O_2 in N_2 at 50 mL/min. The retrieved spent catalysts were analysed using Raman spectroscopy and offline XRD (see Figure 8.3).

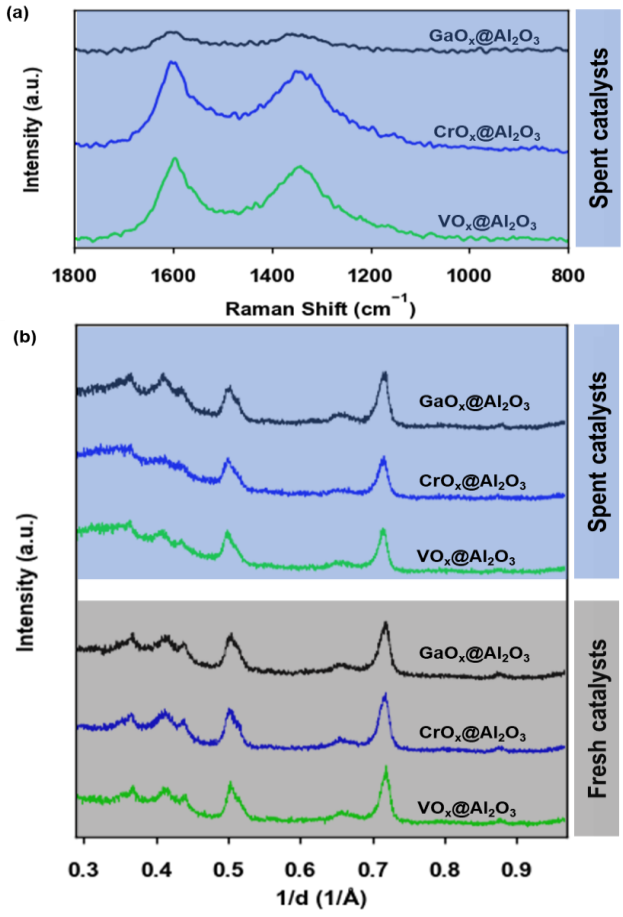

Figure 8.3: (a) Raman spectra and (b) XRD patterns of spent $MO_x@Al_2O_3$ overlayer catalysts after exposure to CO_2-ODHE conditions for 24 h. The XRD patterns of the fresh $MO_x@Al_2O_3$ overlayers are also included.

All the spent $MO_x@Al_2O_3$ exhibiting considerable activity show very little change in their respective diffraction patterns compared to the fresh materials after synthesis. An additional broad hump is observed between 0.3 and 0.4 $Å^{-1}$ which could be associated to the deposition of amorphous carbon. No new reflexes suggesting sintering and crystallite formation/growth of the overlayer materials are observed.

The Raman spectra of the spent $MO_x@Al_2O_3$ overlayers are characterized by two bands at 1600 cm^{-1} and 1350 cm^{-1} associated with the G- and D-bands of the sp^2-bond vibrations of carbon atoms. This confirms the deposition of carbonaceous species as suggested by XRD. Interestingly, this carbon is slightly less graphitic on $GaO_x@Al_2O_3$ which displays a better stability than the other materials with considerable activity under CO_2-ODHE conditions. With an increase of acidity to $CrO_x@Al_2O_3$ and $VO_x@Al_2O_3$, the carbon deposited becomes more graphitic and is paralleled, as previously discussed, with an enhanced deactivation [302]. This is based on the ratio of the D- to G- bands intensities (I_D/I_G) of 0.88 for $GaO_x@Al_2O_3$, which is lower than the 0.90 obtained for both $CrO_x@Al_2O_3$ and $VO_x@Al_2O_3$ (see Figure 10.5 in Appendix). It can be concluded that the deactivation observed for the overlayer materials in the CO_2-ODHE is, at least in part, associated to carbon deposition.

To counter the loss of activity over the $MO_x@Al_2O_3$ overlayers due to carbon deposition, CO_2-ODHE was also performed using a modified feed gas composition with a CO_2 (10.4 mL/min) : C_2H_6 (2.1 mL/min) molar ratio of 5 and an inert dilution of 50 vol.-% at atmospheric pressure and 600 °C for 24 h. [123]. The over-stoichiometric amount of CO_2 in the feed is expected to aid in the removal of the carbon deposits *via* the reverse Boudouard reaction as demonstrated in previous studies [9,11,146,174]. The overlayers were pre-treated in a stream of H_2 for 3 h at 500 °C mimicking the reduction of the oxidic Fe_xNi_y precursors to an alloy in subsequent experiments. Under these CO_2-ODHE conditions, a thermodynamic equilibrium conversion limit of C_2H_6 of 61.9% for CO_2-ODHE and 52.4% for DRE is calculated.

The conversions obtained under this modified feed ratio are unsuitable for direct comparison with those from the equimolar feed as CO_2 conversions are significantly lower while C_2H_6 conversions are higher merely due to the change of composition (see Figure 10.7 in the Appendix). Since there is a significantly higher amount of CO_2 in the feed, a lower percentage of CO_2 converted is expected. To circumvent this, the molar flow rates of CO_2 and C_2H_6 converted are reported to allow for better comparison with the results obtained under the equimolar feed (see Figure 8.4).

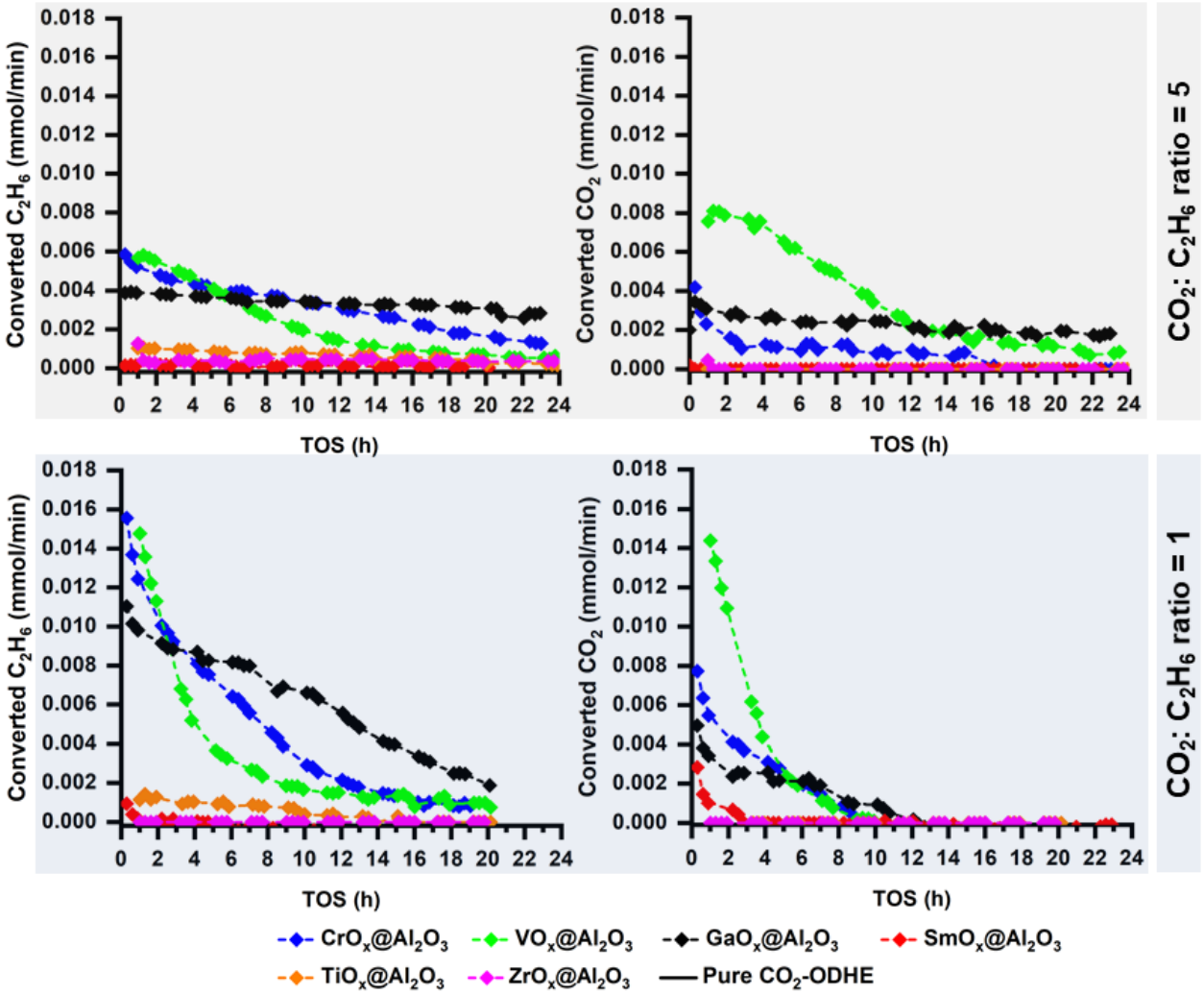

Figure 8.4: Converted C_2H_6 and CO_2 flow rates obtained during CO_2-ODHE under a feed with a CO_2 (10.4 mL/min) : C_2H_6 (2.1 mL/min) molar ratio of 5 (top) as well as under a feed with CO_2 (6.25 mL/min) : C_2H_6 (6.25 mL/min) molar ratio of 1 (bottom) both with an inert dilution of 12.5 ml/min over the various $MO_x@Al_2O_3$ overlayers. Conditions: temperature = 600 °C, pressure = 1 atm and total space velocity = 15 $L \cdot h^{-1} \cdot g_{cat}^{-1}$.

The overall trend of increasing initial activity (*i.e.* rates of C_2H_6 and CO_2 converted) with increasing total and Lewis acid site strength of the overlayers is still observed (see Figure 8.4, top). However, unlike in the equimolar feed, the overlayer with the weakest acid sites, $SmO_x@Al_2O_3$, has negligible activity for both CO_2-ODHE and DRE just as $ZrO_x@Al_2O_3$. The weakly acidic $TiO_x@Al_2O_3$ still displays only C_2H_6-activation, at a very low level with nearly no CO_2-activation functionality. The more acidic $GaO_x@Al_2O_3$, $CrO_x@Al_2O_3$ and $VO_x@Al_2O_3$, still exhibit considerable initial rates of C_2H_6 conversion of up to 0.0040, 0.0060 and 0.0060 mmol/min with corresponding rates of CO_2 conversion of 0.0033, 0.0042 and 0.0080 mmol/min, respectively. Compared to the equimolar feed, an improved CO_2-activation ability is observed. The initial rates of CO_2 converted in the equimolar feed are nearly half the initial rates of C_2H_6 converted for

$GaO_x@Al_2O_3$ and $CrO_x@Al_2O_3$ while they are about equal for $VO_x@Al_2O_3$ (see Figure 8.4, bottom). Despite this enhancement, the absolute amount of CO_2 and C_2H_6 converted is lower in the CO_2-rich feed in the initial 6 h TOS.

With increasing TOS, a progressive deactivation which is slower than in the equimolar feed is observed. The rate of deactivation increases with increasing acid site strength of the overlayers as previously discussed for the equimolar feed. However, compared to the equimolar feed where the CO_2-activation functionality is lost within 12 h TOS for all materials, this functionality is sustained, albeit its rate of deactivation is still higher compared to C_2H_6. This suggest, an enhanced catalyst stability which might be attributed to an improved catalyst re-oxidation and the reverse Boudouard reaction, suppressing/reducing carbon deposition.

At the start of the reaction, the C_2H_4 yields increase with surface acid site strength (see Figure 8.5, top). Compared to the equimolar feed (see Figure 8.1, middle) the ratios of converted CO_2 : C_2H_6 are higher and more stable with TOS. DD of C_2H_6 seems supressed as evidenced by the lower C_2H_4 selectivity and increased CO selectivity. It is not possible to assign this enhanced CO-formation to a single reaction based on the data available and it could be a result of enhanced CO_2-ODHE, the reverse Boudouard reaction, catalyst re-oxidation, DRE and the RWGS.

For $GaO_x@Al_2O_3$, the fraction of converted CO_2 : C_2H_6 is closest to the theoretical value of 1 for pure CO_2-ODHE. The C_2H_4 and CO selectivity are also closest to the theoretical values for pure CO_2-ODHE. These parameters suggest that the enhanced CO_2-activation improves the RWGS reaction which reduces the DD activity observed in the equimolar feed resulting in an overall improved CO_2-ODHE activity. The enhanced stability of this material and the initial decrease of CO selectivity coupled with the increase of C_2H_4 selectivity imply that the presence of the reverse Boudouard reaction, limiting coking, and other CO-forming routes cannot be excluded. Interestingly, cracking, attributed to the presence of a low population of very strong acid sites, is slightly enhanced compared to the equimolar feed for this material while it is lower for the other bare overlayers (see Figure 10.6 in the Appendix). A similar behaviour is recorded for $CrO_x@Al_2O_3$ which is however characterized by a lower degree of enhancement of the CO_2-activation functionality resulting in a ratio of converted CO_2 : C_2H_6 of below 1. While $TiO_x@Al_2O_3$ shows some performance, CO_2-activation functionality is much lower and the analysis of CO_2 converted was unfeasible.

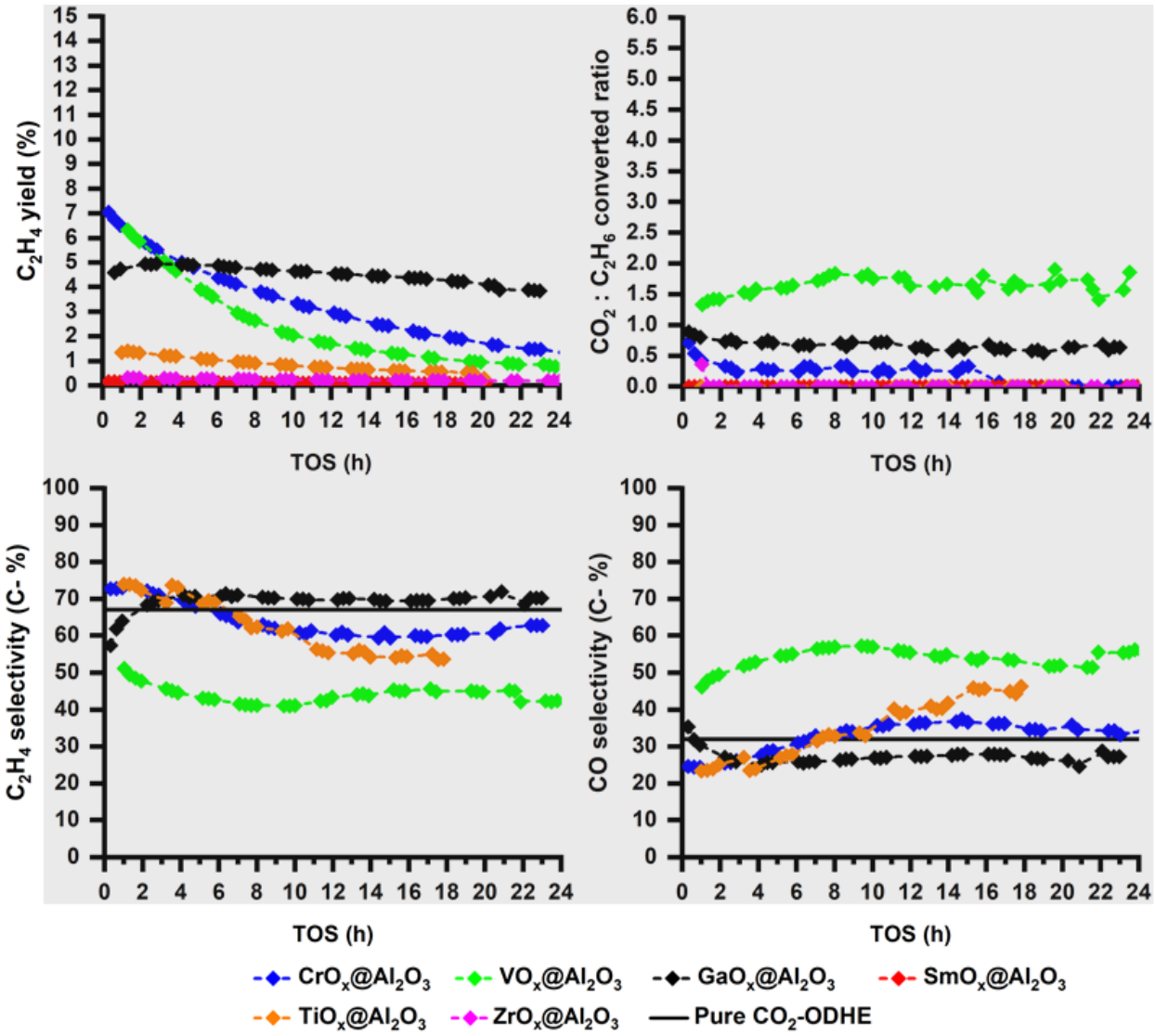

Figure 8.5: C_2H_4 yields and converted CO_2 : C_2H_6 flow rates ratios (top) as well as C_2H_4 and CO selectivity (bottom) obtained during the reaction of C_2H_6 (2.1 mL/min) and CO_2 (10.4 mL/min) diluted with an inert (12.5 mL/min) over the various $MO_x@Al_2O_3$ overlayers. Conditions: temperature = 600 °C, pressure = 1 atm, space velocity = 15 $L \cdot h^{-1} \cdot g_{cat}^{-1}$, CO_2: C_2H_6 ratio = 5. Maximum possible carbon based C_2H_4 and CO selectivity for pure CO_2-ODHE are indicated by the black solid lines.

For $VO_x@Al_2O_3$, the ratio of converted CO_2 : C_2H_6 is above 1 (almost 1.5) and stable with TOS due to the higher degree of CO_2-activation. This is complemented by an overall decreased C_2H_4 selectivity which is below the maximum for pure CO_2-ODHE with a higher CO selectivity most likely due to DRE and the reverse Boudouard reaction. Despite these differences, the C_2H_4 and CO selectivity still scales with acidity as discussed for the equimolar feed, with the exclusion of $TiO_x@Al_2O_3$.

These observations suggest that a higher CO_2 : C_2H_6 molar ratio in the feed results in improved C_2H_6 conversions as well as CO_2-activation ability which is also sustained, compared to the equimolar feed. However, the overall C_2H_4 selectivity is reduced due to minimal DD activity which is suppressed/surpassed by the CO-forming routes increasing CO selectivity (likely RWGS, reverse Boudouard reaction, DRE and catalysts re-oxidation). This results in an overall dominant CO_2-ODHE activity over $GaO_x@Al_2O_3$, $CrO_x@Al_2O_3$ and $TiO_x@Al_2O_3$ and enhanced DRE compared to the equimolar feed. Thus, in addition to the overlayer acid site strength, the feed composition also influences the overall reaction pathways through which the C_2H_4 and CO products form making the acidity a design parameter for CO_2-ODHE catalysts.

After 24 h TOS, these materials were exposed to a flow of inert N_2 at 50 mL/min, cooled to 50 °C and then passivated by exposure to a stream of 1 vol.-% O_2 in N_2 at 50 mL/min. The retrieved spent catalysts that exhibited considerable activity were analysed using Raman spectroscopy (see Figure 8.6, bottom). Similar to the equimolar feed, the Raman spectra of the spent overlayers in the over-stoichiometric feed are characterized by two bands at 1600 cm^{-1} and 1350 cm^{-1} associated to the G- and D-bands of the sp^2-bond vibrations of carbon atoms confirming surface carbon deposition. This carbon deposition does not seem to exhibit a correlation with acid site strength as well as the I_D/I_G band ratio (see Figure 10.8 in Appendix) but could be least significant on $GaO_x@Al_2O_3$, as it shows a better stability. Relying on the stability suggests that, with a further increase or decrease of the acid site strength, carbon deposits increase. This results clearly demonstrate that coke deposition still contributes to the loss of activity observed. While unreliable, it is noteworthy that compared to the equimolar feed (see Figure 8.6, top), the intensity of the Raman bands obtained under this feed is lower which could be a result of reduced carbon deposits or experimental parameters during Raman.

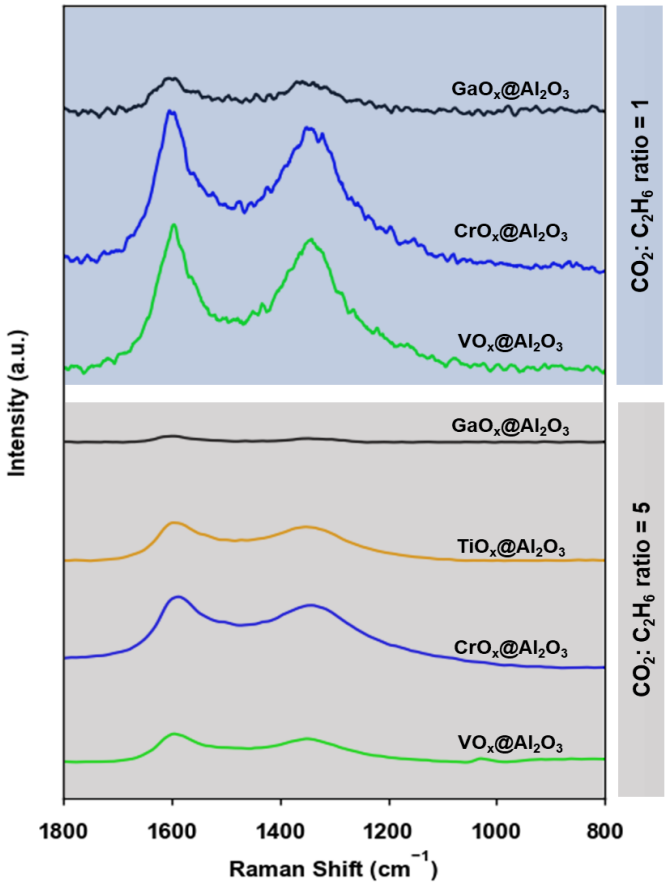

Figure 8.6: Comparison of the Raman spectra of the spent bare $MO_x@Al_2O_3$ overlayer catalysts after exposure to CO_2-ODHE conditions for 24 h in an equimolar (top) and the over-stoichiometric amount of CO_2 (bottom) feeds. The samples from the equimolar feed were analysed in a RENISHAW spectrometer while those from the feed with $CO_2 : C_2H_6$ ratio of 5 were analysed in a WITec Confocal Raman Microscope.

The results presented clearly show that the activity, selectivity and stability of metal oxides depend strongly on the combination of the reducibility, acid site strength and the feed composition. Only the reducible overlayers display activity while the unreducible overlayers are mostly inactive. $GaO_x@Al_2O_3$ is assumed to be a special case, partially reducible under reaction conditions despite being unreducible under H_2-TPR conditions as suggested by Saito *et al*. [301]. Alternatively, $GaO_x@Al_2O_3$ is reported to undergo CO_2-ODHE *via* the heterolytic dissociative adsorption of C_2H_6 followed by RWGS instead of the typical redox pathway and may thus, show activity [250].

The acid site strength influences the initial activity, selectivity and catalyst stability. Stronger acid sites result in the highest initial activity, lowest C_2H_4 selectivity and a fast deactivation, probably due to enhanced cracking leading to carbon deposition and limited provision of surface oxygen

species. Under the equimolar feed, CO_2-activation is limited and carbon deposition is more prevalent. An over-stoichiometric amount of CO_2 in the feed improves and sustains the CO_2-activation functionality possibly due to enhanced reverse Boudouard reaction, DRE, re-oxidation and hydrogen removal (RWGS) yielding overall performances closer to ideal CO_2-ODHE (except for $VO_x@Al_2O_3$). The elevated CO_2-activation functionality also allows sustained C_2H_6-activation and improved catalyst stability. The model catalysts still deactivate, most significantly the reducible and strongly acidic $CrO_x@Al_2O_3$ and $VO_x@Al_2O_3$, and a further enhancement of the CO_2-activation might result in an overall improved catalytic performance.

8.2 Iron-nickel nano-alloys anchored on metal oxide overlayers: Effect of the nano-alloy metallic composition and the overlayer

It is proposed that the Fe_xNi_y nano-alloys in the formulations presented in Chapter 7 will improve activity and stability of the overlayer materials by enhancing the catalyst's CO_2-activation ability. This will enhance the provision of surface oxygen species both for the removal of hydrogen yielding water and for the replenishment of the overlayer oxygen vacancies in a Mars van Krevelen-type C_2H_6-activation. These Fe_xNi_y nano-alloys have already demonstrated CO_2-activation ability as discussed in Chapter 7. Based on those studies, the degree CO_2-activation on Fe_xNi_y nano-alloys is a function of crystal structure which in turn is a function of Fe : Ni atomic ratio and reduction temperature. It remains essential to understand the efficiency of CO_2-activation under CO_2-ODHE conditions, *i.e.* in the presence of C_2H_6 as a reducing agent.

The Fe_xNi_y oxidic precursors, TT1.1, TT1.3 and TT1.5, with ICP-based Fe : Ni atomic ratios of 1.2, 2.5 and 4.4 (see Table 6.2 in Chapter 6) were anchored on the $CrO_x@Al_2O_3$ and $ZrO_x@Al_2O_3$ overlayers. $CrO_x@Al_2O_3$ is reducible with strong surface acid sites and exhibits considerable initial CO_2 and C_2H_6 activity followed by a progressive deactivation when tested bare (see Figure 8.1,top). On the other hand, $ZrO_x@Al_2O_3$ is unreducible with weaker surface acid sites and shows no intrinsic activity under CO_2-ODHE conditions. All samples as well as the bare overlayers were tested for CO_2-ODHE under an equimolar feed of CO_2 (6.25 mL/min) and C_2H_6 CO_2 (6.25 mL/min) with an inert dilution of 50 vol.-% (12.5 mL/min) at atmospheric pressure and 600 °C after reduction in H_2 for 3 h at 500 °C (see Figure 8.7 and Figure 8.8). For clarity, the $MO_x@Al_2O_3$-supported TT1.1, TT1.3 and TT1.5 samples tested are presented as $Fe_1Ni_1/MO_x@Al_2O_3$, $Fe_3Ni_1/MO_x@Al_2O_3$ and $Fe_5Ni_1/MO_x@Al_2O_3$, on the basis of the target atomic compositions of the alloy phase.

The presence of Fe_xNi_y nano-alloys on the $ZrO_x@Al_2O_3$ overlayer hardly increases the C_2H_6 conversion (< 1%) but a considerable initial CO_2 conversion is observed with a rapid deactivation over 2 to 3 h (see Figure 8.7, top). This behaviour is probably due to active site transformation *via* re-oxidation of the reduced Fe_xNi_y nano-alloys. While the conversions are very low, the C_2H_4 yields as well as the CO and C_2H_4 selectivity of these $Fe_xNi_y/ZrO_x@Al_2O_3$ catalysts could be computed. For all $Fe_xNi_y/ZrO_x@Al_2O_3$ catalysts, the C_2H_4 selectivity is initially between 20 and 30 C-%. While $Fe_1Ni_1/ZrO_x@Al_2O_3$ shows no change in selectivity, samples with higher Fe-content in the alloy show an increase in C_2H_4 selectivity in the first 20 h TOS to 50 and 65 C-% for

$Fe_3Ni_1/ZrO_x@Al_2O_3$ and $Fe_5Ni_1/ZrO_x@Al_2O_3$, respectively (see Figure 8.7, bottom). While the increase in selectivity is in parallel to the decrease in CO_2-activation functionality, the rates of change are not comparable. The opposite trend is observed in terms CO selectivity with TOS. Thus, CO-forming routes (probably DRE in parallel with the initial Fe_xNi_y nano-alloy re-oxidation) are initially dominant over these materials. The increase of C_2H_4 and corresponding decrease of CO selectivity with TOS on the Fe-rich $Fe_5Ni_1/ZrO_x@Al_2O_3$ and $Fe_3Ni_1/ZrO_x@Al_2O_3$ is probably due to these CO-forming routes becoming less dominant while the C_2H_4-forming routes (DD or CO_2-ODHE) remain stable as evidenced by the constant C_2H_4 yields. This may suggest, the deactivation of active sites for the CO-forming routes on the Fe-rich samples. The CO and C_2H_4 selectivity of $Fe_1Ni_1/ZrO_x@Al_2O_3$ are not affected by the initial CO_2-activation ability which is higher than over the Fe-rich samples, suggesting constant promotion of CO-forming DRE. While it is still not fully understood, the initial CO_2-activation over the Fe-rich samples is ascribed to the re-oxidation of the alloy's bcc phase whereas on the Ni-rich catalyst it is probably due to the inherent ability of Ni or the fcc alloy phase to promote DR. The DR activity of the Ni-rich Fe_xNi_y alloy was also observed in a study by Chen *et al*. [212] but focusing on DRM. Other studies also support this for DR of ethane, propane and butane with Ni-support interfaces proposed to be responsible for the activity in addition to the sites on the fcc Ni-rich Fe_xNi_y alloy [17,62,209,211].

The low C_2H_6 activity/high C_2H_4 selectivity behaviour is in stark contrast to the previously described behaviour of Fe_3Ni_1/ZrO_2 reported by Chen *et al*. [18], which was characterised by a high initial DRE activity (CO_2 conversion > 25%) and deactivation *via* coking over 14 h TOS. The differences might be due to the different preparation techniques employed for the Fe_xNi_y catalysts. While Chen *et al*. [18] employed simultaneous impregnation and relied on the reduction process to yield the alloy, the surfactant-free hydrothermal method employed here, allows to synthesize oxidic $(Ni_xFe_{1-x})Fe_2O_4$ inverse spinel phases as alloy precursors. It also needs to be noted that the $ZrO_x@Al_2O_3$ overlayer differs in physicochemical characteristics from a bulk ZrO_2 which allowed high dispersion of the proposed Ni-ZrO_2 DRE active sites which are prone to coking. While it was not discussed in detail, the poor activity of an Fe_3Ni_1 alloy with a higher CO_2 than C_2H_6 conversion on an inert and unreducible support (SiO_2) was also observed [18].

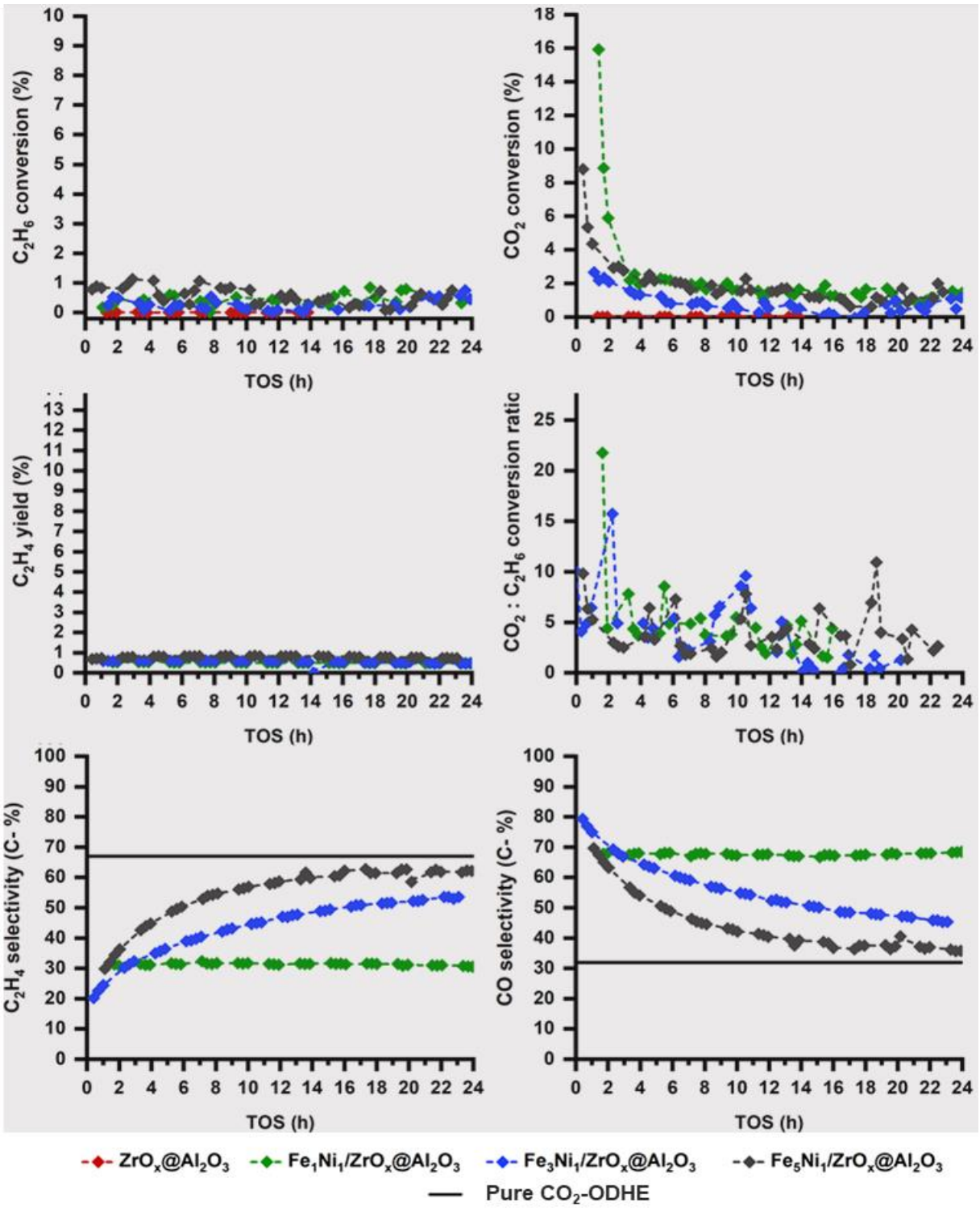

Figure 8.7: C_2H_6 and CO_2 conversions (top), C_2H_4 yield and CO_2: C_2H_6 ratio (middle) as well as carbon based C_2H_4 and CO selectivity (bottom) obtained during reaction of C_2H_6 (6.25 mL/min) and CO_2 (6.25 mL/min) with an inert dilution of 50 vol.-% (12.5 mL/min) over the bare overlayer and the various $Fe_xNi_y/ZrO_x@Al_2O_3$ catalysts. Conditions: temperature = 600 °C, pressure = 1 atm, space velocity = 15 $L \cdot h^{-1} \cdot g_{cat}^{-1}$, $CO_2 : C_2H_6$ ratio = 1. Maximum possible C_2H_4 and CO selectivity for a pure CO_2-ODHE are indicated by the black solid lines.

The deposition of the Fe_xNi_y nano-alloys onto the acidic and reducible $CrO_x@Al_2O_3$ has a significant impact on activity, stability and selectivity compared to the bare overlayer and the $Fe_xNi_y/ZrO_x@Al_2O_3$ catalysts presented above (see Figure 8.8). The fact that the Fe_xNi_y nano-alloys have a strong impact on catalytic performance on this reducible support compared to the unreducible $ZrO_x@Al_2O_3$ strongly suggests the presence of a bifunctional/tandem catalyst system. In the suggested mechanism, C_2H_6 is activated on the reducible $CrO_x@Al_2O_3$ and CO_2 is dissociated on the Fe_xNi_y nano-alloy sites, with the generated oxygen species spilling-over to the partially reduced $CrO_x@Al_2O_3$ to facilitate its re-oxidation. In addition to the DR sites mentioned above, Chen *et al*. [209,226] also suggested that the activation of both C_2H_6 and CO_2 in the CO_2-ODHE reaction occurs on the same active site. This site is proposed to be the interface between metallic Ni or a Ni-rich fcc alloy phase and exsoluted amorphous Fe-oxide forming on the support under reaction conditions. The formation of either sites was found to be influenced by the support and Fe : Ni atomic ratio. While a partial oxidation of the bcc or Fe-rich phase could be confirmed in the present study (see Figure 8.9 (b)), the insignificant activity enhancement on $Fe_xNi_y/ZrO_x@Al_2O_3$ suggests, the proposed interfacial site between metallic Ni/Ni-rich alloy and an amorphous Fe-oxide alone cannot sustain the CO_2-ODHE.

The addition of the Fe-rich Fe_5Ni_1 nano-alloy has only little effect on the C_2H_6 conversion but increases the initial CO_2 conversion, probably due to re-oxidation (see Figure 8.8, top). After 5 h TOS, the CO_2 conversion approaches the one of the bare overlayer. However, compared to $CrO_x@Al_2O_3$ both the conversion ratio and the C_2H_4 and CO selectivity over $Fe_5Ni_1/CrO_x@Al_2O_3$ suggest a higher contribution of CO_2-ODHE and less DD (see Figure 8.8, middle and bottom). This is supported by a stable C_2H_4 and CO selectivity which is closer to the CO_2-ODHE optimum of 67 C-% and 33 C-% respectively (see Figure 8.8, bottom). The catalyst follows the deactivation trend of the bare $CrO_x@Al_2O_3$ albeit without ever fully loosing activity.

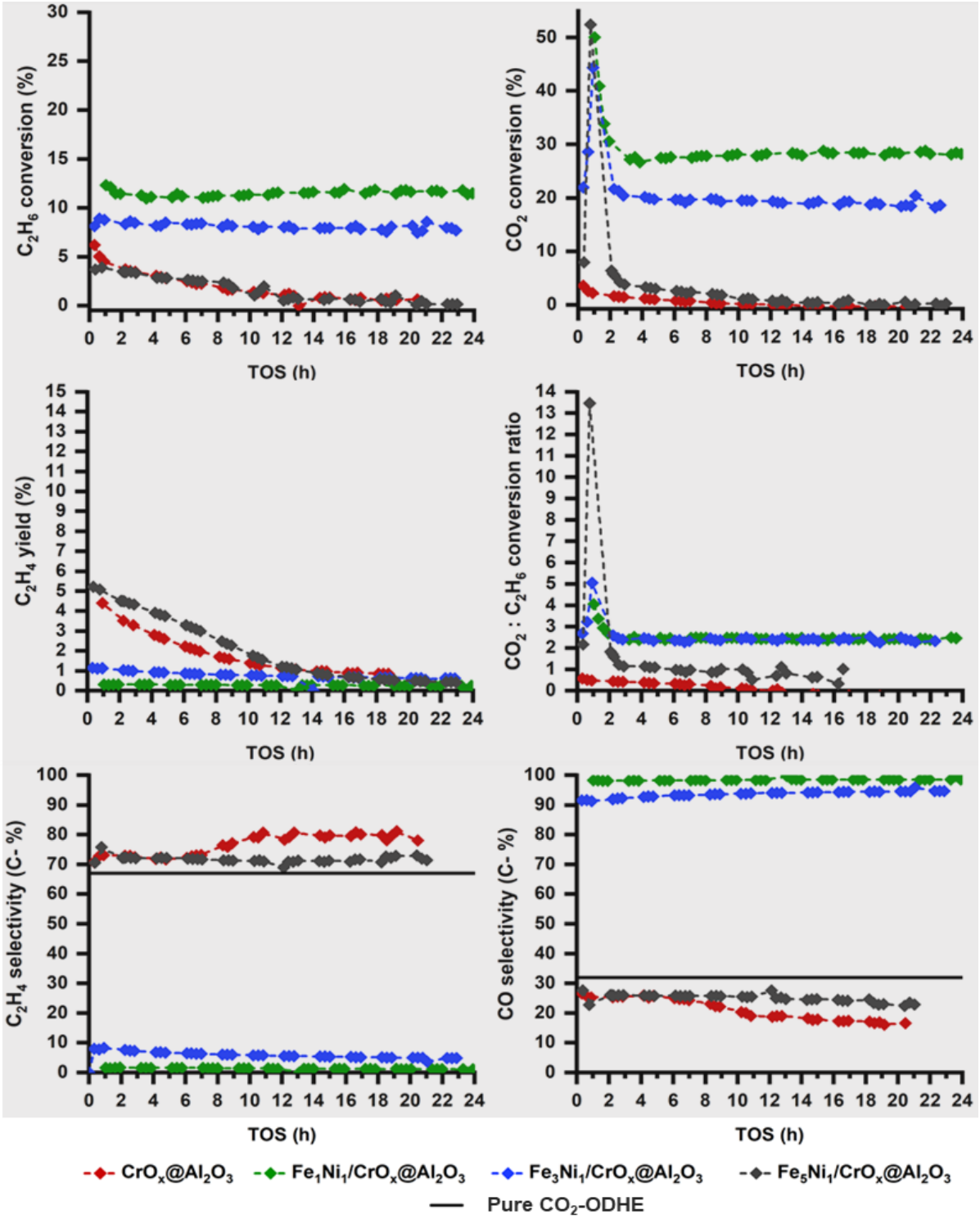

Figure 8.8: C_2H_6 and CO_2 conversions (top), C_2H_4 yield and CO_2: C_2H_6 ratio (middle) as well as carbon based C_2H_4 and CO selectivity (bottom) obtained during reaction of C_2H_6 (6.25 mL/min) and CO_2 (6.25 mL/min) with an inert dilution of 50 vol.-% (12.5 mL/min) over the bare overlayer and the various $Fe_xNi_y/CrO_x@Al_2O_3$ catalysts. Conditions: temperature = 600 °C, pressure = 1 atm, space velocity = 15 $L \cdot h^{-1} \cdot g_{cat}^{-1}$, $CO_2 : C_2H_6$ ratio = 1. Maximum possible C_2H_4 and CO selectivity for a pure CO_2-ODHE are indicated by the black solid lines.

The C_2H_4 yield of > 4% in the first 2 h TOS is amongst the highest reported for a Fe_xNi_y system in the CO_2-ODHE reaction. Interestingly, increasing the Ni content in the Fe_xNi_y nano-alloy catalyst formulation both increases and stabilizes the C_2H_6 and CO_2 conversions. This effect is more pronounced on CO_2 conversion resulting in a CO_2 : C_2H_6 conversion ratio about 2.5 after 2 h TOS which is slightly above the DRE ratio of 2. Thus, while the selectivity to C_2H_4 clearly drops with increasing Ni content and the CO selectivity from CO-forming routes other than CO_2-ODHE increases, the proceeding reaction is not pure DRE. 5 to 8 C-% C_2H_4 selectivity equating to 0.2 to 1.5 C-% C_2H_4 yield is retained for the duration of the experiment over $Fe_3Ni_1/CrO_x@Al_2O_3$ and $Fe_1Ni_1/CrO_x@Al_2O_3$, respectively.

A potential pathway accounting for the higher CO_2 conversion and the CO_2 : C_2H_6 conversion ratio as well as CO selectivity, beyond the maximum for DRE and CO_2-ODHE, is the reverse Boudouard reaction. This reaction has been previously postulated to hold the potential to counter catalyst deactivation *via* coke gasification [9,11,146,174]. In a simplified reaction network of CO_2-ODHE, DRE and the Boudouard reaction, approximately 20% of the CO_2 conversion would be the result of the carbon gasification reaction on these Ni-rich catalysts. While no direct evidence for the reverse Boudouard reaction is available, the stability of both conversion and product composition of $Fe_3Ni_1/CrO_x@Al_2O_3$ and $Fe_1Ni_1/CrO_x@Al_2O_3$ supports the absence of a strong deactivation mechanism.

Based on the results presented, it is clear that both the metal oxide overlayer and the Fe_xNi_y nano-alloy are complementary pieces in a tandem catalytic conversion of CO_2 and C_2H_6 *via* CO_2-ODHE to form C_2H_4 and DRE to form *syngas*. Depending on its chemical properties (*i.e.* interlinked reducibility and surface acid site strength), the metal oxide has a significant influence on the overall bifunctional catalyst activity while the Fe_xNi_y nano-alloy significantly influences the activity, reaction pathway (selectivity) and catalyst stability depending on the Fe : Ni atomic ratio. This is demonstrated by the fact that the Fe_xNi_y nano-alloy has a minimal effect on the overall activity, irrespective of composition, when anchored onto the unreducible $ZrO_x@Al_2O_3$ with weaker acid sites. On the reducible $CrO_x@Al_2O_3$ with stronger acid sites, the alloy is able to assist the overlayer resulting in enhanced Fe : Ni atomic ratio-dependant catalytic performance (activity, stability and selectivity). As proposed, the role of the Fe_xNi_y nano-alloy is seemingly to enhance CO_2-activation which avails oxygen species that, possibly *via* a spill-over type mechanism, re-oxidise the $CrO_x@Al_2O_3$ reduced upon C_2H_6 activation. The effect of alloy composition over $CrO_x@Al_2O_3$ on activity is in stark contrast to the results obtained from the temperature-

programmed CO_2-activation studies on KIT-6 reported in Chapter 7. In these experiments, a higher degree of CO_2-activation is associated to an Fe-rich Fe_5Ni_1/KIT-6 which has a larger fraction of the bcc phase of the Fe_xNi_y alloy after reduction. Under the CO_2-ODHE conditions, significantly enhanced CO_2-activation and catalyst activity and stability as well as CO formation *via* DRE are observed with increasing Ni content and thus, the fcc phase in the Fe_xNi_y nano-alloys. Therefore, the fcc phase in the Fe_xNi_y nano-alloys likely promotes CO_2-activation *via* the DRE pathway. This is not unexpected as Ni-based systems are known for their DR activity, especially DRM, and probably also explains the high DRM activity and stability of the Ni-rich $Fe_1Ni_4/Mg_xAl_yO_z$ reported by Müller *et al.* [212]. As explained in the case of $ZrO_x@Al_2O_3$ above, studies by Chen *et al*. [17,62,209,211] also support this conclusion for DR of ethane, propane and butane. The Fe_xNi_y alloy involved in those studies is the fcc allotrope as reduced Ni-rich Fe_xNi_y alloys can only exist in fcc phase according to the alloy equilibrium phase diagram (see Figure 2.17 in Chapter 2) and as observed in this current study [223]. On the Fe-rich samples, Chen *et al*. [209,226] proposed the interface between metallic Ni or a Ni-rich fcc alloy phase and exsoluted amorphous Fe-oxide forming on the support as the active sites for CO_2-ODHE. This exsolution of Fe behaviour was also proposed on FePd alloys for CO_2-ODHE [226] and on Fe_xNi_y alloys under RWGS [125] conditions. Whether this holds in this study is uncertain at this stage but our observations suggest the CO_2-ODHE activity emanates from enhanced CO_2-activation and minimised DD activity as a result of the presence of high fractions of the alloy bcc phase in Fe-rich samples. Thus, the crystallographic phases (fcc or bcc) of the Fe_xNi_y nano-alloys supported on $CrO_x@Al_2O_3$ overlayer play a crucial role on the reaction pathways promoted during conversion of CO_2 and C_2H_6.

The spent catalysts were retrieved from the fixed bed reactor after a 24 h TOS and studied with offline XRD (see Figure 8.9). Both overlayers are unaffected while the anchored Fe_xNi_y nano-alloys show significant crystallographic phase and size changes. In all cases, the Fe- and Ni-containing phases are present in the form of an fcc Fe_xNi_y nano-alloy and the oxidic inverse spinel structure (see Figure 8.9 (a) and (b)). No $Ni(OH)_2$ or NiO phase is detected. The relative phase composition reflects the trends observed for Fe_xNi_y nano-alloys anchored on KIT-6 in temperature-programmed CO_2 activation studies (see Chapter 7). No bcc metallic phase of the Fe_xNi_y nano-alloy is detected and an increasing amount of the oxidic inverse spinel structure with increasing Fe concentration is observed. This suggests re-oxidation of the alloy as proposed above and in literature [209,226]. However, this re-oxidation is seemingly limited to the bcc phase of the alloy. This trend is also largely independent of the nature of the metal oxide onto which the

Fe_xNi_y nano-alloy is anchored. It is proposed that under the applied CO_2-ODHE conditions, independent of the significant concentration of the reducing agents CO and C_2H_6, the bcc phase of the Fe_xNi_y nano-alloy re-oxidises while the fcc phase is unaffected. This possibly supports that the DRE activity is due to this fcc phase and the CO_2-ODHE activity due to the bcc phase which deactivates with TOS upon re-oxidation. More experiments will have to be conducted to shed more light into these relationships.

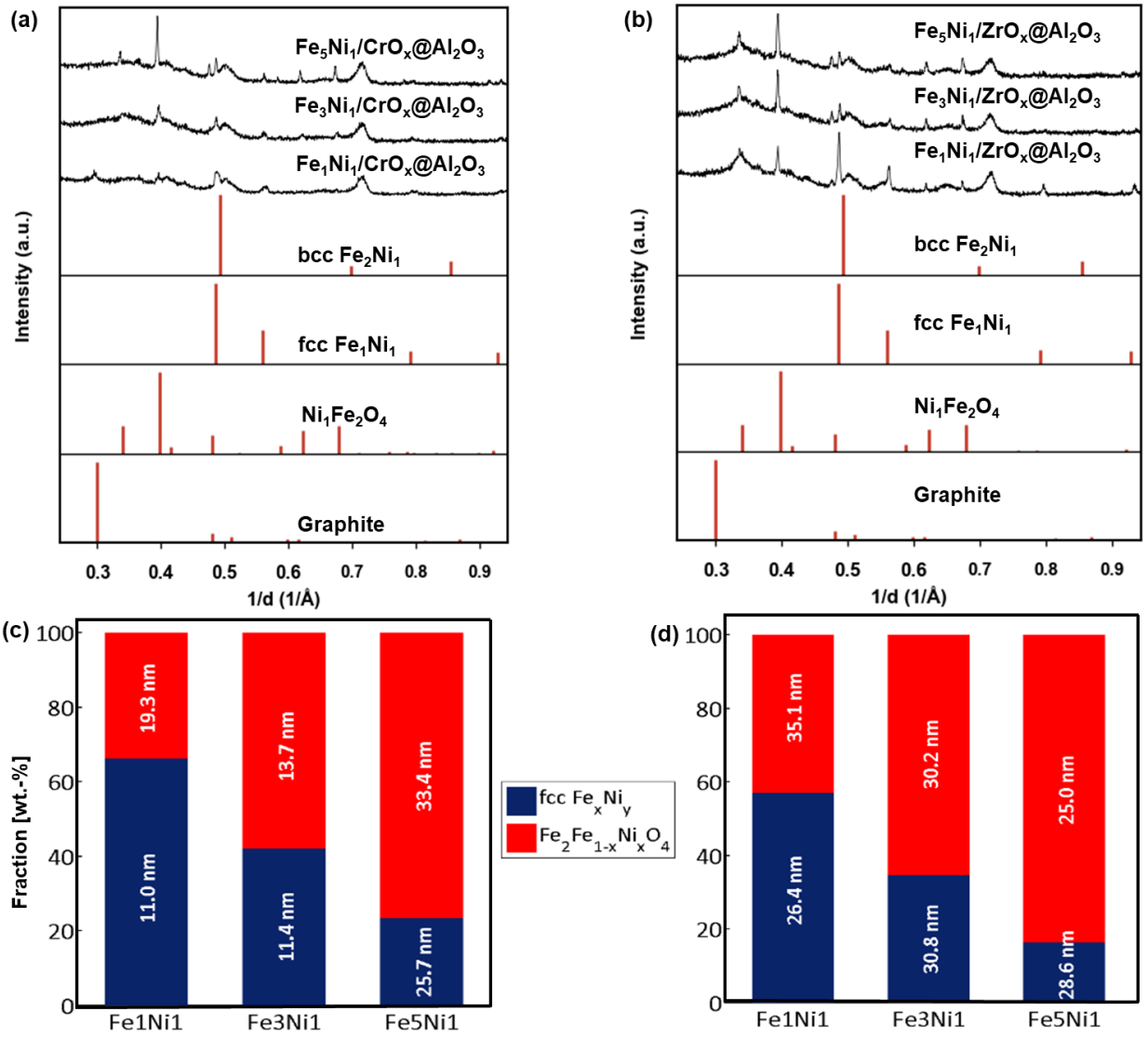

Figure 8.9: Stacked offline XRD patterns of spent Fe_xNi_y nano-alloy catalysts, anchored onto $CrO_x@Al_2O_3$ (a) and $ZrO_x@Al_2O_3$ (b) overlayers, after exposure to CO_2-ODHE conditions for 24 h. Crystallographic structural compositions of the Fe- and Ni- containing phases and the associated average crystallite sizes of the spent Fe_xNi_y nano-alloy catalysts anchored onto $CrO_x@Al_2O_3$ (c) and $ZrO_x@Al_2O_3$ (d) overlayers calculated via Rietveld refinement. The reference patterns provided correspond to graphite (PDF-4 01-073-5918), $NiFe_2O_4$ (PDF-4 04-014-8286), fcc Fe_1Ni_1 (PDF-4 04-003-3531) and bcc Fe_2Ni_1 (PDF-4 04-018-7295).

Clear differences can be observed when comparing the crystallite sizes of the different Fe_xNi_y nano-alloy phases. While $Fe_1Ni_1/CrO_x@Al_2O_3$ and $Fe_3Ni_1/CrO_x@Al_2O_3$ show only a minor degree of sintering when compared to the freshly reduced state, $Fe_5Ni_1/CrO_x@Al_2O_3$ as well as all the Fe_xNi_y nano-alloy catalysts anchored on $ZrO_x@Al_2O_3$ display a significant increase in crystallite size (see Figure 8.9 (c) and (d)). Although the increased sintering on $ZrO_x@Al_2O_3$ may be associated to a potential weaker interaction of the Fe_xNi_y nano-alloy with the overlayer due to its unreducible nature, all the samples which underwent sintering show low C_2H_6 and CO_2 conversion but high C_2H_4 selectivity. While, Chen *et al.* have shown for their Fe_3Ni_1/CeO_2 system that the effect of different conversion levels in the CO_2-ODHE on C_2H_4 selectivity is small [18,62], to confirm a causal relation between the observed selectivity and crystallite size in the spent catalysts requires further targeted investigations.

Raman analysis was performed to investigate the presence of carbon or carbonaceous species (see Figure 8.10 (a) as well as Figure 10.10 and Figure 10.11 in Appendix). The Raman spectra are characterized by two bands at about 1600 cm^{-1} and 1350 cm^{-1} associated with the G- and D-bands of the sp^2-bond vibrations of carbon atoms confirming the deposition of carbonaceous species. While Raman analysis is unreliable for this, the bare overlayers probably show more carbon deposition than in the presence of Fe_xNi_y nano-alloys. For the samples with Fe_xNi_y nano-alloys deposited on the $CrO_x@Al_2O_3$ overlayer, the relative amount of carbon deposition decreases with increasing Ni content correlating well with the stability trends observed during catalytic testing. This also supports that, the loss of activity observed is at least in part due to coking, especially for $Fe_5Ni_1/CrO_x@Al_2O_3$ and that when CO_2-activation is enhanced, deactivation *via* coke formation is reduced possibly *via* the reverse Boudouard reaction. A higher I_D/I_G ratio of 1.2 is obtained for $Fe_1Ni_1/CrO_x@Al_2O_3$ suggesting a more graphitic nature of the carbon deposited than on $Fe_3Ni_1/CrO_x@Al_2O_3$ and $Fe_5Ni_1/CrO_x@Al_2O_3$ both with a ratio of 0.85 (Figure 10.11 in Appendix).

For the samples on $ZrO_x@Al_2O_3$, the extent of carbon deposition follows an opposite trend with the material exhibiting the lowest CO_2 conversion displaying the least deposition and more graphitic carbon (see Figure 10.10 in Appendix). This probably suggests that the increased oxide phase observed in XRD provides activation sites for C_2H_6 ultimately causing carbon deposition. This carbon is seemingly more detrimental for active sites of CO-forming routes in Fe-rich samples. Again, it is worth mentioning that the relative amount of carbon deposits acquired *via* Raman analysis is not reliable as various acquisition areas on the surface of the catalyst may

have different contents. Furthermore, the Raman spectra of the overlayer samples were acquired in a different instrument using different parameters making comparisons challenging.

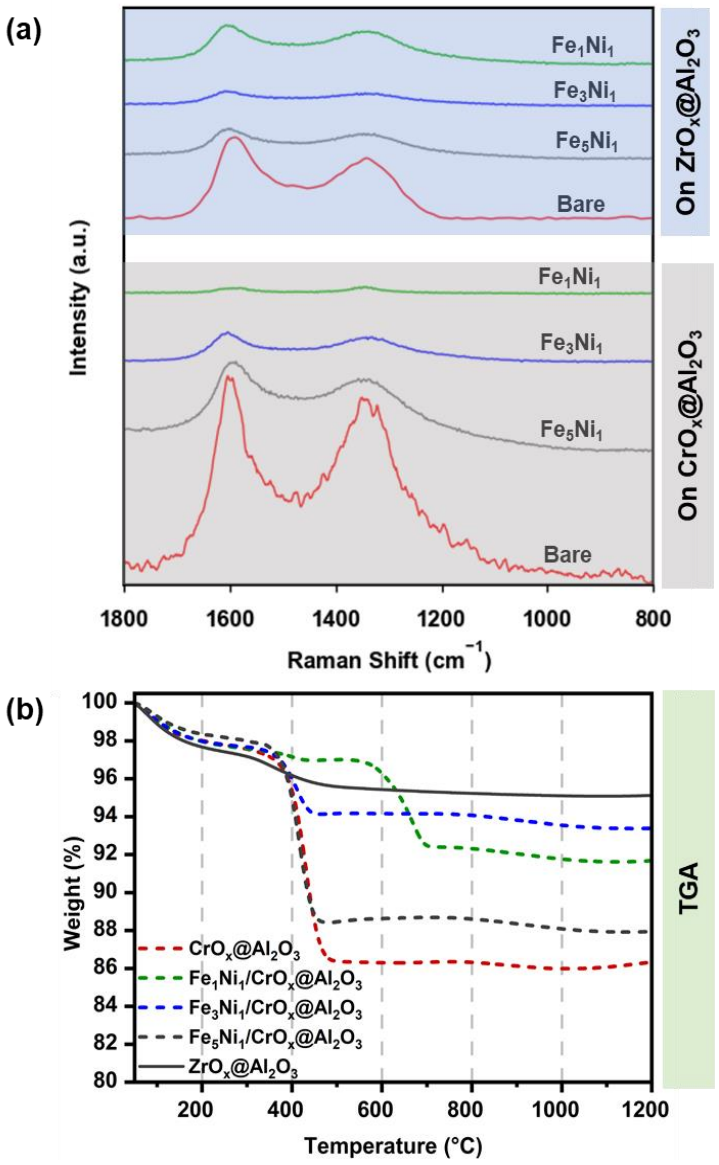

Figure 8.10: (a) Raman spectra of all the spent catalysts for the identification and relative quantification of the carbon deposits as well as (b) TGA weight loss profiles of selected spent catalysts for the quantification of the carbon deposits. The overlayer Raman analysis were done in a RENISHAW spectrometer while other samples were analysed in a WITec Confocal Raman Microscope.

To accurately quantify the amount of carbon or carbonaceous species in these spent catalysts, selected samples were exposed to increasing temperatures in flowing air, monitoring their weight loss (see Figure 8.10 (b)). All samples show an initial weight loss of 1.5 to 2% below 300 °C associated to the removal of water. At a temperature range of 300 to 400 °C $CrO_x@Al_2O_3$,

$Fe_5Ni_1/CrO_x@Al_2O_3$ and $Fe_3Ni_1/CrO_x@Al_2O_3$ experience a second decrease in weight of 12, 10 and 4%, respectively, probably due to carbon removal. This suggests that carbon deposition decreases with increasing Ni content in the Fe_xNi_y nano-alloy as observed in the Raman analysis of the spent catalysts anchored on $CrO_x@Al_2O_3$. However, $Fe_1Ni_1/CrO_x@Al_2O_3$ deviates as it experiences a weight loss of about 6%, which is greater than the weight loss experienced by the $Fe_3Ni_1/CrO_x@Al_2O_3$. The on-set temperature of this weight loss is about 600 °C, which is higher than for all the other materials. XRD and Raman results suggest that a more polymeric or graphitic carbon is deposited on this material probably explaining the removal at a high temperature and the deviation in the relative amount of carbon deposition observed *via* Raman analysis compared to the TGA analysis. The unreactive $ZrO_x@Al_2O_3$ experiences a weight loss of only 2%, also at a temperature range of 300 to 400 °C. While low, according to the Raman results, this is the highest C-content amongst the $ZrO_x@Al_2O_3$ samples. Thus, the unreactive $ZrO_x@Al_2O_3$-based samples have less carbon deposition. The carbon formation mechanisms as well as the parameters directing carbon speciation and quantity on these catalysts are complex. Influencing factors could be the overlayer surface acid site strength, amount of metallic phase present, the level of CO_2 conversion, or potentially the crystallite size as has been reported in dry reforming over Ni catalysts [303].

Similar to the bare overlayers, the $CrO_x@Al_2O_3$ and $ZrO_x@Al_2O_3$ supported Fe_xNi_y nano-alloys were also tested for CO_2-ODHE in a feed with an over-stoichiometric amount of CO_2 (10.4 mL/min with C_2H_6 at 2.1 mL/min) and an inert dilution of 50 vol.-% (12.5 mL/min) at atmospheric pressure and 600 °C (see Figure 8.11 and Figure 10.9). Especially for $Fe_5Ni_1/CrO_x@Al_2O_3$, which showed a promising initial performance but gradual deactivation associated with carbon deposition at equimolar feed, an over-stoichiometric amount of CO_2 in the feed might enhance its stability through removal of the carbon deposits [9,11,146,174].

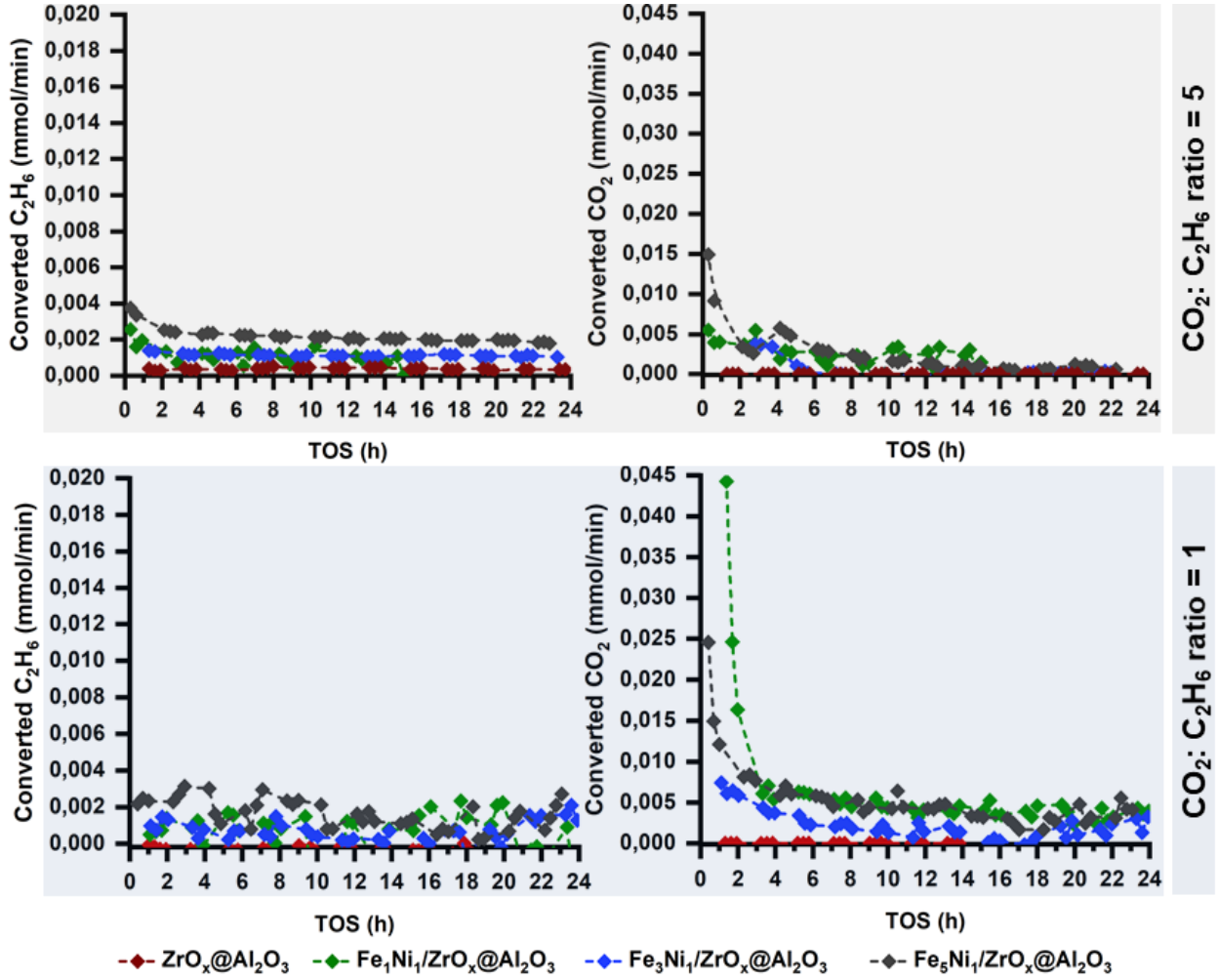

Figure 8.11: Converted C_2H_6 and CO_2 flow rates obtained during CO_2-ODHE under a feed with a CO_2 (10.4 mL/min) : C_2H_6 (2.1 mL/min) molar ratio of 5 (top) as well as under a feed with CO_2 (6.25 mL/min) : C_2H_6 (6.25 mL/min) molar ratio of 1 (bottom) both with an inert dilution of 12.5 ml/min over the $Fe_xNi_y/ZrO_x@Al_2O_3$ catalysts. Conditions: temperature = 600 °C, pressure = 1 atm and total space velocity = 15 $L \cdot h^{-1} \cdot g_{cat}^{-1}$.

The $Fe_xNi_y/ZrO_x@Al_2O_3$ catalysts retain very low levels of activity (see Figure 8.11). The rate of C_2H_6 conversion is nearly unaffected by the change in feed gas composition. Interestingly, the CO_2-activation seems to be reduced compared to the equimolar feed. The initial CO_2 conversion followed by a rapid deactivation is not as prominent at higher CO_2 partial pressures. A possible explanation could be an enhanced re-oxidation of the alloy, especially the bcc allotrope of the alloy. The deactivation then proceeds too fast for the gas analysis to record and also causes total loss of the CO_2-activation capability with TOS.

Further information regarding the product yields and carbon-based selectivity can be found in the Appendix (see Figure 10.9). The converted CO_2 : C_2H_6 molar flow rate ratio confirm a faster loss

of CO_2-activation than C_2H_6 activation ability with TOS compared to the equimolar feed. Seeing that the CO selectivity suggests some CO is formed until the end of the experiment, it is presumed that the CO_2-activation is never completely lost but reaches levels where reliable gas analysis is unfeasible. Furthermore, despite the differences in its evolution with TOS and metallic composition, the initial carbon-based product selectivity obtained in both feeds still suggest this low activity is predominantly as a result of CO-forming routes (*i.e.* alloy re-oxidation and DRE). The C_2H_4 yields and selectivity also suggests some CO_2-ODHE and/or DD activity cannot be ruled out.

For the Fe_xNi_y /CrO_x@Al_2O_3 catalysts, the change in gas composition has a notable effect (Figure 8.12). Especially the samples with strong DRE activity, *i.e.* $Fe_1Ni_1/CrO_x@Al_2O_3$ and $Fe_3Ni_1/CrO_x@Al_2O_3$, are affected. The rate of C_2H_6 and CO_2 conversion is reduced by a factor of two to three and both catalyst compositions show similar conversions. This behaviour of reduced activity with an over-stoichiometric amount of CO_2 in the feed was also observed over the bare overlayer and was attributed to the reduced concentration of the DRE limiting reactant C_2H_6. The initial loss of activity is also less significant than in the equimolar feed probably due to reduced overall activity.

Converse to the equimolar feed, $Fe_5Ni_1/CrO_x@Al_2O_3$ retains a comparable initial activity which is even higher than for the bare overlayer and comparable to $Fe_1Ni_1/CrO_x@Al_2O_3$ and $Fe_3Ni_1/CrO_x@Al_2O_3$ as well as an improved stability attributed to suppressed deactivation in the CO_2-activation functionality. In contrast to the Ni-richer samples, $Fe_5Ni_1/CrO_x@Al_2O_3$ catalyses the CO_2ODHE reaction, comparable to the behaviour under the equimolar feed gas composition but its enhancement of the C_2H_4 yield compared to the bare overlayer is strong in the presence of higher CO_2 concentrations. Thermodynamically, an over-stoichiometric amount of CO_2 in the feed is also supporting increased activity [60].

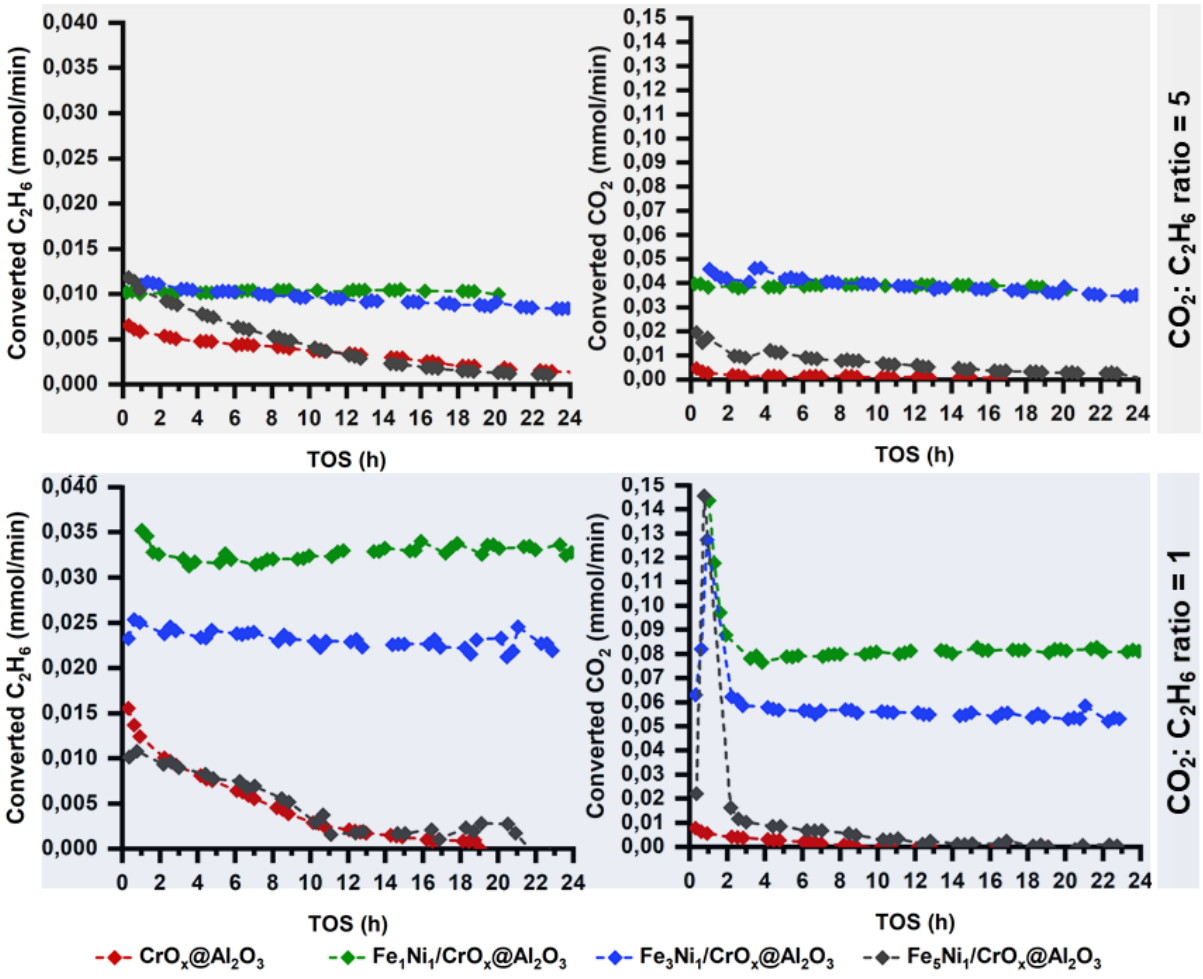

Figure 8.12: Converted C_2H_6 and CO_2 flow rates obtained during CO_2-ODHE under a feed with a CO_2 (10.4 mL/min) : C_2H_6 (2.1 mL/min) molar ratio of 5 (top) as well as under a feed with CO_2 (6.25 mL/min) : C_2H_6 (6.25 mL/min) molar ratio of 1 (bottom) both with an inert dilution of 12.5 ml/min over the $Fe_xNi_y/CrO_x@Al_2O_3$ catalysts. Conditions: temperature = 600 °C, pressure = 1 atm and total space velocity = 15 $L \cdot h^{-1} \cdot g_{cat}^{-1}$.

For all the $Fe_xNi_y/CrO_x@Al_2O_3$ catalysts, the stability increases with a decrease of the Fe content as observed in the equimolar feed. The initial loss in CO_2-activation, attributed to re-oxidation of the bcc phase, is less significant for all the catalysts but is still more apparent with increasing Fe content.

Similar to the activity, no significant difference in product composition is evident for $Fe_1Ni_1/CrO_x@Al_2O_3$ and $Fe_3Ni_1/CrO_x@Al_2O_3$. Both do not form any appreciable amounts of ethylene with CO representing nearly 100% of the converted carbon. The ratio of converted CO_2

to C_2H_6 is 4, which suggests that in addition to DRE, CO is formed via an additional pathway, probably the reverse Boudouard reaction.

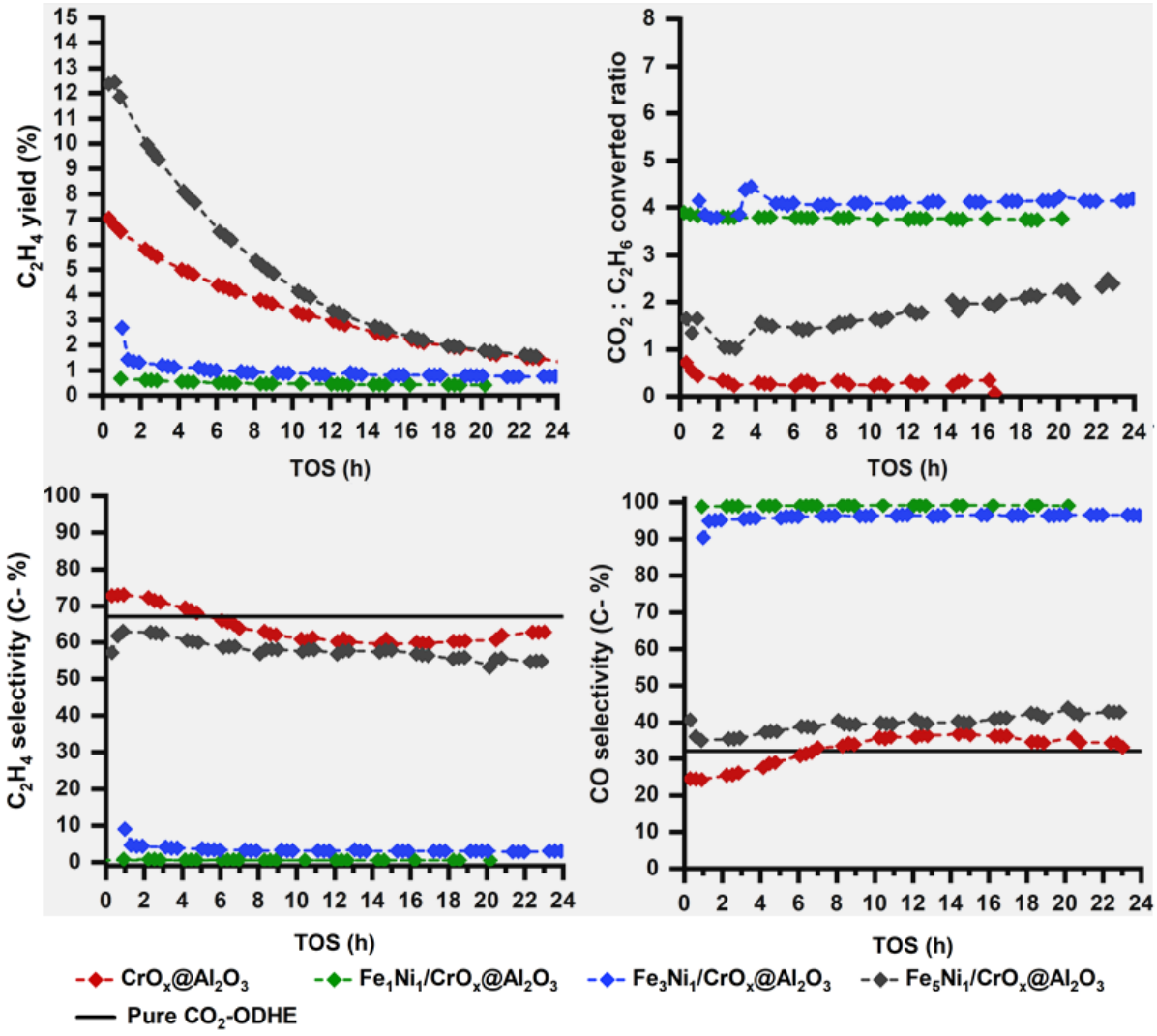

Figure 8.13: C_2H_4 yields and converted CO_2 : C_2H_6 flow rates ratios (top) as well as C_2H_4 and CO selectivity (bottom) obtained during the reaction of C_2H_6 (2.1 mL/min) and CO_2 (10.4 mL/min) diluted with an inert (12.5 mL/min) over the $Fe_xNi_y/CrO_x@Al_2O_3$ catalysts. Conditions: temperature = 600 °C, pressure = 1 atm, space velocity = 15 $L \cdot h^{-1} \cdot g_{cat}^{-1}$, CO_2: C_2H_6 ratio = 5. Maximum possible carbon based C_2H_4 and CO selectivity for a pure CO_2-ODHE are indicated by the black solid lines.

$Fe_5Ni_1/CrO_x@Al_2O_3$ in turn converts double the amount of CO_2 compared to C_2H_6. This ratio even increases slightly with TOS and in parallel to an overall deactivation, suggesting that the ethane activation functionality deactivates faster. Despite this conversion ratio, suggesting DRE, the product selectivity is close to pure CO_2-ODHE, with a slightly higher CO formation. The C_2H_4 yield in the initial hours of the reaction surpass those obtained with an equimolar feed composition

significantly. Throughout the experiment, $Fe_5Ni_1/CrO_x@Al_2O_3$ sustains an C_2H_6 dehydrogenation functionality and additional CO_2 converted is most likely stabilizing the catalyst through the gasification of carbon deposits. The observed deactivation can either be associated to re-oxidation of the bcc alloy phase or, more likely because of the largely unaffected product selectivity, to the formation of carbon deposits that cannot fully be prevented by the reverse Boudouard reaction.

Despite the efforts of testing the materials in this feed to reduce or completely mitigate carbon deposition, the Raman analyses of the spent catalysts still confirm the presence of carbon deposits on all the materials shown by the G- and D-bands of the sp^2-bond vibrations of carbon atoms (see Figure 8.14 as well as Figure 10.12 and Figure 10.13 in Appendix). This suggests that although the high CO_2 concentration in the feed improves the stability of the materials by enhancing the reverse Boudouard reaction, carbon deposition still occurs. Thus, despite the probable deactivation *via* alloy re-oxidation, to some extent the loss of activity observed is also due to carbon deposition, especially for $Fe_5Ni_1/CrO_x@Al_2O_3$. It might be reduced but not completely mitigated. Carbon deposition is also observed for the catalysts with a pure DRE and reverse Boudouard activity showing very limited deactivation.

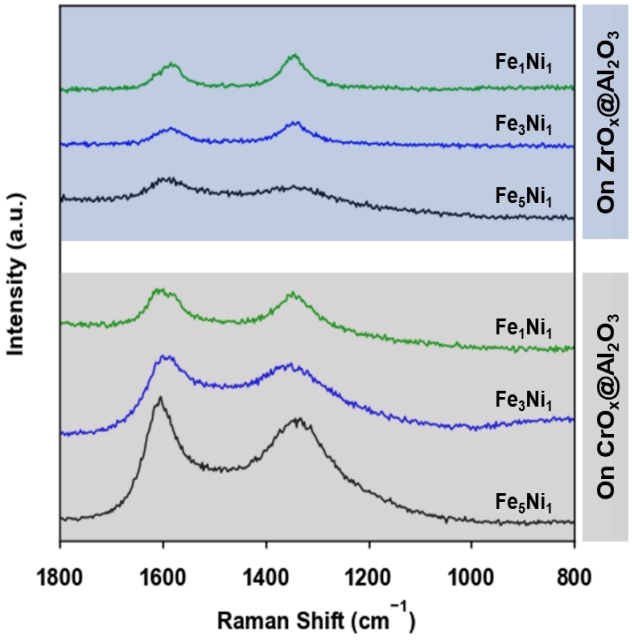

Figure 8.14: Raman spectra of spent $Fe_xNi_y/ZrO_x@Al_2O_3$ and $Fe_xNi_y/CrO_x@Al_2O_3$ catalysts after testing under a feed with an over-stoichiometric amount of CO_2. All the Raman analyses were done in a WITec Confocal Raman Microscope.

8.3 Effect of the metal oxide overlayer on catalytic performance of iron-nickel nano-alloys synthesized in a different autoclave

The results presented in Section 8.2 clearly show that the addition of Fe_xNi_y nano-alloys to active metal oxide supports can enhance their catalytic activity. They also support the proposed effect of the Fe : Ni atomic ratio on the catalytic pathway, with Fe_5Ni_1 supporting the target CO_2-ODHE at minor activity improvements, while Fe_1Ni_1 shifts the catalytic activity to the DRE with significant enhancements in activity and stability. Fe_3Ni_1, while predominantly enhancing DRE still sustains a stable yield of C_2H_4. With the CO_2-ODHE being the target reaction in the present study, Fe_5Ni_1 and Fe_3Ni_1 were further studied on a library of overlayers as presented in Section 8.1 (*i.e.* $GaO_x@Al_2O_3$, $VO_x@Al_2O_3$, $SmO_x@Al_2O_3$ and $TiO_x@Al_2O_3$). The Fe_xNi_y nano-alloys obtained from the second batch of Fe_xNi_y oxidic precursors (TT1-3.3 and TT1-3.5) with ICP-based Fe : Ni atomic ratios of 2.9 and 4.8 (see Table 6.2 in Chapter 6), respectively, were utilized. For clarity, the tested $MO_x@Al_2O_3$-supported TT1-3.3 and TT1-3.5 will also be presented as $Fe_3Ni_1/MO_x@Al_2O_3$ and $Fe_5Ni_1/MO_x@Al_2O_3$.

The $GaO_x@Al_2O_3$, $VO_x@Al_2O_3$, $SmO_x@Al_2O_3$ and $TiO_x@Al_2O_3$ supported Fe_3Ni_1 and Fe_5Ni_1 nano-alloys were tested for CO_2-ODHE in an equimolar feed of CO_2 (6.25 mL/min) and C_2H_6 (6.25 mL/min) with an inert dilution of 50 vol.-% (12.5 mL/min) at atmospheric pressure and 600 °C (see Figure 8.15 and Figure 8.16). The results obtained clearly show that, due to the varying acid site strength and reducibility of the overlayers, the catalytic performance varies significantly. Note that the acid site strength, refers to the strength of the intermediate acid sites obtained *via* NH_3-TPD which are predominant and represent the average acidity correlating well with the acidity quantification obtained *via* DR-UV/Vis.

Overall, the $Fe_3Ni_1/MO_x@Al_2O_3$ catalysts still exhibit improved activity, compared to the bare overlayers discussed in Section 8.1, with CO_2 conversion levels higher than C_2H_6 conversions confirming an enhanced CO_2-activation ability introduced by the alloy (see Figure 8.15, top). Just as shown for the bare overlayers, the catalytic activity (CO_2 and C_2H_6 conversions) increases with acid site strength.

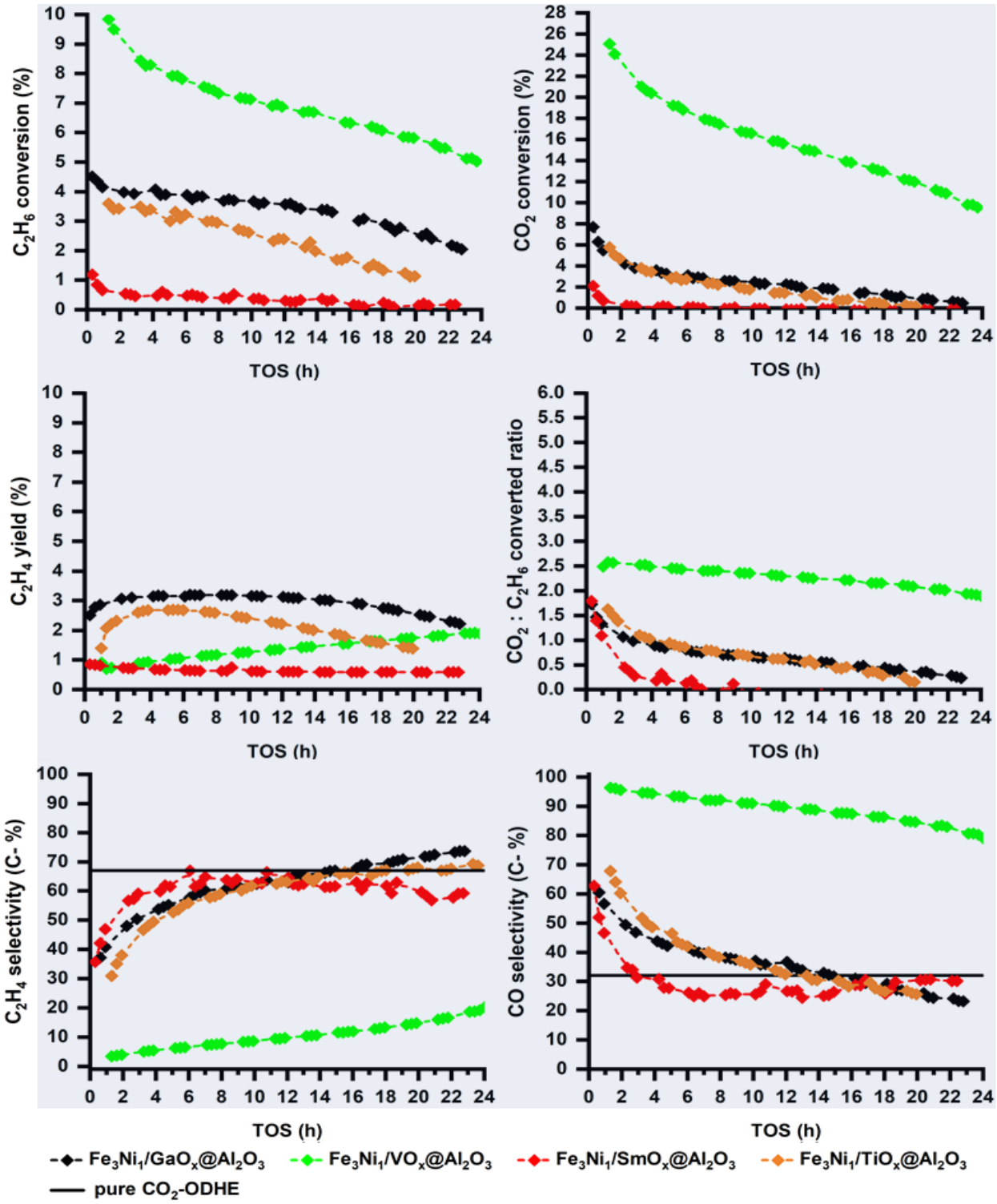

Figure 8.15: C_2H_6 and CO_2 conversions (top), C_2H_4 yield and CO_2: C_2H_6 ratio (middle) as well as carbon based C_2H_4 and CO selectivity (bottom) obtained during reaction of C_2H_6 (6.25 mL/min) and CO_2 (6.25 mL/min) with an inert dilution of 50 vol.-% (12.5 mL/min) over the various $Fe_3Ni_1/MO_x@Al_2O_3$ catalysts. Conditions: temperature = 600 °C, pressure = 1 atm, space velocity = 15 $L \cdot h^{-1} \cdot g_{cat}^{-1}$, CO_2 : C_2H_6 ratio = 1. Maximum possible C_2H_4 and CO selectivity for a pure CO_2-ODHE are indicated by the black solid lines.

On the most acidic and reducible overlayer, $VO_x@Al_2O_3$, the deposition of the Fe_3Ni_1 nano-alloy results in the highest measured activity with initial CO_2 and C_2H_6 conversions of 26% and 10%, respectively (see Figure 8.15, top). A clear deactivation, slightly stronger for CO_2 than for the C_2H_6 conversion, is observed. The CO_2 : C_2H_6 conversion ratio is initially 2.5 and drops to 2 by the end of the experiment confirming the faster loss of the CO_2-activation functionality. This is complemented by a decrease of CO selectivity (96.5 C-% initially to 81 C-% at 24 h TOS) with increasing C_2H_4 selectivity (3.5 C-% initially to 19 C-% at 24 h TOS) suggesting a gradual shift from CO-forming to a more dehydrogenation-based (*i.e.* CO_2-ODHE/DD) pathway. Probably, the initial high CO_2-activation functionality causes an active site transformation *via* catalyst re-oxidation resulting in the formation of additional active sites for a parallel C_2H_4-forming route. However, the CO-forming routes are still dominant even at the end of the experiment.

The proposed CO-forming pathways are mostly DRE coupled with some minor reverse Boudouard reaction and/or alloy re-oxidation. The reverse Boudouard reaction and/or alloy re-oxidation are expected to contribute more in the early hours of the reaction, when the CO_2 : C_2H_6 conversion ratio is above the stoichiometric value of DRE and slowly diminish with TOS. Stable DRE is of great interest as its product, *syngas*, is vital in the petrochemical industry and could represent a CO_2 utilization route. This catalytic behaviour is different from the bare overlayer which displayed a C_2H_4 selectivity above 50 C-% but lost activity, especially CO_2 conversion, very rapidly (see Figure 8.1 in Section 8.1). Thus, although the alloy improves the activity and stability by enhancing CO_2-activation as proposed, this activity is predominantly due to promotion of CO-forming routes resulting in a low C_2H_4 selectivity. While there are some differences in catalyst stability and selectivity and their evolution with TOS, the performance of $Fe_3Ni_1/VO_x@Al_2O_3$ resembles the performance of the Fe_3Ni_1 nano-alloy supported on $CrO_x@Al_2O_3$, a carrier which is also acidic and reducible (see Figure 8.8 in Section 8.2). A similar behaviour is observed for the Fe-rich $Fe_5Ni_1/VO_x@Al_2O_3$ catalyst (see Figure 8.16). However, the CO_2-activation functionality is even more enhanced (higher and stable CO_2 : C_2H_6 conversion ratio above 2.5) resulting in a better catalyst stability and a much reduced shift from CO-forming to dehydrogenation pathways with TOS. This is unlike over the $CrO_x@Al_2O_3$ overlayer where the Fe_5Ni_1 nano-alloy predominantly supports the CO_2-ODHE pathway with activity close to that of the bare overlayer and a slightly improved CO_2-activation functionality and stability (see Figure 8.8 in Section 8.2).

On the unreducible $GaO_x@Al_2O_3$ with intermediate acidity, the Fe_3Ni_1 nano-alloy exhibits lower conversion levels compared to the strongly acidic $Fe_3Ni_1/VO_x@Al_2O_3$ and $Fe_3Ni_1/CrO_x@Al_2O_3$. However, the catalytic activity is significantly enhanced compared to the bare overlayer. This effect is stronger for the CO_2-activation functionality resulting in an initial CO_2 : C_2H_6 conversion ratio of about 1.8. The deactivation of the catalyst with TOS is less severe compared to the bare overlayer. This supports the proposal that enhanced CO_2-activation improves the stability of metal oxides by enhancing re-oxidation during the redox mechanism or by removing carbonaceous deposits via the reverse Boudouard reaction. Still, deactivation is observed with TOS and the loss of the CO_2-activation functionality is faster, especially in the first 4 h TOS. In stark contrast to the behaviour on $VO_x@Al_2O_3$ and $CrO_x@Al_2O_3$ the Fe_3Ni_1 alloy supported on $GaO_x@Al_2O_3$ primarily supports dehydrogenation pathways. From an initial C_2H_4 selectivity of 35 C-%, the alkene selectivity increases rapidly in the first 6 h TOS reaching values close to 60 C-%, followed by a gradual monotonic increase over the full experiment. After 24 h TOS a C_2H_4 selectivity of 74 C-% indicates the presence of DD pathways. The observed increase in selectivity is mirrored by the decrease in CO_2 conversion. It is proposed that the high initial CO_2-activation causes active site transformation resulting in the formation of additional C_2H_4-forming (CO_2-ODHE and/or DD) active sites. From the observed catalytic performance, it can be hypothesized that over the $GaO_x@Al_2O_3$ support, the Fe_3Ni_1 promotes a CO_2-ODHE reaction which comprises of a consecutive DD and RWGS. Upon deactivation of the CO_2 activation, i.e. the RWGS reaction, DD activity persist for some time. The combination of the discussed effects results in a very stable C_2H_4 yield of approximately 3%.

It is interesting that the bare $GaO_x@Al_2O_3$ and $CrO_x@Al_2O_3$ perform similar in terms of the reaction pathways with minor differences in stability and activity (see Figure 8.1) but significantly different with the Fe_3Ni_1 nano-alloy added. This also emphasises the importance of cooperativity between alloy composition and overlayer acidity/reducibility. The Fe_5Ni_1 nano-alloy on $GaO_x@Al_2O_3$ exhibits lower C_2H_6 and especially CO_2 conversion levels compared to the $Fe_3Ni_1/GaO_x@Al_2O_3$ catalyst suggesting a reduction of activity with increasing Fe-content (see Figure 8.16, top), similar to the observations on $CrO_x@Al_2O_3$. Furthermore, with increasing Fe-content, the material becomes less stable as indicated by a faster loss of activity due to a low CO_2-activation functionality. Higher levels of C_2H_4 and low CO selectivity are also attained ascribed to a DD pathway. However, just as observed for $Fe_3Ni_1/GaO_x@Al_2O_3$ versus $Fe_3Ni_1/CrO_x@Al_2O_3$, this Fe-rich $Fe_5Ni_1/GaO_x@Al_2O_3$ is also more active and stable than $Fe_5Ni_1/CrO_x@Al_2O_3$ (see Figure 8.16) and the $GaO_x@Al_2O_3$ overlayer due to a slightly more sustained CO_2 conversion with TOS.

$Fe_3Ni_1/TiO_x@Al_2O_3$ exhibits a similar catalytic behaviour (*i.e.* CO_2-ODHE activity) as $Fe_3Ni_1/GaO_x@Al_2O_3$ although with a slightly faster deactivation and lower activity in line with its limited reducibility and intermediate acidity. On the other hand, while $Fe_3Ni_1/SmO_x@Al_2O_3$ also exhibits a CO_2-ODHE behaviour, the activity is significantly lower, with CO_2 conversion essentially reaching 0% after 2 hours TOS. Increasing the Fe-content in the alloy over $TiO_x@Al_2O_3$ and $SmO_x@Al_2O_3$ reduces the activity further, rendering both essentially inactive (see Figure 8.16).

It is clear that while the Fe : Ni atomic ratio of the alloy has a significant influence on the catalytic performance of the studied catalyst systems, the interplay between alloy and support has a significant role guiding the reaction. This emphasizes that both the alloy and overlayer interact together to form a bifunctional tandem catalyst in which the performance depends strongly on the cooperativity or suitability of both the alloy composition and the overlayer reducibility/acidity. For both the $Fe_3Ni_1/MO_x@Al_2O_3$ and $Fe_5Ni_1/MO_x@Al_2O_3$ catalyst systems including those presented in Section 8.2, the initial activity decreases with reducing overlayer acidity as observed for the bare overlayers. The C_2H_4 selectivity is low when the overlayer acidity is strongest and when it is weakest but is elevated at intermediate acidity. The CO selectivity shows an opposite trend. This suggests the optimum overlayer acidity necessary to achieve CO_2-ODHE activity is in the medium strength for the Fe_3Ni_1 nano-alloy. However, increasing the Fe-content in the alloy shifts the optimum of overlayer acidity necessary slightly towards the stronger side as even $Fe_5Ni_1/CrO_x@Al_2O_3$ with a strongly acidic overlayer exhibits activity towards the desired CO_2-ODHE reaction.

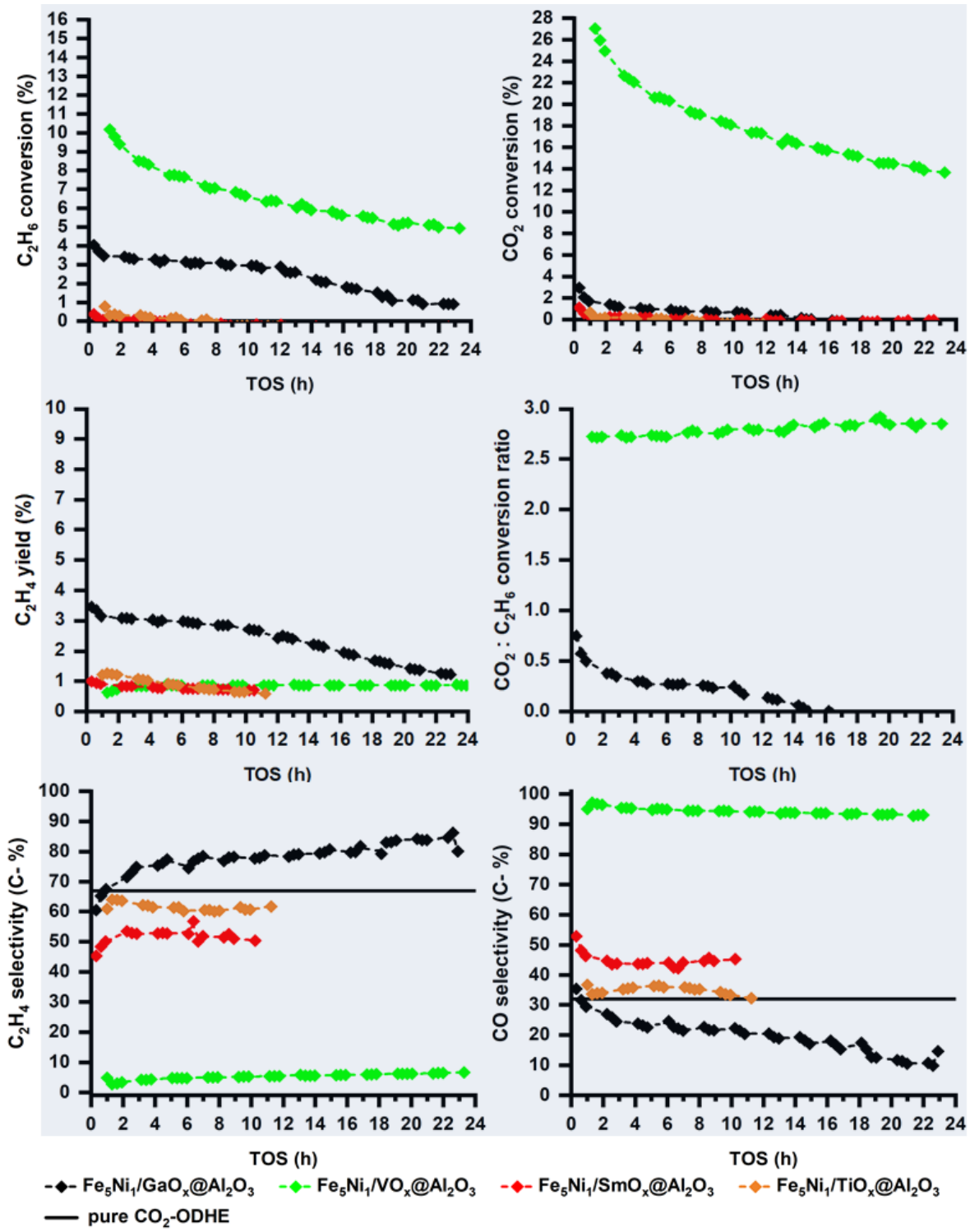

Figure 8.16: C_2H_6 and CO_2 conversions (top), C_2H_4 yield and CO_2: C_2H_6 ratio (middle) as well as carbon based C_2H_4 and CO selectivity (bottom) obtained during reaction of C_2H_6 (6.25 mL/min) and CO_2 (6.25 mL/min) with an inert dilution of 50 vol.-% (12.5 mL/min) over the various $Fe_3Ni_1/MO_x@Al_2O_3$ catalysts. Conditions: temperature = 600 °C, pressure = 1 atm, space velocity = 15 $L \cdot h^{-1} \cdot g_{cat}^{-1}$, CO_2 : C_2H_6 ratio = 1. Maximum possible C_2H_4 and CO selectivity for pure CO_2-ODHE are indicated by the black solid lines.

The suspected initial re-oxidation is still attributed to the bcc phase of the alloy. Seemingly its re-oxidation results in the formation of additional active sites with a dehydrogenation ability. The rate of the formation of these active sites in both alloy systems is seemingly slowest on the strongly acidic $VO_x@Al_2O_3$ and faster with further weakening of the overlayer acidity. Increasing the Fe-content from Fe_3Ni_1 to Fe_5Ni_1 only slows this rate over the strongly acidic $VO_x@Al_2O_3$ and accelerates the rate over the other overlayers. Thus, depending on the alloy composition and on the overlayer acidity/reducibility, the formation of these active sites can be slowed or accelerated resulting in the overall promotion of either the CO_2-ODHE or the DRE reaction. Studies by Chen *et al*. [18] have shown that indeed the support can interact differently with the alloy resulting in active sites that can promote either DRE or CO_2-ODHE for their Fe_3Ni_1 alloy. Their studies suggest the occurrence of re-oxidation of the exsoluted Fe resulting in the formation of the interface between support and Ni-FeO_x or between support and metallic Ni or a Ni-rich fcc alloy. These are considered distinct active sites for the DRE or CO_2-ODHE, respectively. The dominance of either reaction depends on the dispersion of the interfaces which in turn depends on the support. Both our work and literature suggest the occurrence of alloy re-oxidation which influences active sites for the overall promotion of either reaction. However, so far, no report of the existence of the alloy in different allotropes and the effect of phase on the re-oxidation process has been reported.

The offline XRD analyses of the retrieved spent catalysts for both systems (*i.e.* $Fe_3Ni_1/MO_x@Al_2O_3$ and $Fe_5Ni_1/MO_x@Al_2O_3$) show significant crystallographic phase changes of the nano-alloys while the metal oxide overlayers remain seemingly unaffected (see Figure 8.17).In all cases, the Fe- and Ni-containing phases are present in the form of a mixture of the fcc phase of the alloy and the oxidic inverse spinel structure confirming re-oxidation of the bcc allotrope during the reaction. Whether the active site formed *via* re-oxidation to the fully oxidised inverse spinel phase or a partial oxide formed from the metallic bcc phase is uncertain. No sign of such a partial oxide phase is observed in XRD. However, literature reports it to be amorphous, *i.e.* invisible in X-ray-diffraction [1,2,17–20,62,63,125,209,211,226]. The formation of the oxidic inverse spinel structure phase occurs independently of the differences in the alloy composition and the metal oxide overlayer as the bcc phase is not detected in any sample including those exhibiting a slow re-oxidation or active site transformation rate. On the $Fe_3Ni_1/VO_x@Al_2O_3$ and $Fe_3Ni_1/GaO_x@Al_2O_3$ catalysts, graphitic carbon is detected but interestingly not when the Fe-content in the alloy is increased.

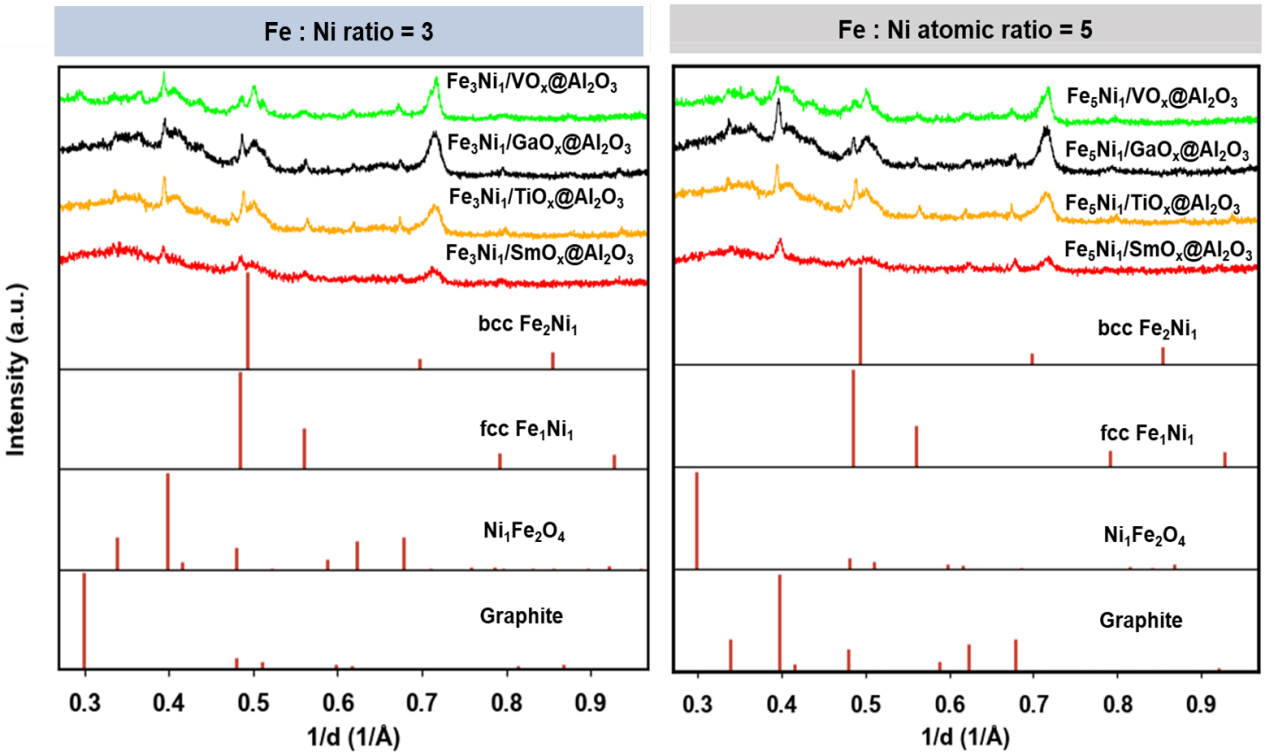

Figure 8.17: Stacked offline XRD patterns of spent $Fe_3Ni_1/MO_x@Al_2O_3$ (left) and $Fe_5Ni_1/MO_x@Al_2O_3$ (right) catalysts retrieved after a 24 h testing for CO_2-ODHE under an equimolar feed. The reference patterns provided correspond to graphite (PDF-4 01-073-5918), $NiFe_2O_4$ (PDF-4 04-014-8286), fcc Fe_1Ni_1 (PDF-4 04-003-3531) and bcc Fe_2Ni_1 (PDF-4 04-018-7295).

In a feed with a CO_2 (10.4 mL/min) : C_2H_6 (2.1 mL/min) molar ratio of 5, a similar overall catalytic behaviour as in the equimolar feed is observed for the $Fe_3Ni_1/MO_x@Al_2O_3$ catalysts (see Figure 8.18 and Figure 8.19). However, just as observed for $CrO_x@Al_2O_3$-supported alloys, all samples except $Fe_3Ni_1/TiO_x@Al_2O_3$ display lower levels of activity with improved CO_2-activation functionality resulting in enhanced stability (Figure 8.18). $Fe_3Ni_1/TiO_x@Al_2O_3$ seemingly loses the CO_2-activation functionality rapidly which results in a faster deactivation probably due to its high initial activity comparable to the equimolar feed. The initial loss in the CO_2-activation functionality is faster and the resulting active site transformation is clearer for all samples compared to the equimolar feed suggesting that the increased CO_2 concentration in the feed accelerates the suspected alloy re-oxidation.

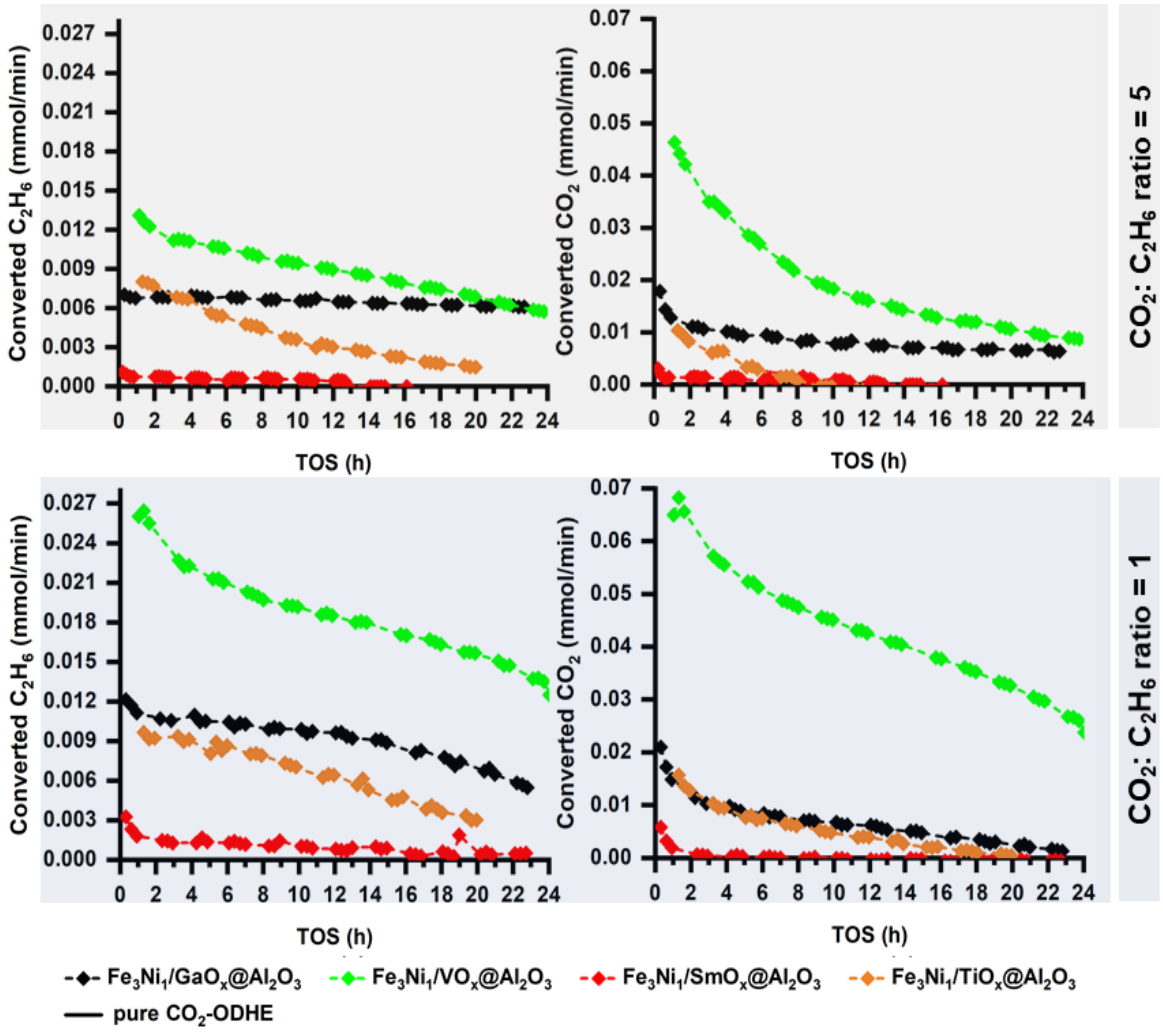

Figure 8.18: Converted C_2H_6 and CO_2 flow rates obtained during CO_2-ODHE under a feed with a CO_2 (10.4 mL/min) : C_2H_6 (2.1 mL/min) molar ratio of 5 (top) as well as under a feed with CO_2 (6.25 mL/min) : C_2H_6 (6.25 mL/min) molar ratio of 1 (bottom) both with an inert dilution of 12.5 ml/min over the $Fe_3Ni_1/MO_x@Al_2O_3$ catalysts. Conditions: temperature = 600 °C, pressure = 1 atm and total space velocity = 15 $L \cdot h^{-1} \cdot g_{cat}^{-1}$.

The accelerated loss of CO_2-activation functionality is also apparent in the molar ratio of converted CO_2 : C_2H_6 which shows a rapid initial decrease followed by a gradual decrease with TOS (see Figure 8.19, top). Thus, after re-oxidation, the materials are able to attain some stability which is improved compared to the performance in the equimolar feed. This stability is highest on the promising $Fe_3Ni_1/GaO_x@Al_2O_3$. The subsequent gradual decrease is only apparent for $Fe_3Ni_1/VO_x@Al_2O_3$ and $Fe_3Ni_1/GaO_x@Al_2O_3$ as they retain significant activity after the initial deactivation.

The formation period (initial increase) of C_2H_4 and CO selectivity as well as C_2H_4 yields, which is attributed to the formation of CO_2-ODHE active sites *via* the accelerated re-oxidation, is also faster

in the over-stoichiometric feed (see Figure 8.19). This results in the maximum C_2H_4 yields and selectivity being reached faster. The elevated ratio of converted CO_2 to C_2H_6 and CO selectivity above the stoichiometric maximum of CO_2-ODHE indicate the presence of an additional CO-forming route. Based on the enhanced stability of materials, this reaction is likely the reverse Boudouard reaction which is able to reduce catalyst deactivation *via* coking. The C_2H_4 selectivity still exhibits a trend of increasing with a weakening of the overlayer acid site strength as observed in the equimolar feed. Interestingly, $Fe_3Ni_1/TiO_x@Al_2O_3$ exhibits the highest C_2H_4 selectivity. This selectivity can be associated to DD as the CO_2-activation functionality vanishes with TOS.

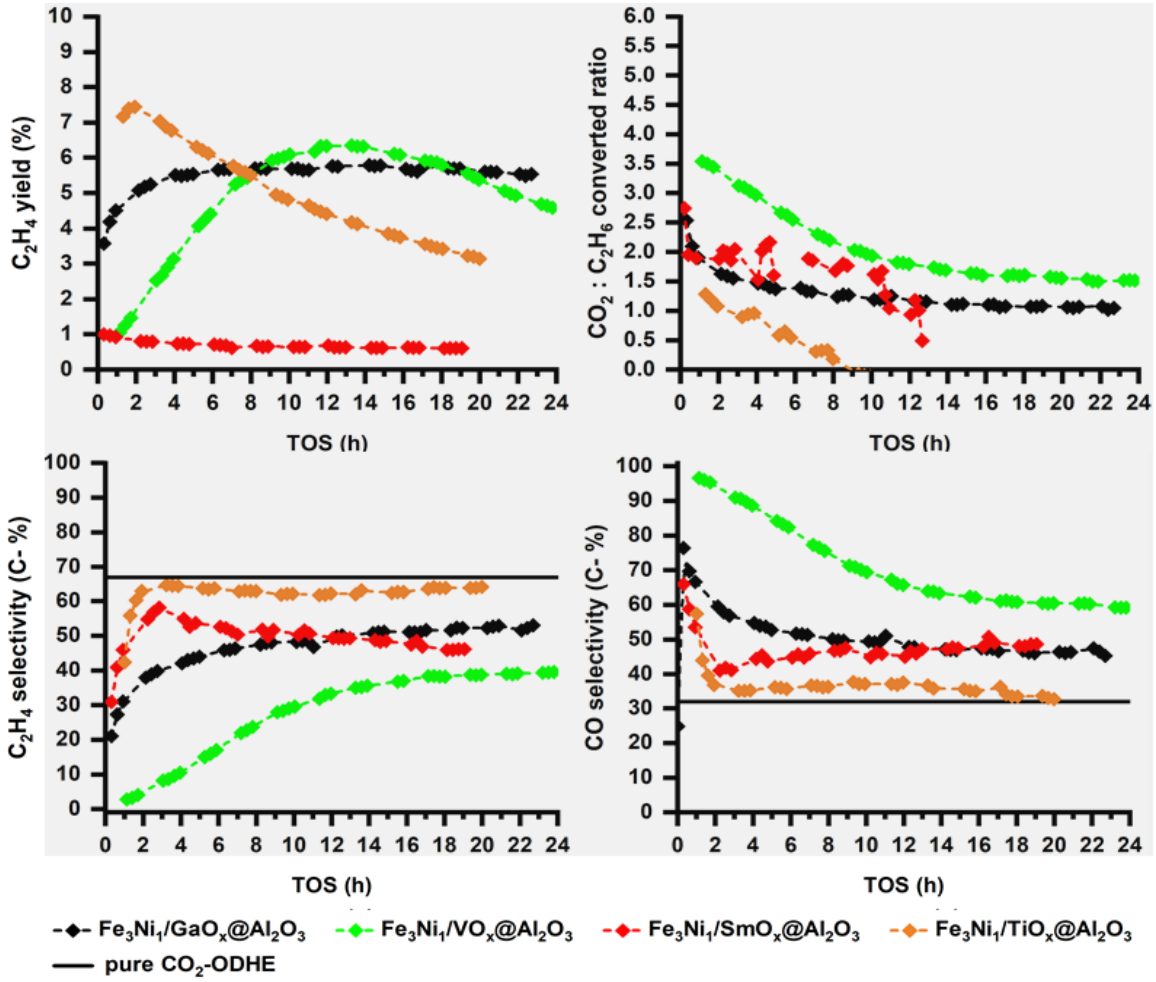

Figure 8.19: C_2H_4 yields and converted CO_2 : C_2H_6 flow rates ratios (top) as well as C_2H_4 and CO selectivity (bottom) obtained during the reaction of C_2H_6 (2.1 mL/min) and CO_2 (10.4 mL/min) diluted with an inert (12.5 mL/min) over the $Fe_3Ni_1/MO_x@Al_2O_3$ catalysts. Conditions: temperature = 600 °C, pressure = 1 atm, space velocity = 15 $L \cdot h^{-1} \cdot g_{cat}^{-1}$, CO_2: C_2H_6 ratio = 5. Maximum possible carbon based C_2H_4 and CO selectivity for pure CO_2-ODHE are indicated by the black solid lines.

A similar influence of an increased CO_2 concentration in the feed is observed over the $Fe_5Ni_1/MO_x@Al_2O_3$ catalysts (see Figure 10.14 and Figure 10.15 in the Appendix). However, $Fe_5Ni_1/VO_x@Al_2O_3$ appears to be stable against active site reconstruction under these conditions resulting in small changes in the C_2H_4 and CO. The XRD analyses of the spent catalysts reveal similar crystallographic changes as observed in the equimolar feed (see Figure 10.16 in the Appendix).

9 Summary, conclusions and future work recommendations

The work presented seeks to create an understanding of the influence of the physicochemical properties of bifunctional catalysts made out of Fe_xNi_y nano-alloys anchored on model metal oxide overlayer supports on the conversion of CO_2 and C_2H_6 *via* the CO_2-ODHE. Special focus is directed to the influence of overall and Lewis surface acid site strength and reducibility of the model metal oxide overlayer supports as well as the metallic composition of the anchored Fe_xNi_y nano-alloys. The study can be divided into two main parts:

1. The separate synthesis of the overlayer supports and the Fe_xNi_y nano-alloys which were ultimately combined to form the target bifunctional model catalyst systems. The synthesis of the model metal oxide overlayers with varying relative total and Lewis surface acid site strength as well as reducibility but comparable pore textural properties was achieved by using an incipient wetness impregnation route [257,259,272,274]. For the synthesis of the Fe_xNi_y nano-alloys, nanoparticles of oxidic precursors consisting of $Ni(OH)_2$ and/or Ni-ferrite inverse spinel structure were synthesized, supported and their reducibility in H_2 atmosphere was investigated. A modified surfactant-free solvothermal synthesis route was employed and the synthesis parameters necessary to yield the oxidic precursors with target metallic compositions and a uniform particle size (10 nm) were investigated [239,241]. In addition to the synthesis, a major emphasis was put on characterization of the catalysts in each of the synthesis steps as well as their evolution during and after reduction/temperature-programmed CO_2-activation reaction.

2. The catalytic performance evaluation of the prepared catalysts was conducted at under two different feed compositions at 600 °C and atmospheric pressure for 24 h in a fixed-bed reactor. The catalytic performance evaluation is presented in the form of feed conversions and rates of feed converted as well as C_2H_4 yields and product selectivity which provides understanding of activity and stability as well as the reaction pathways promoted. Spent catalyst characterization gave insights of possible deactivation causes and interpretation of the activity and selectivity obtained.

The **catalysts preparation** is also divided into two parts *viz*: Synthesis and characterization of the model metal oxide overlayer supports and synthesis and characterization of the Fe_xNi_y nano-alloys oxidic precursor nanoparticles.

The modified incipient wetness impregnation technique enabled synthesis of a series of model overlayer supports comprising of either VO_x, CrO_x, GaO_x, TiO_x, ZrO_x or SmO_x surface metal oxides coated at the periphery of a γ-Al_2O_3 carrier [257,259,272,274]. This technique allowed the formation of the respective oxide overlayers with comparable pore structure properties. DR-UV/Vis of surface-adsorbed alizarin confirmed that the materials span a broad-range of relative average Lewis acid site strength stemming from the coordinatively unsaturated metals on the surface. NH_3-TPD revealed the existence of three different acid sites; weak, intermediate and strong, which also vary across the different overlayers. The range of intermediate acid sites correlate to Lewis acid sites measured by DR-UV/Vis. In addition, the metal oxides also proved to differ regarding their reducibility, probed in H_2-TPR. Raman and XRD analyses confirmed their existence as amorphous surface chemical species.

The synthesis parameters required to yield monodisperse oxidic Fe_xNi_y alloy precursor nanoparticles with control of the metallic composition (*i.e.* the overall Fe : Ni atomic ratio) using a modified surfactant-free benzyl alcohol solvothermal method were investigated. The results obtained show that the combination of a high volume of ammonium hydroxide, a higher concentration of the metal precursor and a high reaction temperature are necessary to attain monodisperse nanoparticles of approximately 10 nm with a close to target composition. These conditions were adopted for the synthesis of oxidic Fe_xNi_y nano-alloy precursors of overall Fe : Ni atomic ratios of 1, 3 and 5 in the form of $Ni(OH)_2$ and/or $(Ni_xFe_{1-x})Fe_2O_4$ depending on composition. The characterization of these oxidic Fe_xNi_y nano-alloy precursors when supported on the overlayers revealed that they evolve into a mixture of the bcc and fcc phases of the alloy under reduction conditions. The ratio of bcc and fcc phases formed at a given temperature depends strongly on the overall Fe : Ni atomic ratio and is largely independent of the support. With increasing Fe content, the bcc phase of the alloy becomes dominant over the fcc phase. Under a CO_2 atmosphere, only the bcc phase of the alloy is re-oxidised while the fcc phase remains metallic. A previous study suggests exsolution or segregation of Fe in an oxidic form from a proposed alloy structure obtained *via* co-impregnation whereas Ni remains metallic under a CO_2 atmosphere [300]. Future studies should focus on further extensive *in situ* characterization, using techniques such as magnetometry and X-ray absorption spectroscopy, to elucidate the process of oxidation under a CO_2 atmosphere and under reaction conditions to provide further conclusions on the nature of the active site.

The **catalytic evaluation of the bare overlayers** clearly shows that while samples suffer from severe deactivation, the activity, selectivity and stability of metal oxides depend strongly on the combination of the acidity/reducibility and the feed composition. Only the reducible overlayers display activity while the unreducible overlayers are mostly inactive. $GaO_x@Al_2O_3$ is reported to be partially reducible under reaction conditions despite being apparently unreducible under H_2-TPR conditions [301]. An alternative proposal states that $GaO_x@Al_2O_3$ is indeed unreducible and its activity stems from its ability to undergo CO_2-ODHE *via* a heterolytic dissociative adsorption of C_2H_6 followed by RWGS instead of the typical redox pathway [250]. Of the clearly reducible $CrO_x@Al_2O_3$ and $VO_x@Al_2O_3$, the easily reducible $CrO_x@Al_2O_3$ is more stable under reaction conditions. Further studies with a larger library of reducible materials to clarify if the ease of reduction indeed influences catalyst stability and selectivity are recommended. Stronger acid sites result in the highest initial activity, lowest C_2H_4 selectivity (promotion of DRE pathway) and a faster deactivation due to coke deposition and limited provision of surface oxygen species. A decrease from strong to intermediate acid sites of the overlayer results in a reduced initial activity improved stability and increased C_2H_4 selectivity *via* CO_2-ODHE/DD pathways. Overlayers with weaker acid sites are essentially inactive except for some minor ability to activate CO_2, especially at the lowest studied acidity due to the associated basic sites. Under the equimolar feed, CO_2-activation is limited and carbon deposition is more prevalent resulting in catalyst deactivation. An over-stoichiometric amount of CO_2 in the feed improves and maintains the CO_2-activation functionality for an extended period due to an enhanced reverse Boudouard reaction, DRE, catalyst re-oxidation or hydrogen removal (RWGS). This in turn improves catalyst stability and C_2H_6 conversion but reduces the C_2H_4 selectivity. It is evident that the overlayers deactivated mostly due to limited CO_2-activation functionality, essential for coke removal and catalyst re-oxidation, which could be improved by increasing the CO_2 concentration in the feed.

The addition of the alloys to the reducible and acidic $CrO_x@Al_2O_3$ results in an overall Fe : Ni atomic ratio-dependent enhancement of the CO_2-activation functionality, overall activity and stability as well as reaction pathways promoted. An Fe-rich alloy with a Fe : Ni atomic ratio of 5 only slightly improves the CO_2-ODHE activity due to a slight enhancement of the CO_2-activation which also improves the catalyst stability. A significantly enhanced CO_2-activation functionality, overall activity and stability as well as CO-formation *via* the DRE pathway is observed with increasing Ni content in the alloy. At an Fe : Ni atomic ratio of 1 (*i.e.* maximum Ni content) the CO_2-ODHE/DD activity is completely supressed while about 10 C-% C_2H_4 selectivity is sustained at a ratio of 3. This suggests that the optimum metallic composition of the alloy to balance activity

and a high CO_2-ODHE selectivity is between an Fe : Ni atomic ratio of 3 and 5. Future studies should explore this range in more detail to identify the optimum composition. With a higher concentration of CO_2 in the feed, a further improvement of CO_2-activation and a slight decrease C_2H_4 selectivity with increased CO selectivity is observed. This parallel CO-forming route is presumably the reverse Boudouard reaction which is able to reduce carbon deposition and improves catalyst stability. The Fe_xNi_y nano-alloys have a minimal effect on the overall activity, irrespective of overall Fe : Ni atomic ratio and feed composition, when anchored onto the unreducible $ZrO_x@Al_2O_3$. Based on these observations, it is proposed that both the metal oxide overlayer and the Fe_xNi_y nano-alloy are complementary pieces forming a bifunctional tandem catalyst for conversion of CO_2 and C_2H_6 *via* CO_2-ODHE to form C_2H_4 and *via* DRE to form *syngas*. Depending on its chemical properties (*i.e.* interlinked reducibility and surface acid site strength), the metal oxide has a significant influence on the overall bifunctional catalyst activity while the Fe_xNi_y nano-alloy influences the activity, reaction pathway (selectivity) and catalyst stability depending on the Fe : Ni atomic ratio. The analyses of the spent catalysts have shown that to some extent, the deactivation of these materials is due to carbon deposition. However, this carbon deposition is seemingly not detrimental when the DRE activity is dominant. The analyses of the spent catalysts also reveal that the bcc phase of the alloy is re-oxidized into an inverse spinel phase under reaction conditions. It is still not understood how the different fractions of the alloy phases interact with the overlayers to results in either the DRE or CO_2-ODHE activity, but it is clear that a larger fraction of the fcc phase results in the promotion of the DRE while a larger fraction of the bcc phase promotes CO_2-ODHE in the case of the $CrO_x@Al_2O_3$ overlayer.

The catalytic performance of $GaO_x@Al_2O_3$-, $VO_x@Al_2O_3$-, $SmO_x@Al_2O_3$- and $TiO_x@Al_2O_3$-supported Fe_3Ni_1 and Fe_5Ni_1 nano-alloys also emphasize the importance of cooperativity between alloy composition and overlayer acidity/reducibility. Fe_3Ni_1 and Fe_5Ni_1 supported on the strongly acidic and reducible $VO_x@Al_2O_3$ result in highly active and predominantly DRE promoting catalyst systems. On the $GaO_x@Al_2O_3$ overlayer, which exhibits a similar catalytic behaviour as $CrO_x@Al_2O_3$ when tested bare, the Fe_3Ni_1 alloy exhibits a stable CO_2-ODHE activity which is in stark contrast to the DRE activity observed over the Fe_3Ni_1/ $CrO_x@Al_2O_3$ catalyst. Increasing the Fe-content in the alloy results in a reduced CO_2-activation functionality, overall activity and stability with some enhancement of DD, similar to the behaviour on $CrO_x@Al_2O_3$. $Fe_3Ni_1/TiO_x@Al_2O_3$ exhibited a similar trend in selectivity compared to $Fe_3Ni_1/GaO_x@Al_2O_3$ at a much lower conversion level. Increasing the Fe-content in the alloy renders the catalyst essentially inactive. These observations again emphasize that both the alloy and overlayer

interact together to form a bifunctional tandem catalyst in which the performance depends strongly on the respective characteristics of both the alloy composition and the overlayer reducibility/acidity. For both the $Fe_3Ni_1/MO_x@Al_2O_3$ and $Fe_5Ni_1/MO_x@Al_2O_3$ catalyst systems, the initial activity decreases with reducing overlayer acidity as observed for the bare overlayers. The C_2H_4 selectivity is low both when the overlayer acidity is strongest and when it is weakest and is increased when the acidity is intermediate. The CO selectivity shows an opposite trend. Future studies should focus on the combination of metal oxides of intermediate acidity with alloys of overall Fe : Ni atomic ratios between 3 and 5 to optimize CO_2-ODHE activity, selectivity and stability. An active site transformation which can be accelerated by increasing the CO_2 concentration in the feed occurs during the reaction. Seemingly, this active site transformation is associated with higher CO_2-activation functionalities which also cause re-oxidation of the bcc phase of the alloy during the reaction. This transformation results in the formation of active sites with a CO_2-ODHE activity. Despite this, a higher CO_2-concentration has a similar effect on the catalytic behaviour of the overlayer supported alloys compared to the bare overlayers (improves CO_2-activation, stability but reduces C_2H_4 selectivity). The analysis of the spent catalysts confirms the re-oxidation of only the bcc phase of the alloy under reaction conditions while the fcc phase remains metallic. This probably suggests that the re-oxidation of this phase coupled with its interaction with the fcc phase as well as the support results in the formation of active sites responsible for either the CO_2-ODHE or the DRE. Overall, it could be demonstrated, that the Fe_xNi_y nano-alloys are suitable partners for metal oxide catalysts for the enhanced CO_2-activation during simultaneous conversion of CO_2 and C_2H_6. This means, as initially hypothesized, the alloy is able to enhance the CO_2-activation functionality of the metal oxide overlayers.

While it is still uncertain at this stage what active sites are responsible for the observed DRE or CO_2-ODHE activity, it is evident they depend on the physicochemical properties of the overlayer and the alloy. *Operando* studies of the materials as well as gas switching experiments using labelled isotopic gases should be attempted to provide mechanistic understanding as well as identify the active sites.

10 Appendix

10.1 Supplementary figures and tables

Table 10.1: Raman Bands assignments of the bulk metal oxides used as references for overlayers

Bulk oxides	
V_2O_5:	149 cm^{-1} (B_{3g} mode, V-O-V chains, also indicates layered structure lattice)
	201 cm^{-1} (layered structure lattice vibration)
	288 and 410 cm^{-1} (Bending mode, V=O bonds)
	309 and 484 cm^{-1} (Bending mode, V-O-V and V_3-O bonds)
	532 cm^{-1} (Stretching mode, edge-shared oxygens of V_3-O bonds)
	705 cm^{-1} (Stretching mode, corner-shared oxygens of V_2-O bonds)
	999 cm^{-1} (Ag stretching mode, terminal unshared oxygens of V=O bonds). [304]
Cr_2O_3:	325, 363 and 621 cm^{-1} (E_g symmetry modes)
	562 cm^{-1} (A_{1g} symmetry mode) [305]
Sm_2O_3	138 cm^{-1} (E_g symmetry mode)
	363 cm^{-1} (F_g+ A_g symmetry mode)
	440 and 574 cm^{-1} (A_g symmetry mode) [306]
TiO_2	146, 197 and 640 cm^{-1} (E_g symmetry modes)
	398 cm^{-1} (B_{1g} symmetry mode)
	518 cm^{-1} (A_{1g} + B_{1g} symmetry mode) [307]
Ga_2O_3	163 cm^{-1} (B_g symmetry mode), 187 and 220
	cm^{-1} (A_g symmetry modes) → Libration and translation of tetrahedra-octahedra chains
	340, 367, 434and 495 cm^{-1} (A_g symmetry modes) → Deformation of Ga_2O_6 octahedra
	648, 672 and 784 cm^{-1} (A_g symmetry modes) → stretching and bending of GaO_4 tetrahedra [308]
ZrO_2	All monoclinic bands [309]

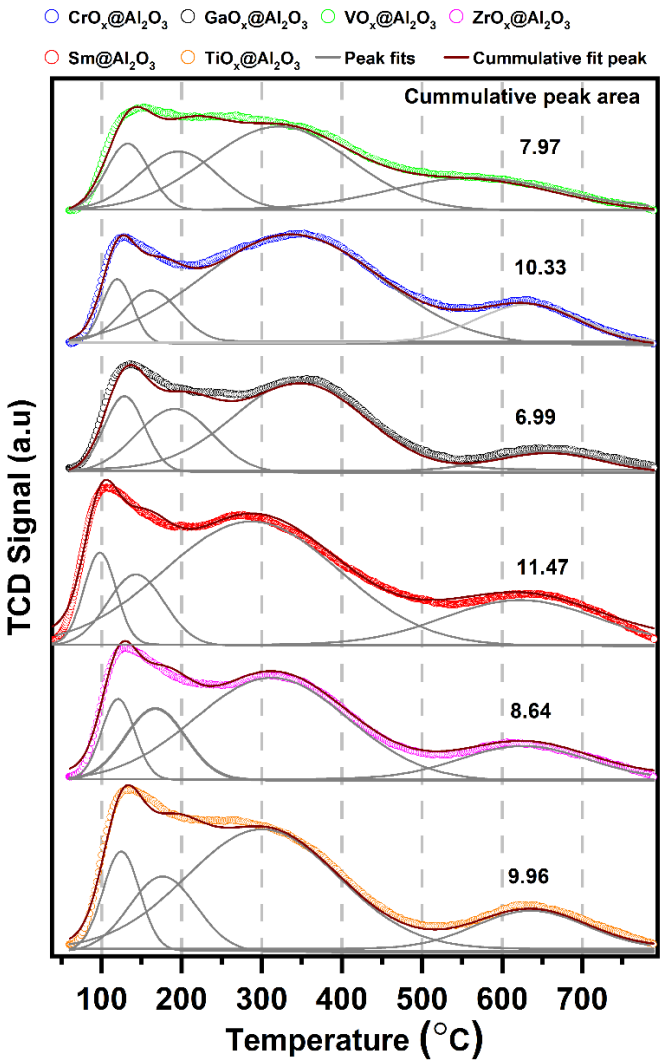

Figure 10.1: Fitted NH_3-TPD profiles of the various $MO_x@Al_2O_3$ supports.

Table 10.2: Summary of fitted NH_3-TPD profiles.

Sample	Desorption Temperatures (°C)				Total desorption peak area
$VO_x@Al_2O_3$	133	196	324	565	7.97
$CrO_x@Al_2O_3$	123	165	337	633	10.33
$GaO_x@Al_2O_3$	128	190	346	658	6.99
$SmO_x@Al_2O_3$	97	142	286	622	11.47
$ZrO_x@Al_2O_3$	123	167	312	625	8.64
$TiO_x@Al_2O_3$	124	176	300	635	9.96

Table 10.3: Summary of all the parameters obtained from Rietveld refinements of the offline XRD data for the nanoparticles with errors included.

Sample	ICP-OES Fe : Ni atomic ratio	Lattice parameters [Error] (Å)	Crystallite size [Error] (nm)
T1.3	3.8	8.353 [0.0004]	11.9 [0.1]
T2.3	4.7	8.355 [0.0021]	8.5 [0.1]
T3.3	3.5	8.351 [0.0010]	7.1 [0.1]
T4.3	6.7	8.360 [0.0005]	11.7 [0.1]
T5.3	3.4	8.350 [0.0008]	6.0 [0.1]
T6.3	3.5	8.323 [0.0037]	2.9 [0.1]
T7.3	2.8	8.336 [0.0160]	3.3 [0.1]
T8.3	6.4	8.379 [0.0080]	7.5 [0.1]
T9.3	10.9	8.355 [0.0010]	10.2 [0.1]
TT1.1	1.2	$Ni(OH)_2$ = 45%, 3.123 * 4.616 [0.0004 * 0.0009] $NiFe_2O_4$ = 55%, 3.364 [0.001]	20.5 [0.5] 9.4 [0.1]
TT1.3	2.5	8.347 [0.0005]	10.6 [0.1]
TT1.5	4.4	8.373 [0.0011]	12.1 [0.1]
TT1-2.3	2.9	8.352 [0.0007]	10.6 [0.1]

TT1-2.5	3.0	8.357 [0.0017]	11.0 [0.1]
TT1-3.3	2.9	8.358 [0.0007]	8.0 [0.1]
TT1-3.5	4.8	8.378 [0.0009]	13.4 [0.1]

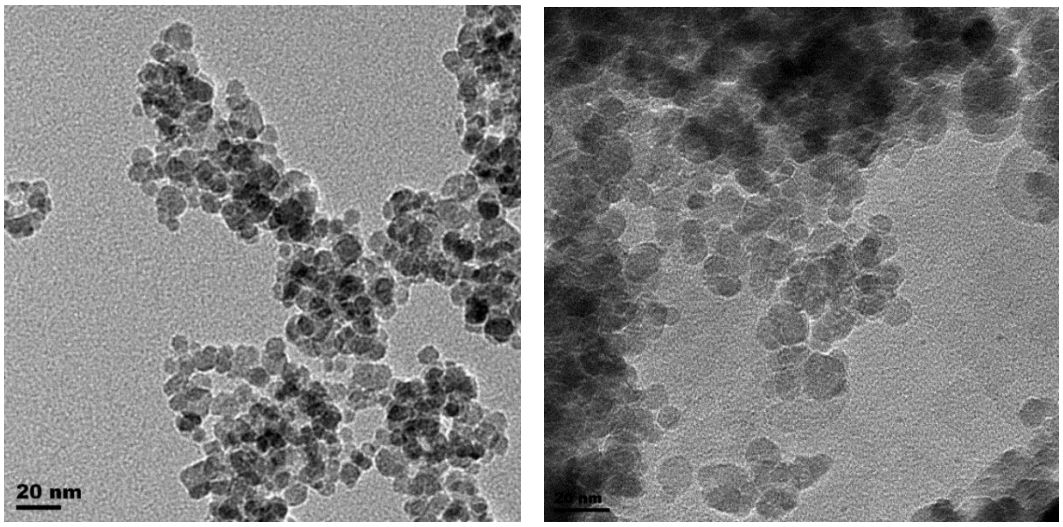

Figure 10.2:TEM images of $(M_xFe_{1-x})Fe_2O_4$ nanoparticles of varying Fe : Ni atomic ratios in samples TT1-2.3 and TT1-2.5 which were synthesized in the small in-house autoclave.

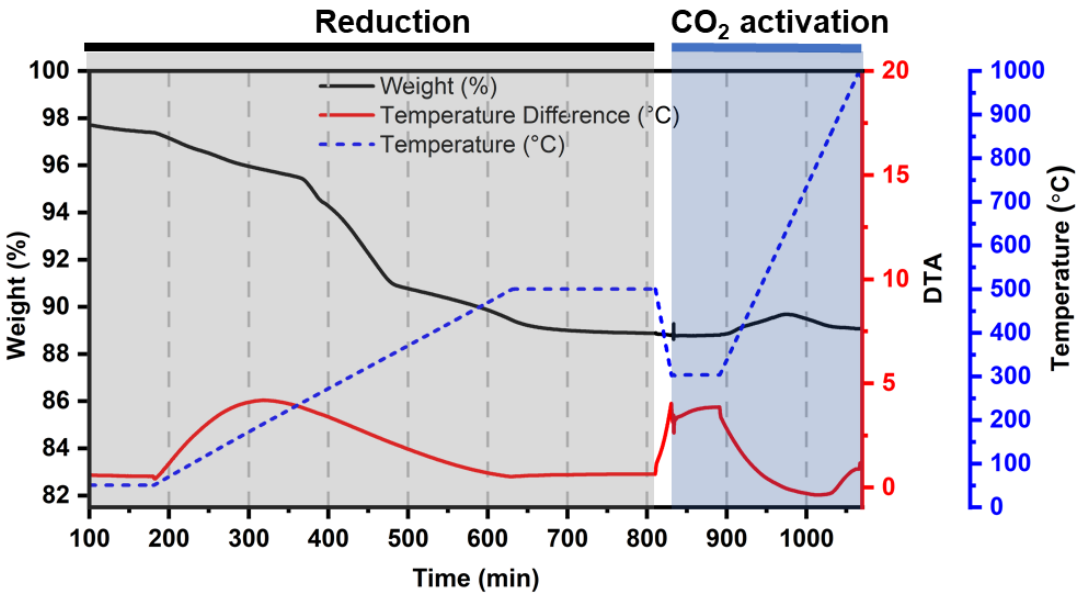

Figure 10.3: TGA/DTA analysis of sample TT1.3 under reduction and the subsequent CO_2 activation conditions. Note the difference in the holding time which is shorter (60 mins) compared to other reported samples.

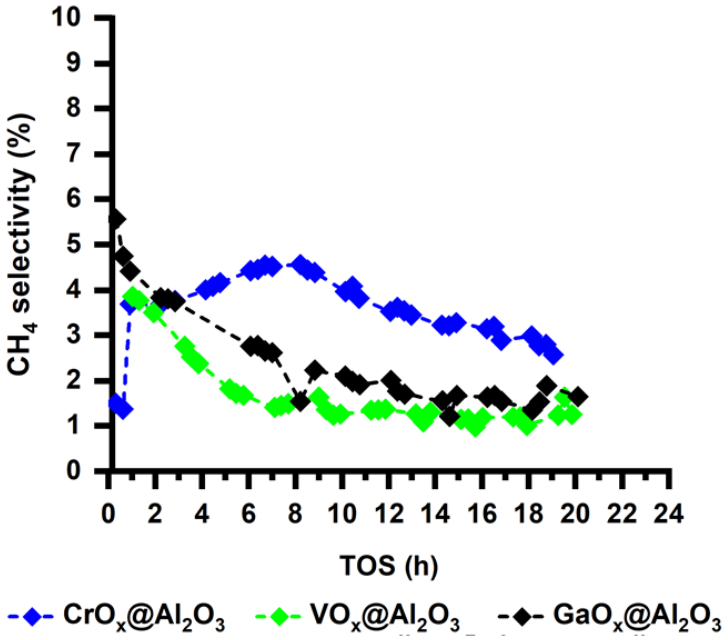

Figure 10.4: CH_4 selectivity obtained during reaction of C_2H_6 (6.25 mL/min) and CO_2 (6.25 mL/min) with a dilution of 50 vol.-% (12.5 mL/min) over the acidic bare overlayers. Conditions: temperature = 600 °C, pressure = 1 atm, space velocity = 15 $L \cdot h^{-1} \cdot g_{cat}^{-1}$, CO_2 : C_2H_6 ratio = 1.

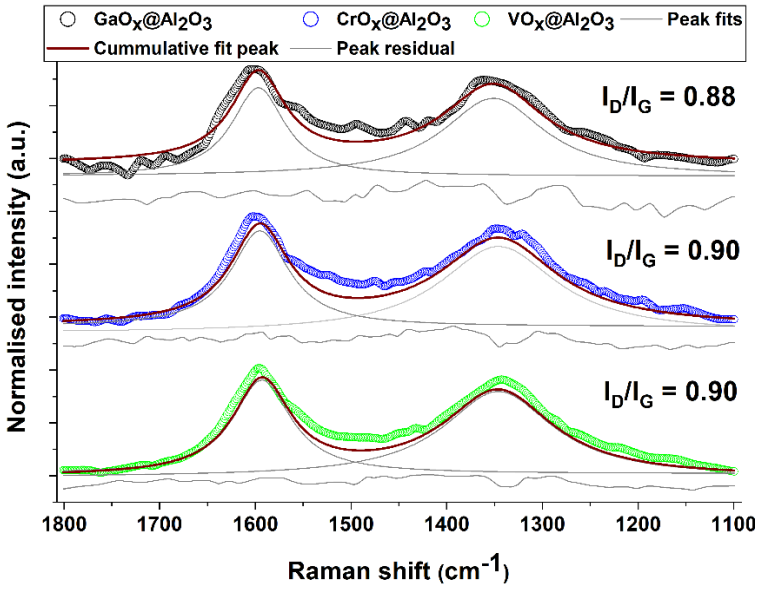

Figure 10.5: Fitted Raman spectra and I_D/I_G ratios of selected spent $MO_x@Al_2O_3$ overlayer catalysts after exposure to CO_2-ODHE conditions in the equimolar feed for 24 h.

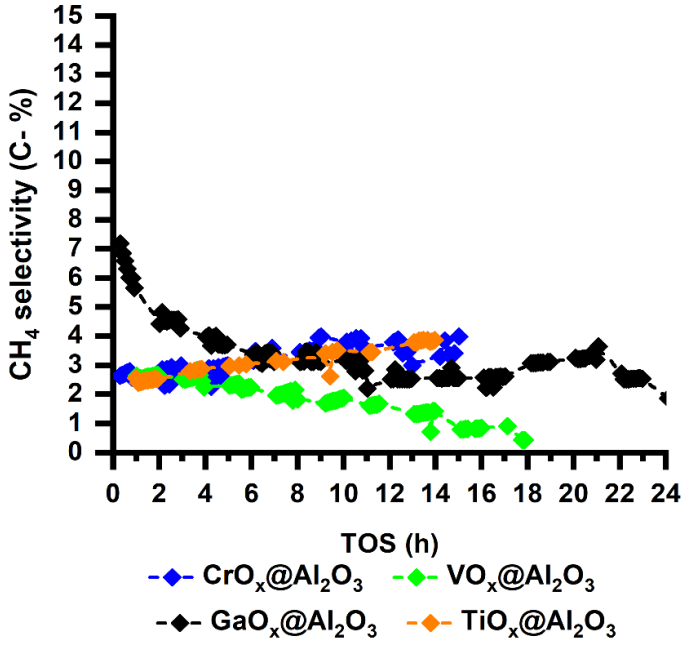

Figure 10.6: CH_4 selectivity obtained during reaction of C_2H_6 (2.1 mL/min) and CO_2 (10.4 mL/min) with a dilution of 50 vol.-% (12.5 mL/min) over the acidic bare overlayers. Conditions: temperature = 600 °C, pressure = 1 atm, space velocity = 15 $L \cdot h^{-1} \cdot g_{cat}^{-1}$, $CO_2 : C_2H_6$ ratio = 5.

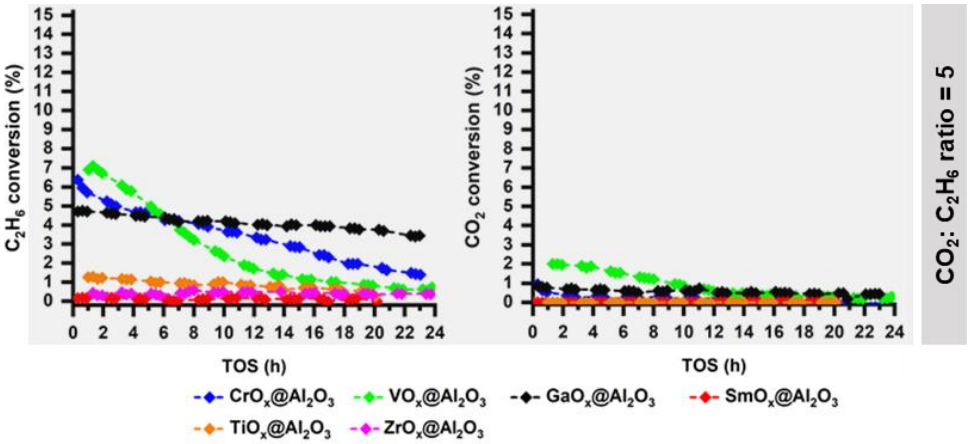

Figure 10.7: C_2H_6 and CO_2 conversions obtained during CO_2-ODHE under a feed with C_2H_6 (2.1 mL/min) : CO_2 (10.4 mL/min) molar ratio of 5 diluted with an inert (12.5 mL/min) over the various MOx@Al2O3 overlayers. Conditions: temperature = 600 °C, pressure = 1 atm and space velocity = 15 $L \cdot h^{-1} \cdot g_{cat}^{-1}$.

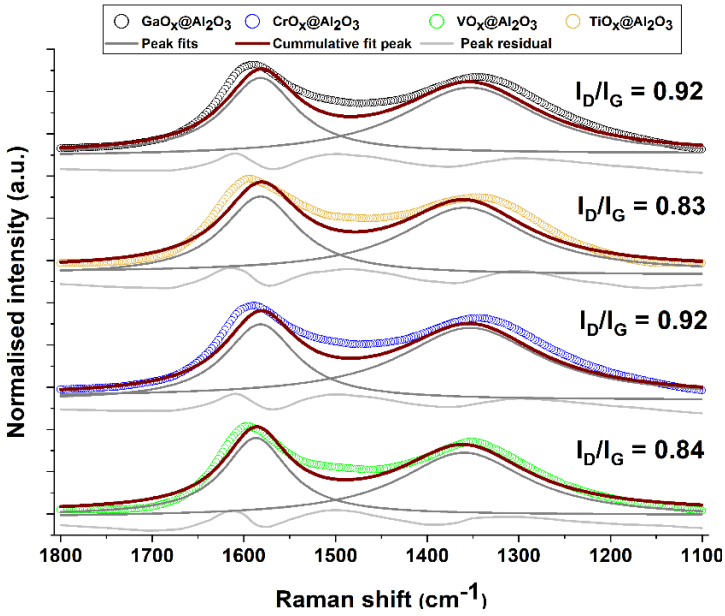

Figure 10.8: Fitted Raman spectra and I_D/I_G ratios of selected spent $MO_x@Al_2O_3$ overlayer catalysts after exposure to CO_2-ODHE conditions in a feed with a CO_2 : C_2H_6 ratio of 5 for 24 h.

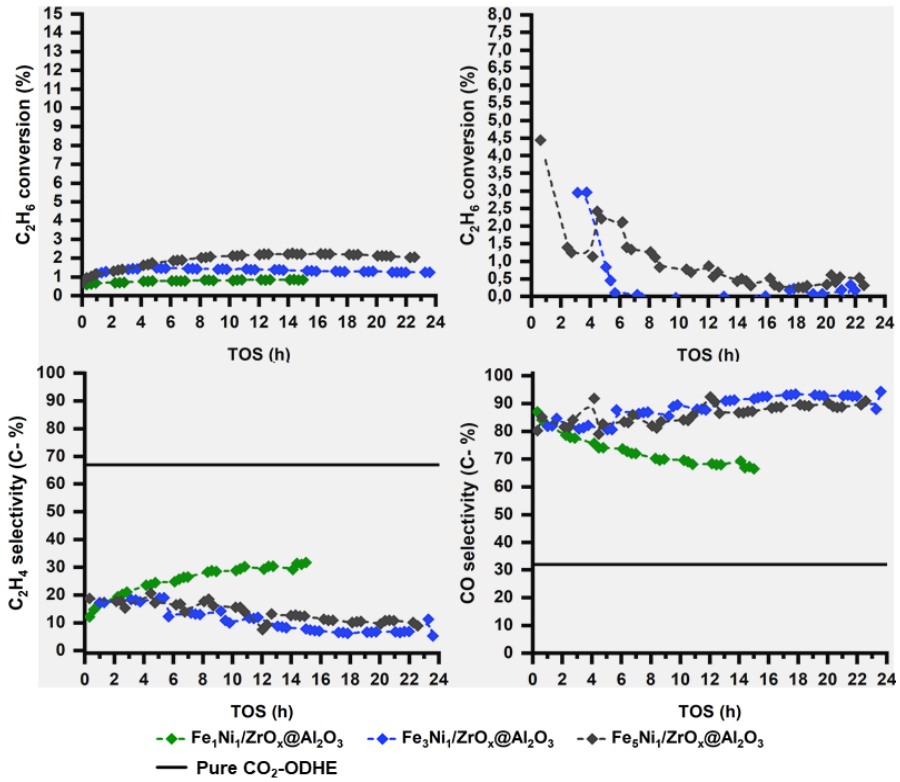

Figure 10.9: C_2H_4 yields and converted CO_2 : C_2H_6 flow rates ratios (top) as well as C_2H_4 and CO selectivity (bottom) obtained during the reaction of C_2H_6 (2.1 mL/min) and CO_2 (10.4 mL/min) diluted with an inert (12.5 mL/min) over the $Fe_xNi_y/ZrO_x@Al_2O_3$ catalysts. Conditions: temperature = 600 °C, pressure = 1 atm, space velocity = 15 $L \cdot h^{-1} \cdot g_{cat}^{-1}$, CO_2: C_2H_6 ratio = 5. Maximum possible carbon based C_2H_4 and CO selectivity for pure CO_2-ODHE are indicated by the black solid lines.

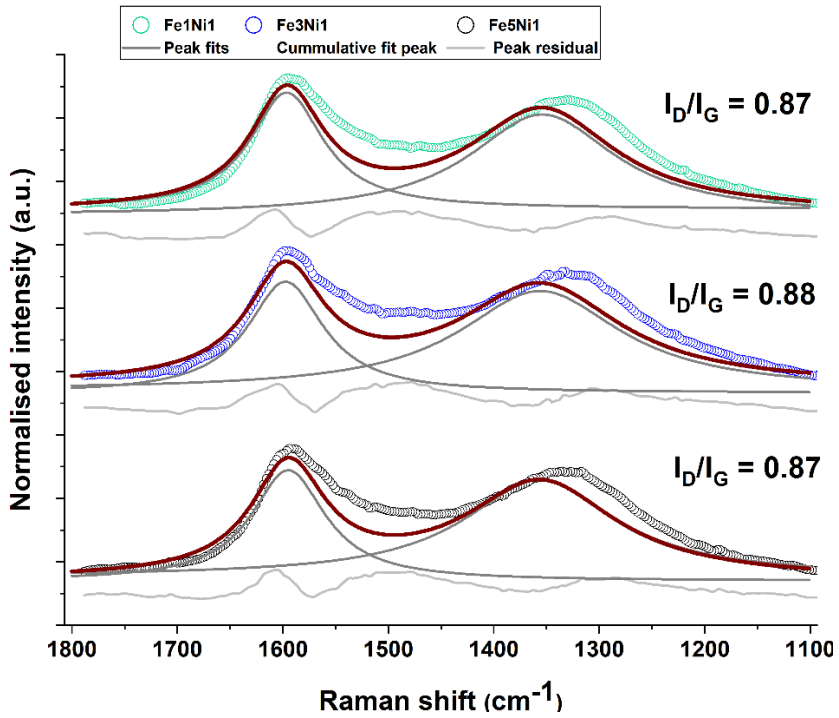

Figure 10.10: Fitted Raman spectra and I_D/I_G ratios of selected spent $Fe_xNi_y/ZrO_x@Al_2O_3$ catalysts after exposure to CO_2-ODHE conditions in the equimolar feed for 24 h.

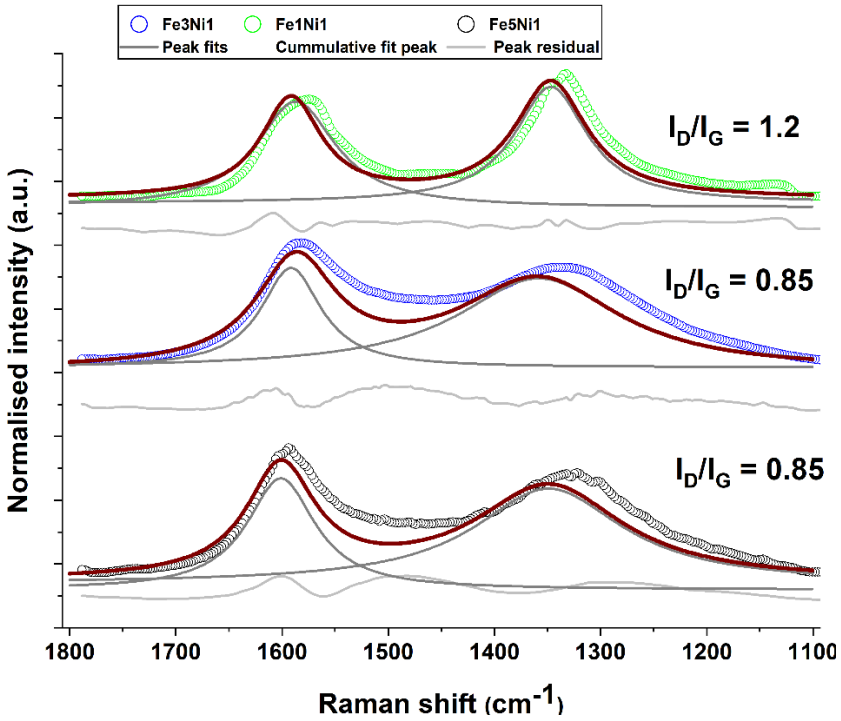

Figure 10.11: Fitted Raman spectra and I_D/I_G ratios of selected spent $Fe_xNi_y/CrO_x@Al_2O_3$ catalysts after exposure to CO_2-ODHE conditions in the equimolar feed for 24 h.

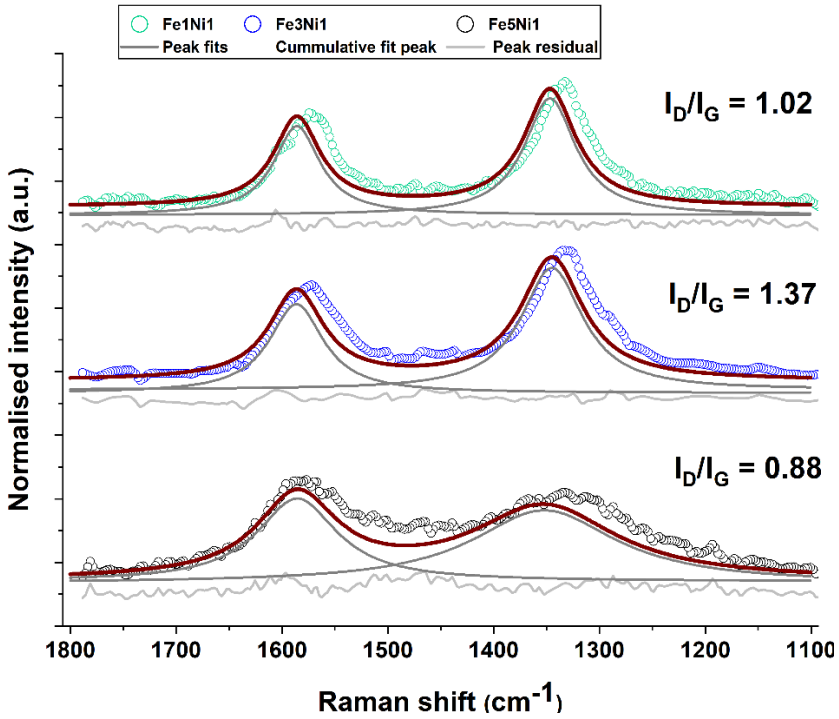

Figure 10.12: Fitted Raman spectra and I_D/I_G ratios of selected spent $Fe_xNi_y/ZrO_x@Al_2O_3$ catalysts after exposure to CO_2-ODHE conditions in a feed with a CO_2 : C_2H_6 ratio of 5 for 24 h.

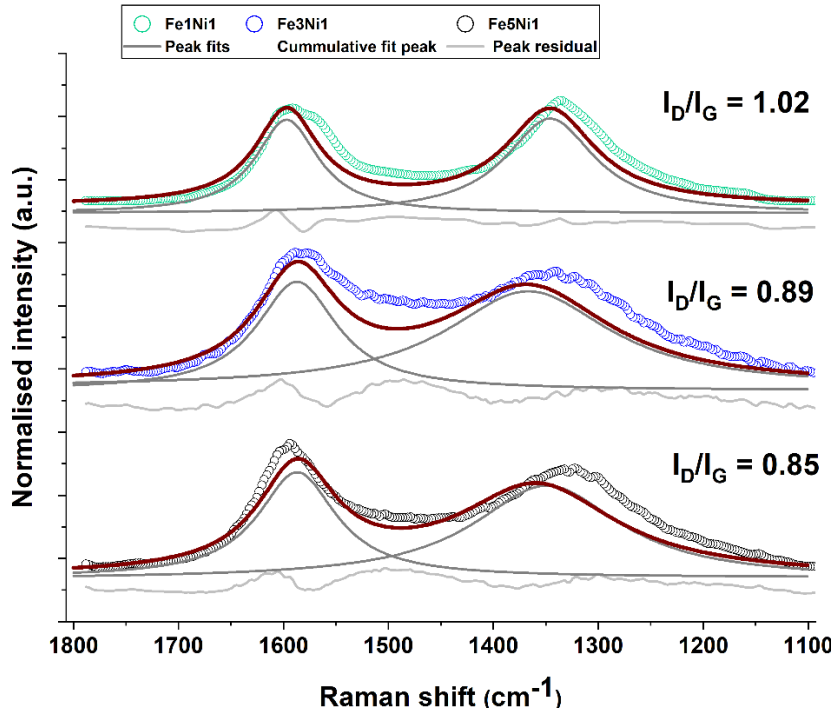

Figure 10.13: Fitted Raman spectra and I_D/I_G ratios of selected spent $Fe_xNi_y/CrO_x@Al_2O_3$ catalysts after exposure to CO_2-ODHE conditions in a feed with a CO_2 : C_2H_6 ratio of 5 for 24 h.

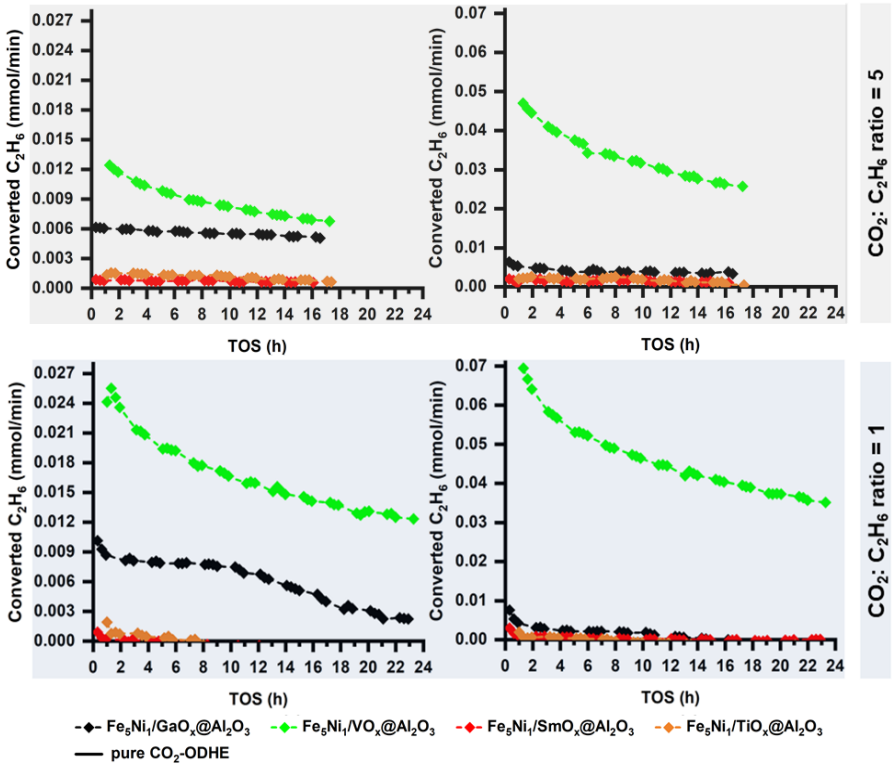

Figure 10.14: Converted C_2H_6 and CO_2 flow rates obtained during CO_2-ODHE under a feed with a CO_2 (10.4 mL/min) : C_2H_6 (2.1 mL/min) molar ratio of 5 (top) as well as under a feed with CO_2 (6.25 mL/min) : C_2H_6 (6.25 mL/min) molar ratio of 1 (bottom) both with an inert dilution of 12.5 ml/min over the $Fe_5Ni_1/MO_x@Al_2O_3$ catalysts. Conditions: temperature = 600 °C, pressure = 1 atm and total space velocity = 15 $L \cdot h^{-1} \cdot g_{cat}^{-1}$.

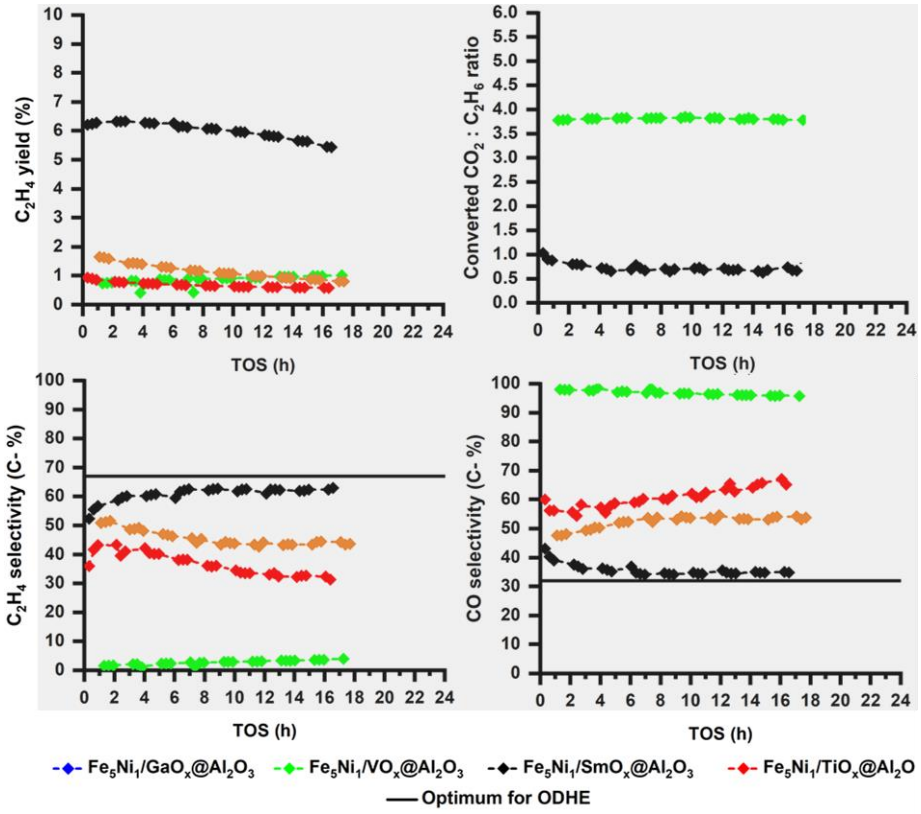

Figure 10.15: C_2H_4 yields and converted CO_2 : C_2H_6 flow rates ratios (top) as well as C_2H_4 and CO selectivity (bottom) obtained during the reaction of C_2H_6 (2.1 mL/min) and CO_2 (10.4 mL/min) diluted with an inert (12.5 mL/min) over the $Fe_5Ni_1/MO_x@Al_2O_3$ catalysts. Conditions: temperature = 600 °C, pressure = 1 atm, space velocity = 15 $L \cdot h^{-1} \cdot g_{cat}^{-1}$, CO_2: C_2H_6 ratio = 5. Maximum possible carbon based C_2H_4 and CO selectivity for pure CO_2-ODHE are indicated by the black solid lines.

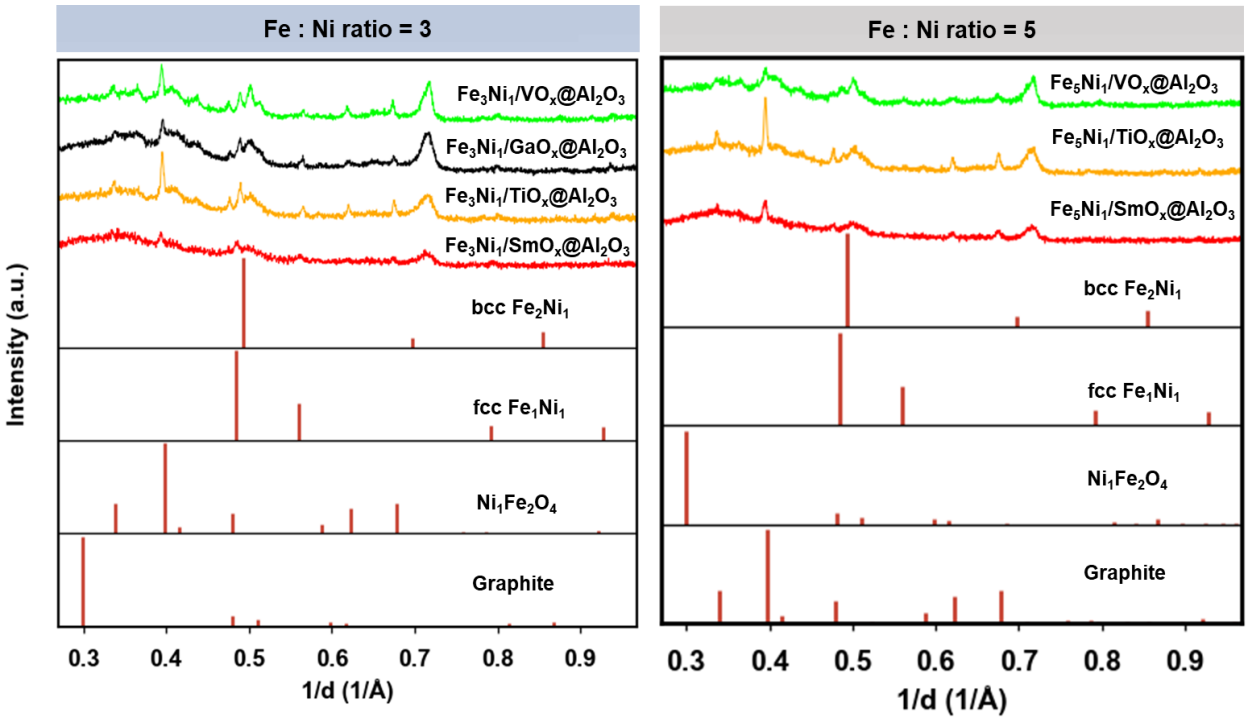

Figure 10.16: Stacked offline XRD patterns of spent $Fe_3Ni_1/MO_x@Al_2O_3$ (left) and $Fe_5Ni_1/MO_x@Al_2O_3$ (right) catalysts retrieved after a 24 h testing for CO_2-ODHE under a feed with a CO_2 : C_2H_6 ratio of 5 . The reference patterns provided correspond to graphite (PDF-4 01-073-5918), $NiFe_2O_4$ (PDF-4 04-014-8286), fcc Fe_1Ni_1 (PDF-4 04-003-3531) and bcc Fe_2Ni_1 (PDF-4 04-018-7295).

10.2 Curriculum Vitae

22 Station Road, Unit 46, Mowbray, Cape Town, 7700 • +27799058588 • *sraseala@gmail.com*

Personal Details

Title	First name: Shaine	Surname: Raseale
Nationality: South African	Race: Black	Place of birth: Johannesburg
Date of birth: 1991-04-05	Marital Status: Single	Health: Moderate Myopia
ID No: 9104056066088		
Online profiles: Linkedin	https://www.linkedin.com/in/shaine-raseala-905b6b79	
Researchgate	https://www.researchgate.net/profile/Shaine-Raseale	
ORCID	https://orcid.org/my-orcid?orcid=0000-0001-7633-3627	

Education

1. Doctor of Philosophy (Chemical engineering, 2017-2022)	*University of Cape Town (South Africa)*
2. Master of Science (Structural Chemistry & Spectroscopy, 2014-2017)	*Universität Leipzig (Germany)*
3. Bachelor of Science Honours (Chemistry, 2013)	*University of Limpopo (South Africa)*
4. Bachelor of Science (Chemistry and Biochemistry, 2010-2012).	*University of Limpopo (South Africa)*
5. National Seniour Certificate (Matriculation, 2009).	*Molai Jubilee Sec. school (South Africa)*
6. Computer Literacy Diploma certificate (Microsoft Office, 2008).	*Flying High art foundations (South Africa)*

Work Experience

Research Assistant	Department of Chemical Engineering, University of Cape Town (South Africa)	2021
Teaching Assistant	Department of Chemistry, University of Limpopo (South Africa)	2012-2014
Laboratory demonstrator	Department of Chemistry, University of Limpopo (South Africa)	2014
Examination assistant for NSC marking	Limpopo Department of Education (South Africa)	2012-2013

Awards and scholarships

- DST-NRF Centre of Excellence in Catalysis c*change PhD bursary (2017-2020)
- NRF Freestanding doctoral scholarship (2018-2020)
- Erasmus Mundus-Eurosa Scholarship (2014-2017)
- SASOL Inzalo foundation NRF fellowship (2014)
- SASOL Inzalo foundation bursary (2013-2014)
- NSFAS (2010-2012)
- South African Chemical Institute (SACI), 2013 Limpopo symposium 2nd best young chemist oral presentation award
- University of Limpopo Merit awards (2012, 2013 and 2014)
- Best Mathematics learner in Modjadji circuit certificate (2009)

Research travel and workshops

- Synchrotron beamtime access for *in situ* XPS, Beamline: B07, Diamond Light Source, Harwell, England, United Kingdom (2019)

  Hosts: Georg Held
- Research visit for catalyst characterization, Max-Planck-Institut für Kohlenforschung, Mülheim an der Ruhr, Germany (2019)

  Hosts: Dr. Gonzalo Prieto and Prof. Dr. Ferdi Schüth
- Research visit for catalyst synthesis, Max-Planck-Institut für Kohlenforschung, Mülheim an der Ruhr, Germany (2018)

  Hosts: Dr. Gonzalo Prieto and Prof. Dr. Ferdi Schüth
- Attendance to ANSDAC workshop, Department of Chemical Engineering, University of Cape town, South Africa (2019)

  Hosts: A. Prof. Nico Fischer
- Student visit for XPS workshop, Department of Physics, University of Johannesburg, South Africa (2018)

  Hosts: Prof. Bryan Doyle

List of publications (including collaborations)

1. *S. Raseale, W. Marquart, K. Jeske, G. Prieto, M. Claeys, N. Fischer, Supported Fe_xNi_y catalysts for the co-activation of CO_2 and small alkanes, Faraday Discuss. 229 (2020) 208-231. https://doi.org/10.1039/C9FD00130A.*
2. *W. Marquart, S. Raseale, M. Claeys, N. Fischer, Promoted Mo_xC_y-based catalysts for the CO2 oxidative dehydrogenation of ethane, ChemCatChem, (2022) 1-13. https://doi.org/10.1002/cctc.202200267.*

3. *W. Marquart, S. Raseale, G. Prieto, A. Zimina, B. B. Sarma, J-D. Grunwaldt, M. Claeys, N. Fischer, CO_2 Reduction over Mo_2C-Based Catalysts, ACS Catal., (2021) 1624–1639. https://doi.org/10.1021/acscatal.0c05019.*

Other research involvements and experience

1. **Master thesis title: Modified Biogenic Silica for adsorption applications** (Supervisors: Prof. Dr. D Enke and Mr. S Sander, *Universität Leipzig*, Germany). 2017
2. **Honours degree mini-dissertation tittle: Synthesis of 2-monosubstituted Quinoxaline derivatives using Methanesulfonyloxy as a leaving group and their biological applications.** (Supervisor: Dr. W. Nxumalo, *University of Limpopo*, South Africa). 2013
3. Synthesis and characterization of metal-oxide over-layers (Supervisor: Dr. G. Prieto, *Max-Planck-Institut für Kohlenforschung,* Germany). Research visit on a collaboration project, 2018.
4. Synthesis of novel Rare earth hydride oxide materials (Supervisors: Prof. Dr. H Kohlmann and Mr. A Werwein, *Universität Leipzig*, Germany). University-coordinated and mandatory internship project, 2016.
5. Influence of synthetic impurities on the reversible cis-trans isomerization of a selected Aminoazobenzene derivative. (Supervisor: Dr. K Siefermann, *Leibniz institute of surface modification (IOM)*, Germany). University-coordinated and mandatory internship project, 2015.
6. Structural characterization of solid-state catalysts. (Supervisors: Prof. Dr. D Enke and Dr J Kullmann, *Universität Leipzig*, Germany). University-coordinated and mandatory internship project, 2015.

Conference presentations

1. The 27th North American Catalysis Society Meeting (NAM27), New York City, USA, May 2022. Oral presentation by Wijnand Marquart: Oxidative Dehydrogenation of Ethane with CO_2 over Metal Oxide Overlayer Supported Fe_xNi_y Catalysts: Overlayer Support Effects.
2. 17th International Congress on Catalysis (ICC2020), San Diego, USA, June 2020, Abstract accepted for Oral presentation and published due to conference cancellation in light of COVID-19: Oxidative dehydrogenation of ethane with CO_2 over iron-nickel nanoalloys.
3. Catalysis Society of South Africa (CATSA) conference, Western Cape province, November 2019. Oral presentation: Oxidative dehydrogenation of ethane with CO_2 over FeNi nanoalloys supported on metal oxide overlayers.
4. Catalysis Society of South Africa (CATSA) 2017 conference, North-west province, 19-22 November 2017. Poster presentation: ODH of ethane with CO_2 over FeNi nanoalloys supported on metal-oxide over-layers.
5. Syngas convention 3, international conference hosted in Cape Town, 25-28 March 2018.

Poster presentation: ODH of ethane with CO_2 over FeNi nanoalloys supported on metal-oxide over-layers.

6. Catalysis Society of South Africa (CATSA) 2017 conference, North-west province, 19-22 November 2017. Poster presentation: ODH of ethane with CO_2 over FeNi nanoalloys supported on metal-oxide over-layers.
7. c*Change DST-NRF centre for excellence in catalysis symposium 2017, Gauteng province, 17-19 November 2017. Oral presentation: ODH of ethane with CO_2 over FeNi nanoalloys supported on metal-oxide over-layers.
8. 18th Vortragstagung Fachgruppe Festkörperchemie und Materialforschung, September 2016, Universität Innsbruck, Austria. Poster presentation: Synthesis of new rare earth hydride oxides LnHO (Ln = Sm,Gd,Ho,Er)
9. South African Chemical Institute Limpopo symposium, October 2013, University of Venda, Limpopo province. Oral presentation: Synthesis of 2-monosubstituted Quinoxaline derivatives using Methanesulfonyloxy as a leaving group and their biological applications. *2nd prize awarded.*

Additional

- 4th year Chemical engineering project supervision of about 4 students (2017-2018). *University of Cape Town*
- Co-founded and participated in running a village community-based organization (Juvenilles' ladder to success) that tutor, mobilize and motivate grade 12 high school learners in Modjadji circuit (2009-2012).
- Fluent in English, Sepedi, Sotho and Tsonga.

References

1. Prof. Dr. D Enke, Master thesis supervisor: dirk.enke@uni-leipzig.de
2. Prof. Dr. R Denecke, Dean of International MSc program at Leipzig University: denecke@uni-leipzig.de
3. Prof. Dr. H Kohlmann, Practical project course supervisor: holger.kohlmann@uni-leipzig.de
4. A. Prof. N Fischer, PhD main supervisor: nico.fischer@uct.ac.za
5. A. Prof. W Nxumalo, Honours degree mini thesis supervisor: winston.nxumalo@ul.ac.za
6. Dr. K.D Modibane, Senior Lecturer (University of Limpopo): Kwena.Modibane@ul.ac.za
7. Mr. S Sander, Master thesis co-supervisor: stephan.sander@physik.uni-halle.de

11 References

[1] E. Gomez, B. Yan, S. Kattel, J.G. Chen, Carbon dioxide reduction in tandem with light-alkane dehydrogenation, Nat Rev Chem 7 (2019) 2580. https://doi.org/10.1038/s41570-019-0128-9.

[2] Z. Xie, E. Gomez, J.G. Chen, Simultaneously upgrading CO 2 and light alkanes into value-added products, AIChE J 4 (6) (2021) 3. https://doi.org/10.1002/aic.17249.

[3] H. Deng, H. Chen, H. Li, Synthesis of crystal MFe2O4 (M=Mg, Cu, Ni) microspheres, Materials Chemistry and Physics 101 (2-3) (2007) 509–513. https://doi.org/10.1016/j.matchemphys.2006.10.002.

[4] H. Deng, X. Li, Q. Peng, X. Wang, J. Chen, Y. Li, Monodisperse magnetic single-crystal ferrite microspheres, Angew. Chem. Int. Ed Engl. 44 (18) (2005) 2782–2785. https://doi.org/10.1002/anie.200462551.

[5] S. Deng, S. Li, H. Li, Y. Zhang, Oxidative Dehydrogenation of Ethane to Ethylene with CO 2 over Fe−Cr/ZrO 2 Catalysts, Ind. Eng. Chem. Res. 48 (16) (2009) 7561–7566. https://doi.org/10.1021/ie9007387.

[6] S. Deng, H. Li, Y. Zhang, Oxidative Dehydrogenation of Ethane with Carbon Dioxide to Ethylene over Nanosized Cr2O3 Catalysts, Chinese Journal of Catalysis 24 (10) (2003) 744–750.

[7] N. Mimura, M. Okamoto, H. Yamashita, S.T. Oyama, K. Murata, Oxidative dehydrogenation of ethane over Cr/ZSM-5 catalysts using CO2 as an oxidant, J. Phys. Chem. B 110 (43) (2006) 21764–21770. https://doi.org/10.1021/jp061966l.

[8] N. Mimura, I. Takahara, M. Inaba, M. Okamoto, K. Murata, High-performance Cr/H-ZSM-5 catalysts for oxidative dehydrogenation of ethane to ethylene with CO2 as an oxidant, Catalysis Communications 3 (6) (2002) 257–262. https://doi.org/10.1016/S1566-7367(02)00117-6.

[9] K. Nakagawa, C. Kajita, K. Okumura, N.-o. Ikenaga, M. Nishitani-Gamo, T. Ando, T. Kobayashi, T. Suzuki, Role of Carbon Dioxide in the Dehydrogenation of Ethane over Gallium-Loaded Catalysts, Journal of Catalysis 203 (1) (2001) 87–93. https://doi.org/10.1006/jcat.2001.3306.

[10] S. Wang, K. Murata, T. Hayakawa, S. Hamakawa, K. Suzuki, Dehydrogenation of ethane with carbon dioxide over supported chromium oxide catalysts, Applied Catalysis A: General 196 (1) (2000) 1–8. https://doi.org/10.1016/S0926-860X(99)00450-0.

[11] K. Nakagawa, M. Okamura, N. Ikenaga, T. Suzuki, T. Kobayashi, Dehydrogenation of ethane over gallium oxide in the presence of carbon dioxide, Chem. Commun. (9) (1998) 1025–1026.

[12] K. Murata, T. Hayakawa, S. Hamakawa, K. Suzuki, Effect of promoters on catalytic performance of Cr/SiO2 catalysts in oxidative dehydrogenation of ethane with carbon dioxide.

[13] T.A. Bugrova, V.V. Dutov, V.A. Svetlichnyi, V. Cortés Corberán, G.V. Mamontov, Oxidative dehydrogenation of ethane with CO2 over CrOx catalysts supported on Al2O3, ZrO2, CeO2 and CexZr1-xO2, Catalysis Today 333 (2019) 71–80. https://doi.org/10.1016/j.cattod.2018.04.047.

[14] J. C. Védrine, Heterogeneous Partial (amm)Oxidation and Oxidative Dehydrogenation Catalysis on Mixed Metal Oxides, Catalysis 6 (22) (2016).

[15] J. C. Védrine, The Role of Redox, Acid-Base and Collective Properties and of Cristalline State of Heterogeneous Catalysts in the Selective Oxidation of Hydrocarbons, Topics in Catalysis 21 (2002) 97–106.

[16] J. Ko, B.-K. Kim, J.W. Han, Density Functional Theory Study for Catalytic Activation and Dissociation of CO 2 on Bimetallic Alloy Surfaces, J. Phys. Chem. C 120 (6) (2016) 3438–3447. https://doi.org/10.1021/acs.jpcc.6b00221.

[17] E. Gomez, Z. Xie, J.G. Chen, The effects of bimetallic interactions for CO 2 -assisted oxidative dehydrogenation and dry reforming of propane, AIChE J 65 (8) (2019). https://doi.org/10.1002/aic.16670.

[18] B. Yan, S. Yao, J.G. Chen, Effect of oxide support on catalytic performance of FeNi-based catalysts for CO2-assisted oxidative dehydrogenation of ethane, ChemCatChem 10 (2019).

[19] M. Myint, B. Yan, J. Wan, S. Zhao, J.G. Chen, Reforming and oxidative dehydrogenation of ethane with CO2 as a soft oxidant over bimetallic catalysts, Journal of Catalysis 343 (2016) 168–177. https://doi.org/10.1016/j.jcat.2016.02.004.

[20] Elaine Gomez, Shyam Kattel, Binhang Yan, Siyu Yao, Ping Liu, Jingguang G. Chen, Combining CO2 reduction with propane oxidative dehydrogenation over bimetallic catalysts.

[21] K. Tomishige, D. Li, M. Tamura, Y. Nakagawa, Nickel–iron alloy catalysts for reforming of hydrocarbons: Preparation, structure, and catalytic properties, Catal. Sci. Technol. 7 (18) (2017) 3952–3979. https://doi.org/10.1039/C7CY01300K.

[22] R.A. Sheldon, Engineering a more sustainable world through catalysis and green chemistry, J. R. Soc. Interface 13 (2016).

[23] E. McFarland, Unconventional chemistry for unconventional natural gas, Science 338 (6105) (2012) 340–342. https://doi.org/10.1126/science.1226840.

[24] J.J. Siirola, The impact of shale gas in the chemical industry, AIChE J. 60 (3) (2014) 810–819. https://doi.org/10.1002/aic.14368.

[25] W. Tittle, A. Chan, W. Wang, D. Chen, Market outlook: US ethane to go global: US ETHANE SUPPLY AND DEMAND, 2015. https://www.icis.com/explore/resources/news/2015/02/26/9864511/market-outlook-us-ethane-to-go-global/.

[26] S. Sarin, Ethane Export Terminal: PEP Review 2020-12, 2020. https://ihsmarkit.com/products/pep-review-2020-12-ethane-export-terminal.html (accessed 10 February 2021).

[27] F. Cavani, N. Ballarini, A. Cericola, Oxidative dehydrogenation of ethane and propane: How far from commercial implementation? Catalysis Today 127 (1-4) (2007) 113–131. https://doi.org/10.1016/j.cattod.2007.05.009.

[28] A. Qiao, V.N. Kalevaru, J. Radnik, A. Martin, Oxidative dehydrogenation of ethane to ethylene over Ni-Nb-M-O catalysts: Effect of promoter metal and CO 2 -admixture on the performance, Catalysis Today 264 (2016) 144–151. https://doi.org/10.1016/j.cattod.2015.08.043.

[29] Mark Eramo, Global Ethylene market outlook. Inagural ethylene forum, 2017. https://www.ihs.com/products/world-petro-chemical-analysis-ethylene.html (accessed 7 July 2017).

[30] G. M., Ethylene production capacity globally 2030, 2019. https://www.statista.com/statistics/1067372/global-ethylene-production-capacity/ (accessed 8 June 2020.887Z).

[31] V.Z. Fridman, Pathways of light compounds formation during propane and isobutane dehydrogenation on Al-Cr catalysts, Applied Catalysis A: General 382 (2) (2010) 139–147. https://doi.org/10.1016/j.apcata.2010.04.026.

[32] H.N. Pham, J.J.H.B. Sattler, B.M. Weckhuysen, A.K. Datye, Role of Sn in the Regeneration of Pt/γ-Al2O3 Light Alkane Dehydrogenation Catalysts, ACS Catal. 6 (4) (2016) 2257–2264. https://doi.org/10.1021/acscatal.5b02917.

[33] R. Grabowski, Kinetics of Oxidative Dehydrogenation of C 2 -C 3 Alkanes on Oxide Catalysts, Catalysis Reviews 48 (2) (2006) 199–268. https://doi.org/10.1080/01614940600631413.

[34] H. Al-Megren, T. Xiao, Petrochemical catalyst materials, processes, and emerging technologies, Engineering Science Reference, Hershey, PA, 2016.

[35] P. Tang, Q. Zhu, Z. Wu, D. Ma, Methane activation: The past and future, Energy Environ. Sci. 7 (8) (2014) 2580–2591. https://doi.org/10.1039/C4EE00604F.

[36] M. Aresta, A. Dibenedetto, E. Quarantana, Reaction Mecahnisms in Carbon Dioxide Conversion, Springer, Berlin, Heidelberg, 2016.

[37] I. Amghizar, J.N. Dedeyne, D.J. Brown, G.B. Marin, K.M. van Geem, Sustainable innovations in steam cracking: CO 2 neutral olefin production, React. Chem. Eng. 5 (2) (2020) 239–257. https://doi.org/10.1039/C9RE00398C.

[38] M. Soltanieh, A. Zohrabian, M.J. Gholipour, E. Kalnay, A review of global gas flaring and venting and impact on the environment: Case study of Iran, International Journal of Greenhouse Gas Control 49 (2016) 488–509. https://doi.org/10.1016/j.ijggc.2016.02.010.

[39] G.P. Peters, R.M. Andrew, S. Solomon, P. Friedlingstein, Measuring a fair and ambitious climate agreement using cumulative emissions, Environ. Res. Lett. 10 (10) (2015) 105004. https://doi.org/10.1088/1748-9326/10/10/105004.

[40] Y.A. Daza, J.N. Kuhn, CO 2 conversion by reverse water gas shift catalysis: Comparison of catalysts, mechanisms and their consequences for CO 2 conversion to liquid fuels, RSC Adv. 6 (55) (2016) 49675–49691. https://doi.org/10.1039/C6RA05414E.

[41] M. Aresta, Carbon dioxide as chemical feedstock, Wiley-VCH, Weinheim, 2010.

[42] K.M.K. Yu, I. Curcic, J. Gabriel, S.C.E. Tsang, Recent advances in CO2 capture and utilization, ChemSusChem 1 (11) (2008) 893–899. https://doi.org/10.1002/cssc.200800169.

[43] Funsho Babarinde Mayowa Ayodele Adio, A Review of Carbon Capture and Sequestration Technology, Journal of Energy Technology and Environment 2 (2020) 1–11.

[44] G. Turan, L. Temple-Smith, Global CCS Institute welcomes the 20th and 21st large-scale CCS facilities into operation, Global CCS intitute, Washington, DC, USA, 3-June-2020.

[45] Global CCS institute, The Global Status of CCS: 2020, 2020. https://www.globalccsinstitute.com/wp-content/uploads/2020/12/Global-Status-of-CCS-Report-2020_FINAL_December11.pdf (accessed 10 February 2021).

[46] S. Deutz, A. Bardow, Life-cycle assessment of an industrial direct air capture process based on temperature–vacuum swing adsorption, Nat Energy 8 (2021) 325. https://doi.org/10.1038/s41560-020-00771-9.

[47] Q. Zhu, Developments on CO2-utilization technologies, Clean Energy 3 (2) (2019) 85–100. https://doi.org/10.1093/ce/zkz008.

[48] D.W. Keith, G. Holmes, D. St. Angelo, K. Heidel, A Process for Capturing CO2 from the Atmosphere, Joule 2 (8) (2018) 1573–1594. https://doi.org/10.1016/j.joule.2018.05.006.

[49] Climeworks, Direct air capture: A technology to reverse climate change. Climeworks develops, builds and operates direct air capture machines. https://climeworks.com/co2-removal (accessed 08-Feb-2021).

[50] XPRIZE, TURNING CO2 INTO PRODUCTS: XPRIZE. Transforming CO2 into Valuable Products. 2019. https:// carbon.xprize.org/prizes/carbon (10 January 2019, date last accessed), 2020. https://carbon.xprize.org/prizes/carbon (accessed 10 April 2020).

[51] N. Fischer, M. Claeys, Phase changes studied under in situ conditions—A novel cell, Catalysis Today 275 (2016) 149–154. https://doi.org/10.1016/j.cattod.2016.03.003.

[52] N. Fischer, B. Clapham, T. Feltes, E. van Steen, M. Claeys, Size-Dependent Phase Transformation of Catalytically Active Nanoparticles Captured In Situ, Angew. Chem. Int. Ed. 53 (5) (2014) 1342–1345. https://doi.org/10.1002/anie.201306899.

[53] M.C.M. Claeys, N.F. Fischer (Claeys, Michael Christian Miximilian; Fischer, Nico Frederik) US 8,597,598 B2, 2012.

[54] Hannah Ritchie, Max Roser, CO_2 and Greenhouse Gas Emissions, Our World in Data (2017).

[55] S. Monkman, M. MacDonald, R.D. Hooton (Eds.), Using Carbon Dioxide as a Beneficial Admixture in Ready-Mixed Concrete, 2014.

[56] A. Martino, Sunshine to Petrol: Solar Recycling of Carbon Dioxide into Hydrocarbon Fuels, 2009. http://energy.sandia.gov/wp-content/gallery/uploads/S2P_SAND2009-5796P.pdf (accessed 10 April 2020).

[57] M. Jendrischik, CO2 as a raw material for waxes and fuels, 2016. https://setis.ec.europa.eu/publications/setis-magazine/carbon-capture-utilisation-and-storage/co2-raw-material-waxes-and-fuels (accessed 10 April 2020).

[58] CRI, Technology and Services - CRI - Carbon Recycling International, 2018. https://www.carbonrecycling.is/technology-and-services#services-banner-1 (accessed 10 April 2020).

[59] B. Jerew, Vulcanol – Synthetic Fuel Made From Carbon Dioxide and Volcano Power - The Green Optimistic, 2013. https://www.greenoptimistic.com/vulcanol-synthetic-fuel-made-carbon-dioxide-volcano-power-20131129/ (accessed 10 April 2020).

[60] S. Raseale, W. Marquart, K. Jeske, G. Prieto, M. Claeys, N. Fischer, Supported FexNiy catalysts for the co-activation of CO2 and small alkanes, Faraday Discuss. (2020). https://doi.org/10.1039/C9FD00130A.

[61] J.C. Védrine, Heterogeneous Partial (amm)Oxidation and Oxidative Dehydrogenation Catalysis on Mixed Metal Oxides, Catalysts 6 (2) (2016) 22. https://doi.org/10.3390/catal6020022.

[62] B. Yan, S. Yao, S. Kattel, Q. Wu, Z. Xie, E. Gomez, P. Liu, D. Su, J.G. Chen, Active sites for tandem reactions of CO2 reduction and ethane dehydrogenation, Proc. Natl. Acad. Sci. U. S. A. 115 (33) (2018) 8278–8283. https://doi.org/10.1073/pnas.1806950115.

[63] M.D. Porosoff, M.N.Z. Myint, S. Kattel, Z. Xie, E. Gomez, P. Liu, J.G. Chen, Identifying Different Types of Catalysts for CO2 Reduction by Ethane through Dry Reforming and Oxidative Dehydrogenation, Angew. Chem. Int. Ed Engl. 54 (51) (2015) 15501–15505. https://doi.org/10.1002/anie.201508128.

[64] F. Solymosi, R. Németh, A. Oszkó, The oxidative dehydrogenation of propane with CO2 over supported Mo2C catalyst, in: F. Solymosi, R. N6meth and A. Oszk6 (Ed.), The oxidative dehydrogenation of propane with CO2 over supported M02C catalyst, Elsevier, Amsterdam, London, 2001, pp. 339–344.

[65] W. Marquart, M. Claeys, N. Fischer, Conversion of CO2 and small alkanes to platform chemicals over Mo2C-based catalysts, Faraday Discuss. (2021). https://doi.org/10.1039/D0FD00138D.

[66] P. Ciambelli, P. Galli, L. Lisi, M.A. Massucci, P. Patrono, R. Pirone, G. Ruoppolo, G. Russo, TiO2 supported vanadyl phosphate as catalyst for oxidative dehydrogenation of ethane to ethylene, Applied Catalysis A: General 203 (2000) 133–142.

[67] A.H. Elbadawi, M.S. Ba-Shammakh, S. Al-Ghamdi, S.A. Razzak, M.M. Hossain, H.I. de Lasa, Phenomenologically based kinetics of ODH of ethane to ethylene using lattice oxygen of VOx/Al2O3–ZrO2 catalyst, Chemical Engineering Research and Design 117 (15) (2017) 733–745. https://doi.org/10.1016/j.cherd.2016.11.015.

[68] M.A. Vuurman, I.E. Wachs, In situ Raman spectroscopy of alumina-supported metal oxide catalysts, J. Phys. Chem. 96 (12) (1992) 5008–5016. https://doi.org/10.1021/j100191a051.

[69] T. Grygar, L. Čapek, J. Adam, V. Machovič, V(V) species in supported catalysts: Analysis and performance in oxidative dehydrogenation of ethane, Journal of Electroanalytical Chemistry 633 (1) (2009) 127–136. https://doi.org/10.1016/j.jelechem.2009.05.003.

[70] L. Lisi, G. Ruoppolo, M.P. Casaletto, P. Galli, M.A. Massucci, P. Patrono, F. Pinzari, Vanadium-metal(IV)phosphates as catalysts for the oxidative dehydrogenation of ethane, Journal of Molecular Catalysis A: Chemical 232 (1-2) (2005) 127–134. https://doi.org/10.1016/j.molcata.2005.01.035.

[71] S. Matar, L.F. Hatch, Chemistry of petrochemical processes, 2nd ed., Gulf Professional Pub, Boston, 2010.

[72] Mark Erama (Ed.), Global Ethylene Market Outlook: Low Cost Feedstocks Fuel The Next Wave Of Investments In North America and China, 2013.

[73] IHS Markit, Ethylene: Chemical Economics Handbook (CEH), 2020. https://ihsmarkit.com/products/ethylene-chemical-economics-handbook.html (accessed 16 October 2020).

[74] C. Boyadjian, K. Seshan, L. Lefferts, A.G.J. van der Ham, H. van den Berg, Production of C 3 /C 4 Olefins from n -Hexane: Conceptual Design of a Catalytic Oxidative Cracking Process and Comparison to Steam Cracking, Ind. Eng. Chem. Res. 50 (1) (2011) 342–351. https://doi.org/10.1021/ie101432r.

[75] J.H. Lee, S. Kang, Y. Kim, S. Park, New Approach for Kinetic Modeling of Catalytic Cracking of Paraffinic Naphtha, Ind. Eng. Chem. Res. 50 (8) (2011) 4264–4279. https://doi.org/10.1021/ie1014074.

[76] Z. Heinz, W. Roland, Ullmann's Encyclopedia of Industrial Chemistry, Wiley, 2000.

[77] A. Chauvel, G. Lefebvre, Petrochemical processes: Technical and economic characteristics / Alain Chauvel, Gilles Lefebvre, Technip, Paris, 1989.

[78] R. van Mao, H. Yan, A. Muntasar, N. Al-Yassir, Blending of Non-Petroleum Compounds with Current Hydrocarbon Feeds to Use in the Thermo-Catalytic Steam-Cracking Process for the Selective Production of Light Olefins, in: S.L. Suib (Ed.), New and future developments in catalysis. Hybrid materials, composites, and organocatalysts, Elsevier, Amsterdam, 2013, pp. 143–173.

[79] A. Qiao, V.N. Kalevaru, J. Radnik, A. Martin, Oxidative dehydrogenation of ethane to ethylene over Ni-Nb-M-O catalysts: Effect of promoter metal and CO2-admixture on the performance, Catalysis Today 264 (2016) (2016) 144–151.

[80] I. Amghizar, L.A. Vandewalle, K.M. van Geem, G.B. Marin, New Trends in Olefin Production, Engineering 3 (2) (2017) 171–178. https://doi.org/10.1016/J.ENG.2017.02.006.

[81] K. Gajendra, A. Michael, Steam Cracking of Crude Oil, 2015. https://ihsmarkit.com/pdf/RP29J-toc_239794110917062932.pdf (accessed 29 June 2020).

[82] T. REN, M. PATEL, K. BLOK, Olefins from conventional and heavy feedstocks: Energy use in steam cracking and alternative processes, Energy 31 (4) (2006) 425–451. https://doi.org/10.1016/j.energy.2005.04.001.

[83] H. Karimi, B. Olayiwola, H. Farag, K.B. McAuley, Modelling coke formation in an industrial ethane-cracking furnace for ethylene production, Can J Chem Eng 98 (1) (2019) 158–171. https://doi.org/10.1002/cjce.23619.

[84] D. Decroocq, Catalytic cracking of heavy petroleum fractions, Technip, Paris, 1984.

[85] A. Aitani, Maximization of FCC light olefins by high severity operation and ZSM-5 addition, Catalysis Today 60 (1-2) (2000) 111–117. https://doi.org/10.1016/S0920-5861(00)00322-9.

[86] Shell, Pearl GTL - overview, 2020.000Z. https://www.shell.com/about-us/major-projects/pearl-gtl/pearl-gtl-an-overview.html (accessed 2 July 2020).

[87] M.E. Dry, High quality diesel via the Fischer-Tropsch process - a review, J. Chem. Technol. Biotechnol. 77 (1) (2002) 43–50. https://doi.org/10.1002/jctb.527.

[88] H.M. Torres Galvis, K.P. de Jong, Catalysts for Production of Lower Olefins from Synthesis Gas: A Review, ACS Catal. 3 (9) (2013) 2130–2149. https://doi.org/10.1021/cs4003436.

[89] H.M. Torres Galvis, A.C.J. Koeken, J.H. Bitter, T. Davidian, M. Ruitenbeek, A.I. Dugulan, K.P. de Jong, Effects of sodium and sulfur on catalytic performance of supported iron catalysts for the Fischer–Tropsch synthesis of lower olefins, Journal of Catalysis 303 (2013) 22–30. https://doi.org/10.1016/j.jcat.2013.03.010.

[90] C. CHANG, The conversion of methanol and other O-compounds to hydrocarbons over zeolite catalysts II. Pressure effects, Journal of Catalysis 56 (2) (1979) 169–173. https://doi.org/10.1016/0021-9517(79)90103-9.

[91] C. CHANG, A.J. Silverstri, The Conversion of Methanol and Other O-Compounds to Hydrocarbons over Zeolite Catalysts, Journal of Catalysis 47 (1977) 249–259.

[92] F.J. Keil, Methanol-to-hydrocarbons: Process technology, Microporous and Mesoporous Materials 29 (1-2) (1999) 49–66. https://doi.org/10.1016/S1387-1811(98)00320-5.

[93] J.Q. Chen, A. Bozzano, B. Glover, T. Fuglerud, S. Kvisle, Recent advancements in ethylene and propylene production using the UOP/Hydro MTO process, Catalysis Today 106 (1-4) (2005) 103–107. https://doi.org/10.1016/j.cattod.2005.07.178.

[94] G. KELLER, Synthesis of ethylene via oxidative coupling of methane I. Determination of active catalysts, Journal of Catalysis 73 (1) (1982) 9–19. https://doi.org/10.1016/0021-9517(82)90075-6.

[95] T. Kazuhiro, Catalytic Conversion of Methane: Carbon Dioxide Reforming and Oxidative Coupling, Journal of the Japan Petroleum Institute 55 (1) (2012) 1–12.

[96] J.J. Spivey, K.M. Dooley, K. Seshan, N. Bion (Eds.), Catalysis ; a review of recent literature, Royal Society of Chemistry, Cambridge, 2010.

[97] A. Galadima, O. Muraza, Revisiting the oxidative coupling of methane to ethylene in the golden period of shale gas: A review, Journal of Industrial and Engineering Chemistry 37 (2016) 1–13. https://doi.org/10.1016/j.jiec.2016.03.027.

[98] J. Carlos Colmenares, Novel Trends in the Utilization of CO2 as a Reagent and Mild Oxidant in the C-C Coupling Reactions, COS 7 (6) (2010) 533–542. https://doi.org/10.2174/157017910794328600.

[99] N.S. Hayek, N.S. Lucas, C. Warwar Damouny, O.M. Gazit, Critical Surface Parameters for the Oxidative Coupling of Methane over the Mn–Na–W/SiO 2 Catalyst, ACS Appl. Mater. Interfaces 9 (46) (2017) 40404–40411. https://doi.org/10.1021/acsami.7b14941.

[100] T.N. Nguyen, T.T.P. Nhat, K. Takimoto, A. Thakur, S. Nishimura, J. Ohyama, I. Miyazato, L. Takahashi, J. Fujima, K. Takahashi, T. Taniike, High-Throughput Experimentation and Catalyst Informatics for Oxidative Coupling of Methane, ACS Catal. 10 (2) (2019) 921–932. https://doi.org/10.1021/acscatal.9b04293.

[101] A. Palermo, j.P. Vazquez, A.F. Lee, S.T. Mintcho, R.M. Lambert, Critical Influence of the Amorphous Silica-to-Cristobalite Phase Transition on the Performance of Mn/Na2WO4/SiO2 Catalysts for the Oxidative Coupling of Methane, Journal of Catalysis 177 (1998) 259–266.

[102] V.R. Choudhary, V.H. Rane, A novel method for measuring base strength distribution on basic solid catalysts under operating conditions, Catal Lett 4 (1) (1990) 101–106. https://doi.org/10.1007/BF00764876.

[103] V.R. Choudhary, S.A.R. Mulla, B.S. Uphade, Oxidative coupling of methane over alkaline earth oxides deposited on commercial support precoated with rare earth oxides, Fuel 78 (4) (1999) 427–437. https://doi.org/10.1016/S0016-2361(98)00168-9.

[104] J.J.H.B. Sattler, J. Ruiz-Martinez, E. Santillan-Jimenez, B.M. Weckhuysen, Catalytic dehydrogenation of light alkanes on metals and metal oxides, Chem. Rev. 114 (20) (2014) 10613–10653. https://doi.org/10.1021/cr5002436.

[105] C.A. Gartner, A.C. van Veen, J.A. Lercher, Oxidative Dehydrogenation of Ethane: Common Principles and Mechanistic Aspects, ChemCatChem 5 (2015) 3196–3217.

[106] M.M. Bhasin, J.H. McCain, B.V. Vora, T. Imai, P.R. Pujadó, Dehydrogenation and oxydehydrogenation of paraffins to olefins, Applied Catalysis A: General 221 (1) (2001) 397–419. https://doi.org/10.1016/S0926-860X(01)00816-X.

[107] Mcdermott technology, CATOFIN-Dehydrogenation, 2018. https://www.cbi.com/getattachment/9c663848-b4ae-4c51-b51a-49db1154c47f/CATOFIN-Dehydrogenation.aspx (accessed 21 August 2020).

[108] F.T. Zangeneh, S. Sahebdelfar, M. Bahmani, Propane Dehydrogenation over a Commercial Pt-Sn/Al2O3 Catalyst for Isobutane Dehydrogenation: Optimization of Reaction Conditions, Chinese Journal of Chemical Engineering 21 (7) (2013) 730–735. https://doi.org/10.1016/S1004-9541(13)60537-6.

[109] G. Raju, B.M. Reddy, B. Abhishek, Y.-H. Mo, S.-E. Park, Synthesis of C4 olefins from n-butane over a novel VOx/SnO2–ZrO2 catalyst using CO2 as soft oxidant, Applied Catalysis A: General 423-424 (2012) 168–175. https://doi.org/10.1016/j.apcata.2012.02.040.

[110] F. Cavani, F. Trifiro, The oxidative dehydrogenation of ethane and propane as an alternative way for the production of light olefins, Catalysis Today 24 (1995) 307–313.

[111] W.-D. Lu, D. Wang, Z. Zhao, W. Song, W.-C. Li, A.-H. Lu, Supported Boron Oxide Catalysts for Selective and Low-Temperature Oxidative Dehydrogenation of Propane, ACS Catal. 9 (9) (2019) 8263–8270. https://doi.org/10.1021/acscatal.9b02284.

[112] J.T. Grant, C.A. Carrero, F. Goeltl, J. Venegas, P. Mueller, S.P. Burt, S.E. Specht, W.P. McDermott, A. Chieregato, I. Hermans, Selective oxidative dehydrogenation of propane to propene using boron nitride catalysts, Science 354 (6319) (2016) 1566–1570. https://doi.org/10.1126/science.aag2671.

[113] A. Held, J. Kowalska, K. Nowińska, Nitrous oxide as an oxidant for ethane oxydehydrogenation, Applied Catalysis B: Environmental 64 (3-4) (2006) 201–208. https://doi.org/10.1016/j.apcatb.2005.11.017.

[114] Shanfu Liu, Allison M. Arinaga, Tracy L. Lohr, Tobin J. Marks, High Ethylene-Yield Oxidative Dehydrogenation of Ethane Using Sulfur Vapor as a “Soft” Oxidant, ChemCatChem 12 (18) (2020) 4538–4542. https://doi.org/10.1002/cctc.202000858.

[115] E. Nowicka, C. Reece, S.M. Althahban, K.M.H. Mohammed, S.A. Kondrat, D.J. Morgan, Q. He, D.J. Willock, S. Golunski, C.J. Kiely, G.J. Hutchings, Elucidating the Role of CO 2 in the Soft Oxidative Dehydrogenation of Propane over Ceria-Based Catalysts, ACS Catal. 8 (4) (2018) 3454–3468. https://doi.org/10.1021/acscatal.7b03805.

[116] D. Mukherjee, S.-E. Park, B.M. Reddy, CO2 as a soft oxidant for oxidative dehydrogenation reaction: An eco benign process for industry, Journal of CO2 Utilization 16 (2016) 301–312. https://doi.org/10.1016/j.jcou.2016.08.005.

[117] X. Jiang, L. Sharma, V. Fung, S.J. Park, C.W. Jones, B.G. Sumpter, J. Baltrusaitis, Z. Wu, Oxidative Dehydrogenation of Propane to Propylene with Soft Oxidants via Heterogeneous Catalysis, ACS Catal. (2021) 2182–2234. https://doi.org/10.1021/acscatal.0c03999.

[118] Yan Zhang, Suresh Kumar Megarajan, Xia Xu, Jingting Lu and Heqing Jiang, Catalytic Abatement of Nitrous Oxide Coupled with Ethane Oxydehydrogenation over Mesoporous Cr/Al2O3 Catalyst, Catalysts 137 (7) (2017) 1–11.

[119] N. SHIJU, M. ANILKUMAR, S. MIRAJKAR, C. GOPINATH, B. RAO, C. SATYANARAYANA, Oxidative dehydrogenation of ethylbenzene over vanadia-alumina catalysts in the presence of nitrous oxide: Structure-activity relationship, Journal of Catalysis 230 (2) (2005) 484–492. https://doi.org/10.1016/j.jcat.2005.01.010.

[120] O.V. Krylov, A.K. Mamedov, S.R. Mirzabekova, Catalytic Oxidation of Hydrocarbons and Alcohols by Carbon Dioxide on Oxide Catalystss. Oxidative dehydrogenation of light alkanes

and using carbon dioxide as a nontraditional mild oxidant, Ind. Eng. Chem. Res. 34 (1995) 474–482.

[121] L. Xu, J. Liu, H. Yang, Y. Xu, D. Wang, W. Lin, Regeneration behaviors of Fe/Si-2 and Fe-Mn/Si-2 catalysts for C2H6 dehydrogenation with CO2 to C2H4, Catal. Lett. 62 (1999) 185.

[122] K. Takehira, Y. Ohishi, T. Shishido, T. Kawabata, K. Takaki, Q. Zhang, Y. Wang, Behavior of active sites on Cr-MCM-41 catalysts during the dehydrogenation of propane with CO2, Journal of Catalysis 224 (2) (2004) 404–416. https://doi.org/10.1016/j.jcat.2004.03.014.

[123] X. Longya, L. Liwu, W. Qingxia, Y. Li, W. Debao, L. Weichen, A New Route for C2H4 Production by Reacting C2H6 with CO2 over a Catalyst of Chromium Oxide Supported on Silicalite-2 Type Zeolite, pp. 605–610.

[124] D. Wang, M. Xu, C. Shi, J.H. Lunsford, Effect of carbon dioxide on the selectivities obtained during the partial oxidation of methane and ethane over Li+/MgO catalysts, Catal Lett 18 (4) (1993) 323–328. https://doi.org/10.1007/BF00765277.

[125] B. Yan, B. Zhao, S. Kattel, Q. Wu, S. Yao, D. Su, J.G. Chen, Tuning CO2 hydrogenation selectivity via metal-oxide interfacial sites, Journal of Catalysis 374 (2019) 60–71. https://doi.org/10.1016/j.jcat.2019.04.036.

[126] Hannah Ritchie and Max Roser, Fossil Fuels: Global fossil fuel consumption, 2017. https://ourworldindata.org/fossil-fuels (accessed 2021).

[127] GISTEMP Team, GISS Surface Temperature Analysis (GISTEMP), version 4. data.giss.nasa.gov/gistemp/ (accessed 21 March 2021).

[128] IEA (2021) team, Global Energy review: CO2 emissions in 2020, 2021. https://www.iea.org/articles/global-energy-review-co2-emissions-in-2020 (accessed March 2021).

[129] L. Rebecca, Climate Change: Atmospheric Carbon Dioxide, 2020. Climate.gov (accessed 21 March 2021).

[130] Esmeralda Fratta Dormond di Rickli, Report of the Conference of the Parties on its twenty-first session, held in Paris from 30 November to 11 December 2015. Addendum. Part two: Action taken by the Conference of the Parties at its twenty-first session., United nations (2016).

[131] IPCC team, Global Warming of 1.5 °C. https://www.ipcc.ch/sr15/ (accessed March 2021).

[132] S. De, A. Dokania, A. Ramirez, J. Gascon, Advances in the Design of Heterogeneous Catalysts and Thermocatalytic Processes for CO 2 Utilization, ACS Catal. 10 (23) (2020) 14147–14185. https://doi.org/10.1021/acscatal.0c04273.

[133] IEA team, Global Energy Review 2020, 2020. https://www.iea.org/reports/global-energy-review-2020/renewables (accessed March 2021).

[134] N. von der Assen, L.J. Müller, A. Steingrube, P. Voll, A. Bardow, Selecting CO2 Sources for CO2 Utilization by Environmental-Merit-Order Curves, Environ. Sci. Technol. 50 (3) (2016) 1093–1101. https://doi.org/10.1021/acs.est.5b03474.

[135] X. Wu, Y. Yu, Z. Qin, Z. Zhang, The Advances of Post-combustion CO2 Capture with Chemical Solvents: Review and Guidelines, Energy Procedia 63 (1) (2014) 1339–1346. https://doi.org/10.1016/j.egypro.2014.11.143.

[136] Global Thermostat team, About Carbon Capture and Use, 2021. https://globalthermostat.com/ (accessed March 2021).

[137] Carbon Engineering team, Our Technology, 2021. https://carbonengineering.com/ (accessed March 2021).

[138] Climeworks, The rapid construction of Climeworks' new direct air capture and storage plant Orca has started, 2020.

[139] Climeworks, Climeworks (9 June 2020).

[140] E. Alper, O. Yuksel Orhan, CO 2 utilization: Developments in conversion processes, Petroleum 3 (1) (2017) 109–126. https://doi.org/10.1016/j.petlm.2016.11.003.

[141] Q. Zhang, L. Pastor-Pérez, S. Gu, T. Ramirez Reina, Transition Metal Carbides (TMCs) Catalysts for Gas Phase CO2 Upgrading Reactions: A Comprehensive Overview, Catalysts 10 (9) (2020) 955. https://doi.org/10.3390/catal10090955.

[142] Linde Engineering, Recycling CO_2– the efficient way | Linde Engineering, 2021. https://www.linde-engineering.com/en/about-linde-engineering/success-stories/recycling-co2.html (accessed 27 April 2021).

[143] 3. W. Marquart, S. Raseale, G. Prieto, A. Zimina, B. B. Sarma, J-D. Grunwaldt, M. Claeys, N. Fischer, CO2 Reduction over Mo2C-Based Catalysts, ACS Catal. (2021) 1624–1639. https://doi.org/10.1021/acscatal.0c05019.

[144] W. Wang, Y. Zhang, Z. Wang, J.-m. Yan, Q. Ge, C.-j. Liu, Reverse water gas shift over In 2 O 3 –CeO 2 catalysts, Catalysis Today 259 (2016) 402–408. https://doi.org/10.1016/j.cattod.2015.04.032.

[145] X. Zhang, X. Zhu, L. Lin, S. Yao, M. Zhang, X. Liu, X. Wang, Y.-W. Li, C. Shi, D. Ma, Highly Dispersed Copper over β-Mo 2 C as an Efficient and Stable Catalyst for the Reverse Water Gas Shift (RWGS) Reaction, ACS Catal. 7 (1) (2016) 912–918. https://doi.org/10.1021/acscatal.6b02991.

[146] B. Dale, H. Emerson, R. Min-Hon, Carbon dioxide as hydrogen acceptor in dehydrogenation of alkanes, Ind. Eng. Chem. Prod. Res. DeV 11 (444) (1972).

[147] F. Solymosi, R. Nemeth, The oxidative dehydrogenation of ethane with CO2 over Mo2C/SiO2 catalyst 62 (1999) 197–200. https://doi.org/10.1007/978-1-4615-4777-8_1.

[148] K. Chen, A.T. Bell, E. Iglesia, Kinetics and Mechanism of Oxidative Dehydrogenation of Propane on Vanadium, Molybdenum, and Tungsten Oxides, J. Phys. Chem. B 104 (6) (2000) 1292–1299. https://doi.org/10.1021/jp9933875.

[149] A. Álvarez, M. Borges, J.J. Corral-Pérez, J.G. Olcina, L. Hu, D. Cornu, R. Huang, D. Stoian, A. Urakawa, CO2 Activation over Catalytic Surfaces, Chemphyschem 18 (22) (2017) 3135–3141. https://doi.org/10.1002/cphc.201700782.

[150] R. Koirala, O.V. Safonova, S.E. Pratsinis, A. Baiker, Effect of cobalt loading on structure and catalytic behavior of CoO x /SiO 2 in CO 2 -assisted dehydrogenation of ethane, Applied Catalysis A: General 552 (2018) 77–85. https://doi.org/10.1016/j.apcata.2017.12.025.

[151] A.S. Al-Awadi, S.M. Al-Zahrani, A.M. El-Toni, A.E. Abasaeed, Dehydrogenation of Ethane to Ethylene by CO2 over Highly Dispersed Cr on Large-Pore Mesoporous Silica Catalysts, Catalysts 10 (1) (2020) 97. https://doi.org/10.3390/catal10010097.

[152] P. Mars, D.W. van Krevelen, Oxidations carried out by means of vanadium oxide catalysts, Chemical Engineering Science 3 (1954) 41–59.

[153] S.A. Theofanidis, C. Loizidis, E. Heracleous, A.A. Lemonidou, CO2-oxidative ethane dehydrogenation over highly efficient carbon-resistant Fe-catalysts, Journal of Catalysis 388 (2020) 52–65. https://doi.org/10.1016/j.jcat.2020.05.004.

[154] J.A. Lercher, F.N. Naraschewski, C-H activation of alkanes in slective oxidation reactions on solid oxide catalysts, in: C. Hess, R. Schlogl (Eds.), Nanostructured Catalysts—Selective Oxidations, 1st ed., Royal Society of Chemistry, Cambridge, 2011, pp. 5–32.

[155] O.O. James, S. Mandal, N. Alele, B. Chowdhury, S. Maity, Lower alkanes dehydrogenation: Strategies and reaction routes to corresponding alkenes, Fuel Processing Technology 149 (9) (2016) 239–255. https://doi.org/10.1016/j.fuproc.2016.04.016.

[156] P. Ciambelli, L. Lisi, R. Pirone, G. Ruoppolo, G. Russo, Comparison of behaviour of rare earth containing catalysts in the oxidative dehydrogenation of ethane, Catalysis Today 61 (2000) 317–323.

[157] Y.A. Agafonov, N.A. Gaidai, A.L. Lapidus, Propane Dehydrogenation on Chromium Oxide and Gallium Oxide Catalysts in the Presence of CO2, Kinet Catal 59 (6) (2018) 744–753. https://doi.org/10.1134/S0023158418060010.

[158] S. Derossi, G. Ferraris, S. Fremiotti, E. Garrone, G. Ghiotti, M.C. Campa, V. Indovina, Propane Dehydrogenation on Chromia/Silica and Chromia/Alumina Catalysts, Journal of Catalysis 148 (1) (1994) 36–46. https://doi.org/10.1006/jcat.1994.1183.

[159] P. Thirumala Bai, S. Srinath, K. Upendar, T.V. Sagar, N. Lingaiah, K.S. Rama Rao, P.S. Sai Prasad, Oxidative dehydrogenation of ethane with carbon dioxide over Cr2O3/SBA-15 catalysts: The influence of sulfate modification of the support, Appl Petrochem Res 7 (2-4) (2017) 107–118. https://doi.org/10.1007/s13203-017-0182-5.

[160] A. Hakuli, A. Kytökivi, A.O.I. Krause, Dehydrogenation of i-butane on CrOx/Al2O3 catalysts prepared by ALE and impregnation techniques, Applied Catalysis A: General 190 (1-2) (2000) 219–232. https://doi.org/10.1016/S0926-860X(99)00310-5.

[161] X. Shi, S. Ji, K. Wang, C. Li, Oxidative Dehydrogenation of Ethane with CO 2 over Novel Cr/SBA-15/Al 2 O 3 /FeCrAl Monolithic Catalysts, Energy Fuels 22 (6) (2008) 3631–3638. https://doi.org/10.1021/ef800567v.

[162] H. Yamashita, M. Anpo, Local structures and photocatalytic reactivities of the titanium oxide and chromium oxide species incorporated within micro- and mesoporous zeolite materials: XAFS and photoluminescence studies, Current Opinion in Solid State and Materials Science 7 (6) (2003) 471–481. https://doi.org/10.1016/j.cossms.2004.02.003.

[163] X. Shi, S. Ji, K. Wang, Oxidative Dehydrogenation of Ethane to Ethylene with Carbon dioxide over Cr–Ce/SBA-15 Catalysts, Catal Lett 125 (3-4) (2008) 331–339. https://doi.org/10.1007/s10562-008-9569-3.

[164] G. Xin, Z. Mingming, S. Jianyi, Catalytic performance of silica-supported chromium oxide catalysts in ethane dehydrogenation with carbon dioxide, React Kinet Catal Lett 77 (1) (2002) 103–108.

[165] A.V. Kucherov, A.A. Slinkin, G.K. Beyer, G. Borbely, The status of chromium in aluminum-free chromosilicate with the ZSM-5 structure, Zeolites 15 (5) (1995) 431–438. https://doi.org/10.1016/0144-2449(95)00014-W.

[166] G. Giannetto, L. García, J. Papa, F. Yánez, M.R. Goldwasser, C. Linares, D. Moronta, B. Mendez, C. Urbina de Navarro, R. Monque, Synthesis and characterization of [Cr,Al]-ZSM-5 zeolites, Zeolites 19 (2-3) (1997) 169–174. https://doi.org/10.1016/S0144-2449(97)00064-X.

[167] Y. Ohishi, T. Kawabata, T. Shishido, K. Takaki, Q. Zhang, Y. Wang, K. Takehira, Dehydrogenation of ethylbenzene with CO2 over Cr-MCM-41 catalyst, Journal of Molecular Catalysis A: Chemical 230 (1-2) (2005) 49–58. https://doi.org/10.1016/j.molcata.2004.12.006.

[168] S. Wang, K. Murata, T. Hayakawa, S. Hamakawa, K. Suzuki, Oxidative dehydrogenation of ethane over sufated zirconia supported oxides catalysts, React Kinet Catal Lett 67 (2) (1999) 219–224. https://doi.org/10.1007/BF02475763.

[169] L. Jin, J. Reutenauer, N. Opembe, M. Lai, D.J. Martenak, S. Han, S.L. Suib, Studies on Dehydrogenation of Ethane in the Presence of CO 2 over Octahedral Molecular Sieve (OMS-2) Catalysts, ChemCatChem 1 (4) (2009) 441–444. https://doi.org/10.1002/cctc.200900149.

[170] V.Z. Fridman, R. Xing, Deactivation Studies of the CrOx/Al 2 O 3 Dehydrogenation Catalysts under Cyclic Redox Conditions, Ind. Eng. Chem. Res. 56 (28) (2017) 7937–7947. https://doi.org/10.1021/acs.iecr.7b01638.

[171] S. Deng, H. Li, S. Li, Y. Zhang, Activity and characterization of modified Cr2O3/ZrO2 nano-composite catalysts for oxidative dehydrogenation of ethane to ethylene with CO2, Journal of Molecular Catalysis A: Chemical 268 (1-2) (2007) 169–175. https://doi.org/10.1016/j.molcata.2006.12.033.

[172] K. Nakagawa, M. Okamura, N. Ikenaga, T. Suzuki, T. Kobayashi, Chem. Commun. (1998) 1025.

[173] A.l. Petre, Acid-base properties of supported gallium oxide catalysts, Thermochimica acta 379 (2001) 177–185.

[174] K. Nakagawa, C. Kajita, Y. Ide, M. Okamura, S. Kato, H. Kasuya, Promoting effect of carbon dioxide on the dehydrogenation and aromatization of ethane over gallium‐loaded catalysts, Catal. Lett. 64 (2000) 215–221.

[175] B. XU, B. ZHENG, W. HUA, Y. YUE, Z. GAO, Support effect in dehydrogenation of propane in the presence of CO2 over supported gallium oxide catalysts, Journal of Catalysis 239 (2) (2006) 470–477. https://doi.org/10.1016/j.jcat.2006.02.017.

[176] R. Koirala, R. Buechel, F. Krumeich, S.E. Pratsinis, A. Baiker, Oxidative Dehydrogenation of Ethane with CO 2 over Flame-Made Ga-Loaded TiO 2, ACS Catal. 5 (2) (2015) 690–702. https://doi.org/10.1021/cs500685d.

[177] P. Michorczyk, J. Ogonowski, Dehydrogenation of propane to propene over gallium oxide in the presence of CO2, Applied Catalysis A: General 251 (2) (2003) 425–433. https://doi.org/10.1016/S0926-860X(03)00368-5.

[178] Z. Shen, J. Liu, H. Xu, Y. Yue, W. Hua, W. Shen, Dehydrogenation of ethane to ethylene over a highly efficient Ga2O3/HZSM-5 catalyst in the presence of CO2, Applied Catalysis A: General 356 (2) (2009) 148–153. https://doi.org/10.1016/j.apcata.2008.12.038.

[179] B. Xu, T. Li, B. Zheng, W. Hua, Y. Yue, Z. Gao, Enhanced Stability of HZSM-5 Supported Ga2O3 Catalyst in Propane Dehydrogenation by Dealumination, Catal Lett 119 (3-4) (2007) 283–288. https://doi.org/10.1007/s10562-007-9232-4.

[180] X. Yuqing, H. Weiming, Y. Yinghong, G. Zi, Dehydrogenation of Propane to Propylene over Ga2O3 Supported on Mesoporous HZSM-5 in the Presence of CO2, Chinese Journal of Chemistry 28 (2010) 1559–1564.

[181] S.P. Batchu, H.-L. Wang, W. Chen, W. Zheng, S. Caratzoulas, R.F. Lobo, D.G. Vlachos, Ethane Dehydrogenation on Single and Dual Centers of Ga-modified γ-Al 2 O 3, ACS Catal. 11 (3) (2021) 1380–1391. https://doi.org/10.1021/acscatal.0c03536.

[182] G. Li, C. Liu, X. Cui, Y. Yang, F. Shi, Oxidative dehydrogenation of light alkanes with carbon dioxide, Green Chem. 23 (2) (2021) 689–707. https://doi.org/10.1039/D0GC03705B.

[183] Y.-x. Pan, C.-j. Liu, D. Mei, Q. Ge, Effects of hydration and oxygen vacancy on CO2 adsorption and activation on beta-Ga2O3(100), Langmuir 26 (8) (2010) 5551–5558. https://doi.org/10.1021/la903836v.

[184] P. Taghavinezhad, M. Haghighi, R. Alizadeh, Sonosynthesis of VOx/MCM-41 nanocatalyst enhanced by various metal oxides (Mg, AL, Zr) for CO2-oxidative dehydrogenation of ethane to ethylene, Microporous and Mesoporous Materials 261 (Part B) (2018) 63–78. https://doi.org/10.1016/j.micromeso.2017.10.057.

[185] M.Y. Khan, S. Al-Ghamdi, S.A. Razzak, M.M. Hossain, H. de Lasa, Fluidized bed oxidative dehydrogenation of ethane to ethylene over VOx/Ce-γAl2O3 catalysts: Reduction kinetics and catalyst activity, Molecular Catalysis 443 (2017) 78–91. https://doi.org/10.1016/j.mcat.2017.09.025.

[186] M.L. Balogun, S. Adamu, M.S. Ba-Shammakh, M.M. Hossain, Promotional effects of CO2 on the oxidative dehydrogenation of propane over mesoporous VOX/γAl2O3 catalysts, Journal of Industrial and Engineering Chemistry 42 (20) (2020) 101329. https://doi.org/10.1016/j.jiec.2020.12.022.

[187] M. Chen, J. Xu, Y.-M. Liu, Y. Cao, H.-Y. He, J.-H. Zhuang, Supported indium oxide as novel efficient catalysts for dehydrogenation of propane with carbon dioxide, Applied Catalysis A: General 377 (1-2) (2010) 35–41. https://doi.org/10.1016/j.apcata.2010.01.011.

[188] M. Chen, J. Xu, Y. Cao, H.-Y. He, K.-N. Fan, J.-H. Zhuang, Dehydrogenation of propane over In2O3–Al2O3 mixed oxide in the presence of carbon dioxide, Journal of Catalysis 272 (1) (2010) 101–108. https://doi.org/10.1016/j.jcat.2010.03.007.

[189] M. Chen, J.-L. Wu, Y.-M. Liu, Y. Cao, L. Guo, H.-Y. He, K.-N. Fan, Study in support effect of In2O3/MOx (M=Al, Si, Zr) catalysts for dehydrogenation of propane in the presence of

CO2, Applied Catalysis A: General 407 (1-2) (2011) 20–28. https://doi.org/10.1016/j.apcata.2011.08.018.

[190] E. HERACLEOUS, A. LEMONIDOU, Ni–Nb–O mixed oxides as highly active and selective catalysts for ethene production via ethane oxidative dehydrogenation. Part I: Characterization and catalytic performance, Journal of Catalysis 237 (1) (2006) 162–174. https://doi.org/10.1016/j.jcat.2005.11.002.

[191] E. HERACLEOUS, A. LEMONIDOU, Ni–Nb–O mixed oxides as highly active and selective catalysts for ethene production via ethane oxidative dehydrogenation. Part II: Mechanistic aspects and kinetic modeling, Journal of Catalysis 237 (1) (2006) 175–189. https://doi.org/10.1016/j.jcat.2005.11.003.

[192] Z. Skoufa, E. HERACLEOUS, A.A. Lemonidou, Unraveling the contribution of structural phases in Ni–Nb–O mixed oxides in ethane oxidative dehydrogenation, Catalysis Today 192 (1) (2012) 169–176. https://doi.org/10.1016/j.cattod.2011.12.022.

[193] E. HERACLEOUS, A. Delimitis, L. Nalbandian, A.A. Lemonidou, HRTEM characterization of the nanostructural features formed in highly active Ni–Nb–O catalysts for ethane ODH, Applied Catalysis A: General 325 (2) (2007) 220–226. https://doi.org/10.1016/j.apcata.2007.02.030.

[194] E. HERACLEOUS, A.A. Lemonidou, Ni–Me–O mixed metal oxides for the effective oxidative dehydrogenation of ethane to ethylene – Effect of promoting metal Me, Journal of Catalysis 270 (1) (2010) 67–75. https://doi.org/10.1016/j.jcat.2009.12.004.

[195] A. Talati, M. Haghighi, F. Rahmani, Oxidative dehydrogenation of ethane to ethylene by carbon dioxide over Cr/TiO 2 –ZrO 2 nanocatalyst: Effect of active phase and support composition on catalytic properties and performance, Advanced Powder Technology 27 (4) (2016) 1195–1206. https://doi.org/10.1016/j.apt.2016.04.003.

[196] J. Zhu, S. Qin, S. Ren, X. Peng, D. Tong, C. Hu, Na2WO4/Mn/SiO2 catalyst for oxidative dehydrogenation of ethane using CO2 as oxidant, Catalysis Today 148 (3-4) (2009) 310–315. https://doi.org/10.1016/j.cattod.2009.07.074.

[197] J. Wang, L. Chou, B. Zhang, H. Song, J. Zhao, J. Yang, S. Li, Comparative study on oxidation of methane to ethane and ethylene over Na2WO4–Mn/SiO2 catalysts prepared by different methods, Journal of Molecular Catalysis A: Chemical 245 (1-2) (2006) 272–277. https://doi.org/10.1016/j.molcata.2005.09.038.

[198] S. Pak, J.H. Lunsford, Thermal effects during the oxidative coupling of methane over Mn/Na2WO4/SiO2 and Mn/Na2WO4/MgO catalysts, Applied Catalysis A: General 168 (1) (1998) 131–137. https://doi.org/10.1016/S0926-860X(97)00340-2.

[199] S. Pak, P. Qui, J.H. Lunsford, Elementary Reactions in the Oxidative Coupling of Methane over Mn/Na2WO4/SiO2and Mn/Na2WO4/MgO Catalysts, Journal of Catalysis 179 (1) (1998) 222–230. https://doi.org/10.1006/jcat.1998.2228.

[200] M.D. Porosoff, X. Yang, J.A. Boscoboinik, J.G. Chen, Molybdenum carbide as alternative catalysts to precious metals for highly selective reduction of CO2 to CO, Angew. Chem. Int. Ed Engl. 53 (26) (2014) 6705–6709. https://doi.org/10.1002/anie.201404109.

[201] Q. Zhang, L. Pastor-Pérez, W. Jin, S. Gu, T.R. Reina, Understanding the promoter effect of Cu and Cs over highly effective β-Mo2C catalysts for the reverse water-gas shift reaction, Applied Catalysis B: Environmental 244 (2019) 889–898. https://doi.org/10.1016/j.apcatb.2018.12.023.

[202] M.D. Porosoff, S. Kattel, W. Li, P. Liu, J.G. Chen, Identifying trends and descriptors for selective CO2 conversion to CO over transition metal carbides, Chem. Commun. (Camb) 51 (32) (2015) 6988–6991. https://doi.org/10.1039/c5cc01545f.

[203] Sergio Posada-Pérez, Francesc Viñes, Pedro J. Ramirez, Alba B. Vidal, José A. Rodriguez, Francesc Illas, The bending machine: CO2 activation and hydrogenation on δ-MoC(001) and β-Mo2C(001) surfaces, Phys. Chem. Chem. Phys. 16 (28) (2014) 14912–14921. https://doi.org/10.1039/C4CP01943A.

[204] P. Liu, J.A. Rodriguez, Effects of carbon on the stability and chemical performance of transition metal carbides: A density functional study, J. Chem. Phys. 120 (11) (2004) 5414–5423. https://doi.org/10.1063/1.1647050.

[205] A.B. Vidal, L. Feria, J. Evans, Y. Takahashi, P. Liu, K. Nakamura, F. Illas, J.A. Rodriguez, CO2 Activation and Methanol Synthesis on Novel Au/TiC and Cu/TiC Catalysts, J. Phys. Chem. Lett. 3 (16) (2012) 2275–2280. https://doi.org/10.1021/jz300989e.

[206] S. Posada-Pérez, P.J. Ramírez, J. Evans, F. Viñes, P. Liu, F. Illas, J.A. Rodriguez, Highly Active Au/δ-MoC and Cu/δ-MoC Catalysts for the Conversion of CO2: The Metal/C Ratio as a Key Factor Defining Activity, Selectivity, and Stability, Journal of the American Chemical Society 138 (26) (2016) 8269–8278. https://doi.org/10.1021/jacs.6b04529.

[207] W. Yu, M.D. Porosoff, J.G. Chen, Review of Pt-based bimetallic catalysis: From model surfaces to supported catalysts, Chem. Rev. 112 (11) (2012) 5780–5817. https://doi.org/10.1021/cr300096b.

[208] M.D. Porosoff, W. Yu, J.G. Chen, Challenges and opportunities in correlating bimetallic model surfaces and supported catalysts, Journal of Catalysis 308 (2013) 2–10. https://doi.org/10.1016/j.jcat.2013.05.009.

[209] Z. Xie, L.R. Winter, J.G. Chen, Bimetallic-Derived Catalysts and Their Application in Simultaneous Upgrading of CO2 and Ethane, Matter 4 (2) (2021) 408–440. https://doi.org/10.1016/j.matt.2020.11.013.

[210] G. Sierra Gallego, C. Batiot-Dupeyrat, J. Barrault, F. Mondragón, Dual Active-Site Mechanism for Dry Methane Reforming over Ni/La 2 O 3 Produced from LaNiO 3 Perovskite, Ind. Eng. Chem. Res. 47 (23) (2008) 9272–9278. https://doi.org/10.1021/ie800281t.

[211] X. Li, B. Yan, S. Yao, S. Kattel, J.G. Chen, T. Wang, Oxidative dehydrogenation and dry reforming of n-butane with CO2 over NiFe bimetallic catalysts, Applied Catalysis B: Environmental 231 (2018) 213–223. https://doi.org/10.1016/j.apcatb.2018.02.063.

[212] S.M. Kim, P.M. Abdala, T. Margossian, D. Hosseini, L. Foppa, A. Armutlulu, W. van Beek, A. Comas-Vives, C. Copéret, C. Müller, Cooperativity and Dynamics Increase the Performance of NiFe Dry Reforming Catalysts, Journal of the American Chemical Society 139 (5) (2017) 1937–1949. https://doi.org/10.1021/jacs.6b11487.

[213] O. T., Recent development of Magnetic recording head core materials by plating method, Electrochimica Acta 44 (1999) 3885–3890.

[214] R. Koohkan, S. Sharafi, H. Shokrollahi, K. Janghorban, Preparation of nanocrystalline Fe–Ni powders by mechanical alloying used in soft magnetic composites, Journal of Magnetism and Magnetic Materials 320 (6) (2008) 1089–1094. https://doi.org/10.1016/j.jmmm.2007.10.033.

[215] L. Zhen, Y.X. Gong, J.T. Jiang, W.Z. Shao, Electromagnetic properties of FeNi alloy nanoparticles prepared by hydrogen-thermal reduction method, Journal of Applied Physics 104 (3) (2008) 34312. https://doi.org/10.1063/1.2959726.

[216] G.V. Kurlyandskaya, I. Madinabeitia, I.V. Beketov, A.I. Medvedev, A. Larrañaga, A.P. Safronov, S.M. Bhagat, Structure, magnetic and microwave properties of FeNi nanoparticles obtained by electric explosion of wire, Journal of Alloys and Compounds 615 (1–8) (2014) S231-S235. https://doi.org/10.1016/j.jallcom.2013.11.164.

[217] S. Vitta, A. Khuntia, G. Ravikumar, D. Bahadur, Electrical and magnetic properties of nanocrystalline Fe100−xNix alloys, Journal of Magnetism and Magnetic Materials 320 (3-4) (2008) 182–189. https://doi.org/10.1016/j.jmmm.2007.05.021.

[218] P. Jing, M. Liu, Y. Pu, Y. Cui, Z. Wang, J. Wang, Q. Liu, Dependence of phase configurations, microstructures and magnetic properties of iron-nickel (Fe-Ni) alloy nanoribbons on deoxidization temperature in hydrogen, Sci. Rep. 6 (2016) 37701. https://doi.org/10.1038/srep37701.

[219] C. A., Thin-film inductive heads, IBM Journal of Research and Development 40 (3) (1996) 283–300.

[220] H. Yang, X. Li, H. Zhou, Y. Zhuang, H. Hu, H. Wu, S. Yang, Monodisperse water-soluble Fe–Ni nanoparticles for magnetic resonance imaging, Journal of Alloys and Compounds 509 (4) (2011) 1217–1221. https://doi.org/10.1016/j.jallcom.2010.09.191.

[221] M. Butta, P. Ripka, M. Janosek, M. Pribil, Electroplated FeNi ring cores for fluxgates with field induced radial anisotropy, Journal of Applied Physics 117 (17) (2015) 17A722. https://doi.org/10.1063/1.4914874.

[222] M.M. Abd-Elmeguid, B. Schleed, H. Micklitz, Pressure-induced antiferromagnetism in fcc Fe-Ni Invar alloys, Journal of Magnetism and Magnetic Materials 72 (3) (1988) 253–257.

[223] S.J. Rosenberg, Nickel and Its Alloys: Ferrous Alloys, 106th ed., NBS, Washington, D.C., 1968 (accessed 27 May 2021).

[224] N. Moghimi, F.R. Rahsepar, S. Srivastava, N. Heinig, K.T. Leung, Shape-dependent magnetism of bimetallic FeNi nanosystems, J. Mater. Chem. C 2 (31) (2014) 6370. https://doi.org/10.1039/C4TC00443D.

[225] W. Pepperhoff, M. Acet, Constitution and Magnetism of Iron and its Alloys, Spinger, Berlin, Heidelberg, 2001.

[226] Z. Xie, D. Tian, M. Xie, S.-Z. Yang, Y. Xu, N. Rui, J.H. Lee, S.D. Senanayake, K. Li, H. Wang, S. Kattel, J.G. Chen, Interfacial Active Sites for CO2 Assisted Selective Cleavage of C–C/C–H Bonds in Ethane, Chem (2020). https://doi.org/10.1016/j.chempr.2020.07.011.

[227] A.A. Adesina, Hydrocarbon synthesis via Fischer-Tropsch reaction: travails and triumphs, Applied Catalysis A: General 138 (1996) 345–367.

[228] Y.J. Huang, J.A. Schwarz, THE EFFECT OF CATALYST PREPARATION ON CATALYTIC ACTIVITY: IV. THE DESIGN OF Ni/A1203 CATALYSTS PREPARED BY INCIPIENT WETNESS, Applied Catalysis 32 (1987) 59–70.

[229] P. Munnik, P.E. de Jongh, K.P. de Jong, Recent developments in the synthesis of supported catalysts, Chem. Rev. 115 (14) (2015) 6687–6718. https://doi.org/10.1021/cr500486u.

[230] Y. Dahman, Nanopolymers**By Yaser Dahman, Kevin Deonanan, Timothy Dontsos, and Andrew Iammatteo, in: Y. Dahman (Ed.), Nanotechnology and functional materials for engineers, Elsevier, Amsterdam, Netherlands, 2017, pp. 121–144.

[231] J.W. Geus, J. van Dillen, Preparation of Supported Catalysts by Deposition–Precipitation, in: Ertl, Gerhard-Handbook of heterogeneous catalysis, 428-467.

[232] C. Perego, P. Villa, Catalyst preparation methods, Catalysis Today 34 (1997) 281–305.

[233] F. Schüth, M. Hesse, K.K. Unger, Precipitation and Coprecipitation, in: Ertl, Gerhard-Handbook of heterogeneous catalysis, pp. 100–119.

[234] Ertl, Gerhard-Handbook of heterogeneous catalysis.

[235] B. Gersten, Solvothermal Synthesis of Nanoparticles, Chemfiles 5 (13).

[236] S. Yáñez-Vilar, M. Sánchez-Andújar, C. Gómez-Aguirre, J. Mira, M.A. Señarís-Rodríguez, S. Castro-García, A simple solvothermal synthesis of MFe2O4 (M=Mn, Co and Ni) nanoparticles, Journal of Solid State Chemistry 182 (10) (2009) 2685–2690. https://doi.org/10.1016/j.jssc.2009.07.028.

[237] A.F. Rebolledo, A.B. Fuertes, T. Gonzalez-Carreño, M. Sevilla, T. Valdes-Solis, P. Tartaj, Signatures of clustering in superparamagnetic colloidal nanocomposites of an inorganic and hybrid nature, Small 4 (2) (2008) 254–261. https://doi.org/10.1002/smll.200700515.

[238] M.C. D'Arrigo, C. Leonelli, Pellacani, S. Komarneni, H. Katsuki, Microwave-Hydrothermal Synthesis of Nanophase Ferrites, J. Am. Ceram. Soc. 81 (11) (1998) 3041–3043.

[239] M. Wolf, N. Fischer, M. Claeys, Surfactant-free synthesis of monodisperse cobalt oxide nanoparticles of tunable size and oxidation state developed by factorial design, Materials Chemistry and Physics 213 (2018) 305–312. https://doi.org/10.1016/j.matchemphys.2018.04.021.

[240] N. Pinna, S. Grancharov, P. Beato, Bonville, P. Antonietti, M., M. Niederberger, Magnetite Nanocrystals: Nonaqueous Synthesis, Characterization, and Solubility, Chem. Mater. 17 (2005) 3044–3049.

[241] M. Wolf, H. Kotzé, N. Fischer, M. Claeys, Size dependent stability of cobalt nanoparticles on silica under high conversion Fischer-Tropsch environment, Faraday Discuss. 197 (2017) 243–268. https://doi.org/10.1039/c6fd00200e.

[242] T.M. Nyati, Supported Cobalt Oxide Catalysts for the Preferential Oxidation of Carbon Monoxide: An in situ Investigation. PhD, Cape Town, South Africa, 2020.

[243] J.A. Moulijn, A.E. van Diepen, F. Kapteijn, Catalyst deactivation: is it predictable? What to do? Applied Catalysis A: General 212 (2001) 3–16.

[244] C.H. Bartholomew, Mechanisms of catalyst deactivation, Applied Catalysis A: General 212 (2001) 17–60.

[245] M. Argyle, C. Bartholomew, Heterogeneous Catalyst Deactivation and Regeneration: A Review, Catalysts 5 (1) (2015) 145–269. https://doi.org/10.3390/catal5010145.

[246] M.V. Twigg (Ed.), CATALYST HANDBOOK, Wolfe Publishing Ltd, 1989.

[247] E. van Steen, M. Claeys, Fischer-Tropsch Catalysts for the Biomass-to-Liquid (BTL)-Process, Chem. Eng. Technol. 31 (5) (2008) 655–666. https://doi.org/10.1002/ceat.200800067.

[248] S. Wang, K. Murata, T. Hayakawa, S. Hamakawa, K. Suzuki, Oxidative dehydrogenation of ethane by carbon dioxide over sulfate-modified Cr2O3/SiO2 catalysts, Catal Lett 63 (1/2) (1999) 59–64. https://doi.org/10.1023/A:1019084030344.

[249] X. Ge, S. Hu, Q. Sun, J. Shen, Surface Acidity/Basicity and Catalytic Reactivity of CeO2/γ-Al2O3 Catalysts for the Oxidative Dehydrogenation of Ethane with Carbon Dioxide to Ethylene, Journal of Natural Gas Chemistry 12 (2003) 199-122.

[250] B. XU, B. ZHENG, W. HUA, Y. YUE, Z. GAO, Support effect in dehydrogenation of propane in the presence of CO2 over supported gallium oxide catalysts, Journal of Catalysis 239 (2) (2006) 470–477. https://doi.org/10.1016/j.jcat.2006.02.017.

[251] W. Marquart, S. Raseale, M. Claeys, N. Fischer, Promoted MoxCy-based catalysts for the CO2 oxidative dehydrogenation of ethane, ChemCatChem (2022). https://doi.org/10.1002/cctc.202200267.

[252] N. Fischer, Preparation of Nano and Ångstrøm sized Cobalt Ensembles and their Performance in the Fischer-Tropsch Synthesis. PhD, Cape Town, South Africa, 2011.

[253] T.M. Nyathi, N. Fischer, A.P.E. York, M. Claeys, Effect of crystallite size on the performance and phase transformation of Co3O4/Al2O3 catalysts during CO-PrOx - an in situ study, Faraday Discuss. 197 (2017) 269–285. https://doi.org/10.1039/c6fd00217j.

[254] C.H. Bartholomew, R.J. Farrauto, Fundamentals of Industrial Catalytic Processes, John Wiley & Sons., 2011.

[255] T.-q. Lei, Y.-h. Cheng, C.-x. Miao, W.-m. Hua, Y.-h. Yue, Z. Gao, Silica-doped TiO2 as support of gallium oxide for dehydrogenation of ethane with CO2, Fuel Processing Technology 177 (2018) 246–254. https://doi.org/10.1016/j.fuproc.2018.04.037.

[256] N.C. Jeong, J.S. Lee, E.L. Tae, Y.J. Lee, K.B. Yoon, Acidity Scale for Metal Oxides and Sanderson's Electronegativities of Lanthanide Elements, Angew. Chem. 120 (52) (2008) 10282–10286. https://doi.org/10.1002/ange.200803837.

[257] G. Prieto, M.I.S. de Mello, P. Concepción, R. Murciano, S.B.C. Pergher, A. Martínez, Cobalt-Catalyzed Fischer–Tropsch Synthesis: Chemical Nature of the Oxide Support as a Performance Descriptor, ACS Catal. 5 (6) (2015) 3323–3335. https://doi.org/10.1021/acscatal.5b00057.

[258] Jonglack Kim, Norbert Pfänder, Gonzalo Prieto, Recycling of CO2 by Hydrogenation of Carbonate Derivatives to Methanol: Tuning Copper–Oxide Promotion Effects in Supported

Catalysts, ChemSusChem 13 (8) (2020) 2043–2052. https://doi.org/10.1002/cssc.202000166@10.1002/(ISSN)1864-564X.hottopic-co2.

[259] G. Prieto, P. Concepción, A. Martínez, E. Mendoza, New insights into the role of the electronic properties of oxide promoters in Rh-catalyzed selective synthesis of oxygenates from synthesis gas, Journal of Catalysis 280 (2) (2011) 274–288. https://doi.org/10.1016/j.jcat.2011.03.025.

[260] F. Kleitz, S.H. Choi, R. Ryoo, Cubic Ia3d large mesoporous silica: Synthesis and replication to platinum nanowires, carbon nanorods and carbon nanotubes, Chem. Commun. (Camb) (17) (2003) 2136–2137. https://doi.org/10.1039/b306504a.

[261] N. Shi, W. Cheng, H. Zhou, T. Fan, M. Niederberger, Facile synthesis of monodisperse Co3O4 quantum dots with efficient oxygen evolution activity, Chem. Commun. (Camb) 51 (7) (2015) 1338–1340. https://doi.org/10.1039/c4cc08179j.

[262] N. Fischer, E. van Steen, M. Claeys, Preparation of supported nano-sized cobalt oxide and fcc cobalt crystallites, Catalysis Today 171 (1) (2011) 174–179. https://doi.org/10.1016/j.cattod.2011.03.018.

[263] P. Kubelka, New Contributions to the Optics of Intensely Light-Scattering Materials Part II: Nonhomogeneous Layers*, J. Opt. Soc. Am. 44 (4) (1954) 330. https://doi.org/10.1364/JOSA.44.000330.

[264] Paul Kubelka, New Contributions to the Optics of Intensely Light-Scattering Materials. Part I, J. Opt. Soc. Am., JOSA 38 (5) (1948) 448–457. https://doi.org/10.1364/JOSA.38.000448.

[265] S. Brunauer, P.H. Emmett, E. Teller, Adsorption of Gases in Multimolecular Layers, Journal of the American Chemical Society 60 (2) (1938) 309–319.

[266] E.P. Barrett, L.G. Joyner, P.P. Halenda, The Determination of Pore Volume and Area Distributions in Porous Substances. I.: Computations from Nitrogen Isotherms, Journal of the American Chemical Society 73 (1) (1951) 373–380.

[267] International centre for diffraction data, Powder Diffraction Files. PDF, 2019.

[268] International centre for diffraction data, Powder Diffraction Files. PDF, 2008.

[269] H.M. Rietveld, A Profile Refinement Method for Nuclear and Magnetic Structures, Journal of Applied Crystallography 2 (1969) 65–71.

[270] W. Rasband, ImageJ, National Institutes of Health, USA.

[271] K.S.W. Sing, D.H. Everett, R.A.W. Haul, R.A. Pierotti, T. Siemieniewska, Reporting physisorption data for gas/solid systems: with special reference to the determination of surface area and porosity, International Union of Pure and Applied Chemistry 57 (4) (1985) 603–619.

[272] J. Kim, B.B. Sarma, E. Andrés, N. Pfänder, P. Concepción, G. Prieto, Surface Lewis Acidity of Periphery Oxide Species as a General Kinetic Descriptor for CO 2 Hydrogenation to Methanol on Supported Copper Nanoparticles, ACS Catal. 9 (11) (2019) 10409–10417. https://doi.org/10.1021/acscatal.9b02412.

[273] G. Prieto, J.D. Meeldijk, K.P. de Jong, P.E. de Jongh, Interplay between pore size and nanoparticle spatial distribution: Consequences for the stability of CuZn/SiO2 methanol synthesis catalysts, Journal of Catalysis 303 (2013) 31–40. https://doi.org/10.1016/j.jcat.2013.02.023.

[274] J. Kim, Oxide promotion effects in copper-catalyzed hydrogenation of CO2 and organic carbonate derivatives. PhD, Bochum, 2019.

[275] Energetics of X-ray-amorphous zirconia and the role of surface energy in its formation, Molodetsky, I; Navrotsky, A; Paskowitz,M.J; Leppert, V.J; Risbud, S.H., Journal of Non-Crystalline Solids 262 (2000) 106–113.

[276] V.G. Keramidas, W.B. White, Raman Scattering Study of the Crystallization and Phase Transformations of ZrO2, Journal of The American Ceramic Society 57 (1) (1974).

[277] M. MARTINEZHUERTA, X. GAO, H. TIAN, I. WACHS, J. FIERRO, M. BANARES, Oxidative dehydrogenation of ethane to ethylene over alumina-supported vanadium oxide catalysts: Relationship between molecular structures and chemical reactivity, Catalysis Today 118 (3-4) (2006) 279–287. https://doi.org/10.1016/j.cattod.2006.07.034.

[278] D. S. S. Padovini, D. S. L. Pontes, C. J. Dalmaschio, F. M. Pontes, E. Longo, Facile synthesis and characterization of ZrO2 nanoparticles prepared by the AOP/hydrothermal route.

[279] C.A. Carrero, R. Schloegl, I.E. Wachs, R. Schomaecker, Critical Literature Review of the Kinetics for the Oxidative Dehydrogenation of Propane over Well-Defined Supported Vanadium Oxide Catalysts, ACS Catal. 4 (10) (2014) 3357–3380. https://doi.org/10.1021/cs5003417.

[280] Z. Wu, H.-S. Kim, P.C. Stair, S. Rugmini, S.D. Jackson, On the structure of vanadium oxide supported on aluminas: UV and visible raman spectroscopy, UV-visible diffuse reflectance spectroscopy, and temperature-programmed reduction studies, J. Phys. Chem. B 109 (7) (2005) 2793–2800. https://doi.org/10.1021/jp046011m.

[281] I.A. Samek, N.S. Bobbitt, R.Q. Snurr, P.C. Stair, Interactions of VO x Species with Amorphous TiO 2 Domains on ALD-Derived Alumina-Supported Materials, J. Phys. Chem. C 123 (13) (2018) 7988–7999. https://doi.org/10.1021/acs.jpcc.8b07424.

[282] X. Zhang, H. Huang, Y. Zhang, D. Liu, N. Tong, J. Lin, L. Chen, Z. Zhang, X. Wang, Phase Transition of Two-Dimensional β-Ga2O3 Nanosheets from Ultrathin γ-Ga2O3 Nanosheets and Their Photocatalytic Hydrogen Evolution Activities, ACS Omega 3 (10) (2018) 14469–14476. https://doi.org/10.1021/acsomega.8b01964.

[283] A. Lahmar, A. Benchaabane, M. Aderdour, A. Zeinert, M. Es-Souni, Temperature influence on microstructure and optical properties of TiO2–Au thin films, Appl. Phys. A 122 (2) (2016) 223. https://doi.org/10.1007/s00339-016-9681-y.

[284] M. Quesada-González, K. Baba, C. Sotelo-Vázquez, P. Choquet, C.J. Carmalt, I.P. Parkin, N.D. Boscher, Interstitial boron-doped anatase TiO 2 thin-films on optical fibres: Atmospheric pressure-plasma enhanced chemical vapour deposition as the key for functional oxide coatings on temperature-sensitive substrates, J. Mater. Chem. A 5 (22) (2017) 10836–10842. https://doi.org/10.1039/C7TA02029E.

[285] A. AmaliRoselin, N. Anandhan, G. Ravi, M. Mummoorthi, T. Marimuthu, Growth and characterization of Sm2O3 thin films by spin coating technique, International Journal of ChemTech Research 6 (2014) 5315–5320.

[286] H. ZHU, Z. Qin, W. Shan, W. Shen, J. Wang, Pd/CeO2-TiO2 catalyst for CO oxidation at low temperature: a TPR study with H2 and CO as reducing agents, Journal of Catalysis 225 (2) (2004) 267–277. https://doi.org/10.1016/j.jcat.2004.04.006.

[287] J. Jin, C. Li, C.-W. Tsang, B. Xu, C. Liang, Catalytic combustion of methane over Pd/Ce–Zr oxides washcoated monolithic catalysts under oxygen lean conditions, RSC Adv. 5 (124) (2015) 102147–102156. https://doi.org/10.1039/C5RA13223A.

[288] J.-G. Kang, B.-K. Min, Y. Sohn, Synthesis and characterization of Sm(OH)3 and Sm2O3 nanoroll sticks, Journal of Material Science 50 (2015) 1958–1964.

[289] Tianwei Wu, Qingbo Yu, Ivo Roghair, Kun Wang, Martin van Sint Annaland, Chemical looping oxidative dehydrogenation of propane: A comparative study of Ga-based, Mo-based, V-based oxygen carriers, Chemical Engineering and Processing - Process Intensification 157 (108137) (2020).

[290] S. Besselmann, C. Freitag, O. Hinrichsen, M. Muhler, Temperature-programmed reduction and oxidation experiments with V2O5/TiO2 catalysts, Phys. Chem. Chem. Phys. 3 (21) (2001) 4633–4638. https://doi.org/10.1039/b105466j.

[291] T.V. Malleswara Rao, Y. Yang, A. Sayari, Ethane dehydrogenation over pore-expanded mesoporous silica supported chromium oxide: 1. Catalysts preparation and characterization, Journal of Molecular Catalysis A: Chemical 301 (2009) 152–158.

[292] D. Shee, A. Sayari, Light alkane dehydrogenation over mesoporous Cr2O3/Al2O3 catalysts, Applied Catalysis A: General 389 (1) (2010) 155–164. https://doi.org/10.1016/j.apcata.2010.09.013.

[293] K. H. H. (Ed.), Transition Metal Oxides: Studies in Surface Science and Catalysis, Elsevier, 1998.

[294] M. Niederberger, G. Garnweitner, Organic reaction pathways in the nonaqueous synthesis of metal oxide nanoparticles, Chemistry 12 (28) (2006) 7282–7302. https://doi.org/10.1002/chem.200600313.

[295] K.N. Han, E. Narita, F. Lawson, THE COPRECIPITATION BEHAVIOR OF Co(II) AND Ni(II) WITH Fe(III), Cr(III) AND Al(III) FROM AQUEOUS AMMONIACAL SOLUTIONS, Hydrometallurgy 8 (1981) 365–377.

[296] P.W. Atkins, Overton,, T.L., J.P. Rourke, M.T. Weller, Inorganic Chemistry, Oxford University Press, Britain, 2010.

[297] O. Kubaschewski, IRON-Binary Phase Diagrams, Springer, Berlin, Heidelberg, 1982.

[298] L. Liu, H. Jiang, H. Liu, H. Li, Recent Advances on the Catalysts for Activation of CO2 in Several Typical Processes, Elsevier, 2013.

[299] L. Liao, Q. Zhang, Z. Su, Z. Zhao, Y. Wang, Y. Li, X. Lu, D. Wei, G. Feng, Q. Yu, X. Cai, J. Zhao, Z. Ren, H. Fang, F. Robles-Hernandez, S. Baldelli, J. Bao, Efficient solar water-splitting using a nanocrystalline CoO photocatalyst, Nature Nanotech 9 (1) (2014) 69–73. https://doi.org/10.1038/nnano.2013.272.

[300] H.-C. Shin, S.-C. Choi, K.-D. Jung, S.-H. Han, Mechanism of M Ferrites (M) Cu and Ni) in the CO2 Decomposition Reaction, Chem. Mater. 13 (2001) 1238–1242.

[301] M. Saito, S. Watanabe, I. Takahara, M. Inaba, K. Murata, Dehydrogenation of propane over a silica-supported gallium oxide catalyst, Catal Lett 89 (2003) 213–217.

[302] L. Lin, M. Lai, H. Li, F. Tian, Y. Chen, J. Sun, J.-M. Lin, Investigation of carbon deposition induced by pyrolytic decomposition of ethylene, RSC Adv. 7 (47) (2017) 29639–29644. https://doi.org/10.1039/C7RA04282E.

[303] I. Luisetto, S. Tuti, C. Battocchio, S. Lo Mastro, A. Sodo, Ni/CeO2–Al2O3 catalysts for the dry reforming of methane: The effect of CeAlO3 content and nickel crystallite size on catalytic activity and coke resistance, Applied Catalysis A: General 500 (2015) 12–22. https://doi.org/10.1016/j.apcata.2015.05.004.

[304] S.-H. Lee, H.M. Cheong, M.J. Seong, P. Liu, C.E. Tracy, A. Mascarenhas, J.R. Pitts, S.K. Deb, Raman spectroscopic studies of amorphous vanadium oxide thin films, Solid State Ionics 165 (1-4) (2003) 111–116. https://doi.org/10.1016/j.ssi.2003.08.022.

[305] P. Bhardwaj, J. Singh, R. Kumar, D. Kumar, V. Verma, R. Kumar, Oxygen defects induced tailored optical and magnetic properties of FexCr2−xO3 (0 ≤ x ≤ 0.1) nanoparticles, Appl. Phys. A 128 (2) (2022) 965. https://doi.org/10.1007/s00339-021-05233-x.

[306] S. Jiang, J. Liu, C. Lin, X. Li, Y. Li, High-pressure x-ray diffraction and Raman spectroscopy of phase transitions in Sm 2 O 3, Journal of Applied Physics 113 (11) (2013) 113502. https://doi.org/10.1063/1.4795504.

[307] M. Lubas, J.J. Jasinski, M. Sitarz, L. Kurpaska, P. Podsiad, J. Jasinski, Raman spectroscopy of TiO2 thin films formed by hybrid treatment for biomedical applications, Spectrochimica Acta Part A: Molecular and Biomolecular Spectroscopy 133 (2014) 867–871. https://doi.org/10.1016/j.saa.2014.05.045.

[308] R. Rao, A.M. Rao, B. XU, J. Dong, S. Sharma, M.K. Sunkara, Blueshifted Raman scattering and its correlation with the [110] growth direction in gallium oxide nanowires, Journal of Applied Physics 98 (9) (2005) 94312. https://doi.org/10.1063/1.2128044.

[309] L. Puust, V. Kiisk, K. Utt, H. Mändar, I. Sildos, Afterglow and thermoluminescence of ZrO2 nanopowders, Open Physics 12 (6) (2014) 371. https://doi.org/10.2478/s11534-014-0456-9.